Realization of atomically smooth defect free InGaAs/InAlAs superlattice on InP(111) substrate by molecular beam epitaxy

by

Ida Sadeghi

A thesis

presented to the University of Waterloo

in fulfillment of the

thesis requirement for the degree of

Doctor of Philosophy

in

Electrical and Computer Engineering

Waterloo, Ontario, Canada, 2021

© Ida Sadeghi 2021

Examining Committee Membership

The following served on the Examining Committee for this thesis. The decision of the Examining Committee is by majority vote.

External Examiner:	Paul Simmonds Professor, Dep. of Physics Boise State university
Supervisor(s):	Zbigniew Wasilewski Professor, Dep. of Electrical and Computer Engineering University of Waterloo
Internal Member:	Guoxing Miao Professor, Dep. of Electrical and Computer Engineering University of Waterloo
Internal Member:	Na Young Kim Professor, Dep. of Electrical and Computer Engineering University of Waterloo
Internal-External Member:	Kam Tong Leung Professor, Dep. of Chemistry University of Waterloo

Author’s declaration

I hereby declare that I am the sole author of this thesis. This is a true copy of the thesis, including any required final revisions, as accepted by my examiners.

I understand that my thesis may be made electronically available to the public.

Abstract

InGaAs and InAlAs epilayers and superlattices were grown on rounded edge InP(111)A and InP(111)B substrates as well as on 0.45°, 1° and 2° misoriented InP(111)B substrates by Molecular Beam Epitaxy (MBE). Rounded edge wafers exposed a broad spectrum of vicinal surfaces with varying misorientation angles. The structures grown were characterized *in-situ* using Reflection High Energy Electron Diffraction (RHEED) and *ex-situ* using Nomarski differential interference contrast (DIC) microscopy, Atomic Force Microscopy (AFM), High Resolution X-Ray Diffraction (HRXRD) and scanning transmission electron microscopy (STEM). Optimum misorientation angle for growth on InP(111)B substrate was found. Conventional MBE growth at many different growth conditions did not result in a smooth surface morphology at the center of the rounded edge wafers, i.e. when growth was done on singular InP(111)A and InP(111)B substrates. However, a smooth surface morphology was observed at the rounded edge for both InP(111)B and InP(111)A substrates, which was more evident for InP(111)B substrate.

It was shown that the optimum misorientation angle for the growth of InGaAs and InAlAs on InP(111)B substrate is different; it is larger for the growth of InAlAs. This is indicative of different migration length of Ga and Al adatoms on the surface. Density Functional Theory (DFT) calculations showed that the adsorption energy of Al atom is larger than that of Ga and In atoms leading to a stronger bond of Al to the surface and consequently a slower diffusion rate on the surface. Therefore, a slower growth rate is needed for the growth of InAlAs layer compared to InGaAs layer. This entails separate optimization of growth condition for the two different layers to eliminate morphological (hillocks) and microstructural (twining and stacking faults) defects.

Morphological defects originate from a low migration length of the adatoms on the surface. Growth on vicinal surfaces with narrowed terrace width to promote the step-flow growth mode is an effective way to avoid hillocks. Scanning Transmission Electron Microscopy (STEM) results revealed the presence of V-type twinning and stacking faults just under the hillocks when growth is performed on singular (111) substrates. At a moderate growth temperature of 460°C, growth of atomically smooth defect free nominally lattice-matched InGaAs/InAlAs superlattice on InP(111)B was achieved for the first time through a systematic optimization of the substrate misorientation angle as well as growth conditions. STEM analysis revealed that in fact the supperlattice is free of any defect.

The presence of strain in the structure introduces defects to account for the mismatch or relieve the strain. It was seen that i) misfit dislocations that are dissociated into stacking faults bounded by partial dislocations at both ends, i) phase separation that is

the formation of regions of rich in In and poor in Ga or Al and vice versa, and iii) rotation of the crystal lattice at some regions within the microstructure are the main mechanisms for strain relief.

The effect of substrate annealing temperature on the surface reconstructions of InP(111)A and InP(111)B was studied using Low energy electron diffraction (LEED). It was seen that InP(111) substrate preserves a (1×1) unreconstructed surface at all the annealing temperatures studied from 250°C to 500°C, therefore, it is thermally stable. On the other hand, InP(111)A changes its reconstruction from (2×2) at low annealing temperatures to a mixture of (2×2) and (3×3) at medium annealing temperatures and eventually to a (3×3) reconstruction at high annealing temperatures, therefore, it is not thermally stable. Since the surface reconstruction plays an important role in the growth quality as was evidenced by the very different growth morphologies achieved on InP(111)A and InP(111)B substrates, different growth temperatures for growth on InP(111)A could result in a very different growth quality, while growth on InP(111)B is less affected by the growth temperature.

Acknowledgements

First and the foremost, I would like to thank my advisor, Zbigniew Wasilewski, for his continuous support and advise during my PhD program. I would not have been where I am today if it was not for his emotional and financial support. I should say add that my PhD program coincided with the COVID era. Although it was not an easy situation for a grad student, Zbig's continuous encouragement kept me stay focused and strong to move forward.

Second, I would like to thank the committee members Profs. Paul Simmonds, Kam Tong Leung, Na Young Kim and Guo-xing Miao for taking the time to read my thesis and attend the defence. Their comments are valuable and sure to improve the thesis.

Third, I would like to thank my collaborator Alexandre Pofelski from Canadian Centre for Electron Microscopy for his dedicated work on scanning transmission electron microscopy imaging of the thin films and for his great aptitude to help. I also would like to thank Hanieh Farkhondeh from WatLab for her great initiation in doing surface studies on the InP(111) substrates that has long been a question. It was unfortunate that the COVID situation interrupted our great experience together.

Fourth, I would like to thank Prof. Kam Tong Leung for giving me the opportunity to collaborate with them and access WatLab, Prof. Guoxing for giving me access to their X-ray diffraction machine, Prof. Pu Chen for giving me access to their atomic force microscope and Prof. Paul Simmonds for his valuable advise on growth on mysterious (111) substrates.

Last but not least, I would like to thank all my group members especially Man Chun Alan Tam for their great help and work during the molecular beam epitaxy system maintenance.

It was such a joy and pleasure to work with all of you.

Dedication

I would like to dedicate this thesis to whom always pushed me on my educational path, to whom kept me motivated in this path that coincided with unfortunate COVID era, and to whom facilitated moving on this path towards its end.

Table of Contents

List of Figures xii

List of Tables xxiv

List of Abbreviations xxvi

1 Introduction 1

1.1 Motivation 1

1.2 Thesis outline 3

2 Photo-Conductive Antenna (PCA) for Terahertz (THz)-Time Domain Spectroscopy (TDS) 5

2.1 THz TDS 5

2.2 Requirements for TDS system 7

2.2.1 Material system 7

2.2.2 Low temperature growth 8

2.2.3 Engineering of the excess arsenic location 12

3 A review of growth on (111) substrates 18

3.1 (111) surface characteristics 18

3.1.1 Migration length 18

3.1.2 Surface reconstruction 21

3.1.3 Dangling bonds 23
3.2 Growth challenges 26
3.2.1 Surface steps (hillocks) 26
3.2.2 Step bunching 29
3.2.3 Twinning and phase instability 30
3.2.4 Short-range ordering 33
3.2.5 Compositional Modulation (CM) 34
3.2.6 Mismatch-induced strain 38
3.3 Growth improvement methods 40
3.3.1 Growth on vicinal surfaces 40
3.3.2 Surfactant-mediated growth 45
3.3.3 Migration Enhanced Epitaxy Migration Enhanced Epitaxy (MEE) . 48
3.3.4 Metal modulation epitaxy (Metal Modulation Epitaxy (MME)) . . . 49
3.3.5 Effect of substrate cleaning 49

4 Experiment **51**
4.1 Fundamentals of Molecular Beam Epitaxy (MBE) 51
4.2 Flux calibration of group III and V cells 52
4.3 *In-situ* growth characterization techniques 58
4.3.1 Reflection high energy electron diffraction Reflection High Energy Electron Diffraction (RHEED) 58
4.3.2 Reflectance monitoring 59
4.3.3 *In-situ* temperature monitoring using Band Edge Thermometry (BET) 60
4.4 *Ex-situ* growth characterization techniques 62
4.4.1 Atomic Force Microscopy (AFM) 62
4.4.2 Nomarski Differential Interference Contrast (DIC) microscopy . . 62
4.4.3 Scanning transmission electron microscopy (Scanning Transmission Electron Microscopy (STEM)) 63

4.4.4 STEM Moiré GPA (SMG) 64
4.4.5 X-ray Photoelectron Spectroscopy (XPS) 65
4.4.6 Low energy electron diffraction (LEED) 67
4.4.7 High Resolution X-Ray Diffraction High Resolution X-Ray Diffraction (HRXRD) 68
4.5 Collaborative works 69

5 Optimum off-cut angle for growth 70
5.1 Experiment 70
5.2 Results and Discussion 73
5.3 Summary 81

6 The origin of the surface steps 84
6.1 Experiment 84
6.2 Results and Discussion 85
6.3 Summary 91

7 Surface analysis of InP(111)A and InP(111)B substrates 93
7.1 Experiment 94
7.2 Results and Discussion 95
7.3 Summary 104

8 Growth of InGaAs-InAlAs superlattice 108
8.1 Experiment 108
8.2 Results and Disscusion 110
8.3 Summary 119

9 Growth of InGaAs-InAlAs superlattice using MEE and MME techniques 120
9.1 Experiment 120
9.2 Results and Discussions 122
9.3 Summary 127

10 Defect analysis in InGaAs-InAlAs superlattices **131**
10.1 Experiment 131
10.2 Results and Discussion 131
10.3 Summary 143

11 Summary and Conclusions **144**

12 Future work **146**

Letters of copyright permission **148**

References **191**

APPENDICES **212**

A Geometrical Phase Analysis (GPA) and SMG **213**
A.1 GPA 213
A.2 SMG 215

B Base change for elasticity matrix **217**

List of Figures

2.1 a) Carrier concentration of Low Temperature (LT) InGaAs. b) Be doping and carrier concentration [46] ©OSA Publishing. Used with permission. c) Schematic of the InGaAs/InAlAs band-diagram with deep cluster-induced defect states [19] ©OSA Publishing. Used with permission. d) Current vs voltage characteristics of the Photo-Conductive Antenna (PCA) made from LT $In_xGa_{1-x}As$ under various excitations at 1.56 μm. The open and filled symbols correspond to $x = 0.53$ and 0.45, respectively [47] ©AIP Publishing. Used with permission. 9

2.2 a) Lattice constant expansion due to the presence of excess arsenic, and b) effect of Beam Equivalent Pressure (BEP) and c) growth temperature on the critical layer thickness that can be grown defect free [53] ©Springer Nature. Used with permission. 10

2.3 A schematic showing arsenic antisite, As_{Ga}, and Ga vacancy, V_{Ga} present in a LT grown GaAs layer [55] ©AIP Publishing. Used with permission. . . . 11

2.4 Depletion regions around arsenic precipitates when a) they just overlap and b) they are distanced causing an undepleted region in between [65] ©Annual Reviews. Used with permission. 13

2.5 a) Arsenic precipitate with Moire pattern [67] ©Springer Nature. Used with permission. b) small region of hexagonal arsenic between two InAlAs grains of different orientations before annealing. Fourier transform in the inset shows the 6-fold symmetry of these defects [58] ©Elsevier. Used with permission. 14

2.6 TEM image of a) A series of 10-period superlattices of progressively wider $Al_{0.3}Ga_{0.7}As$ barriers or GaAs wells grown at low temperatures and then annealed at 700°C for 30 s [65] ©Annual Reviews. Used with permission. b) A structure grown at 260°C. The AlAs layers and the GaAs regions between them were grown by Migration Enhanced Epitaxy (MEE), while the $Al_{0.2}Ga_{0.8}As$ layers were grown by Molecular Beam Epitaxy (MBE) with large excess arsenic [74] ©Elsevier. Used with permission. 15

2.7 Transmission Electron Microscopy (TEM) image of a series of GaAs regions uniformly doped with Si followed by a GaAs region uniformly doped with Be and subsequently annealed at a) 700°C for 30 s and b) 900°C for 30 s. Attraction to and coarsening of arsenic clusters on the negatively charged Si doped regions in GaAs and repulsion of the arsenic clusters from the positively charged Be doped regions is seen [74] ©Elsevier. Used with permission. 16

2.8 Comparison of band edge profiles, spatial probabilities $|\psi|^2$ of finding e, lh, and hh, and expected distribution of excess As for $In_{0.4}Ga_{0.6}As$ well and $In_{0.7}Al_{0.3}As$ barriers grown on InP(001) and InP(111) substrates. Band structures were calculated using nextnano3 software. 17

3.1 A schematic illustration showing the change in Reflection High Energy Electron Diffraction (RHEED) information as the growth mode changes from step-flow to two-dimensional [79] ©AIP Publishing. Used with permission. 19

3.2 The energy levels, ϵ_h, of the sp^3 dangling bond states of GaAs. The energies are derived from the energies of the s, ϵ_s, and p orbitals, ϵ_p [97] ©American Physical Society. Used with permission. 22

3.3 Surface reconstructions of GaAs(111)B as a function of As flux and temperature during MBE growth [111] ©AIP Publishing. Used with permission. . 23

3.4 a) Top view of the single gallium vacancy model of a GaAs(111)A-(2 × 2) reconstruction [98] ©American Physical Society. Used with permission. b) detailed model of GaAs($\overline{111}$)B-($\sqrt{19} \times \sqrt{19}$) large open circles denote top As atoms, medium closed circles denote second-layer Ga atoms, and small open circles denote third-layer three fold coordinated As atoms [113] ©American Physical Society. Used with permission. 24

3.5 a) the charge distribution of InP(111)B along the surface normal. b) The average bulk potential of GaAs and InP along the $[\overline{111}]$ direction. The dashed lines correspond to the electrostatic potentials, while the full lines are the effective potentials [114] ©Elsevier. Used with permission. 24

3.6 Schematic representation of a) dangling bonds of phosphorous atoms chemically absorbed on (111)A, (001) and (111)B surfaces [115] ©Elsevier. Used with permission. b) step disorder in A and B (111) surfaces [116] ©Elsevier. Used with permission. 25

3.7 a) Optical microscope image of the GaAs singular substrate after 0.5 μm homoepitaxial growth, b) an AFM image of the top of the one of the pyramids in a [6] ©American Vacuum Society. Used with permission. c) terrace-step structure of films grown on substrates with different misorientations [9] ©American Vacuum Society. Used with permission. 27

3.8 a) triangular (pyramidal) and b) circular islands formed on singular InP(111)A surface during the Metal Organic Chemical Vapor Deposition (MOCVD) growth of InGaAs [119] ©John Wiley and Sons. Used with permission. . . 28

3.9 RHEED beam intensity change with substrate temperature on GaAs(111)B at a constant arsenic pressure. The open circle shows the starting point that results in a specular surface [22] ©AIP Publishing. Used with permission. 28

3.10 Schematic distribution of surface adatoms on a) a wide terrace with step-flow growth mode and b) a narrow terrace with step bunching [122] ©AIP Publishing. Used with permission. 29

3.11 a) Bright field cross-sectional image of InAlAs grown on InP(111)B. Threading dislocation originated approximately 40nm from the InAlAs/InP interface go to the step edges. Steps run along the misorientation direction. The fringe contrast appearing through the entire film is due to the structural inhomogeneities from compositional modulation (alternative In and Al rich domains). b) Plane view TEM image of the surface. Bunched steps are indicated with black arrows. Dislocations running from the bunched steps along $[\overline{3}21]$ (circle) [2] ©AIP Publishing. Used with permission. . . . 31

3.12 Building blocks of a) Zinc Blende (ZB) and b) Wurtzite (W), c) W(0001) and d) ZB(111), and e) Structure of twin ZB formed by a stacking fault [132] ©American Vacuum Society. Used with permission. f) Schematic representation of V-type twin complex. $(\overline{1}\overline{1}\overline{1})$ and $(11\overline{1})$ are the twin planes (the two variant of 111 planes), which belong to the $[1\overline{1}0]$ zone. Twining of twin I along a non-growth direction created twin III [5] ©AIP Publishing. Used with permission. 32

3.13 Transmission electron diffraction pattern of InGaP grown at 700° C on a) (111)B and b) (001)GaAs substrate [25] ©IOP Publishing. Used with permission. c) Ordering mechanism i: Column V element (P or As)-stabilized (001) plane with an In atom at position s_{00}. The In atom stretches the lattice spacing producing an anisotropic site occupation affinity for Ga and In, which generates a long-range order on a (001) plane. Note the two dangling bond directions on element V. a_0, indicates the column V atom spacing before the In atom sticking. s_{ij} indicates the site positions for column III atoms. Lattice constants for some binaries are reported. In parentheses, lattice constants normalized to that for GaAs are given. d) Ordering mechanism ii: In and Ga rich planes locked in alternative layers [144] ©Elsevier. Used with permission. 35

3.14 a) cross-sectional TEM showing slight corrugation in the nominally lattice-matched AlAs/InAs short period SuperLattice (SL) [135] ©Springer Nature. Used with permission. b) a schematic representation of the consequence of a lateral composition modulation on the TEM contrast via a surface elastic relaxation of the strained InAlAs surface [146] ©Elsevier. Used with permission. c) Phase diagram of epitaxial InGaAs alloy grown at a growth rate of 0.1 ML/s showing two modulated regions (in which the alloy will present a kinetically stabilized composition modulation) with a homogeneous region in between. Two regions of modulated alloys are separated by a homogenous region due to the limitation of growth rate [147] ©AIP Publishing. Used with permission. 36

3.15 Schematic diagram illustrating how a strain-induced surface corrugation can initiate composition modulation for both compressive and tensile strains. Smaller atoms preferentially attach where the lattice is compressed, and larger atoms attach where it is dilated, thus initiating lateral composition modulation [135] ©Springer Nature. Used with permission. . 37

3.16 A schematic showing a) possible atom termination of the steps in GaAs(111)B surface misoriented by 1° towards $[2\bar{1}\bar{1}]$ and b) step bunching of In-rich and N-rich layers [157] ©Elsevier. Used with permission. 39

3.17 a) Strain dependence of surface lattice relaxation for InGaAs obtained from RHEED measurement grown at 510° C. b) Growth temperature dependence of surface lattice relaxation for the growth of $In_xGa_{1-x}As$ with $x = 0.58$ grown on GaAs-(111)B substrates [28] ©AIP Publishing. Used with permission. 41

3.18 Schematic representation of a) a singular and a vicinal surface, and step bunching [169] ©Royal Society of Chemistry. Used with permission. b) Schematic representation of the single-layer and double-layer step structures of a vicinal Si(100) surface. The surface misorientation θ is related to the terrace width L by $tan(\theta) = z_{SL}/L$, where z_{SL} is the height of a single layer step [166] ©American Physical Society. Used with permission. 42

3.19 Nomarski images of the surface morphology of InGaAs grown on a) (100), b) misoriented 1° towards <211> and c) singular InP(111)B. d) High resolution $\theta/2\theta$ scan at <333> reflection of a-c [33] ©AIP Publishing. Used with permission. 43

3.20 Morphology change of a GaAs layer grown on a curved surface towards [100] near the edge region of an exactly (111)B substrate [23]. ©IOP Publishing. Used with permission. 44

3.21 Cross-sectional TEM image of strained InGaAs multi Quantum Well (QW)s grown on (100)InP a) with and b) without Sb surfactant. The thickness undulation of the wells that shows a three-dimensional growth is the origin of the structural defects. Suppression of the defects and undulation when Sb surfactant is used is seen [178] ©AIP Publishing. Used with permission. 46

3.22 effect of Bi surfactant on the surface morphology of GaNAs; a) no Bi, b) Bi BEP $\sim 10^{-7}$ Torr and c) Bi BEP $\sim 1.4 \times 10^{5}$ Torr. In the absence of Bi, surface morphology is anisotropic with surface features elongated in $[01\bar{1}]$ direction shown by arrow. The surface roughness is 1.2 nm. The growth morphology changes dramatically at high Bi flux and an rms roughness of 0.1 nm is achieved as in c). At medium Bi pressure, the surface is fairly isotropic with an rms roughness of 0.4 nm. Bi reduces the adatom bond strength at the step edges by forming GaNAs-Bi complex on the surface [181] ©Elsevier. Used with permission. 47

4.1 Gen 10 MBE system consisting of growth chamber for growth, preparation chamber for oxide desorption prior to growth, cluster tool for storage and load lock for loading the wafers. Gen 10 MBE system is equipped with ion pump, cryopump, RGA to monitor the impurity gas species, RHEED to monitor the surface morphology, Beam Flux Monitoring (BFM) and ion gauges to monitor the fluxes. 53

4.2 Mutual position of effusion cells and substrates in an MBE growth chamber. The dashed and dotted lines represent the axes of cells and substrates, respectively [198] ©Elsevier. Used with permission. 54

4.3 A typical Band Edge Thermometry (BET) a) band-edge spectrum showing the absorption edge and b) real-time temperature monitoring during the growth of sample G showing some oscillation. 61

4.4 Schematic of translational Scanning Moiré Fringe (SMF)s formed by the harmonic interference between lattice spacing d_l and the scanning grating with a spacing of d_s. a) The lattice spacing d_l represents a strain field that linearly increases along the horizontal direction, b) scanning grating spacing as acquired via Scanning Transmission Electron Microscopy (STEM) imaging, and c) SMFs formed by overlapping of the lattice spacing d_l and scanning grating spacing d_s [206] ©AIP Publishing. Used with permission. 66

4.5 Calculated inelastic electron mean free path from experimental optical data as a function of primary electron energy from 41 elemental solids [207] ©John Wiley and Sons. Used with permission. 68

5.1 Lattice constants and bandgaps of common III-V semiconductors. 71

5.2 a) InP mounted on GaAs using In-Ga eutectic and b) free floating InP on sapphire plate ©American Vacuum Society. Used with permission. 72

5.3 AFM height images of the bare InP(111)B singular substrate with rounded edge at a) centre and b-f) increasing distance from the flat centre towards the edge. 75

5.4 Nomarski images taken at the edge of a) sample A1 showing no apparent smooth region and b) sample A2 showing a smooth edge where there is mis-cut. Corresponding Atomic Force Microscopy (AFM) height images of c) sample A1 at the edge showing an Root Mean Square (RMS) roughness of 22.01±3.58 nm and d) sample A2 at the transition from smooth to rough region ©American Vacuum Society. Used with permission. 76

5.5 AFM height images of sample A3 showing a) evolution of the hillocks at the edge, b) monolayer step-flow growth mode adjacent to the pyramidal hillocks at an off-cut angle of 0.4° (RMS roughness = 0.52± 0.04 Å), step bunching at an off-cut angle of c) 1.7° with an average step height of 3.5 monolayers (RMS roughness = 0.74± 0.06 Å) and d) 3° with an average step height of 5.5 monolayers (RMS roughness = 4.3± 0.4 Å). 77

5.6 A contour map illustrating (not in scale) the rough center region (1), transition region where the hillocks are forming (2), smooth region (3) and rough region at the very edge of sample A3 (4). The rough edge region, the smooth region and the transition region are about 75, 150 and 50 μ m wide, and b) the change of RMS roughness versus off-cut angle ©American Vacuum Society. Used with permission. 78

5.7 Step leveling to find the off-cut angle for a) Fig. 5.5.c and b) Fig. 5.5.d ©American Vacuum Society. Used with permission. 79

5.8 The Nomarski Differential Interference Contrast (DIC) images at the edge of sample A3 at different azimuths; a) $[1\bar{2}1]$ and b) $[0\bar{1}1]$ showing different hillocks' geometry. The width of the smooth region is 181 μm 80

5.9 a) Calculated adsorption energies (in eV) for Al (red circles), Ga (blue squares), In (black triangles), and As (grey inverted triangles) adatoms on the P-terminated InP(111)B-1×1 surface as a function of adsorption site. b) Schematic atomic structure (top and side views) for the InP(111)B-1×1 surface. The surface unit cell and the potential adsorption sites are shown. 82

6.1 STEM images of sample A on a-c) singular (111) and d-f) vicinal (111) surface. The striations in Fig. e are the STEM Moiré fringes which are indicative of strain variations in InGaAs and InAlAs epilayers due to compositional non-uniformities and defects. A stacking fault and a twin are circled in Figs. e and b, respectively. The diffraction pattern is shown as the inset of Fig. e. High Resolution Scanning Transmission Electron Microscopy (HRSTEM) images of a stacking fault in the smooth region (f) and a high density of stacking faults at the center of the wafer (c) are shown. 86

6.2 STEM image of sample A at a) higher magnification, b) lower magnification showing the white-ish defect and c,d) Electron Energy Loss Spectroscopy (EELS) maps showing phase separation in the InAlAs layer. 87

6.3 STEM Moiré GPA (SMG) relative deformation maps of sample A recorded in the smooth region using the InP as the unstrained reference state. a) STEM Moiré hologram covering the InP/InAlAs/InGaAs stack and its Fourier transform (inset) highlighting the Moiré vectors used for SMG. Deformation maps from the 2D strain and rotation tensors components b) ϵ_{xx} and c) ϵ_{yy} projected on the orthonormal base $B = (O, (u_x), (u_y))$ oriented along the $[\bar{2}11]$ and [111] directions. d) ϵ_{xx} and ϵ_{yy} deformation profiles along the green rectangles in b) and c). The purple arrows show the In rich lines going along $[11\bar{1}]$ direction indicating phase separation in InAlAs layer. 88

7.1 Schematic representations of take-off angle variation and sampling depth in Angle-Resolved X-Ray Photoelectron Spectroscopy (ARXPS), normal emission (left) showing a take-off angle of 0° and angle-resolved emission (right) showing the take-off angle of θ°. Increased take-off angle results in reduced sampling depth (d). 95

7.2 Low energy electron diffraction (LEED) images of flash annealed substrates at 460° C. a) InP(111)A at a beam energy of 135.6 eV and InP(111)B at a beam energy of 51.9 eV. 96

7.3 InP(111)B a) annealed inside the MBE main chamber (RMS roughness = 6.68±0.94 Å) and b) flash annealed (RMS roughness = 5.28±1.04 Å), at 458° C. 96

7.4 Scanning Tunneling Microscopy (STM) images of InP(111)B at low temperature after flash annealing. 97

7.5 LEED pattern of InP(111)B a) before sputter annealing, Ar ion sputtered at 5kV for 20 min and annealed at b) 250° C, c) 300° C and b) 400° C. Electron beam energies were 75.2 eV, 53.7 eV, 51 eV and 59.1 eV for a, b, c and d, respectively. 98

7.6 LEED pattern of InP(111)A after a) sputtering at 5kV for 20 min and annealed at b) 250° C, c) 300° C, d) 400° C, e) 450° C and f) 500° C. Electron beam energies were 59.1 eV, 60.4 eV, 59.1 eV, 40.8 and 32.7 eV for a, b, c, d and e, respectively. 99

7.7 a) In3d and b) P2p grazing emission X-ray Photoelectron Spectroscopy (XPS) spectra from InP(111)B surface after various annealing treatment. . 102

7.8 a) In3d and b) P2p grazing emission XPS spectra from InP(111)A surface after various annealing treatment. 103

7.9 RHEED pattern of InP(111)A surface showing a (2×2) surface reconstruction. 105
7.10 A shematic showing the buckling In-vacancy (2×2) surface reconstruction of InP(111)A surface. a) top view, b)topmost layer, c) side view of a and d) side view of b. 105
7.11 A shematic showing the P-trimer (2×2) surface reconstruction of InP(111)A surface. a) top view, b)topmost layer, c) side view of a and d) side view of b. 106
7.12 RHEED pattern of InP(111)B surface showing a (1×1) surface reconstruction. 106
7.13 A shematic showing the (1×1) surface reconstruction of InP(111)B surface. a) top view, b)topmost layer, c) side view of a and d) side view of b. 107

8.1 Plot of Bragg angle at different azimuths from 0 to 360° measured by High Resolution X-Ray Diffraction (HRXRD) rocking curves. 109
8.2 Schematic of different structures grown. 109
8.3 AFM height images of the a) sample B showing an RMS roughness of 23.9 ± 5.5 Å, b) sample C showing an RMS roughness of 19.2 ± 3.0 Å, c) sample D showing an RMS roughness of 47.5±10.8 Å, d) sample E showing an RMS roughness of 6.3 ± 0.7 Å, e) sample F showing an RMS roughness of 50.78±10.3 Å and f) sample G showing an RMS roughness of 4.29±0.37 Å. The average Mono-Layer (ML) height is 2.5 ML. Please see table 8.1 for sample description. 112
8.4 Nomarski images of samples a) B, b) C, c) D, d) E, e) F and f) G. 113
8.5 950 nm and 470 nm reflectance monitoring of sample G. 114
8.6 HRXRD on sample G. 116
8.7 STEM images of sample G at a-c) three different magnifications. A cropped Fourier transform of a STEM micrograph in the SL (not present in the figure) is shown as an inset in c) to highlight the resolved crystalline lattices and d) the buffer layer. 118
8.8 a) ϵ_{xx} and b) ϵ_{yy} SMG relative deformation maps. The STEM micrographs on the left of the maps are present to help identifying the different regions (InP, buffer, SL). c) the ϵ_{xx} and ϵ_{yy} vertical deformation profiles from the strain maps in a-b). 119

9.1 A schematic comparison between MBE, MEE and Metal Modulation Epitaxy (MME). 121

9.2 A schematic showing the experiment set-up for MEE and MME growths. 121
9.3 950 nm and 470 nm reflectance monitoring of sample I. 122
9.4 HRXRD and simulation data for growth of sample I. 123
9.5 950 nm and 470 nm reflectance monitoring of sample J. 124
9.6 a)1 μm^2AFM scan of sample J showing an RMS roughness of 0.90 ± 0.13 Å, b) EELS maps at the interface c) low magnification STEM micrograph showing no hillock on the surface and d) higher magnification STEM micrograph showing the presence of numerous stacking faults resulted in phase instability between ZB and Wphases. 125
9.7 950 nm and 470 nm reflectance monitoring of sample a) K and b) L. 126
9.8 RHEED pattern of sample a-b) sample K and c-d) sample L at the high symmetry azimuths. 127
9.9 AFM images of sample K at the a) center with an RMS roughness of 2.0 ± 1.2 nm and b) edge of the wafer with an RMS roughness of $2.65 \pm 1 nm$. The wedding cake in a) is about 6 nm tall and those in b) are in average about 7 nm tall. 128
9.10 a-b) AFM and c-d) STEM images of sample L showing the presence of morphological and microstructural defects. The RMS roughness measured on a) and b) is 2.97 nm. 129
9.11 RHEED pattern at high symmetry azimuths of sample a-b) sample M and c-d) sample N. 130

10.1 950 nm and 470 nm reflectance monitoring of sample H. 132
10.2 HRXRD data and simulation result of sample H. 133
10.3 Nomarski image of the sample H. 134
10.4 AFM height images of sample H showing a) an over view of the surface (RMS roughness=1.63 ± 0.32 nm), b) 5 μm^2 (RMS roughness=7.18 ± 1.53 Å) and c) 2 μm^2 (RMS roughness=4.53 ± 1.11 Å) scans showing surface triangle features and d) smooth surface morphology in between of the triangle features (RMS=2.29 ± 0.5 Å). 135

10.5 STEM micrographs of sample H at different magnifications: a) low magnification High-Angle Annular Dark- Field (HAADF) (left) and diffraction contrast (right) images providing a general overview of the entire growth, b,c) high magnification resolving the crystalline lattices in the SL and d-f) intermediate magnification from the bottom to the top of the stack focusing on the defects' distribution. The left and right images in a) are recorded on the same area with a low Z contrast and a high diffraction contrast camera length, respectively. 136

10.6 Visualization of the defects observed in the buffer layer of sample H. The arrows refer to the families of perturbations mentioned in Fig. 10.5. a) HRSTEM electron micrograph centered on multiple defects in the buffer layer and near the interface with the InP substrate. b-d) digitally magnified version of a) showing a stacking fault defect with the associated Burgers vector along the [112] direction. e) Inset of a) highlighting crystal rotation showed by orange arrow. f) HRSTEM micrograph on the buffer layer highlighting a twin defect. g-h) digitally magnified version of f) focused on the twin and the stacking faults defects. 137

10.7 High magnification STEM images of sample H focusing on different defects pointed out by different color arrows within the SL. a) HRSTEM micrograph in the SL capturing the defects pointed by yellow and orange arrows. b,c) insets from a) showing a stacking fault along the [112] direction. d) inset of a) focused on the crystal rotation near the stacking fault that is propagating along the [110] direction. e) STEM micrograph centered on the defect highlighted by the magenta arrows showing a region of phase separation. f-i) EELS chemical maps from the Al K edge, the As L2,3 edge, the Ga L2,3 and the In M4,5 edge respectively on the defect pointed in e). 139

10.8 Representation of rotational variant nuclei seen in Fig. 10.7.d. The side view of the rotating crystal structures viewed in orthographic projection. The (111) plane showed and marked in purple. The (110) plane is showed by royal blue dashed line. a) unrotated crystal showing the alignment and stack of dumbbells within the crystal along the [111] growth direction, b-d) crystal being rotated along the [110] axis. 140

10.9 a) STEM HAADF image of the sample H. b) ϵ_{xx} strain map showing alternative regions of compressively and tensily strained (yellow and purple arrows). c) ϵ_{yy} showing the presence of alternate compressively and tensily strained epilayers. Any change of contrast shows the presence of defect in the microsctructure. 141

10.10 STEM HAADF image of of sample H from a clean area. b) ϵ_{yy} deformation profile showing the presence of strain along the growth direction in the InGaAs layer, while InAlAs layers are almost unstrained. c) ϵ_{xx} and d) ϵ_{yy} SMG relative deformation maps. InAlAs layer was taken as the reference, therefore, the relative deformation is around 0 within this layer. 142

A.1 Schematic illustration of the interference between the scanning grid (located at the intersection of the grey lines) and the atomic columns (red dots) resulting in the Moiré hologram ("greyscale"green dots) for the case $p < d_C$. The brightness of the green dots is related to the interaction between the atomic columns and the nodes of the scanning grid. Considering a Z-contrast mechanism only, the brightness of the green dots thus represents the intensity collected by the HAADF detector at this specific location. Each quadrant represents a relative strain state compared to the unstrained case displayed in the upper left section; upper right and bottom left show a stretch in the x and the y directions, respectively, and bottom right shows a stretch in both directions. With the same deformation field presented above, the Moiré patterns will evolve in an opposite manner (fringe space) for the case p > dc with the same magnitude [204]. 216

List of Tables

5.1 Summary of the growths. 72

6.1 Elastic properties of InP, InGaAs and InAlAs [216, 217]. 91

7.1 In/P ratio measured by X-ray Photoelectron Spectroscopy (XPS) on InP(111)A and InP(111)B after different annealing treatment. 104

8.1 Summary of the growths. 109

8.2 RADS simulation results. 117

9.1 Summary of the growths. 121

List of Abbreviations

AFM Atomic Force Microscopy iv, 22, 65, 75, 77, 79, 82, 98, 114, 126–129, 133, 134, 137, 140

ALMBE Atomic Layer Molecular Beam Epitaxy 40

ARXPS Angle-Resolved X-Ray Photoelectron Spectroscopy 97, 98

BEP Beam Equivalent Pressure 8, 10, 39, 50, 55, 58, 59, 61

BET Band Edge Thermometry 55, 63, 64, 74, 75

BFM Beam Flux Monitoring 55, 56, 58–60, 74

CM Compositional Modulation 36, 38–40, 95, 145

DFT Density Functional Theory iv, 70, 72, 75, 84, 86, 114

DIC Differential Interference Contrast 65, 75, 77, 83

EELS Electron Energy Loss Spectroscopy 66, 87, 90, 92, 113, 128, 129, 143, 144

FCC Face Centred Cubic 84, 119

FOV Field of View 67, 68, 90, 137

FWHM Full Width at Half Max 45, 97, 103, 104

GPA Geometrical Phase Analysis 67, 68, 87, 113, 143, 198, 200

HAADF High-Angle Annular Dark- Field 67, 68, 87, 88, 113, 141, 147, 148, 201

HCP Hexagonal Close Packed 84

HREM High Resolution Electron Micrograph 198

HRSTEM High Resolution Scanning Transmission Electron Microscopy 87, 89, 111, 142, 144

HRTEM High Resolution Transmission Electron Microscopy 12

HRXRD High Resolution X-Ray Diffraction iv, 10, 59, 71, 72, 111, 112, 118–120, 126, 127, 136, 138

IMFP Inelastic Mean Free Path 70, 71, 104

LED Light Emitting Diode 62, 74

LEED Low energy electron diffraction v, 70–72, 97–102, 130

LT Low Temperature 2, 6–12, 15

MBE Molecular Beam Epitaxy iv, 3, 15, 25, 36, 49, 51, 52, 54–57, 61, 64, 73, 76, 79, 86, 88, 99, 105, 107, 114, 120, 122, 124–126, 130, 136, 151

MEE Migration Enhanced Epitaxy 3, 4, 15, 42, 50–52, 76, 122, 124–128, 130, 150, 151

ML Mono-Layer 15, 81, 82, 85, 88, 104, 114, 115, 118, 124

MME Metal Modulation Epitaxy 3, 4, 40, 52, 124–126, 130, 150

MOCVD Metal Organic Chemical Vapor Deposition 28, 30, 36, 48, 81

PCA Photo-Conductive Antenna 2, 4–9, 151

QW Quantum Well 13, 34, 48, 51

RADS Rocking-Curve Analysis by Dynamical Simulation 72, 118

RGA Residual Gas Analyzer 56, 76

RHEED Reflection High Energy Electron Diffraction iv, 20, 22, 29, 30, 43, 51, 54–56, 61, 62, 70, 74, 77, 105, 107–109, 128, 130, 132, 135

RMS Root Mean Square 65, 79–81, 99, 114, 115, 127, 129, 133, 134, 137, 140, 149, 150

SAD Selected Area Diffraction 90

SAE Selective Area Epitaxy 51, 52

SL SuperLattice 2, 4, 14, 34, 38, 40, 63, 72, 111, 112, 114, 117–122, 124–126, 128, 130, 136, 137, 141, 143–145, 149–151

SMF Scanning Moiré Fringe 68, 69

SMG Scanning Transmission Electron Microscopy (STEM) Moiré Geometrical Phase Analysis (GPA) 67, 68, 72, 87, 91, 92, 113, 120, 122, 143, 148, 198, 200

STEM Scanning Transmission Electron Microscopy iv, 66–69, 84, 87–91, 111, 113, 114, 119–122, 127–129, 134, 137, 141, 143, 144, 147, 148, 198

STM Scanning Tunneling Microscopy 24, 97, 98, 100, 106

TDS Time Domain Spectroscopy 2, 4, 5, 7, 72, 149, 151

TEM Transmission Electron Microscopy 12, 17, 33, 38, 39, 62, 66, 70

THz Terahertz 2, 4–8, 72, 149, 151

UHV Ultra-High Vacuum 54, 55, 73, 97

W Wurtzite 33–35, 88, 95, 113, 127–129

XPS X-ray Photoelectron Spectroscopy 69, 70, 72, 97, 98, 103–107

ZB Zinc Blende 33–36, 88, 95, 113, 127, 129

Chapter 1

Introduction

1.1 Motivation

One of the goals of cutting-edge technology in electronic devices is growth of smooth, defect-free layers of one semiconductor (ternary or quaternary compound) on top of a different substrate. This technologically driven desire stumbles on a fundamental limitation: the potential lattice mismatch even at attempted lattice-match growth that introduces strain into the film. The strain results in a number of defects from stacking faults and twins to misfit dislocations, which could eventually develop into 3D islands on the surface. This transforms the growth mode from 2D layer-by-layer or step flow to 3D Volmer-Weber mode. Overcoming this limitation is of crucial importance, and represents a unique challenge to our understanding of the fundamental growth process. This situation is more pronounced for the growth on (111) substrate as opposed to (001) substrate. Because of the number of dangling bonds and the surface reconstruction of (111) surface, a finer control on the growth kinetics such as adsorption, migration and desorption is required to minimize the tendency towards the surface step or hillock formation and surface morphology degradation. It is even harder to avoid hillocks on (111)A compared to (111)B substrate and many growth conditions result in the formation of surface steps. The formation of hillocks on (111)A surface was attributed to the low sticking coefficient of As on the (111)A compared to (111)B surface that is caused by its surface reconstruction [1].

Growth on (111) substrates was mainly studied in 1970s, 1980s and 1990s with the focus on GaAs [1–9]. However, since most of the growth conditions resulted in a defective and rough surface due to the formation of surface steps, McFee et al. [10] in 1977 concluded

that growth on (111) substrates is too difficult, therefore, efforts should focus on (001) surfaces for reproducible device quality epitaxial layers. Hence, there has not been a continuous research in this field. In recent years, growth on (111) substrates has regained attention due to the emergence of new technologies and applications that demand growth on (111) substrates. For example, spin transport [11, 12], growth of novel tensily strained quantum dots [13–15], synthesis of high quality transition metal dichalcogenides (TMDs) [16] and topological insulators (TIs) [17, 18] could benefit from the advancement of research on (111) substrates. Therefore, achieving high quality epitaxial heterostructures on (111) substrates can pave the way towards understanding other related fields.

InGaAs/InAlAs/InP material system, which is the focus of this research, has received much interest due to its application in optoelectronics. For example, InGaAs/InAlAs SuperLattice (SL) are used as Terahertz (THz) emitters and receivers in Photo-Conductive Antenna (PCA) for Time Domain Spectroscopy (TDS) systems [19]. GaAs grown at Low Temperature (LT) that allows incorporation of excess arsenic in the structure is mostly used for such application. However, LT-GaAs needs bulky and expensive Ta:Sapphire lasers for excitation. On the other hand, InGaAs/InAlAs material system can be excited at a wavelength of 1.55 μm using relatively inexpensive and portable telecom lasers. A SL of InGaAs/InAlAs could serve both as transmitter and receiver. Further enhancements in the performance of such systems can be realized if the structures are deposited on the polar (111)-oriented InP substrates due to the possibility of embedding strong piezoelectric fields through tailoring strain in InGaAs and InAlAs layers. The piezoelectric fields are going to sweep the photo-generated carriers towards the interfaces with InAlAs, shortening their lifetime. This may improve the performance of PCA for THz TDS further, even without embedding excess arsenic. The surface density of such two-dimensional stationary charges generated by piezoelectric effect can be regulated from insignificantly small to electron charges in excess of $10^{21}cm^{2}$. Depending on whether the InGaAs is engineered with tensile or compressive strain by choice of the In compositions in the wells and barriers, the polarity can be reversed.

In order to exploit the advantages of growth on polar (111) substrates, the first step is to achieve high quality expitaxial structures. The main strategy reported to reduce the number of surface steps or to avoid them is the use of misoriented substrates. Growth on off-cut GaAs and InP substrates was reported to promote step-flow growth mode and avoid hillock formation due to the addition of more steps and kink sites [20–22]. Previous studies on optimizing the growth on (111)B surfaces were mainly focused on GaAs substrates [6, 7, 9, 20–30]. The benefits of using misoriented substrates for growth on InP(111) were also reported [2, 4, 10, 31–35]. However, all these reports were focused on specific off-cut angles rather than a systematic study to find the optimum off-cut angle

for growth. Besides growth on vicinal surfaces to avoid hillocks, other techniques such as the use of mobility enhanced epitaxy (Migration Enhanced Epitaxy (MEE) [36–40] and Metal Modulation Epitaxy (MME)) [41] as well as surfactant mediated epitaxy [42, 43] are other paths to improve the surface morphology of growth on singular (111) substrates.

1.2 Thesis outline

Growth of high quality epitaxial InGaAs/InAlAs/InP heterostructures using Molecular Beam Epitaxy (MBE) was the main objective of this research. The epitaxial growth challenges for (111)-oriented substrates include the formation of surface steps and consequent surface roughness (morphological defects), as well as formation of twins and stacking faults, and phase separation (microstructural defects). Elimination of such morphological and microstructural defects was the main objective of the present work.

We first present the influence of substrate misorientation on the surface morphology of InGaAs/InAlAs epilayers grown on InP(111)B and InP(111)A substrates. We did a systematic study to find the optimum off-cut angle for growth on InP(111)B substrate using substrates that were mechanically polished to have bowed edges. The bowed edge provides access to a broad range of off-cut angles and misorientation directions enabling us to find the minimum off-cut angle which ensures atomically smooth morphology. We also show that the azimuth of such off-cut angle is not a critical parameter in eliminating the hillock formation.

We then performed a systematic study to compare the surface reconstruction of InP(111)A and InP(111)B surfaces since the surface reconstruction is an important parameter affecting the growth quality dramatically. We found that InP(111)B surface is a thermally stable surface that has a (1×1) unreconstructed surface regardless of annealing temperature and procedure. On the other hand, InP(111)A surface is thermally unstable. It changes its reconstruction from a (2×2) to a mixture of (2×2) and (3×3) and to a (3×3) reconstruction with increasing the annealing temperature from 250° C to 500° C after the sputtering process.

We achieved the first defect free InGaAs/InAlAs SL on InP(111) substrate through the optimization of the substrate misorientation angle and growth conditions as well as extensive *ex-situ* characterizations and calculations. We found that the realization of step flow growth mode that is obtained by increasing the migration (diffusion) length of the atomic species is the key factor to obtain atomically smooth defect free structures on (111) substrates that was sought after for decades.

Finally, we studied the nature of defects in thick strained SL unintentionally lattice mismatched to the substrate. The results of our study showed that misfit dislocation formation, phase separation and crystal rotation are the mechanisms that relieve strain in mismatched epilayers to the substrate. In addition, we did studied the growth behaviour on singular (111)A and (111)B substrates using MME and MEE techniques. We showed that hillock-free InGaAs/InAlAs SL on InP(111)B substrate can be achieved at low growth temperatures using MEE. Furthermore, we showed that MME improves the surface morphology of InGaAs/InAlAs SL on (111)A substrates.

Our work sets the stage for developing InGaAs/InAlAs/InP(111) PCA for THz-TDS system with properties that can be tuned with doping, excess arsenic incorporation, strain and composition in high-quality epitaxial thin films and for device demonstrations and application as has been long-established for growth on (001) substrates.

Chapter 2

Photo-Conductive Antenna (PCA) for Terahertz (THz)-Time Domain Spectroscopy (TDS)

2.1 THz TDS

THz radiation with frequencies from 100 GHz to 30 THz which lies between the infrared and microwaves has long been studied in fields such as astronomy and analytical science. THz has application in sensing and communication. TDS is one of the most important techniques within the rapidly developing and prosperous field of terahertz technology [44]. THz-TDS is a spectroscopic technique in which the properties of matter are probed with short pulses of broadband THz radiation. THz-TDS has been applied in different fields such as:

- Biological and medical science: on materials such as medicine, cancer tissue, bacteria, DNA and proteins
- Semiconductor technology: to measure properties such as mobility, conductivity and carrier density
- Security: to identify explosive and narcotic materials [45]

THz-TDS method is based on the generation and detection of short broadband THz pulses by semiconductor based PCAs. In the latter case it is crucial to employ a material

that exhibits very short carrier lifetimes in order to obtain broadband THz spectra. A short carrier lifetime is realized by introducing defect states into the semiconductor material. On the other hand, large density of defect is detrimental for the mobility since defects are carrier scattering centres. Low Temperature (LT)-GaAs that has been the state of the art material for generation of THz radiation from PCAs uses bulky and expensive titanium sapphire femto-second lasers at around 800 nm for excitation of THz pulses. LT-GaAs is not sensitive to be optically excited at the telecommunication wavelength of 1550 nm because its optical bandgap is 1.43 eV at room temperature corresponding to 867 nm [19].

There have been attempts to decrease the cost and increase the performance of PCAs. LT-InGaAs sensors that can be excited with the cost effective fibre laser at telecommunication wavelength were proposed to replace LT-GaAs material system. Materials properties such as resistivity, photo-excited carrier mobility and carrier life time need to be tailored to make these sensors useful for THz wave generation and detection. The ideal material should:

- 1) Have very high dark resistivity, so high voltage could be applied to it without inducing excessive dark current,
- 2) Be sensitive to 1550 nm wavelength radiation, i.e. short pulse of this radiation would generate large number of electrons and holes which contribute to the current,
- 3) The photo-generated carriers should have very high mobility, i.e. the resistance of the device should be very small after generating the free carriers with 1.55 μm laser pulse,
- 4) The recombination rate of the photo-generated carriers should be very fast so the current transient would be very short.

All the above-mentioned criteria are met by LT-GaAs except property number 2. Therefore, the key challenge is to develop a material system that meets this property without sacrificing the others.

2.2 Requirements for TDS system

2.2.1 Material system

InGaAs/InAlAs superlattices are proposed for THz emitters and detectors. For a material to be able to be excited with 1.55 μm laser, the band gap should be less than 0.8 eV. Hence, InGaAs material is appropriate for this purpose. However, InGaAs is highly conductive at the low temperature growth mode unlike LT-GaAs. This is because As semi-metallic precipitates induced by low-temperature growth of GaAs and subsequent annealing have Fermi energy within the GaAs bandgap, while the As precipitates in LT grown InGaAs have Fermi energy within InGaAs conduction band. This makes LT-grown InGaAs highly conductive after annealing. With decrease of the growth temperature, the carrier concentration increases by orders of magnitude as shown in Fig. 2.1.a [46]. The resulting high dark conductivity of InGaAs is not acceptable for THz PCA.

The challenge is to increase the dark resistivity. The first approach to compensate for the naturally n-doped InGaAs is the addition of Be atoms as acceptors. However, although the free carrier concentration is significantly reduced with Be doping (Fig. 2.1.b), a perfect balancing of the Be doping and the background carrier concentration is extremely hard to achieve. In addition, although Be doping can reduce the residual carrier density and the photocarrier lifetime, the resultant resistivity is still not very high. Moreover, carrier mobility and light absorption are reduced in high defect materials doped with Be.

The second approach is the addition of InAlAs barrier between InGaAs layers to separate the photocondutive regions that exhibit high carrier mobility from the highly defective regions that have high dark resistivity. InAlAs has a higher bandgap (1.46 eV), therefore, it is transparent at 1.55 μm and does not contribute to the photoconductivity. When InAlAs layer is grown between 300-500° C, phase separation may occur, which results in the formation of regions alternaticely rich and poor in In. These defects creates trap states significantly below the conduction band of InGaAs. If InAlAs layers are sufficiently thin (10-15 nm), the electron wave function of optically excited electrons in the conduction band of InGaAs overlaps with the defect states in the adjacent InAlAs layer. Therefore, electrons from the InGaAs layer tunnel to the trap states in the InAlAs layer and are trapped (Fig. 2.1.c). This process can increase the dark resistivity. Since such a thin layer has very low light absorption and PCA made from this material are very inefficient, multilayer structures of alternating photoconductive (InGaAs) and trapping (InAlAs) layers is the way for improving the amount of absorbed light [19, 46].

Another way to increase the resistivity of the well layer is the reduction of In content in Be doped LT $In_xGa_{1-x}As$. It was shown that decreasing the In content in InGaAs from $x = 0.53$ to $x = 0.45$ results in a very low dark current with a higher resistance in the PCA (Fig. 2.1.d), which comes mostly from the reduced carrier concentration. Therefore, LT $In_{0.45}Ga_{0.55}As$ is much superior than $In_{0.53}Ga_{0.47}As$ as a material for PCA with excitation at 1.55 μm [47].

2.2.2 Low temperature growth

One advantage of growth at low temperature is that the out-diffusion of the impurities from the substrate into the active region [48] or segregation at the interfaces could be reduced. The minimum growth temperature is determined by the onset of non-dissociative adsorption of As_4, while the maximum growth temperature is set by the thermal dissociation of compound semiconductor [49]. Growth at low temperatures such as 200°C (up to 300°C) leads to the off-stoichiometry composition due to the incorporation of excess arsenic. At low temperatures (up to 300° C), low mobility and high sticking coefficient allow the incorporation of a high arsenic concentration. The amount of excess arsenic incorporated is dependant on the growth temperature. The lower the growth temperature, the greater is the amount of excess arsenic that is incorporated [50, 51]. Incorporation of excess arsenic into the lattice leads to an expansion of the lattice constant (Fig. 2.2.a), and hence the epilayer is strained [52, 53]. Excess arsenic up to 1.5% was reported to incorporate into the lattice at a growth temperature of 190°C [54] leading to an increase of 0.15% in the lattice constant in the growth direction (the in-plane lattice constant remains the same as the substrate lattice constant when the layer is fully strained). The layers grown at low temperature have high density of arsenic antisite defects, As_{Ga} [55]. Excess arsenic leads to a mandatory ultrafast carrier recombination rate. Upon annealing, the excess As form semi-metallic As precipitates which act as Schottky junctions effectively depleting GaAs of carriers. This leads to high mobility and ultra-short lifetime of photo-excited carriers, making LT-grown GaAs an excellent material for THz PCAs. [46].

Due to the incorporation of excess arsenic and change in the lattice constant, growth at low temperature proceeds in an epitaxial way only below a certain thickness. Above the critical thickness, an amorphous phase forms, which is in the cone-like form with high density of stacking faults. The breakdown of epitaxy was related to a high density of excess arsenic. The critical layer thickness before defects start to nucleate is highly dependant on the arsenic overpressure or Beam Equivalent Pressure (BEP) and growth temperature [53, 56]. It decreases with increasing BEP (Fig. 2.2.b) or decreasing the

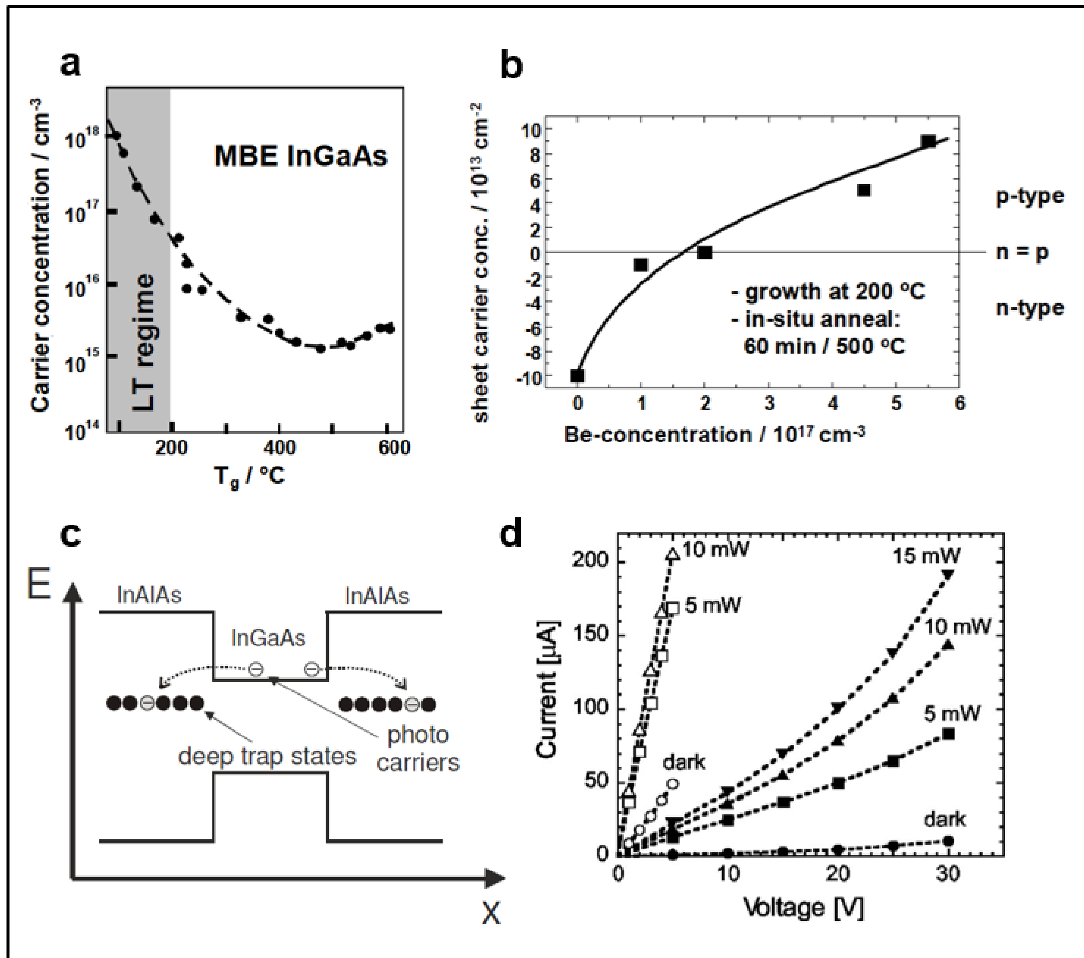

Figure 2.1: a) Carrier concentration of LT InGaAs. b) Be doping and carrier concentration [46] ©OSA Publishing. Used with permission. c) Schematic of the InGaAs/InAlAs band-diagram with deep cluster-induced defect states [19] ©OSA Publishing. Used with permission. d) Current vs voltage characteristics of the PCA made from LT $In_xGa_{1-x}As$ under various excitations at 1.56 μm. The open and filled symbols correspond to $x = 0.53$ and 0.45, respectively [47] ©AIP Publishing. Used with permission.

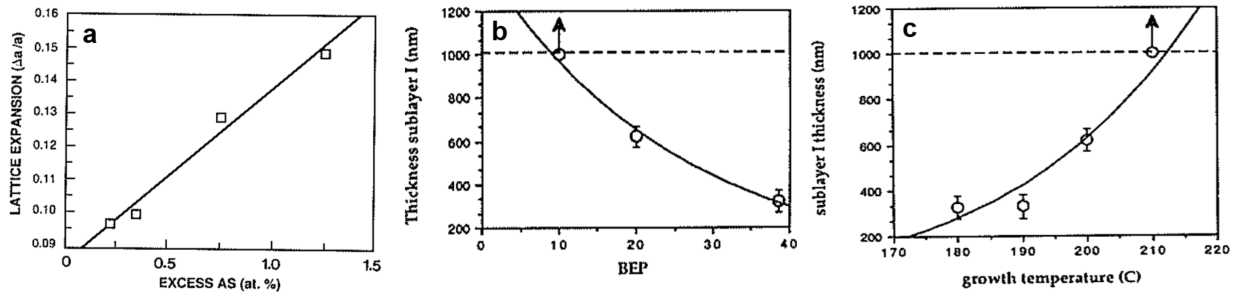

Figure 2.2: a) Lattice constant expansion due to the presence of excess arsenic, and b) effect of BEP and c) growth temperature on the critical layer thickness that can be grown defect free [53] ©Springer Nature. Used with permission.

growth temperature in an Arrhenius relationship (Fig. 2.2.c) [57]. Increasing sample thickness, decreasing the growth temperature or increasing the overpressure leads to the formation of pyramidal defects. Microtwins are believed to be their origin. At high BEPs, the epilayer has three sublayers: the monocrystalline sublayer, the layer with dislocation, stacking faults and microtwins, and the poly crystalline overlayer. In fact, there is an optimum BEP to obtain the maximum monocrystalline layer thickness [58]. Growth at low temperature is greatly improved by using the lowest possible arsenic flux [59]. Very low growth rates such as 0.05 Å/s was shown to lead to a defect free GaAs surface at a growth temperature of 380°C [60]. The volume fraction of the excess arsenic (V_{As}^{Excess}) is proportional to the crystal lattice expansion ($\Delta\alpha/\alpha$) as in Eq. 2.1 [55]. As the arsenic overpressure increases, the volume fraction of excess arsenic increases causing an increase in the lattice expansion which saturates at higher arsenic overpressures. This leads to a shift of epilayer peak from the substrate peak in High Resolution X-Ray Diffraction (HRXRD).

$$V_{As}^{Excess} = 20\Delta\alpha/\alpha \tag{2.1}$$

Another fact about the low temperature growth is that the increased arsenic sticking coefficient at low growth temperatures results in a Ga-deficient surface and hence Ga vacancy leading to another type of deep level trap in the LT grown GaAs. In contrast, at higher growth temperatures, arsenic sticks only if it binds to a surface Ga atom [59]. The LT grown material has a high concentration of arsenic antisite defects and arsenic interstitials [51, 56]. Fig. 2.3 shows a schematic representation of the excess arsenic incorporated into the lattice. If the terrace width is such that the crystal sites for arsenic

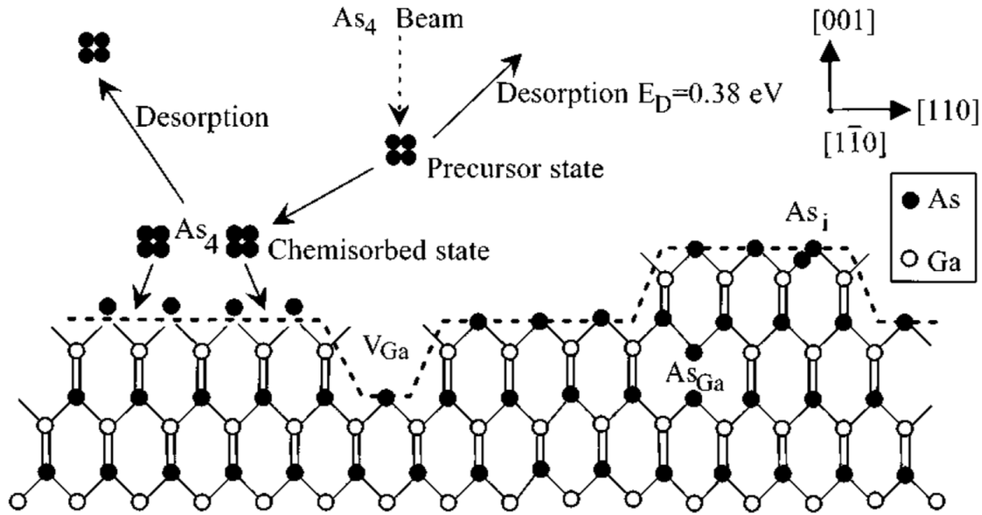

Figure 2.3: A schematic showing arsenic antisite, As_{Ga}, and Ga vacancy, V_{Ga} present in a LT grown GaAs layer [55] ©AIP Publishing. Used with permission.

absorption are fewer than the number of atoms produced by the dissociation of As_4 molecules, the excess arsenic atoms are incorporated as interstitials [55].

When growth is done at normal growth temperatures, the strain due to exceeding the critical layer thickness is relieved by the formation of misfit dislocation loops at the surface, which glide to the interface. However, when growth is done at low temperatures, the strain due to the excess arsenic cannot be relieved by the formation of misfit dislocations because of the kinetic limitations. Hence, misoriented nuclei form that leads to a polycrystalline growth. Dislocations and stacking faults that are unable to glide down to the interface from the surface evolve into pyramidal defects [61]. Arsenic agglomeration was also found as another reason for the pyramidal defect formation. There is a maximum amount of excess arsenic that can be incorporated into the lattice; the rest of excess arsenic agglomerates on the surface [52, 53]. At low growth temperatures, adatom diffusion to nearby steps is slow relative to adatom arrival from the vapor phase; i.e. the adatom diffusion length is short. This results in the interaction and accumulation of adatoms on the terraces between the steps and hence the formation of two-dimensional clusters. On the other hand, adatom diffusion to nearby steps is relatively fast at high temperatures, which results in step flow growth mode [62].

2.2.3 Engineering of the excess arsenic location

At low growth temperatures, as-grown materials have poor electrical and optical properties. However, mobility and photoluminescence are comparable to those grown at high temperatures after annealing the LT grown material [63]. Annealing the LT grown structure above 400°C [64] reduces the arsenic antisite defects and leads to the formation of arsenic precipitates, which brings the lattice constant of the epitaxial layer back to the substrate value and relieves the strain. Annealing also reduces the point defect concentration [56]. Transmission Electron Microscopy (TEM) studies have shown the coarsening of arsenic precipitates when annealing is done at higher temperatures. This coarsening occurs because the two-phase system of the arsenic clusters in the GaAs matrix is minimizing its free energy with annealing by reducing the interfacial area between the arsenic precipitates and the GaAs matrix [65]. Arsenic precipitates are coherent until a critical size is reached.

Arsenic precipitates are semi metal, therefore, they could form a depleted region around them. In fact, arsenic precipitates with the depletion region around them act as embedded Shottky barriers that increase the resistivity [66]. If the background doping is low enough, compared with the spacing of the precipitates, the material will be completely depleted (Fig. 2.4.a), and will exhibit a high resistivity. The resistivity is seen to decrease as the annealing temperature is raised above 700°C because of arsenic precipitate coarsening, which causes the depletion regions around them to no longer overlap (Fig. 2.4.b).

The stress relaxation by the formation of arsenic precipitates can be seen in plan-view High Resolution Transmission Electron Microscopy (HRTEM) by Moiré fringes. Fig. 2.5.a shows arsenic precipitates after annealing a 190°C grown GaAs [67]. These precipitates relax the strain in different crystallographic directions [53]. Formation of As-precipitates in the LT grown InGaAs layer depends on the annealing temperature. No arsenic precipitates were at lower annealing temperatures such as 500°C [68, 69], but arsenic precipitates were seen when the annealing temperature was increased to 600°C [69]. Grandidier et al. [70] showed that formation of the arsenic precipitates in $Al_{0.3}Ga_{0.7}As$ happens at annealing temperatures of above 550°C. For the growth of $In_{0.52}Ga_{0.48}As$ on InP(001) at 150° C, high density of pyramidal defects with inclusion of hexagonal As grains were formed (Fig. 2.5.b). Growth at 200° only led to the incorporation of small amount of excess As in the form of CuPt ordered layers which did not lead to the formation of arsenic precipitates upon subsequent annealing [58, 71].

When growing GaAs/AlGaAs Quantum Well (QW), there is a tendency towards the arsenic precipitates accumulation and coarsening in the wells and depletion of the bar-

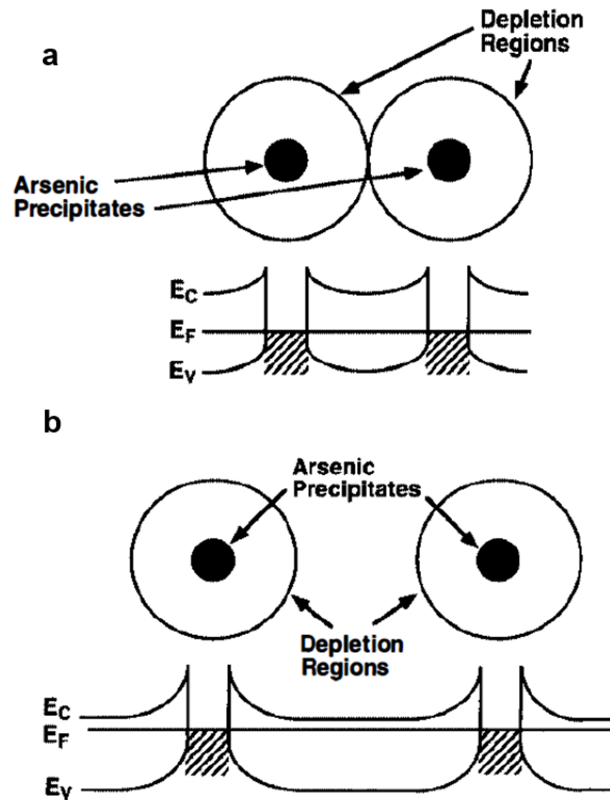

Figure 2.4: Depletion regions around arsenic precipitates when a) they just overlap and b) they are distanced causing an undepleted region in between [65] ©Annual Reviews. Used with permission.

rier from the precipitates upon annealing [72, 73]. Arsenic precipitate coarsening at heterojunctions and superlattices can be explained, for example in the case of GaAs/AlGaAs, based on the difference in interfacial energies between an arsenic precipitate in GaAs and an arsenic precipitate in AlGaAs. Because the Al-As bond is stronger than the Ga-As bond, the interfacial energy will be lower between an arsenic precipitate and GaAs than between an arsenic precipitate and AlGaAs. Therefore, the arsenic precipitates will preferentially coarsen from AlGaAs regions to GaAs regions [65]. Changing the width of the well and barrier affects the incorporation of arsenic precipitate in them. Fig. 2.6.a shows a 10-periods $Al_{0.3}Ga_{0.7}As$/GaAs SuperLattice (SL) with progressively wider $Al_{0.3}Ga_{0.7}As$ barriers or wells. For the wide GaAs wells, the arsenic clusters are completely contained within the GaAs well regions. As the well regions become narrower, the ar-

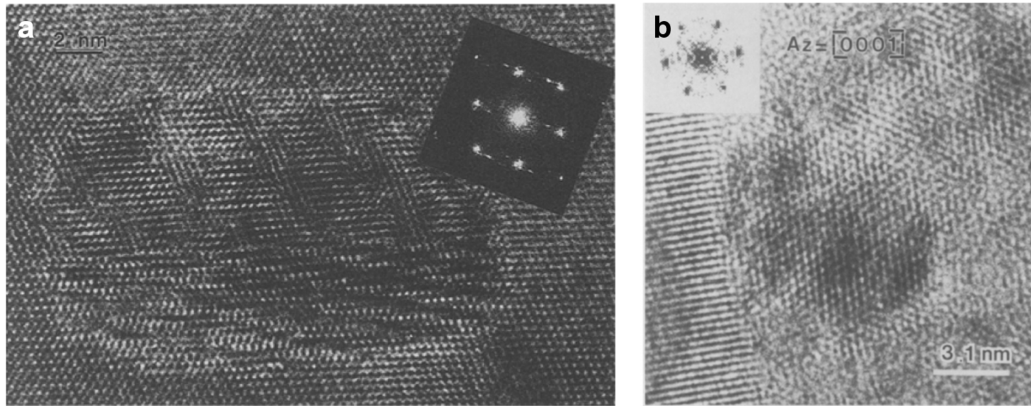

Figure 2.5: a) Arsenic precipitate with Moire pattern [67] ©Springer Nature. Used with permission. b) small region of hexagonal arsenic between two InAlAs grains of different orientations before annealing. Fourier transform in the inset shows the 6-fold symmetry of these defects [58] ©Elsevier. Used with permission.

senic clusters are centered in the GaAs well regions but extend into the AlGaAs barrier regions. Finally, the 10-period SL with the narrowest well is almost devoid of arsenic clusters, but the regions surrounding it contain arsenic clusters [65].

The above-mentioned fact is important when growing heterojunctions. It is desirable to be able to engineer the position of excess arsenic within the SL such as InGaAs/InAlAs system during the growth of heterojunctions. This is facilitated when growing on (111) oriented substrates due to the presence of piezoelectric field along the growth direction [111]. This will selectively minimize the excess arsenic in the current-carrying InGaAs well and maximize the arsenic precipitate content in the InAlAs barrier, which is desirable for fast carrier trapping. Melloch et al. [65] demonstrated some techniques for engineering control of the placement of the excess arsenic and consequently the arsenic precipitates within the structure. These strategies are discussed below:

1) When growing at low substrate temperatures, MEE technique (that will be discussed in Chapter 3) can be used to grow highly stoichiometric epilayers. Since MEE consists of separately supplying one Mono-Layer (ML) of the group III and group V fluxes, it allows the excess arsenic to desorb from the surface. Therefore, by switching between MBE and MEE growth modes , one can change from stoichiometric to non-stoichiometric epitaxy.

Similar approach for GaAs/AlGaAs done by Melloch et al. [65], is speculated for the InGaAs/InAlAs material system of our interest. It is expected that this technique could

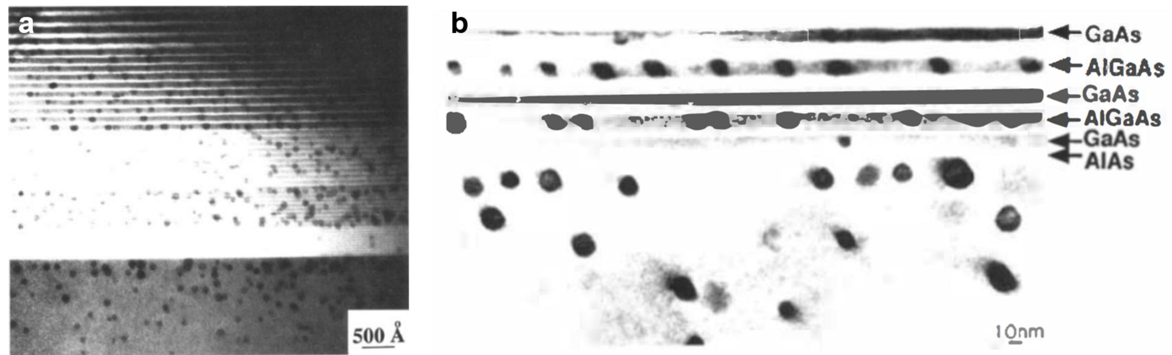

Figure 2.6: TEM image of a) A series of 10-period superlattices of progressively wider $Al_{0.3}Ga_{0.7}As$ barriers or GaAs wells grown at low temperatures and then annealed at 700°C for 30 s [65] ©Annual Reviews. Used with permission. b) A structure grown at 260°C. The AlAs layers and the GaAs regions between them were grown by MEE, while the $Al_{0.2}Ga_{0.8}As$ layers were grown by MBE with large excess arsenic [74] ©Elsevier. Used with permission.

allow the growth of InGaAs wells that are stoichiometric and InAlAs barriers that contain excess As. However, with annealing, the excess arsenic may still coarsen at the InGaAs well regions. To prevent this in GaAs/AlGaAs system, Melloch et al. [75] used a thin AlAs layers as arsenic diffusion barriers between the stoichiometric GaAs wells and the non stoichiometric AlGaAs barriers to retain the excess arsenic and the arsenic precipitates in the AlGaAs barrier regions, as illustrated in Fig. 2.6.b.

2) When dopants are incorporated into LT-GaAs, the arsenic cluster coarsening process can be significantly affected. In MBE, the typical n-type dopant is Si and the typical p-type dopant is Be. With increased annealing, there is a preferential coarsening of the arsenic from the p-LT-GaAs regions to the n-LT-GaAs regions as seen in Fig. 2.7 [76]. Similar observations have been reported by Ibbetson et al. [69]. The behavior of the arsenic cluster-coarsening with doping is believed to be caused by the Schottky nature of the arsenic clusters [76]. In n-GaAs:As, the arsenic clusters are negatively charged, whereas in p-GaAs:As they are positively charged. Therefore, if an arsenic antisite or interstitial is thermally emitted from an arsenic cluster and is ionized, it will be positively charged and attracted to the arsenic cluster in n-GaAs:As but repelled from an arsenic cluster in p-GaAs:As. Thus the arsenic clusters will be more stable in n-GaAs:As than in p-GaAs:As and account for the preferential coarsening in n-doped regions [74].

In addition, location of a precipitate in a strong electric field will not be stable. If a

precipitate thermally emits a charged arsenic interstitial, the arsenic interstitial will be swept away by the electric field. In the InGaAs/InAlAs material system grown lattice-mismatched on (111) substrate, a peizoelectric field exists due to the presence of strain and polar nature of the (111) crystallographic direction. Electric polarization is produced on (111) substrates since the displacement of atoms from their equilibrium positions due to the stress results in an unequal motion of charges and separation of positive and negative charges [30]. Through appropriate strain engineering, taking full advantage of the piezoelectric properties which are strong in this crystalline direction, electric polarization can be precisely tailored giving rise to the field strength in the well in excess of 200,000 V/cm. This happens through the accumulation of positive charge on one interface and an equal amount of negative charges on the other interface. The surface density of such 2D stationary charges can be regulated from insignificantly small to electron charges in excess of $10^{21} cm^2$, more than two orders of magnitude larger than what can be achieved with the so-called δ-doping. Moreover, depending on whether the InGaAs is engineered with tensile or compressive strain (by choice of the In compositions in the wells and barriers), the polarity can be reversed. Presence of such strong electric field has a marked effect on the wave functions of electrons and holes in InGaAs quantum wells. Such strong electric field is expected to facilitate the sweeping of the positively charged arsenic to the negatively charged interfaces.

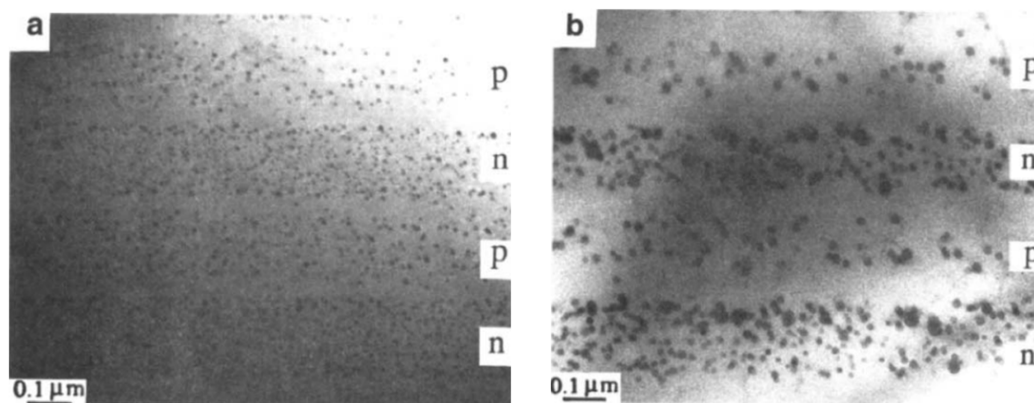

Figure 2.7: TEM image of a series of GaAs regions uniformly doped with Si followed by a GaAs region uniformly doped with Be and subsequently annealed at a) 700°C for 30 s and b) 900°C for 30 s. Attraction to and coarsening of arsenic clusters on the negatively charged Si doped regions in GaAs and repulsion of the arsenic clusters from the positively charged Be doped regions is seen [74] ©Elsevier. Used with permission.

Fig. 2.8 shows the results of band edge modeling for a system of $In_{0.4}Ga_{0.6}As$ well

and $In_{0.7}Al_{0.3}As$ barriers grown on (001) InP and on (111) InP substrates using nextnano3 software. The tilt of the band edges for both conduction (c.b.) and valance (v.b.) bands is seen for the (111) orientation. The wave functions and related probability densities $|\psi|^2$ are markedly modified with both electrons and holes showing increased presence in the energetically forbidden region of the energy barrier. Such effect, the degree of which can be regulated, may serve as a tool to enhance the fast carriers' recombination in the barriers. In the structures grown on (001) substrates the only way to enhance this overlap with barrier is to decrease the well thickness. For the case presented in Fig. 2.8, the electrons would be pushed away from the interface where the guttering of excess arsenic is expected, further boosting their mobility.

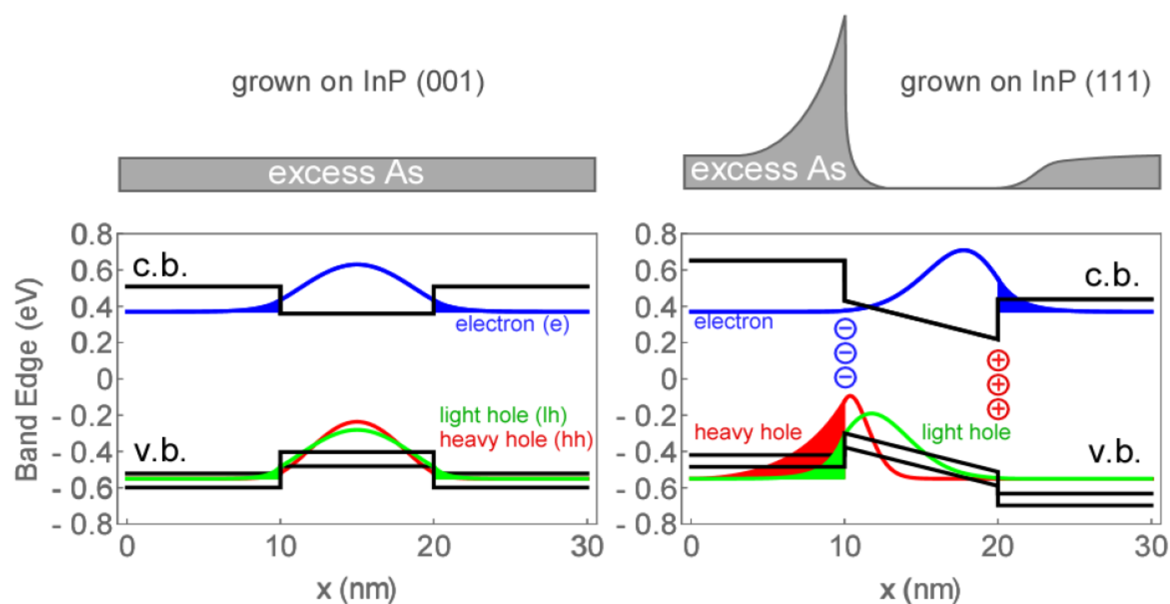

Figure 2.8: Comparison of band edge profiles, spatial probabilities $|\psi|^2$ of finding e, lh, and hh, and expected distribution of excess As for $In_{0.4}Ga_{0.6}As$ well and $In_{0.7}Al_{0.3}As$ barriers grown on InP(001) and InP(111) substrates. Band structures were calculated using nextnano3 software.

Chapter 3

A review of growth on (111) substrates

3.1 (111) surface characteristics

3.1.1 Migration length

Migration (or diffusion) length is the distance that the adatoms migrate on the surface before they attaches to a lattice site. Migration length, L, can be found using Einstein relation as in Eq. 3.1:

$$L = \sqrt{2Dt} \tag{3.1}$$

in which t is the surface lifetime, i.e. the time that the adatom migrates on the surface before it incorporates into a lattice site, and D is the diffusion constant of an adatom given by Eq. 3.2:

$$D = \nu a^2 exp(E_s/kT) \tag{3.2}$$

where ν is adatom vibrational frequency and a is the nearest-neighbour hopping distance and E_s is the activation energy for surface diffusion [77].

When the migration length is larger than or equal half the terrace width, growth proceeds in the step flow mode meaning that the growth proceeds through the adatoms attachments to the steps. As the migration length falls below half the terrace width, adatoms tend to form two-dimensional islands on the terraces rather than attaching to

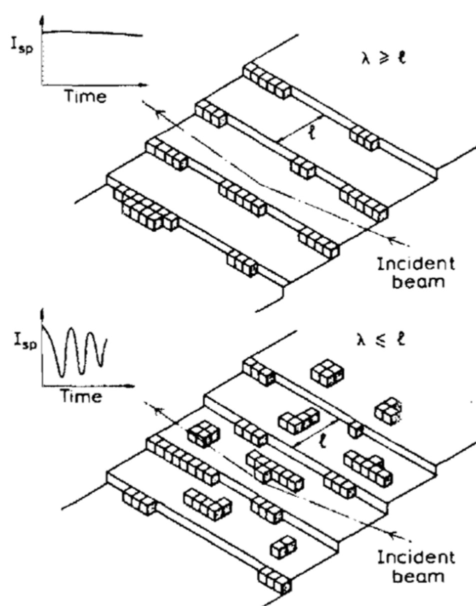

Figure 3.1: A schematic illustration showing the change in RHEED information as the growth mode changes from step-flow to two-dimensional [79] ©AIP Publishing. Used with permission.

the step edges. At migration lengths of less that the mean island radius, further islands form on top of existing islands. At even smaller migration lengths, growth becomes fully three dimensional [78]. No Reflection High Energy Electron Diffraction (RHEED) oscillation is seen when growth is in the step-flow mode, while oscillations start to appear when there is two-dimensional nucleation (Fig. 3.1) [79–81]. Realization of step flow mode is effective in reducing the hillock density [82]. When the growth mode is step-flow, the steps act as a uniform sink for the diffusion of adatoms with no other sinks present on the surface. Step flow growth and smooth surface was reported to establish at lower growth temperatures on GaAs(111)B surface compared to (001) surface [83].

For growth on (111) substrates, it was shown in a study that the migration length is slightly affected by the misorientation angle [4]. However, migration length was shown to be independent of the misorientation directions of [$\bar{2}11$], [$2\bar{1}\bar{1}$] and [$\bar{1}10$] compared in another study. Therefore, it is suggested that the surface migration of adatoms is isotropic and independent of azimuth. However, the azimuth affects the terrace shape; it is straight when the azimuth is [$2\bar{1}\bar{1}$] or zigzag (kinked) when other azimuths are used [6]. Ledges descending towards [$2\bar{1}\bar{1}$] direction were reported to be more stable than those along

$[\bar{2}11]$ [84]. Terrace width was also shown to be more uniform along some misorientation directions, while more disperse along others [77]. The step straightening mechanism was related to the preferential attachment of adatoms to the kink sites on the steps [85]. The formation of zigzag steps was also shown to be an effect of the growth temperature. For growth on nominal surface, the steps are zigzagged at low growth temperatures when the main mechanism is the coalesce of the two-dimensional nuclei. The steps are more straight at higher temperatures when the step-flow mode is dominant. This is due to the longer migration length of the adsorbed species and noticeable desorption rate, which both likely help suppress step roughness [24]. The misorientation direction was also shown to affect the temperature window that smooth growth could be achieved. It was shown to be larger for misorientation direction of $[2\bar{1}\bar{1}]$ compared to $[\bar{2}11]$ [86].

It was shown in one study that the migration length of Al is larger than that of Ga because Al atoms are more difficult to reevaporate. This was attributed to a larger bond energy in AlAs compared to GaAs making it harder to desorb [87]. However, this is only valid at very high growth temperatures when desorption rate is high, otherwise both species have a sticking coefficient of unity. In another study Ga was reported to have a longer migration length compared to Al. The smaller diffusion length of Al atoms was attributed to the adherence of Al atoms to the growth front [88]. The energy barrier for the migration of Al is larger compared to Ga [89]. The migration length of the Ga atoms was shown to be a strong inverse function of As overpressure. This dependence is stronger on (111)B surface compared to (001) [90]. Growth interruption improves the migration of Ga atoms and smoothens the surface, however, noticeable effect on the migration length of Al atoms is seen at higher growth temperatures, i.e. above 660°C [91]. Binding energy also affects the migration length of the adatoms. For example, diffusion of Ga on AlAs(111) surface is slower than on GaAs(111). This was attributed to a higher bonding energy in AlGaAs [92].

Surface morphological features of the grown layers are a consequence of the combination of the competition between the different surface kinetic processes such as surface migration, adsorption and desorption occurring on the growing surface. For example, surface desorption, particularly for As, as well as surface migration are enhanced at higher growth temperature. The nature of the GaAs(111)B surface structure demands a fine control over these kinetic processes. This leads to a very narrow suitable growth region in the phase diagram. This competition manifests itself in the variation of the RHEED intensity [93]. Chen et al. [22] reported on a specular surface morphology free of twins and pyramid on a non-misoriented GaAs(111)B surface using *in-situ* real time monitoring of specular beam intensity of RHEED. They used a combination of correct static surface phase regime and close monitoring of the dynamic specular beam intensity

to obtain such surface. However, they relied only on Nomarski microscopy images, and no Atomic Force Microscopy (AFM) images was taken to show the surface morphology at the atomic scale.

3.1.2 Surface reconstruction

Surface atoms differ from the bulk atoms in that the number of neighbouring atoms and hence the bond coordination is different. The directional covalent bonds in elemental semiconductors or partially covalent-partially ionic bonds in compound semiconductors are broken at the surface leading to associated surface charge densities which contain only one unpaired electron. Such dangling bonds are unstable, therefore, the surface region relaxes from the bulk position to reduce the number of dangling bonds and consequently the surface free energy by forming new bonds. Reaching a structure which exhibits a local minimum in the surface free energy implies that the chemical valencies of the surface species are satisfied in the reconstructed geometry [94]. Rode [95] treated the surface as a distinct membrane lying over the substrate which is attached to it elastically by Peierls-Nabarro stresses. The surface reconstructs due to the misfit of the uppermost layer to the rest of the substrate. The reconstruction pattern is a manifestation of the surface atomic vacancies. The surface reconstructs in order to satisfy dangling bonds, charge neutrality and steepening relaxation (surface roughening on the atomic scale) [94, 96]. Surface reconstructs in a way to satisfy the electron counting rule; i.e. all the dangling bonds on the electropositive element are empty and the dangling bonds on the electronegative element are full so that there is no net charge on the surface. This will result in the lowest-energy surface structure. For example in the case of GaAs, the dangling bond energy of the As atoms is in the valence band and that of the Ga atoms is in the conduction band (Fig. 3.2). Hence, electron transfer from the electropositive Ga atoms to the electronegative As atoms filling all the dangling bonds in the valence band and emptying all in the conduction band lowers the surface energy [97].

Surface reconstruction of GaAs(111)A [98–100] and GaAs(111)B [99–101] as well as that of InP(111)A [102–106] and InP(111)B [107, 108] were previously studied. Two surface reconstructions were reported for InP(111)A; the (2×2) with phosphorous coverage of 0.25 which adopts an indium vacancy structure and $(\sqrt{3} \times \sqrt{3})R30°$ with phosphorous coverage of 1 ML which is a complete layer of phosphorous trimer [103]. Only the (2×2) was shown to obey the electron counting rule. $(\sqrt{3} \times \sqrt{3})R30°$ was shown to not obey the electron counting rule, however, it was observed by Li et al. [103]. The group V trimer is very stable on the (111)A surface. The formation of the $(\sqrt{3} \times \sqrt{3})R30°$ P-trimer over the (2×2) was reported to occur in order to accommodate 33% more P-P bonds [103]. The

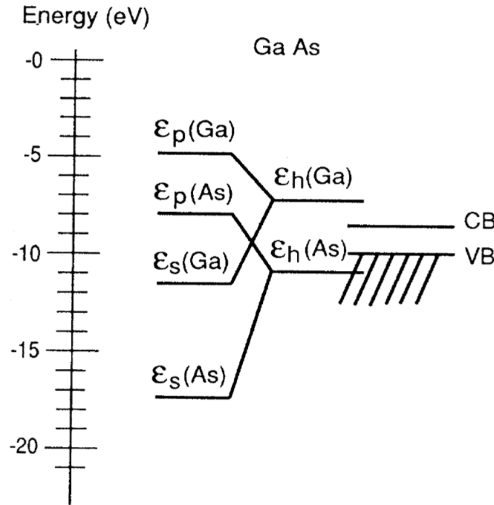

Figure 3.2: The energy levels, ϵ_h, of the sp^3 dangling bond states of GaAs. The energies are derived from the energies of the s, ϵ_s, and p orbitals, ϵ_p [97] ©American Physical Society. Used with permission.

(2×2) reconstruction is stable at indium rich condition and at higher temperatures, while the $(\sqrt{3}\times\sqrt{3})R30°$ at phosphorous rich condition and lower temperatures [102]. Two stable reconstructions exists for a (2×2) unit cell of (111)A surface that are In vacancy and P trimer [109]. An unreconstructed (1×1) surface for InP(111)B [108] and a (2×2) as well as a $(\sqrt{3}\times\sqrt{3})$ reconstructions for hydrogenated InP(111)B [107] were reported. For GaAs(111)A, only a (2×2) [100] and for GaAs(111)B, (2×2) [93], $(1\times1)_{LT}$ (low temperature) which is a mixture of (2×2) and $(\sqrt{19}\times\sqrt{19})$ phases [100, 101], $(\sqrt{19}\times\sqrt{19})R23.4°$ and $(1\times1)_{HT}$ (high-temperature) containing small domains of $(\sqrt{7}\times\sqrt{7})R19.1°$. There is no apparent similarity between the $(1\times1)_{LT}$ and $(1\times1)_{HT}$ reconstructions [93, 100, 110–112] were reported depending on the preparation process. (2×2), $(\sqrt{3}\times\sqrt{3})$, (3×3) and $(\sqrt{19}\times\sqrt{19})$ reconstructions were reported for GaAs(111)B by Ruda [96] depending on the surface preparation process.

Different surface reconstructions are a result of different temperature, surface composition and surface treatment [96]. Stability of different surface reconstructions at different As overpressures and annealing temperatures is shown in (Fig. 3.3). $(\sqrt{3}\times\sqrt{3})R30°$ was also reported for Se-treated GaAs(111)B [101]. (2×2) is an As-rich since it is stable at low temperatures, while $(\sqrt{19}\times\sqrt{19})$ is a Ga-rich reconstructed surface [27, 113]. Figure 3.4 depicts the two aforementioned reconstructions schematically. Scanning Tunneling Microscopy (STM) observations revealed that the GaAs(111)A-(2×2) surface exhibits large

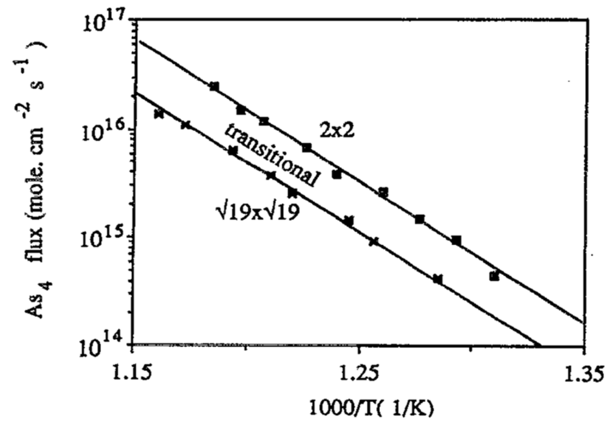

Figure 3.3: Surface reconstructions of GaAs(111)B as a function of As flux and temperature during MBE growth [111] ©AIP Publishing. Used with permission.

ordered regions having the Ga-vacancy buckling structure, while the GaAs(111)B-(2 × 2) surface consists of small domains, where the As trimers are adsorbed on the outermost As layer [100]. The lack of other surface reconstructions on (111)A surface was related to the low sticking coefficient of As [7].

Surface reconstruction was shown to affect the surface morphology. For example Chen et al. [22] reported specular surface for the growth of GaAs on non-misoriented GaAs(111)B when growth is done in the ($\sqrt{19} \times \sqrt{19}$) region. It was shown that the unreconstructed surface of InP(111)B is more stable compared to a reconstructed surface. This is in contrast to GaAs(111)B. The stability of the unreconstructed surface requires that the surface charge transfers from the surface to the bulk to reduce the surface dipole as in the case for InP(111)B (Fig. 3.5.a). If a charge transfer cannot be achieved, the surface reconstructs so that the charge transfers from the surface to the bulk through the atoms repositioning. The stability is related to the bulk potential which is symmetric for GaAs(111)B, while highly asymmetric for InP(111)B (Fig. 3.5.b) that facilitates the charge transfer. This difference in potential is due to the similar covalent atomic radii of Ga and As, while the metal radii is larger compared to group V element in InP [114].

3.1.3 Dangling bonds

The number of surface dangling bonds affects the mobility of the adatoms on the surface. For P-terminated InP substrates, the number of dangling bonds per phosphorous atom

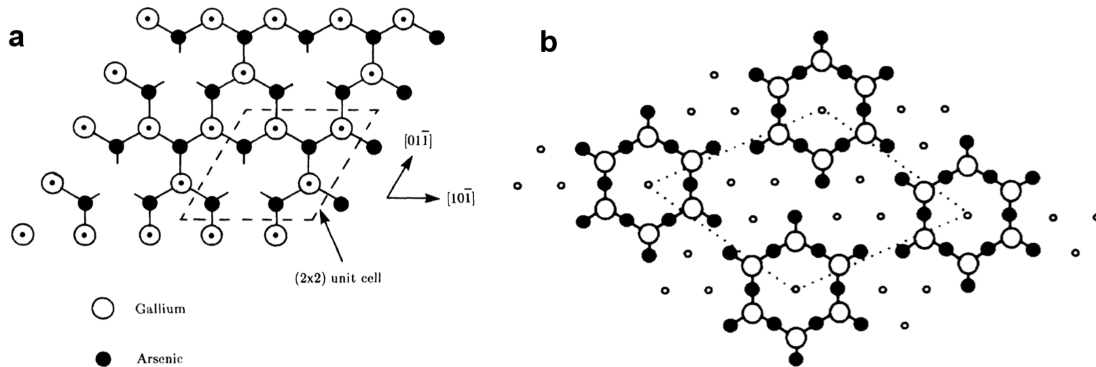

Figure 3.4: a) Top view of the single gallium vacancy model of a GaAs(111)A-(2 × 2) reconstruction [98] ©American Physical Society. Used with permission. b) detailed model of GaAs($\overline{111}$)B-($\sqrt{19} \times \sqrt{19}$) large open circles denote top As atoms, medium closed circles denote second-layer Ga atoms, and small open circles denote third-layer three fold coordinated As atoms [113] ©American Physical Society. Used with permission.

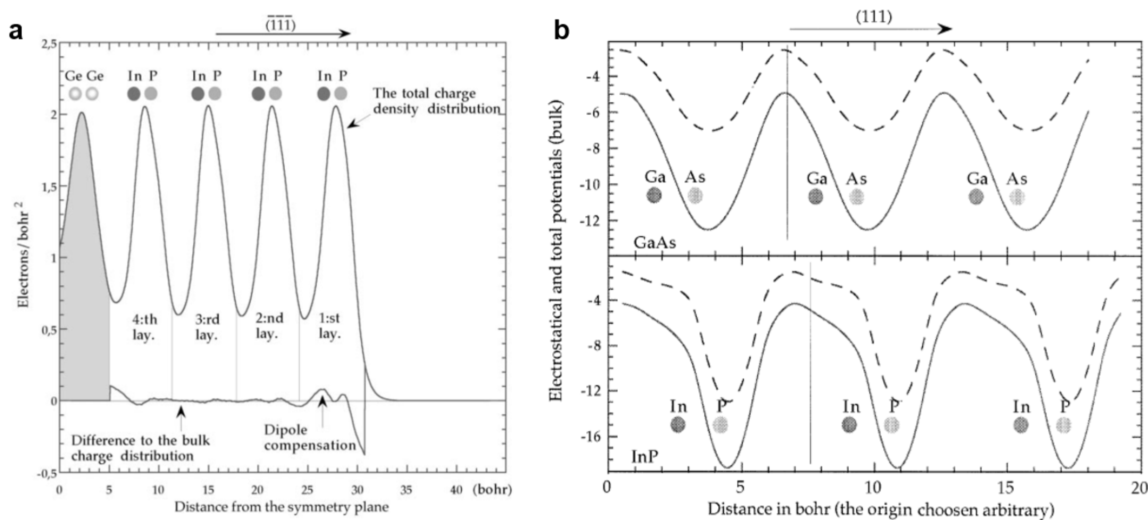

Figure 3.5: a) the charge distribution of InP(111)B along the surface normal. b) The average bulk potential of GaAs and InP along the [$\overline{111}$] direction. The dashed lines correspond to the electrostatic potentials, while the full lines are the effective potentials [114] ©Elsevier. Used with permission.

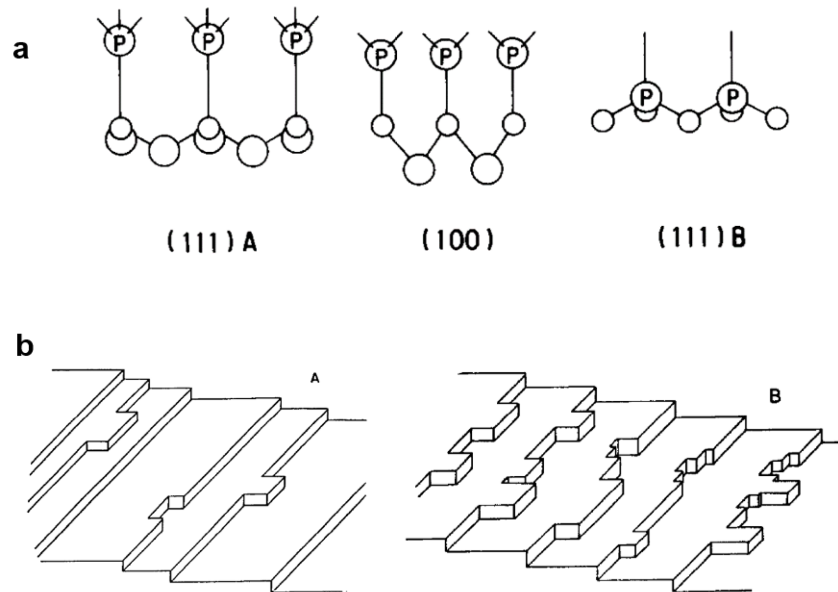

Figure 3.6: Schematic representation of a) dangling bonds of phosphorous atoms chemically absorbed on (111)A, (001) and (111)B surfaces [115] ©Elsevier. Used with permission. b) step disorder in A and B (111) surfaces [116] ©Elsevier. Used with permission.

is three for (111)A surface, one for (111)B and two for (001) surface (Fig. 3.6.a) [115]. Therefore, it is believed that the surface mobility is higher on (111)B compared to (111)A surface. The steps on (111)A surface meander less than those on (111)B (Fig. 3.6.b). Steps on (111)A surface are straight, while those on (111)B have high density of kinks making them more reactive in adatom attachment [116]. These facts make (111)A a less mobile surface. It is energetically more stable for group III atoms to bond with double dangling sites. When the adatoms on the edge of the steps share two dangling bonds, the steps are stable sinks for the incoming atoms. Therefore, (001) facet growth will lead to the formation of hillocks when growth is done on (111) surfaces [4].

Growth on (111) substrates is different than that on (001) substrates because growth rate on (001) surface is primarily dependent on the group III flux, while that on (111) surface is a complex function of growth temperature and V/III ratio. This is a result of the low sticking coefficient of As on (111)A substrate. Although the GaAs(111)A surface is Ga terminated, the accepted surface reconstruction for (111)A surface is a (2×2) with a Ga vacancy in every four Ga surface atomic positions meaning that one Ga atom per unit cell is missing. Therefore, the number of Ga and As dangling bonds per unit cell are

equal, which requires direct interaction between incident Ga and As atoms for growth to occur [3].

3.2 Growth challenges

3.2.1 Surface steps (hillocks)

Pyramidal hillocks are the major challenge for the growth on singular (111) surface. When growing on singular (111)B, vicinal (111)B facets that are pyramid-like immediately form on the surface (Fig. 3.7.a,b). The facets are approximately 2.5° towards the three equivalent $< 2\overline{1}\overline{1} >$ azimuthal directions that are energetically favorable. This suggests that there is a thermodynamic driving force leading to a phase separation that divides the surface into 2.5° facets and singular surface. The surface energy of the singular surface is higher than that of the 2.5° facets. As a result, the singular surface exists until its width becomes large enough to let the nucleation of 2.5° facets [6, 9]. Hence, a misorientation from the exact (111) could avoid the formation of hillocks. That is a vicinal surface tilted towards $[2\overline{1}\overline{1}]$ orientation has a lower surface energy compared to singular (111)B surface. However, the direction of misorientation angle plays an important role as well. According to Schowalter et al. [6], misorientations towards azimuths other than $[2\overline{1}\overline{1}]$ results in a zigzag step edges (Fig. 3.7.c). The most stable steps are those that run along <110> directions [9]. Higher free surface energy of singular surface and the Schwoebel barrier [6] were reported as possible mechanisms for the formation of hillocks. Schwoebel effect is the presence of a potential barrier between the upper and lower steps that leads to the preferred occupation of upper steps compared to lower one. Adatoms must pass through a region with lower coordination number at the step edge to make the jump from upper to lower steps, therefore, they need to overcome a potential barrier [117]. Schwoebel barrier was shown to lead to the formation of large mounds on singular surfaces in the case of GaAs(001) homoepitaxy [118].

Hillocks were shown to form during the MOCVD growth of InGaAs on InP(111)A surface. Formation of hillocks was attributed to the surface reconstruction of InP(111)A surface. The (2×2) In-rich surface reconstruction is stable at higher temperatures, which results in the formation of pyramidal hillocks (Fig. 3.8.a). A circular island growth was reported to occur in the P-rich $(\sqrt{3} \times \sqrt{3})R30°$ reconstruction region (Fig. 3.8.b) [119]. In another study, specular homoepitaxial MOCVD growth on InP(111)A was obtained, however, growth defects persisted to exist on InP(111)B for a wide range of growth conditions. This was attributed to the preferential migration of atoms to (001)

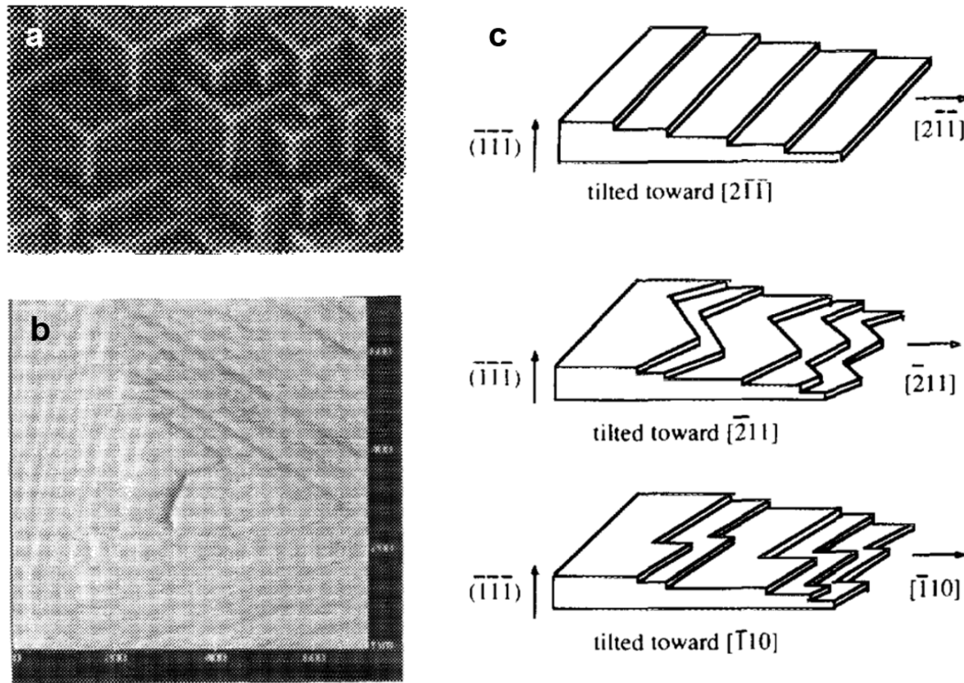

Figure 3.7: a) Optical microscope image of the GaAs singular substrate after 0.5 μm homoepitaxial growth, b) an AFM image of the top of the one of the pyramids in a [6] ©American Vacuum Society. Used with permission. c) terrace-step structure of films grown on substrates with different misorientations [9] ©American Vacuum Society. Used with permission.

facets (i.e. facet growth) when growth is done on (111)B and the lack of such preferential migration on (111)A [84]. The (001) facet growth was explained based on the fact that the phosphorous atoms on (111)B surface have only one dangling bond while they have three and two dangling bonds on (111)A and (001) surface, respectively [115].

Chen et al. [22] used RHEED intensity analysis of the homoepitaxial growth on non-misoriented GaAs(111)B and showed that the specular surface morphology is achievable if the growth is done in the $(\sqrt{19} \times \sqrt{19})$ phase region which results in a constant RHEED intensity versus time (Fig. 3.9). Decreasing the As overpressure improves the surface morphology since it increases the migration lengths of cations. Decrease in the RHEED intensity during the growth shows the formation of macroscopic defects such as pyramids and twins, therefore, surface roughening.

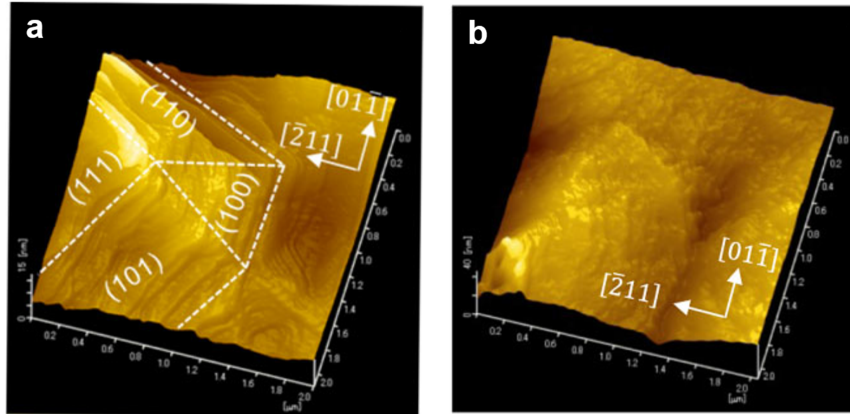

Figure 3.8: a) triangular (pyramidal) and b) circular islands formed on singular InP(111)A surface during the MOCVD growth of InGaAs [119] ©John Wiley and Sons. Used with permission.

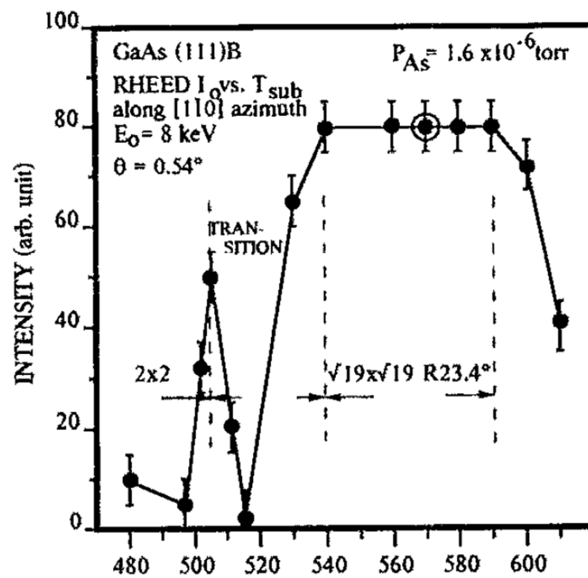

Figure 3.9: RHEED beam intensity change with substrate temperature on GaAs(111)B at a constant arsenic pressure. The open circle shows the starting point that results in a specular surface [22] ©AIP Publishing. Used with permission.

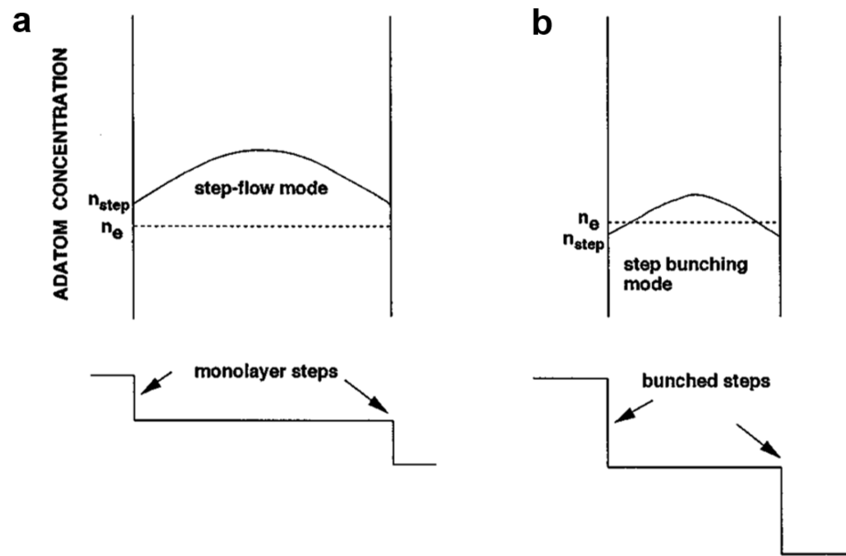

Figure 3.10: Schematic distribution of surface adatoms on a) a wide terrace with step-flow growth mode and b) a narrow terrace with step bunching [122] ©AIP Publishing. Used with permission.

3.2.2 Step bunching

Besides the hillocks for growth on singular surface, step bunching is another cause for the surface roughening on vicinal substrates. There is an elastic interaction between the steps. In the absence of strain, this interaction is the repulsion arising from the intrinsic stress of the steps, which is an inverse function of the terrace width (i.e. the distance between the steps). In the presence of strain/stress in the layers, elastic relaxation at the steps leads to a long-range attractive interaction between the steps. The interaction is attractive since the force at successive steps is in the same direction. The attractive interaction comes from the surface discontinuity at each step. The forces at steps are not balanced resulting in a force monopole. This leads to step bunching instability. Stress and strain determines the magnitude of the diffusion barrier for step bunching. Step bunching reduces at higher growth rates or higher fluxes and at lower growth temperatures [120]. Step bunching occur at a critical film thickness. It is also affected by the terrace width size. Increasing the terrace width keeping the growth condition constant, the critical thickness below which the growth continues via step-flow mode increases [121].

Xie et al. [123] used Monte Carlo simulation to investigate the effect of a negative Ehrlich-Schwoebel barrier when the adatom incorporates into the descending steps versus a positive incorporation barrier when adatoms attaches to the ascending steps. They showed that a positive incorporation barrier results in step bunching, while a negative Ehrlich-Shwoebel barrier usually does not. An incorporation barrier can be introduced by e.g. a surfactant layer during growth. In this case, an atom exchange between the surfactant and the depositing atom at the steps is required for the film growth. This costs extra energy than for adatoms merely diffusing on top of the surfactant layer.

Transition from step-flow growth mode to step bunching occurs at a critical step density (misorientation angle) that depends on the growth temperature. The principle idea is to assume that this transition happens when the concentration of adatoms at the step edge is less than the equilibrium value, i.e. the steps are undersaturated. The adatom concentration is maximum at the terrace centre and minimum at the step edges (Fig. 3.10). The adatom concentration is smaller at the steps at larger misorientation angles due to an increased number of steps leading to step bunching to increase the adatom concentration at the steps towards the equilibrium value. The critical step density decreases at higher growth temperatures. The bunched terrace width increases with increasing growth temperature, but does not depend on the misorientation angle [122].

A thermodynamic model developed by Pond et al. [124] showed that the steps can move freely with the constraint that it costs energy to form kink. Therefore, step bunching is probable when the kink formation energy is high. They showed that homoepitaxy on GaAs(001) misoriented by 1° or 2° towards (111)A direction leads to smooth steps that have bunching tendency, while step edges tend to be rough with less bunching tendency when the misorientation is towards (111)B due to the kink formation energy being lower.

Becourt et al. [2] observed the change of misorientation steps at the InAlAs/InP interface into giant multisteps at the surface top due to step bunching. Step bunching modifies the vicinal surface and decomposes them into terraces and high index facets. The local high stress at the giant steps leads to the formation of threading dislocations, which cross vertically form the InAlAs layer and end below the giant steps (Fig. 3.11).

3.2.3 Twinning and phase instability

III-V compound semiconductors can exist in Zinc Blende (ZB) or Wurtzite (W) crystal phases. ZB is thermodynamically favorable in III-As/Sb/P epitaxy, while W is a metastable phase [125]. Ostwald's step rule states that often thermodynamically stable phases

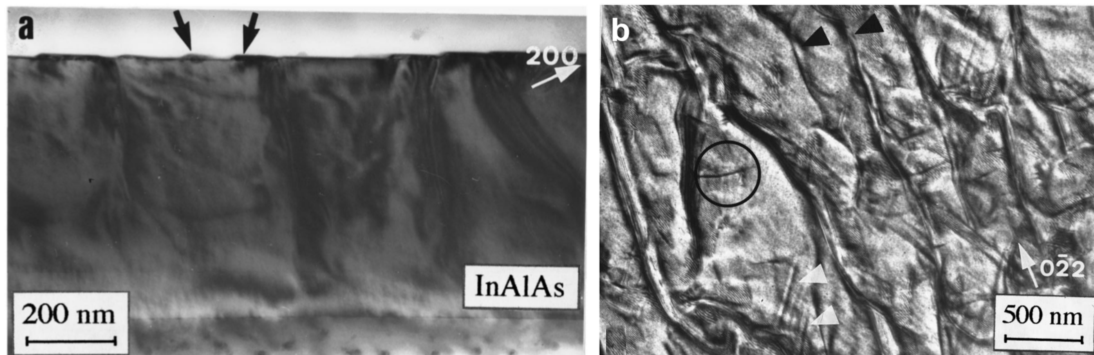

Figure 3.11: a) Bright field cross-sectional image of InAlAs grown on InP(111)B. Threading dislocation originated approximately 40nm from the InAlAs/InP interface go to the step edges. Steps run along the misorientation direction. The fringe contrast appearing through the entire film is due to the structural inhomogeneities from compositional modulation (alternative In and Al rich domains). b) Plane view TEM image of the surface. Bunched steps are indicated with black arrows. Dislocations running from the bunched steps along $[\bar{3}21]$ (circle) [2] ©AIP Publishing. Used with permission.

occur through metastable phases. This rule was suggested to minimize entropy production [126]. If the surface energy of the metastable nucleus is small enough and it is less anisotropic in shape, homogeneous nucleation of the metastable phase prevails [127]. Phase instability that is the presence of ZB and W crystal phase mixtures (polytypism) has been observed during the growth of III-V semiconductor nanowires (NWs). Polytypism functions as trap for carriers, reduces carrier mobility and conductivity. It also results in electron scattering at stacking faults or twin planes which is detrimental to the optical properties and device application [128]. Phase instability was associated to the small energy difference between W and ZB phases and lower surface energy and nucleation barrier of the W phase in comparison with that of the ZB. W is stable at structures with high surface to volume ratios [129, 130]. In general, ZB phase is favored at higher atomic number of anions, i.e. as the anion becomes heavier, (anion rule). The exception to this rule is when the cation in the compound is from the second row such as Be or B [131]. There have been a lot of studies focusing on the phase instability during the growth of nanowires, while whether or not such phase instability happens in Quantum Well (QW) and (SuperLattice (SL)) is questionable.

Growth twins are easy to form when growth is done in <111> direction since {111} is the primary twin plane. Twins are formed by an insertion of a stacking fault between two ZB structures. A stacking fault in the ZB structure is the insertion of one monolayer

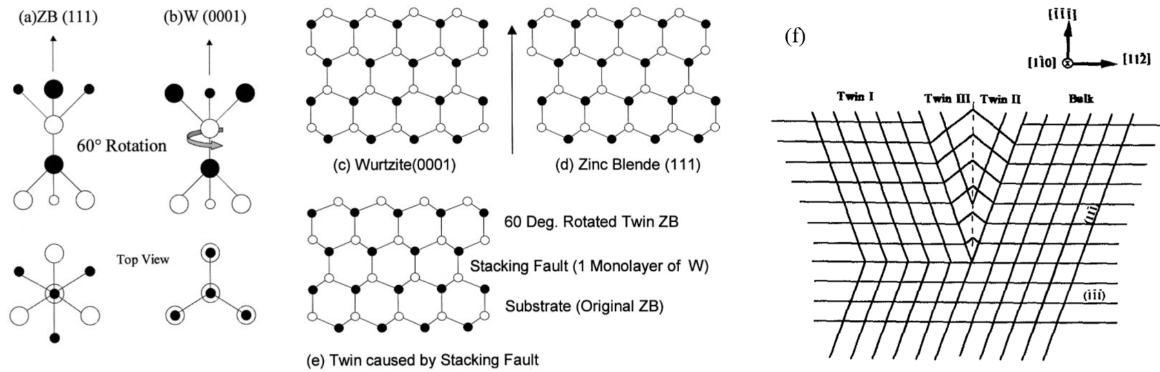

Figure 3.12: Building blocks of a) ZB and b) W, c) W(0001) and d) ZB(111), and e) Structure of twin ZB formed by a stacking fault [132] ©American Vacuum Society. Used with permission. f) Schematic representation of V-type twin complex. $(\overline{1}\overline{1}\overline{1})$ and $(11\overline{1})$ are the twin planes (the two variant of 111 planes), which belong to the $[1\overline{1}0]$ zone. Twining of twin I along a non-growth direction created twin III [5] ©AIP Publishing. Used with permission.

of W structure between two ZB structures (Fig. 3.12.a-e) [132]. The ease of the formation of growth twins on {111} substrate in the case of GaAs was attributed to the attachment of Ga adatoms to the terrace with single bond leaving the other three bonds free to rotate about the growth direction. However, if the Ga adatoms are bonded to the surface steps with more bonds, the chance of twining is substantially reduced. Hence, twinning can be reduced by the use of misoriented substrates with increased number of steps, or the use of growth conditions such as a slow growth rate or growth techniques such as migration enhanced epitaxy that allow for the longer adatom migration to reach the surface steps. The twinning has V-type characteristic (Fig. 3.12.f) [5].

Stacking sequence of ZB is ABCABC, while that of W is ABABAB. When a misplacement of bilayer takes place in a W structure, it gives a sequence of AB$\underline{\text{ABC}}$BCB leading to a single unit of ZB structure. However, a misplacement of a single bilayer in ZB structure only gives rise to a twin but not a stacking fault; ABCACB. In fact two twins are needed to create a stacking fault, i.e., four bilayers; AB$\underline{\text{CACA}}$. This means that the smallest W segment in ZB phase is larger than the smallest ZB segment in W phase [133]. Stacking faults which originate from the heterocrystalline W-ZB interface were shown to introduce electronic levels within the band gap close to the valence band [134].

3.2.4 Short-range ordering

The thermodynamic of the alloy system in ternary or quaternary alloy often produces some degree of microscopic and macroscopic ordering. Short-range ordering occurs when atoms adopt correlated neighboring positions over distances of the order of few lattice spacing. This is seen in the preferential association of like atoms such as in clustering or chemical ordering (for example, CuPt type ordering). Long-range ordering occurs over many tens of lattice spacing such as in phase separation [135]. Long range ordering or superstructure is atomic scale deviation from the random distribution of group III atoms on the column III sublattice, which results in band gap change and observation of {1/2,1/2,1/2} superlattices [25, 136, 137]. CuAu-I type ordering was shown to be the most stable ordered structure thus far to occur in III-V ternary alloys. The superstructure which have reflection from {hkl} indices that are (odd, odd, even) or (even, even, odd) are of CuAu-I type superstructures. These reflections are allowed only if a long range order exists. In the case of InGaAs, Ga atoms preferentially occupy the {0, 0, 0} and {1/2, 1/2, 0} sites and In atoms preferentially occupy the {1/2, 0, 1/2} and {0, 1/2, 1/2} sites in each unit cell [138, 139].

The most important factor controlling the degree of ordering is the surface mobility of the depositing species during the growth. The higher the surface mobility in the growth direction, the stronger is the ordering [138]. The smoother is the growth, the lower is the degree of ordering. The stability of an ordered phase stems from its ability to reduce the strain energy by accommodating two dissimilar bond lengths. Hence, an ordered phase is more favored and thermodynamically stable in alloy systems with dissimilar bond lengths [140]. This shows the dependence of the ordering on the alloy system and its composition. The growth technique was shown to affect the degree and type of ordering [138]. Growth temperature also affects the ordering process. At low temperatures, ordering is not seen due to the insufficient surface mobility [139].

Misorientation from the exact orientation [137] as well as the surface reconstruction are other factors that affects the formation and degree of ordering. It was shown that GaAsSb grown on (001)InP has a CuPt-type ordering, while growth on misoriented InP(111)B for 3° towards $[\overline{1}\overline{1}2]$ does not develop ordering. This was attributed to the (2×) surface reconstruction for the growth on (001) substrate [141]. Gomyo et al. [25] also reported on non-existence of such ordering for the MOCVD growth of $In_{0.5}Ga_{0.5}P$ on GaAs(111)B substrate 0.5° misoriented towards $[01\overline{1}]$. However, such superstructure exists for growth on GaAs(001) (Fig. 3.13a,b).Cho et al. [142] reported on the temperature dependent presence of ordering for growth of InAlAs on InP(001). Kuan et al. [138] reported on the existence of a CuAu-I type superstructure in MBE grown $In_{0.5}Ga_{0.5}As$

on InP(110) substrates misoriented by 4° towards (111)A and (111)B poles. A perfectly ordered structure consists of alternating InAs and GaAs monolayers along the [110] growth direction or the [001] direction normal to the growth axis. The occurrence of ordering in $In_{0.53}Ga_{0.47}As$ on InP(001) was observed along one of the four <111> directions. Appearance of half-way spots in the diffraction pattern shows twice the ZB periodicity in the [111] direction [143].

Suziki and Gomyo [144] reported on the ordering mechanism of the naturally formed {1/2,1/2,1/2} SL on the column III sublattice that was observed in $In_{0.5}Ga_{0.5}P$ grown on GaAs(001) 2° off towards (011); they explained the ordering mechanism as i) the intra-planar ordering, i.e. ordering within each plane (alternative rows of rich in Ga and In), and ii) inter-plane ordering, i.e. ordering of the successive planes. Mechanism (i) is related to the fact that the bond lengths and angles in ternary alloys differ from their constituent binaries. Due to a large bond length difference and a dangling bond direction asymmetry on the (001) planes, there is an anisotropic site occupation affinity for group III adatoms. This anisotropy minimizes the stress and acts as a driving force for the long range order of group III atoms (Fig. 3.13.c). Mechanism (ii) is related to the phase locking behaviour of the [110] atomic steps that aligns the atomic lines belonging to adjacent planes in-phase and prohibits random walk (Fig. 3.13.d). They proposed that this mechanism can apply to any kinds of alloy semiconductors such as InGaAs, InGaP or InGaAsP.

3.2.5 Compositional Modulation (CM)

CM or phase separation or spinodal decomposition refers to a spontaneous formation of a phase-separated, self-organized periodic structure that leads to a surface corrugation/undulation as seen in Fig. 3.14.a [135]. CM leads to strain inhomogeneity and lowers the electron mobility. The reason behind phase separation can be explained based on the Gibbs free energy. The Gibbs free energy has two terms of enthalpy and entropy. At low temperatures, the enthalpy term prevails, therefore, the free energy decreases as the number of bonds increases. This leads to the formation of patchy surfaces with regions having zero coverage and near-unity coverage. This results in a concave down Gibbs free energy curve, meaning that phase separation reduces the Gibbs free energy. Once the spinodal decomposition of the ternary alloy into its binary constituent starts, the preferential segregation of the adatoms towards the compressive or tensile regions is responsible for the continuation of the decomposition during the growth. On the other hand, at high temperatures, the entropy term dominates. This leads to a random distribu-

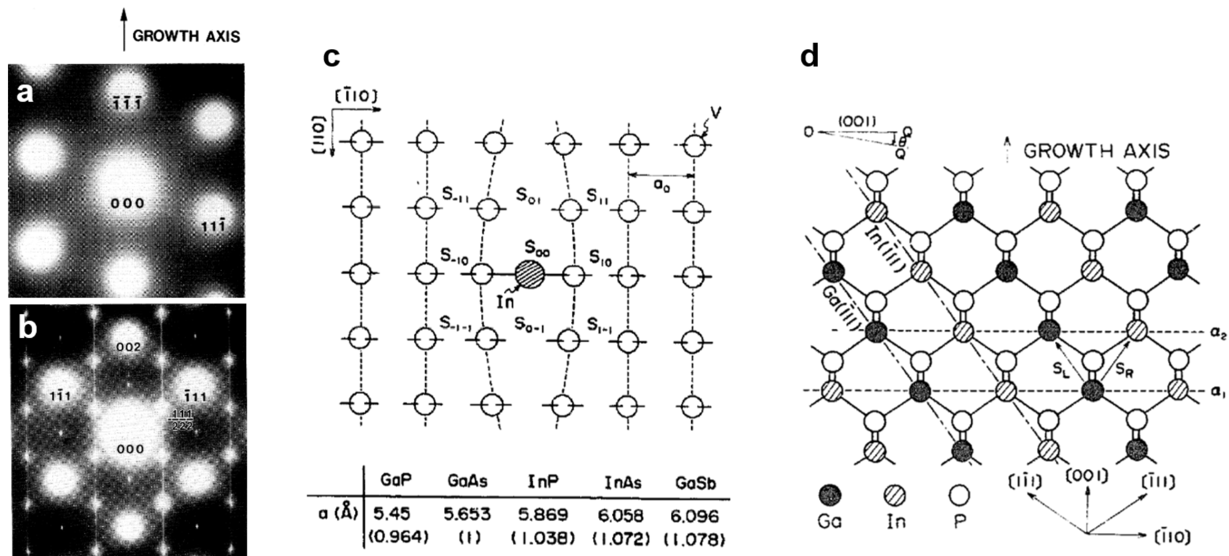

	GaP	GaAs	InP	InAs	GaSb
a (Å)	5.45	5.653	5.869	6.058	6.096
	(0.964)	(1)	(1.038)	(1.072)	(1.078)

Figure 3.13: Transmission electron diffraction pattern of InGaP grown at 700° C on a) (111)B and b) (001)GaAs substrate [25] ©IOP Publishing. Used with permission. c) Ordering mechanism i: Column V element (P or As)-stabilized (001) plane with an In atom at position s_{00}. The In atom stretches the lattice spacing producing an anisotropic site occupation affinity for Ga and In, which generates a long-range order on a (001) plane. Note the two dangling bond directions on element V. a_0, indicates the column V atom spacing before the In atom sticking. s_{ij} indicates the site positions for column III atoms. Lattice constants for some binaries are reported. In parentheses, lattice constants normalized to that for GaAs are given. d) Ordering mechanism ii: In and Ga rich planes locked in alternative layers [144] ©Elsevier. Used with permission.

tion of adatoms on the surface in order to maximize the entropy term and consequently minimize the Gibbs free energy [62, 145].

Different mechanisms were proposed to explain CM. Glas [148, 149] showed that the elastic energy is minimized for a critical modulation wavelength of a given film thickness. However, the CM itself does not strain-stabilize the epitaxial film and a further strain relaxation mechanism which is surface elastic relaxation is accountable. Therefore, a lattice-matched alloy with a finite lateral CM is always unstable against undulations of its free surface. CM is said to exist in immiscible alloys where changes in composition results in a change in lattice parameter and induces strain.

Another mechanism for initiation of CM was explained in terms of misfit stresses

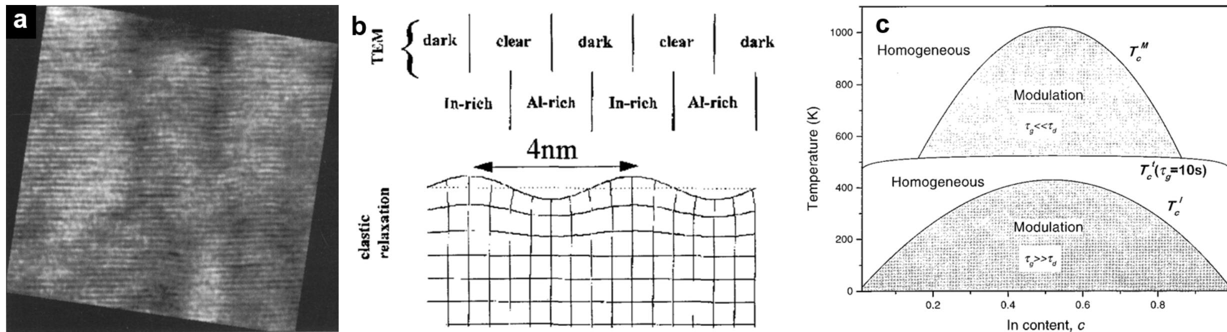

Figure 3.14: a) cross-sectional TEM showing slight corrugation in the nominally lattice-matched AlAs/InAs short period SL [135] ©Springer Nature. Used with permission. b) a schematic representation of the consequence of a lateral composition modulation on the TEM contrast via a surface elastic relaxation of the strained InAlAs surface [146] ©Elsevier. Used with permission. c) Phase diagram of epitaxial InGaAs alloy grown at a growth rate of 0.1 ML/s showing two modulated regions (in which the alloy will present a kinetically stabilized composition modulation) with a homogeneous region in between. Two regions of modulated alloys are separated by a homogenous region due to the limitation of growth rate [147] ©AIP Publishing. Used with permission.

in strained dislocation-free films. Misfit stresses produce morphological instabilities in lattice-mismatched films. Hence, the film may become corrugated. When there is compression, the lattice parameter of the flat film is smaller than its stress-free value. Therefore, the lattice parameter is larger at the protuberances and smaller at the depressions compared to the coherent flat film. This leads to the preferential migration of larger atoms to the protuberances and smaller atoms to the depressions. The situation is reverse for when there is tensile strain. The larger atoms diffuse to the depressions and the smaller atoms to the protuberances resulting in the depletion of smaller and larger atoms at the depressions and protuberances, respectively (Fig. 3.15). Thus, surface corrugation and preferential migration of atoms induced by misfit strain can initiate CM [150, 151].

In fact, phase separation happens as a result of equilibrium between: (i) an intrinsic alloy strain energy that decreases if phase separation occurs; (ii) an extrinsic alloy strain energy induced by the lattice mismatch between the epilayers and the substrate (CM leads to mismatch-induced strain relaxation); and (iii) a roughening which increases the surface energy but allows both intrinsic and extrinsic strain energies to relax [146].

Phase separation is strongly dependant on growth parameters such as growth tem-

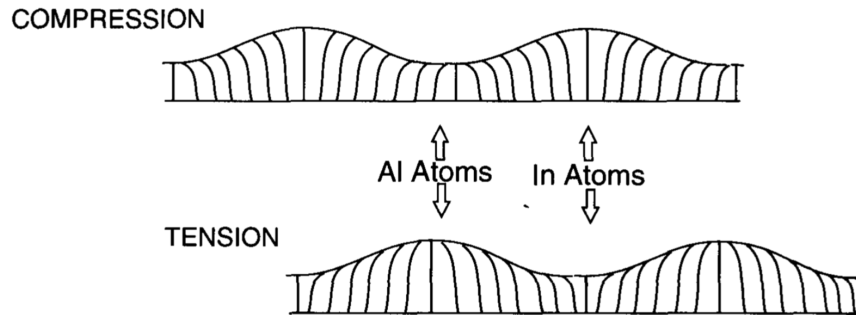

Figure 3.15: Schematic diagram illustrating how a strain-induced surface corrugation can initiate composition modulation for both compressive and tensile strains. Smaller atoms preferentially attach where the lattice is compressed, and larger atoms attach where it is dilated, thus initiating lateral composition modulation [135] ©Springer Nature. Used with permission.

perature, V/III Beam Equivalent Pressure (BEP) ratio, growth rate, and the presence of misorientation steps. It diminishes when the growth kinetic is limited by an increase of the V/III ratio and/or of the growth rate. Fig. 3.14.b shows a schematic representation of lateral CM on the TEM contrast via a surface elastic relaxation of strained clusters [146]. Gonzalez et al. [147] calculated a phase separation diagram for $In_{0.5}Ga_{0.5}As$ (Fig. 3.14.c). They showed that CM disappears above a critical temperature. There is also a temperature window at lower growth temperature that a homogeneous alloy can again be grown. These temperatures are affected by the growth rate. An increase in the growth rate enlarges the window at which the composition is homogeneous. At higher growth rates, the atomic diffusion does not allow the system to reach the kinetic equilibrium. Phase separation was seen at low temperature growth of InAlAs on InP (001) [142]. Energy per deposited atom calculations showed that phase separation does not happen if the growth front is perfectly flat, however, a 3 ML roughness is enough to allow a partial elastic relaxation and stabilize phase separation in InAlAs grown on InP(001) [146].

Woo et al. [152] showed suppression of phase separation in InGaN films grown on Si(111) substrate by the use of Metal Modulation Epitaxy (MME). They showed that phase separation is strongly dependent on the In flux supply and at the optimized In pulse time, spinodal decomposition is suppressed due to improved surface migration of In atoms. Spinodal decomposition could also be avoided using growth techniques such as Atomic Layer Molecular Beam Epitaxy (ALMBE) at low growth temperatures (200-300° C) [147].

Follstaedt et al. [153] studied the effect of strain on CM in InGaAs/InAlAs short period SL grown on InP(001). They showed that at global strain, ϵ, (global strain is defined as

$\epsilon = (a_{\|} - a_{epi})/a_{epi}$, where a_{epi} and $a_{\|}$ are the in plane and perpendicular lattice constants) of higher than $+/-0.7\%$, CM disappears. The degree of CM is maximum at strain level of zero. CM depends also on the film thickness; it happens above a critical thickness during low temperature growth [154]. In another study, Herrera et al. [155] investigated the degree of plastic deformation caused by CM in InGaAs/GaAs layers grown by ALMBE at low temperature (200° C) on on-axis GaAs(001). They showed that CM causes internal stress/strain, which is responsible for the plastic relaxation of the low temperature grown InGaAs layers. CM also impedes the glide of dislocations causing strain hardening of the alloy. The wavelength of the CM was shown to be different along different azimuths. The anisotropy of the CM was related to different diffusion lengths related to the surface reconstruction [135]. Diffusion is impeded in the misorientation direction due to the existence of the step-fronts perpendicular to the misorientation direction (Shwoebel barrier) [156]. Since the surface reconstruction determines the fast and slow diffusion directions, substrate misorientation could alter the diffusion kinetics. CM is suppressed at high misorientation angle of 15° due to the small step width [154].

Vertical CM was also reported for the growth of (In,Ga)(N,As) on vicinal GaAs(111)B versus lateral CM on (001) substrates. This was related to the spinodal decomposition of the step-flow grown (In,Ga)(N,As) alloy. Steps with different atom configuration termination propagate with different velocity creating step bunches with In-rich and N-rich layers (Fig. 3.16). The formation of step bunches of alternating composition causes vertical CM. A smaller misorientation angle reduces the step density, which could suppress the decomposition trend [157].

Phase separation and ordering are important as they limit the band gap engineering due to reducing the band gap. However, unlike phase separation, ordering can be eliminated by annealing. The degree of phase separation and ordering reduces at higher growth temperatures. The degree of phase separation and ordering are maximum at low and medium growth temperatures, respectively [142].

3.2.6 Mismatch-induced strain

Growing lattice mismatched layers, misfit strain is induced in the epilayers, which is accommodated by the competing process of dislocation formation and elastic deformation. When the epilayer is too thin, formation of a large number of misfit dislocations costs more energy than the energy stored due to the elastic deformation, therefore, strain results in the elastic deformation leading to the tetragonal distortion in the lattice in the plane of the growth [30, 158]. This means that there is a critical layer thickness before

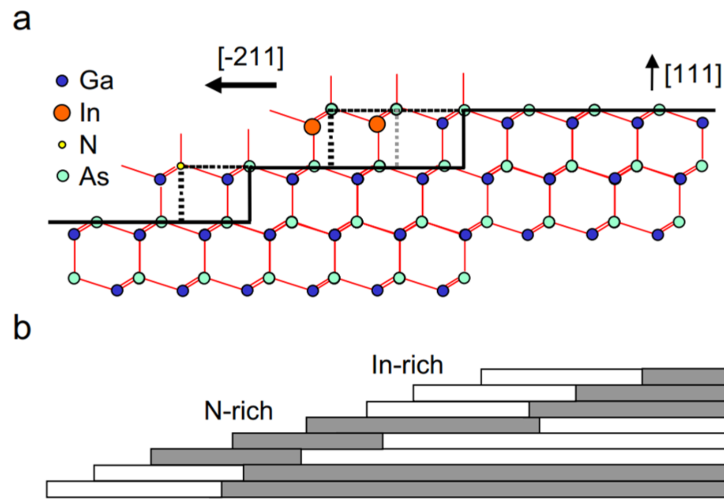

Figure 3.16: A schematic showing a) possible atom termination of the steps in GaAs(111)B surface misoriented by 1° towards $[2\bar{1}\bar{1}]$ and b) step bunching of In-rich and N-rich layers [157] ©Elsevier. Used with permission.

misfit dislocations formation becomes energetically favorable, and they start to appear. The mechanical equilibrium theory by Mathews and Blakeslee was used to compute the critical layer thickness of InGaAs/GaAs heteroepitaxy on GaAs(111)B compared to (001). It was shown that the critical layer thickness is larger when growth is in the [111] direction (Fig. 3.17.a). This was attributed to a larger driving force for the formation of misfit dislocation in the [001] direction. Growth temperature also affects the critical layer thickness since dislocation formation is a thermally activated process. Therefore, the critical layer thickness is larger at lower growth temperatures, but it reaches a plateau eventually (Fig. 3.17.b). Mismatched $In_xGa_{1-x}As$ and $In_yAl_{1-y}As$ to InP can be grown with high quality up to 3-9 times the Matthews-Blakeslee [159] critical layer thickness if the mismatch does not exceed ±%1. Larger mismatch was shown to be tolerated by InAlAs in tension than compression, while no obvious difference was seen for InGaAs layers [160]. When growing lattice-mismatched, layer-by-layer growth persists at higher strains when growth is done by Migration Enhanced Epitaxy (MEE) [161].

Dislocations in diamond crystals were shown to glide on (111) planes and their Burgers vectors is along the [110] direction since the slip system in FCC crystal is (111)[110]. The shortest lattice vectors that are allowed as Burgers vectors are 1/2<110>, i.e. half the diagonal of a cube face or one of the short edge of the tetragonal cell. a/2<110> is the Burgers vector of the lowest energy perfect dislocations, where a is the lattice constant

along the [110] direction. When the stacking fault energy is low, a perfect dislocation dissociate into two partials. The separation distance depends on the stacking fault energy. Any stacking fault is bounded by two partials: one at the left side and one at the right side. Since the stacking faults are two-dimensional imperfections they have to be bounded by one dimensional imperfections: dislocations. The split of a perfect dislocation that is not parallel to the glide plane to an extended dislocation with a stacking fault parallel to the glide plane is energetically more favorable. This follows Frank's rule which says that the dislocation reaction is favorable if $b_2^2 + b_3^2 < b_1^2$, where b_1, b_2 and b_3 are the Burgers vectors of the perfect dislocation and the two partials, respectively [162].

Stacking faults could be intrinsic or extrinsic. Considering a diamond crystal lattice with AaBbCc stacking in which Aa, Bb and Cc are the bilayers, an intrinsic stacking fault is formed by missing a bilayer. An extrinsic stacking fault is formed by insertion of a bilayer. Such insertion or removal of atomic planes changes the direction of bonds between the atomic planes and creates twin planes. Since twins are easily formed, they presumably have a low surface energy, and the surface energy of the stacking faults will also be low. Therefore, energetically there will be no serious difficulty in the formation of partial dislocations with the stacking faults [162].

3.3 Growth improvement methods

3.3.1 Growth on vicinal surfaces

Vicinal surface is a miscut surface in a specific direction from a low index plane. The surface of a vicinal surface consists of a low index plane with monoatomic steps. Surface steps due to the misorientation from the singular (111) surface are the principle reason for the surface morphology improvement when growth is done on vicinal surfaces. This prevents (001) facet growth [163]. As_4 molecules preferentially decomposes at surface steps when growing on misoriented substrate due to the higher valence electron density of Ga dangling bond sites at the steps than the terraces. This leads to a lateral growth at the steps [164].

Growth on vicinal surfaces is explained by Burton, Cabrera and Frank (BCF) theory [163], which states that growth proceeds in a step-flow growth mode provided that the adatoms are mobile enough. This is achieved when the growth temperature is high or the atomic flux is low or in other word when the encountering probability of the adatoms is sufficiently low. The adatom interaction becomes significant at low growth

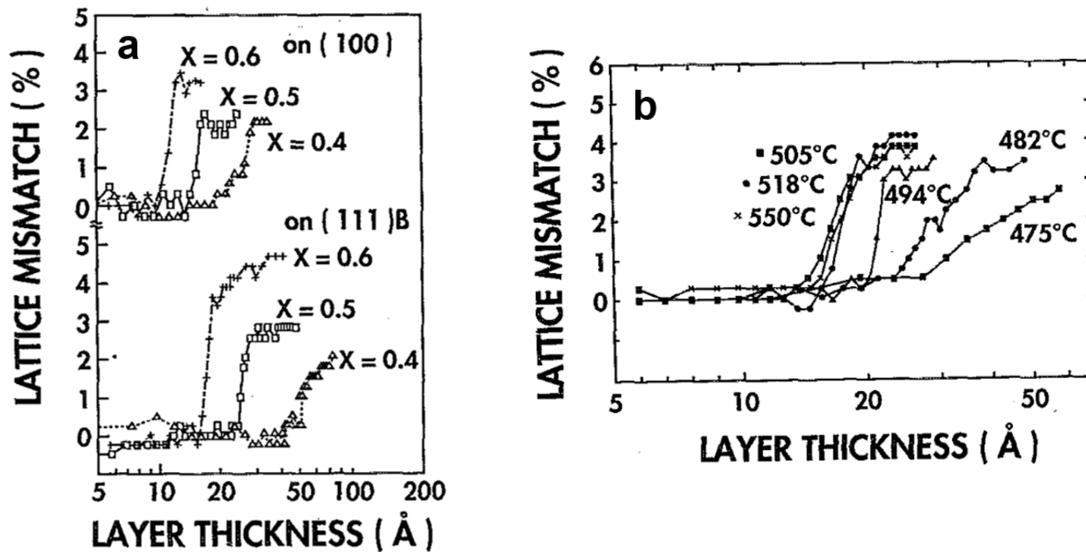

Figure 3.17: a) Strain dependence of surface lattice relaxation for InGaAs obtained from RHEED measurement grown at 510° C. b) Growth temperature dependence of surface lattice relaxation for the growth of $In_xGa_{1-x}As$ with $x = 0.58$ grown on GaAs-(111)B substrates [28] ©AIP Publishing. Used with permission.

temperatures or high atomic flux, which leads to island nucleation and coalescence to be the dominant growth mode. Fig. 3.18.a shows a schematic representation of the singular and vicinal surfaces. In general, vicinal surfaces do not have uniform terrace lengths. To overcome this situation, a buffer layer can be grown assuming that the buffer layer grows by step flow mode and the atoms attach predominantly at the up-step of each terrace. This makes the larger terraces to shrink and the smaller ones to expand [165]. Atomically smooth surface morphology is achieved on vicinal surfaces when the cation migration length matches the terrace width and growth proceeds by step flow mode [22]. At larger mis-cut angles when the steps become closer together, step bunching which is coalescence of two or more steps is probable. This results in the formation of macrosteps which are several nanometer tall (Fig. 3.18.a) [6]. The steps on vicinal surfaces provide a lattice stress source that interacts with overlapping stress fields of nearby steps. These step interactions are found to be energetically attractive. The long range coherent interactions leads to a significant reduction of surface energy [95].

Crystal surfaces exactly parallel to a low-index Miller plane were believed to have a lower surface energy compared to vicinal surfaces [6]. However, there have been

studies reporting on the lower surface energy of vicinal surfaces compared to singular surfaces. They attributed the lower energy of a misoriented surface to the presence of double-layer steps compared to single-layer steps on singular surfaces in the case of Si(001) (Fig. 3.18.b) [166, 167]. Single-layer steps are present at smaller misorientation angle and there is a transition to double-layer steps at a higher critical angle [166, 168]. Double-layer steps were found energetically favorable compared to single-layer steps.

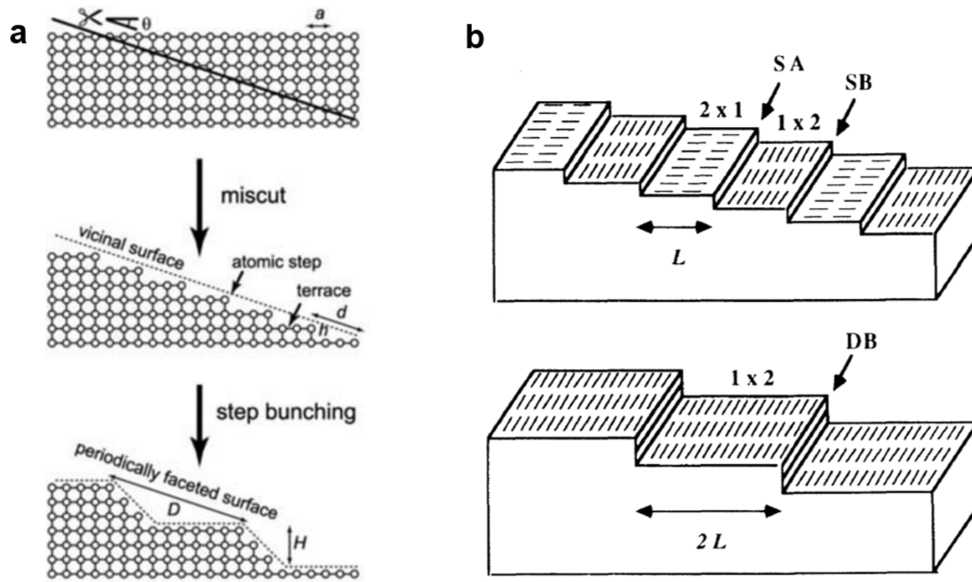

Figure 3.18: Schematic representation of a) a singular and a vicinal surface, and step bunching [169] ©Royal Society of Chemistry. Used with permission. b) Schematic representation of the single-layer and double-layer step structures of a vicinal Si(100) surface. The surface misorientation θ is related to the terrace width L by $tan(\theta) = z_{SL}/L$, where z_{SL} is the height of a single layer step [166] ©American Physical Society. Used with permission.

Use of misoriented substrates to eliminate hillocks were reported. Different misorientation angles have been reported for the growth mainly on GaAs(111) [6, 8, 26, 86], but there are several reports for growth on InP(111) as well [2, 10, 13, 31, 33, 35, 84]. For example, Schowalter et al. [6] showed that a very smooth homoepitaxial growth on GaAs $(\overline{1}\overline{1}\overline{1})$ is obtained with the steps running along the $[01\overline{1}]$ direction at a misorientation angle of 3° toward $[2\overline{1}\overline{1}]$. Growth at misorientation angle of less than 2° results in the appearance of hillocks on the surface. The smaller the misorientation angle, the higher the growth temperature required to achieve a smooth surface morphology [20]. Yeo et al.

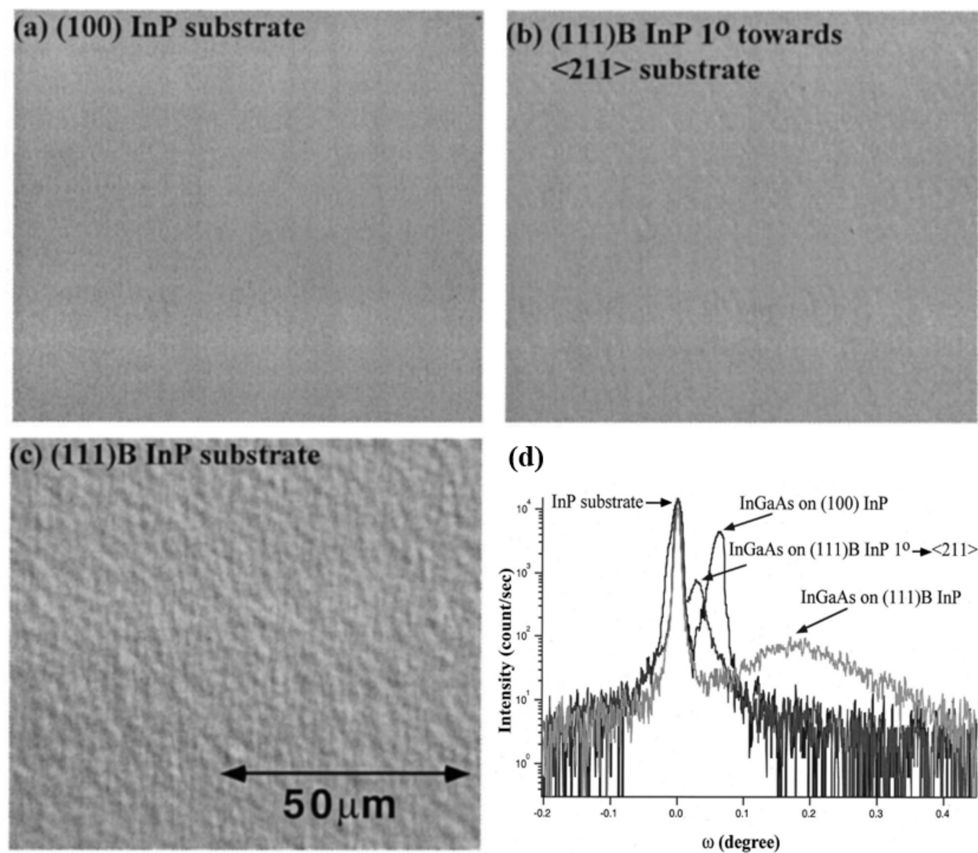

Figure 3.19: Nomarski images of the surface morphology of InGaAs grown on a) (100), b) misoriented 1° towards <211> and c) singular InP(111)B. d) High resolution $\theta/2\theta$ scan at <333> reflection of a-c [33] ©AIP Publishing. Used with permission.

[33] reported the growth of InGaAs on InP(001), InP(111)B and InP(111)B misoriented by 1° towards <211> (Fig. 3.19). They observed some elliptical shaped features for growth on misoriented InP(111)B but overall smooth surface morphology. The high resolution x-ray diffraction measurements showed a narrower Full Width at Half Max (FWHM) for the growth on misoriented substrate compared to exact (111)B suggesting higher density of defects such as stacking faults and twins on singular substrate due to the lack of steps (Fig. 3.19.c). There are also few reports on the use of rounded edge substrates to investigate the effect of off-cut substrate on the growth morphology and to find the optimum off-cut angle [10, 23, 26, 170–172]. For example, Tsutsui et al. [23] showed that a misorientation of 1.5° is needed for hillock-free growth of GaAs on GaAs(111)B substrates (Fig. 3.20).

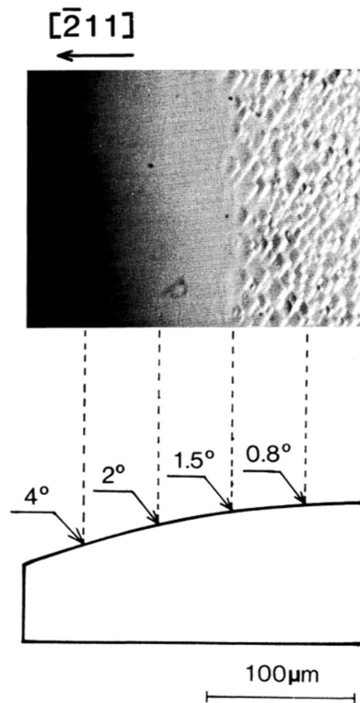

Figure 3.20: Morphology change of a GaAs layer grown on a curved surface towards [100] near the edge region of an exactly (111)B substrate [23]. ©IOP Publishing. Used with permission.

Sadeghi et al. [173] showed that a misorientation angle of 0.4° can avoid hillocks for the growth of InGaAs on InP(111)B at the optimized growth condition. Studies also have reported substantial improvement on the surface morphology of (111)B when growth is performed on vicinal or misoriented surfaces. However, the effect of misorientation was reported to be less for (111)A substrates [21].

Dependence of the morphology on the azimuth was studied by McFee et al. [10]. They showed that for the homoepitaxy of InP ($\overline{111}$) on lens-shaped substrates, a wider smooth region is found along [$2\overline{11}$] direction compared to [$01\overline{1}$]. The misorientation angle that the smooth region occurs was shown to be different at different azimuths. It was also shown that the presence of a smooth region depends on growth temperature; the smooth region disappears and surface becomes completely granular at growth temperatures lower than 315° C. Below 350° C, the epitaxial layer become polycrystalline with an increased number of defects such as stacking faults. However, Hayakawa et al. [26] reported that the specular surface is achieved with slight misorientation of 0.5° from

exact GaAs(111)B irrespective of the misorientation direction.

3.3.2 Surfactant-mediated growth

The use of a surfactant was shown to improve the surface morphology. Surfactant is a species that controls the growth by manipulating the free energy of the surface it adheres to. It alters the growth kinetics and modifies the relative energies of different crystallographic faces for growth so that an islanded surface becomes unstable [174]. The primary requirements for the surfactants are that it lowers the surface free energy of both the surface and the overlayer, and that it is sufficiently mobile to avoid incorporation. In other words, the surfactant must not preferentially adsorb to either substrate or overlayer, and it must surface segregate with high efficiency [175]. The ability of a surfactant to segregate on the surface does not necessarily guarantee it is effective in promoting two-dimensional growth mode. This fact leads to classification of surfactants into two groups; i) those which increase the migration length of adatoms and improve the crystal quality during the growth and ii) those which decrease the migration length and delay the two-dimensional to three-dimensional growth transition during heteroepitaxy and increase the critical thickness. The latter and former types are called non-reactive and reactive surfactant, respectively. Type (i) surfactants incorporate interstitially. They reduce the bond strength and energy barrier for hopping leading to an increased migration length. In contrast, type (ii) surfactants incorporate substitutionally and can no longer diffuse once incorporated into the growing film. Therefore, in order for the semiconductor adatom to migrate, it has to break the bond between surfactant, which leads to a high energy barrier for hopping and a reduced migration length [176, 177].

Pb [177], Sb [178–180], As [120] and Bi [43, 181–183] were reported to act as non-reactive surfactants and improve the surface morphology. Sato et al. [178] reported on the suppression of three-dimensional islands in MOCVD grown strained InGaAs multi QW using Sb as surfactant (Fig. 3.21). Bi is a difficult atom to incorporate into III-V semiconductor during MBE growth since it segregates on the surface and evaporates at the typical 400-700° C III-V growth temperature or it forms droplets at temperatures below 400° C. Optimum amount of As on the growing surface functions as an effective reactive surfactant assisting Bi incorporation [183]. At sufficiently high flux, Bi leads to a step flow growth mode even at low substrate temperatures (Fig. 3.22). It increases surface migration length relative to As-terminated surface [181]. Bi changes the reconstruction of InGaAs surface grown on GaAs(001) from As-stabilized (2×4) to Bi-stabilized (1×3). Bi was also shown to reduce the interface roughness and width during the InGaAs/GaAs SL growth on GaAs(001), which was attributed to a reduction in In segregation [43]. Te

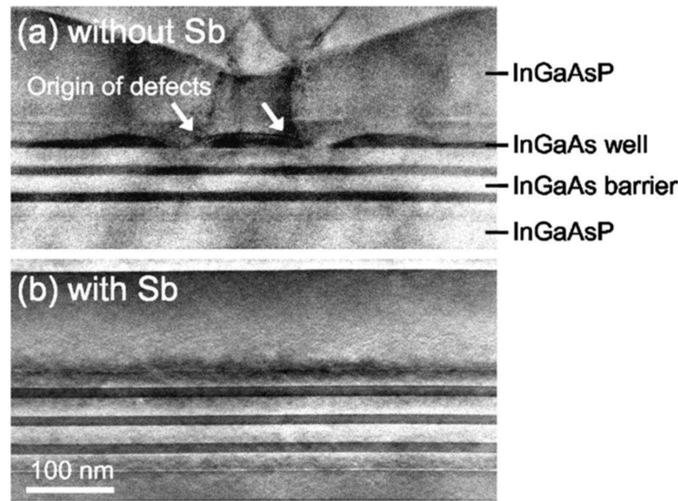

Figure 3.21: Cross-sectional TEM image of strained InGaAs multi QWs grown on (100)InP a) with and b) without Sb surfactant. The thickness undulation of the wells that shows a three-dimensional growth is the origin of the structural defects. Suppression of the defects and undulation when Sb surfactant is used is seen [178] ©AIP Publishing. Used with permission.

[177] was shown to act as a reactive surfactant for highly strained material systems such as InGaAs on GaAs. Ilg et al. [42] reported enhancement in the surface morphology of homoepitaxy on 0.5° misoriented GaAs(111)B using In surfactant segregant on the surface. They showed that MBE growth without In surfactant results in either metal-rich (1×1) or metal-stable $(\sqrt{19} \times \sqrt{19})$ structure depending on the substrate temperature and V/III ratio. However, growth proceeds in a well defined unreconstructed (1×1) surface at all growth conditions when using In surfactant.

Growth in metal-rich condition was explained as virtual surfactant MBE. During virtual surfactant MBE, the group V species As_4 is growth-limiting species. The sticking coefficient and dissociation rate of the As_4 molecules are maximal on a cation-stable (i.e. metal-rich) surface. Thus, a metal-rich surface acts as a catalyst for the dissociation and incorporation of As_4. Consequently, kinetic limitations are relaxed and island information is suppressed [176].

Kandel and Kaxiras [184] reported on the physical mechanism by which the surfactant changes the mode of growth from three-dimensional Volmer-Weber to layer-by-layer growth. They attributed this to the chemical passivation of the step edges as well as the flat surfaces due to the saturation of surface dangling bonds by surfactant atoms.

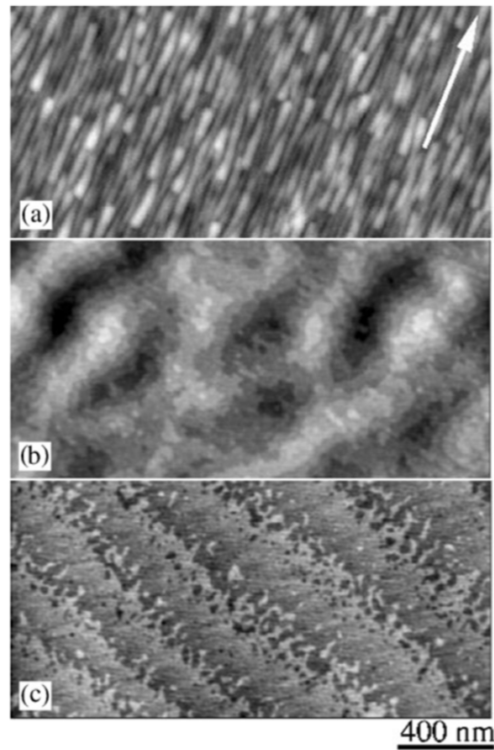

Figure 3.22: effect of Bi surfactant on the surface morphology of GaNAs; a) no Bi, b) Bi BEP $\sim 10^{-7}$ Torr and c) Bi BEP $\sim 1.4 \times 10^{5}$ Torr. In the absence of Bi, surface morphology is anisotropic with surface features elongated in $[01\bar{1}]$ direction shown by arrow. The surface roughness is 1.2 nm. The growth morphology changes dramatically at high Bi flux and an rms roughness of 0.1 nm is achieved as in c). At medium Bi pressure, the surface is fairly isotropic with an rms roughness of 0.4 nm. Bi reduces the adatom bond strength at the step edges by forming GaNAs-Bi complex on the surface [181] ©Elsevier. Used with permission.

Therefore, the system energy is lowered when the surfactant is on top rather than buried under the newly deposited atoms. The surfactant thus tends to float on the top of the film surface. The authors considered a kinetic exchange process between surfactant and the deposited atoms. The energy barrier for exchange E_{ex} and the barrier for diffusion E_d of atoms on top of the surfactant control the process. Their theoretical calculation on Si(111) substrate suggested that the probability of an exchange is much smaller than the probability of a diffusion hop (i.e. $E_d < E_{ex}$). This means that the adatom diffuses a long distance before it exchanges. This is because the exchange process involves interlayer

atomic motion and breaking of chemical bonds, while the diffusion barrier is presumably small due to the chemical passivation of the surface by the surfactant.

3.3.3 Migration Enhanced Epitaxy MEE

Migration enhanced epitaxy (MEE) is a growth method in which group III and V atomic species are alternatively supplied. This leads to an increased migration lengths of group III species in the absence of group V. MEE can produce smooth surface morphology on non-misoriented substrates [36–40, 185]. In MEE, layer-by-layer growth takes place. Group III atoms migrate actively on the surface in the absence of group V atoms and form a complete monolayer coverage. The sticking probability of impinging group V atoms highly depends on the group III coverage on the surface. For a monolayer coverage of group III, the initial sticking coefficient is unity [186]. Atomically flat surface is achieved when the number of group III atoms deposited per cycle equals the number of surface sites N_s. The surface roughness is 1ML even with an incommensurate deposition. Since the migration distance is quite large, new islands do not form until the growth of the base layer is complete. Annealing further improves the surface smoothness when it is done after the group III deposition since annealing further enhances the migration length. Annealing after the group V deposition leads to an interruption of the MBE growth, hence, modulated RHEED oscillations survive [39, 185]. This is due to the fact that MEE leads to a condition such as step-flow growth mode that could result in a specular morphology at an optimized growth condition when cation migration length is in the order of terrace width at that misorientation angle [22]. Using MEE growth of atomically flat structures and interfaces have been achieved even at low growth temperatures. Examples are GaAs/AlGaAs QW on GaAs(001) [36–39] and AlGaAs on exactly GaAs(111)B [40].

MEE was shown to be effective for growth on GaAs(111)B surface with an As-stabilized $(\sqrt{19}\times\sqrt{19})$ reconstruction since deposited Ga atoms first fill the Ga vacancy sites resulted from the $(\sqrt{19}\times\sqrt{19})$ reconstruction and then form droplets after the full monolayer coverage which are consumed when As is supplied. However, MEE growth mode is not suitable for (111)A surface since it is a metal-rich (2×2) reconstruction even during the As supply, hence, it is hard to form As-stabilized surface. Deposited Ga atoms only form droplets on the surface without occupying the missing Ga sites on the surface (one Ga atom in each (2×2) unit cell is missing). This makes MEE growth mode a not suitable technique for growth on (111)A substrate since As-stabilized surface is hard to form [187].

Selective area epitaxy (Selective Area Epitaxy (SAE)) as an application of MEE has been reported to produce a smooth and uniform growth of GaAs on GaAs(111)B when

annealing is done after Ga deposition. With annealing after As deposition polycrystalline deposition occurred. Group III atoms were reported to easily evaporate from the SiO_2 mask during the annealing process provided that a high growth temperature is used [188]. However, SAE on GaAs(111)A substrate resulted in hillocks formation [189].

3.3.4 Metal modulation epitaxy (MME)

Metal modulation epitaxy was proposed by Burnham et al. [190] to improve the surface morphology of AlN during the MBE growth and widen the window of growth conditions that can be used for more reproducible results. As opposed to MEE which modulates both cations and anions fluxes, MME modulates only the cations fluxes. The cation flux is much higher than the anion in MME ensuring a metal-rich growth condition. When growth is done in group III rich condition, the mobility of group III atomic species increases and they diffuse across many steps leading to an increased diffusion length. This is due to the i) ease of migration when there is metallic bond and ii) absence of enough of group V with unsaturated chemical bonds to fix group III atoms at the step edges [165].

There are only a few reports on the exploit of MME. For example, Wistey et al. [41] used MBE, MEE and MME for the growth of InGaAs/InAlAs on SiO_2/Si_3N_4 masked InP(001) substrates. They showed that growth using MME technique produced the best surface morphology due to the uniform surface mobility and homogeneous growth across the whole wafer, including the areas near the masks. Woo et al. [191] used MME to obtain high quality low temperature GaN with a low defect density. MME was also used to enhance the doping efficiency in GaN films by modulating Ga and dopant atoms [192]. Modulation of P beam supply with the continuous supply of In for homoepitaxial growth of InP on InP(111)B substrate was shown to produce a featureless homoepitaxial InP(111)B growth. Termination of P improves In surface migration [4].

3.3.5 Effect of substrate cleaning

There are fewer reports for growth on InP substrates compared to GaAs, which may be due to the fact that it is challenging to clean InP surface. The phosphorous and indium surface oxides desorb by heating at 458° C for 5-10 min, while lower heating temperatures such as 453° C will lead to the desorption of indium oxide only [193]. Longer heating times will lead to preferential P depletion. It was shown in another study that oxide desorption at 460° C can be done safely without noticeable P depletion, however, the time needed for

complete desorption is about two hours [194]. Annealing at higher temperature which is needed to clean the surface may also lead to P desorption as well as In droplet formation. Cleaning the InP surface under As_4 imposes even more difficulties due to the formation of InAs layer on top of the oxide layer, which slows down the oxide desorption rate and requires higher temperatures such as 520° C or higher for complete desorption of the oxide [195]. Cleaning InP(111)A by Ar ion sputtering and annealing at low temperature of 200° C was reported to produce (1×1) surface reconstruction [196]. Formation of a sacrificial surface oxide using UV/ozone followed by thermal annealing was reported to produce atomically clean InP surface [197].

Chapter 4

Experiment

4.1 Fundamentals of Molecular Beam Epitaxy (MBE)

Epitaxial depositions were done using MBE technique, which is a well-developed method for high quality epitaxial thin film growth of III-V semiconductors. In MBE, thin films crystalize via reactions between molecular or atomic beams of the constituent elements and a substrate surface which is maintained at an elevated temperature in Ultra-High Vacuum (UHV). The composition of the grown epilayers depends on the relative arrival rates of the constituent elements, which in turn depends on the temperatures of the appropriate sources. For group III elements thermal evaporation cells and for group V elements valved cracker cells are used.

What distinguishes MBE from other vacuum deposition techniques is its significantly more precise control of the beam fluxes and growth conditions. Because of vacuum deposition, MBE growth is carried out under conditions far from equilibrium and it is governed mainly by the kinetics of the surface processes occurring when the impinging beams react with the outermost atomic layers of the substrate crystal. In addition, since MBE is realized in an UHV environment, it can be controlled *in-situ* by surface diagnostic tools such as Reflection High Energy Electron Diffraction (RHEED) to avoid much of the guesswork [165].

Our MBE system consists of 4 modules: growth, preparation, load lock and cluster tool modules. Substrates are loaded through the load lock where they experience the first outgassing process at a pressure of about 10^{-8} Torr. The second outgassing process is done inside the preparation module which is maintained at a pressure of 10^{-9}. Cluster

tool acts as a storage for keeping the wafers. The last outgassing process is done on the substrate just before the growth inside the main chamber which is maintained at 10^{-11} Torr. MBE system is maintained at UHV by the use of ion and cryo vacuum pumps that remove the gas impurities from the system. The pumps are separated from the system by the use of high conductance valve during the venting process to keep their cleanliness and effectiveness in pumping. Turbo pumps on preparation module and load lock compress the vacuum gas to a vented outlet held at 10^{-3} Torr or below, where it is removed by a "backing" pump. Liquid nitrogen cryopanels provide very large pumping speeds for condensable gases, particularly H_2O and heavier hydrocarbons. Therefore, cryopanelling surrounding the deposition region is an essential secondary pump for achieving high quality growth for water sensitive materials, e.g., Al-bearing compounds.

Besides vacuum pumps, our Veeco Gen 10 MBE system (Fig. 4.1) is equipped with two of each indium, gallium and aluminum thermal and one of each beryllium and silicon evaporation cells, and one cracker valved cell for each arsenic and antimony elements. It is not equipped with phosphorous cell since phosphorous is pyrophoric. Phosphorous necessitates safe pumping via backing line trap. It is also equipped with ion gauges to measure the Beam Equivalent Pressure (BEP) of the cells. Beam Flux Monitoring (BFM) in extended position that reaches the substrate measures the BEP of group III cells. An ion gauge located at the elbow to cryopump is used to measure the group V overpressure. The system is also equipped with *in-situ* monitoring tools such as RHEED to monitor the surface reconstruction, Band Edge Thermometry (BET) to measure the temperature and reflectance monitoring to monitor the growth surface quality. The MBE system is run by Molly 2000 software to run the deposition recipes.

4.2 Flux calibration of group III and V cells

The cells used for group III elements are Knudsen cells or thermal evaporation cells that generate beams by thermal evaporation or sublimation of materials. Cells temperatures are accurately set by closed-loop controllers which assure stability in the order of tenths of $^\circ$ C as well as fast temperature variations. In order to calculate fluxes of beams impinging on the substrate, the effusion cells are approximated by Knudsen cell, where equilibrium exist between the vapor and the solid (or liquid) phase. According to the Knudsen and Langmuir's theories of evaporation of liquids and solids, respectively, the flux Φ_c of species effusing in UHV from an orifice per unit area per unit time is given by Eq. 4.1: [198].

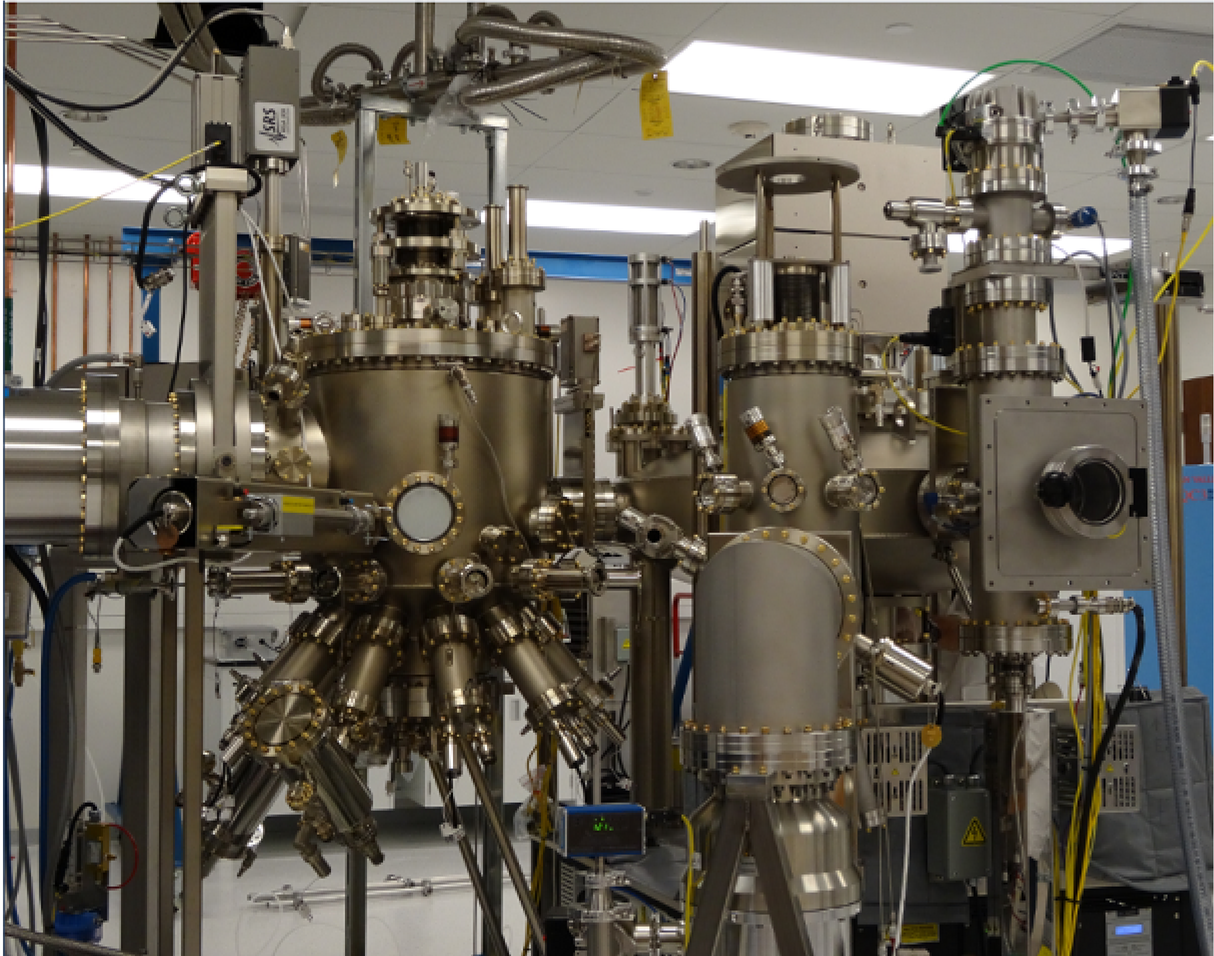

Figure 4.1: Gen 10 MBE system consisting of growth chamber for growth, preparation chamber for oxide desorption prior to growth, cluster tool for storage and load lock for loading the wafers. Gen 10 MBE system is equipped with ion pump, cryopump, RGA to monitor the impurity gas species, RHEED to monitor the surface morphology, BFM and ion gauges to monitor the fluxes.

$$\Phi_c = \frac{P(T)}{\sqrt{2\pi M k_B T}} \tag{4.1}$$

where k_B, M and T are the Boltzmann's constants, the molecular weight of the evaporating species and its absolute temperature, while $P(T)$ is the equilibrium pressure of the evaporant at a temperature T.

The flux that reaches a point P on a substrate situated at a distance r_P from the orifice and following a path at an angle $(\theta + \phi)$ with the substrate axis (ϕ and θ being the angles between cell and substrate axes and between cell axis and path, respectively (Fig. 4.2)), is given by Eq. 4.2:

$$\Phi_P = \frac{\Phi_c}{\pi}\frac{1}{r_P^2}cos\theta cos(\theta + \phi) \tag{4.2}$$

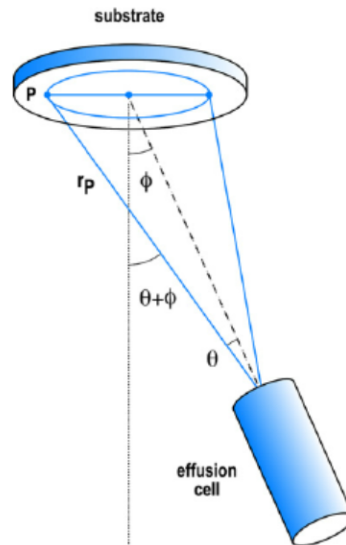

Figure 4.2: Mutual position of effusion cells and substrates in an MBE growth chamber. The dashed and dotted lines represent the axes of cells and substrates, respectively [198] ©Elsevier. Used with permission.

However, since Knudsen cells have orifices too small to give a reasonable flux, open-ended crucibles with relatively large apertures are generally used. Therefore, fluxes from such crucibles cannot be predicted by the above equations based on the equilibrium

between the vapor and solid (or liquid). The fluxes depend largely on the crucible shape (conical or cylindrical), height-to-diameter ratios and their relative position to the substrate. Therefore, real fluxes are deduced from BEPs on beams by using ion gauges or growth rate. The angled position of cells with respect to the substrate necessitates the continuous azimuthal rotation of the substrate during growths if high layer thickness uniformity is desirable.

The atomic flux can be calculated based on its relationship with the BEP (Ψ) measured by BFM and the cell temperature (Eq. 4.4). Not all the atoms entering the ion gauge will ionize and contribute to the BEP. The ionization probability is proportional to the time that the atoms stay inside the gauge ($P \propto$t). Considering the atoms enter a gauge with an area of A and length of L and stay inside the gauge for t seconds and that $t = L/v$:

$$\Phi = \frac{D\Psi}{At} = \frac{D\Psi v}{AL} \tag{4.3}$$

where D is a constant. Since velocity of gas molecules v is proportional to $\sqrt{T}$:

$$\Phi = C\Psi\sqrt{T} \tag{4.4}$$

where C is a coefficient correlated with the ion gauge geometry and ionization probability. Combining Eq. 4.1 and 4.4, we find the relationship between the flux and the BEP as expressed in Eq. 4.5.

$$\Psi = \frac{P(T)}{CT\sqrt{2\pi m k_B}} \tag{4.5}$$

Considering that P(T) follows an Arrhenius relationship with T, BEP can be expressed as a function of Cell temperature (Eq. 4.6):

$$\Psi = \frac{A}{T}e^{-\frac{B}{T}} \tag{4.6}$$

where A is correlated with C and the equilibrium pressure and B is correlated with the activation energy of the element inside the crucible. Therefore, Φ can be expressed as in Eq. 4.7:

$$\Phi = \frac{AC}{\sqrt{T}}e^{-\frac{B}{T}} \tag{4.7}$$

Φ can be readily correlated with the growth rate, G using $\Phi = N_k G$. N_k is the number of atom k per unit volume and is expressed according to $N_k = 4/[(a_k^{\parallel})^2 a_k^{\perp}]$ since there are 4 cation atoms per unit cell. Therefore, Φ is expressed as in Eq. 4.8:

$$\Phi = \frac{4G_k}{[(a_k^{\parallel})^2 a_k^{\perp}]} \tag{4.8}$$

$a_k^{\parallel}$ and $a_k^{\perp}$ are the lattice parameters parallel and perpendicular to the interface, respectively. It is important to note that N_k depends not only on the alloy composition but also on the strain situation of the layer that grows. If the layer is unstrained, $(a_k^{\parallel})^2 a_k^{\perp}$ is equal to $(a_k)^3$, where a_k is the lattice parameter of free-standing layer. However, if the layer is pseudomorphic due to the tetragonal distortion of the lattice, it follows that $a_k^{\parallel} = a_s$ and [199]:

$$a_k^{\perp} = a_k \frac{1+\nu_k}{1-\nu_k} - a_s \frac{2\nu_k}{1-\nu_k} \tag{4.9}$$

where ν_k and a_s are the Poisson ratio of the layer and the lattice parameter of the unstrained substrate, respectively. Combining Eqs. 4.4 and Eq. 4.8, coefficient C can be calculated as in Eq. 4.10:

$$C = \frac{4G_k}{(a_k^{\parallel})^2 a_k^{\perp} \Psi \sqrt{T}} \tag{4.10}$$

Coefficient A and B are determined by a BFM calibration measurement test. BEP of each cell is measured at an increasing temperature steps. A and B are found by fitting the data point in a linear plot of $log(\Psi T)$ vs T. Coefficient C is determined by growing a calibration structure. $a_k^{\perp}$ can be found from High Resolution X-Ray Diffraction (HRXRD) measurements and $a_k^{\parallel}$ is assumed the lattice parameter of the substrate. Knowing T, Ψ, $a_k^{\parallel}$ and $a_k^{\perp}$, one can find C coefficient using Eq. 4.10.

After finding A, B and C coefficient, growth rate, G_k, can be found as in Eq. 4.11:

$$G_k = \frac{ACe^{-\frac{B}{T}}(a_k^{\parallel})^2 a_k^{\perp}}{4\sqrt{T}} \tag{4.11}$$

Eq. 4.11 assumes that the sticking coefficient of the elements is unity. It should be mentioned that the cell's flux is only stable for a limited period of time owing to the (i)

consumption of material, (ii) material degassing, (iii) redistribution of the material inside the cell and iv) change of the cell environment, therefore, re-calibration is required. Coefficient A is re-determined after each growth using Eq. 4.6, but the re-determination of coefficients B and C requires additional BFM and cell calibration growths. These coefficients could change for each campaign depending on the cell reconfiguration, for example by re-positioning the crucible within the cell or changing the cell port or replacing the cell.

For the case of ternary compounds, the unstrained lattice constant and Poisson ratio are found linearly according to Vegard's law as expressed in Eq. 4.12 and Eq. 4.13:

$$a_{ij} = x a_i + (1 - x) a_j \tag{4.12}$$

$$\nu_{ij} = x \nu_i + (1 - x) \nu_j \tag{4.13}$$

Since each monolayer (ML) is half a lattice constant and hence contains 2 atoms, the flux becomes $\Phi = 2M/(a_k^{\|})^2$, where M stands for growth rate in ML/s. Therefore, M can be written as in Eq. 4.14:

$$M = \frac{\Phi (a_k^{\|})^2}{2} \tag{4.14}$$

Combining Eq. 4.8 with Eq. 4.14, M can be related to G:

$$M = \frac{2G}{a_k^{\perp}} \tag{4.15}$$

For growth of ternary compounds, the total flux of cations is readily the sum of them:

$$\Phi_{ij} = \Phi_i + \Phi_j \tag{4.16}$$

Similarly, the total growth rate in ML/s is the sum of the growth rates of the two binary compounds provided that there is no relaxation, i.e. $a_k^{\|} = a_s$:

$$M_{ij} = M_i + M_j \tag{4.17}$$

Converting to G, we have:

$$\frac{G_{ij}^{\perp}}{a_{ij}^{\perp}} = \frac{G_i}{a_i^{\perp}} + \frac{G_j}{a_j^{\perp}} \tag{4.18}$$

For group V elements, two-zone thermal dissociation cells or cracker cells were used. The main purpose of the cracker is to provide a single effusion component which combines the two functions of group V evaporation and tetramer to dimer dissociation. Cracker cells were developed due to the advantageous usage of dimer (As_2) compared to tetramer (As_4). Dimers have an inherent advantage over tetramers arising from the need for one half of the flux to maintain the stoichiometric composition, which doubles the source lifetime. In the case of phosphorous, the safety concerns are also satisfied since P_2 that gets deposited on the cryopanel is non-pyrophoric as opposed to P_4.

Determination of group V overpressures cannot be done using the aforementioned equations since unlike group III elements, the sticking coefficient of group V elements is not unity due to their high vapor pressure. Therefore, any excess arsenic that does not bond to the group III atoms readily desorbs from the surface. Calibration of group V is done by growing a calibration layer and monitoring the surface reconstruction using RHEED, while the arsenic valve is reduced step-wise. The moment the growth switches from group V rich to group III rich condition, the RHEED reconstruction pattern changes. The As flux at this valve opening that is read by the ion gauge (Ψ_{ref}) corresponds to the minimum As flux, P_{min} needed to maintain a 1:1 V to III flux. To adjust for a particular overpressure during the growth, one should adjust the valve opening in order for the ion gauge to read the target BEP, which is related to the ratio of the target growth rate (G_{target}) to the growth rate of the calibration growth, G_{ref} as expressed in Eq. 4.19:

$$(\frac{V}{III})_{target} = \frac{\Psi_{target}}{\Psi_{ref}} \frac{G_{ref}}{G_{target}} \tag{4.19}$$

4.3 *In-situ* growth characterization techniques

4.3.1 Reflection high energy electron diffraction RHEED

RHEED is one of the most common and useful *in-situ* metrology tools used in MBE. It is used to characterize the surface reconstruction and surface morphology of the growing epilayer. When growth is proceeding in a layer-by-layer or step-flow mode, RHEED

pattern is streaky showing a smooth surface morphology. On the other hand, when there are islands growing on the surface, RHEED pattern becomes spotty indicative of surface roughness. The atomically flat surface of a crystal is a two-dimensional lattice and consequently, the reciprocal lattice consists of rods extending out of the two-dimensional plane of the crystal surface infinitely in the out-of-plane direction. For any practical case the electron beam is not perfectly monochromatic and the variation in the electron energy broadens the Ewald's sphere shell, and the intersections with the lattice rods can be elongated vertically resulting in streaky RHEED pattern. In the case of an island growth mode, however, the electron beam penetrates the islands and RHEED works in the so-called transmission mode, resulting in a spotty pattern that is the typical diffraction pattern of a three-dimensional crystal when electrons penetrate a bulk crystal. This is the same diffraction pattern as would be observed in Transmission Electron Microscopy (TEM) [200].

Also, RHEED is a powerful method to deduce the growth rate. RHEED specular beam intensity oscillation can be recorded to monitor the deposition rate as one oscillation period corresponds to one ML. Nonetheless, this growth rate fitting method was not implemented in this study since for such intensity oscillation measurements substrate should be stationary. However, for all the growths done in this study substrates were set to rotation to minimize the thickness gradient across the substrate. Additionally, with stationary wafer there is a steep gradient of growth rate across the substrate, so what is measured depend strongly on the location of the RHEED beam on the wafer. Therefore, the RHEED camera is no longer looking at the same spot and same wafer orientation over time, and the rotation artifact added to the oscillation makes it complicated to analyze and extract growth rate information.

4.3.2 Reflectance monitoring

The wafers were illuminated by a pair of Light Emitting Diode (LED)s at 470 and 950 nm and the reflected light beams were collected by the SVT camera as a function of time. Since the refractive indices of InGaAs and InAlAs are different, reflected 470 and 950 nm beams exhibited a sinusoidal-like pattern versus time due to interference. Reflectance at 470 nm reveals epitaxial quality. A steady reflectance at 470 nm shows that the surface is smooth, while a gradual decrease in the reflectance is a sign of surface becoming rough during the growth.

The reflectance fitting could be used to find the growth rate, however, the method has some limitations. The epilayer has to be sufficiently thick, preferably several thousand Å

or more, in order to acquire enough oscillation periods for growth rate fitting. Therefore, it is usually not applicable to structures with multiple heterogeneous and thin epilayers, e.g. SuperLattice (SL). In addition, the refractive index, n, and extinction coefficient, k, that are parameters needed for such calculations, are only very well known for binary compounds. The growth rate fittings of ternary compounds such as InGaAs and InAlAs that were the focus of this study are more complicated as their n and k vary with group III compositions.

4.3.3 *In-situ* temperature monitoring using BET

Since both rotating and radiatively heated substrates are preferred during epitaxial growth, physical contact between the substrate and the temperature sensor is not practical. Therefore, thermocouples are radiatively coupled to the substrate and consequently have a large temperature offset compared to the substrate. Furthermore, this offset depends on substrate and heater temperature, doping level and type, and on the changing absorptance and emittance of the epilayer during growth [201].

BET or band-edge absorption spectroscopy (BAS) which is a non-contact, real-time, absolute wafer and thin-film temperature monitoring tool was used to measure the temperature during thin-film deposition. BET provides semiconductor temperature monitoring in ranges that pyrometry does not work; for instance, substrates that are transparent in the infrared as well as growth at low temperatures could benefit from BET temperature measurements. At room temperature, many semiconductors are essentially transparent in the infra-red (IR) range of the spectrum (900-1700nm). However, semiconductors experience a reduction of their bandgap energy E_g as the temperature increases. This shift can be described by the empirical Varshni formula as expressed in Eq. 4.20:

$$E_g(T) = E_g(0) - \frac{\alpha T^2}{\beta + T} \tag{4.20}$$

where α and β are material dependant parameters. Semiconductors start absorbing incident light in part of this wavelength range and the absorption edge shifts with temperature. For high bandgap material (e.g., sapphire) the visible range is favored, while for lower-bandgap semiconductors like GaAs, the near-infrared spectral range from 800 to 1400 nm is appropriate for detection of the absorption edge. Light with higher energy than the bandgap energy is strongly absorbed when passing the semiconductor, while lower-energy photons are transmitted nearly without losses. This leads to an optical

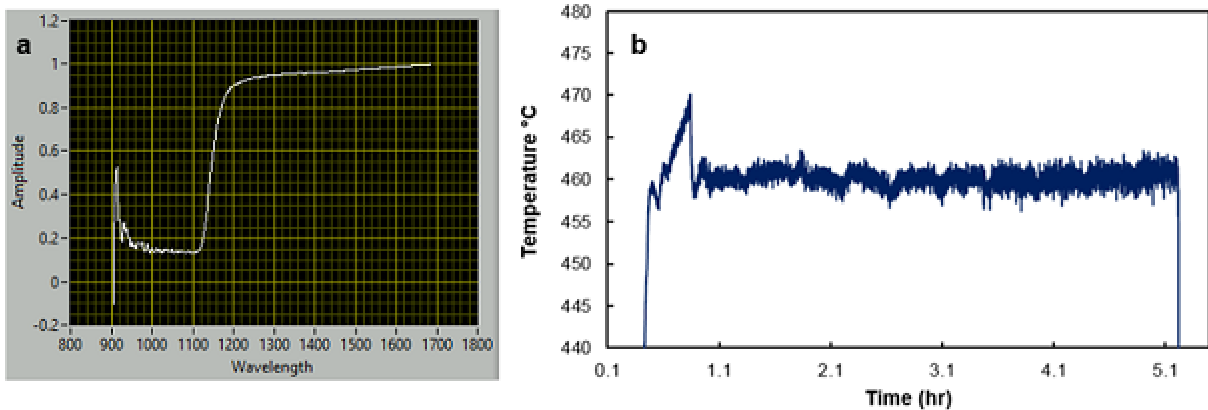

Figure 4.3: A typical BET a) band-edge spectrum showing the absorption edge and b) real-time temperature monitoring during the growth of sample G showing some oscillation.

spectrum as shown in Fig. 4.3.a. BET works by measuring the IR radiation from an incident source (substrate heater or an external halogen lamp if heater power is not sufficient, i.e, during low temperature growth) that is transmitted by the substrate. The substrate temperature can be calculated by measuring the position of the transmitted light absorption edge. For our setup, the light transmitted through the wafer is measured using an InGaAs spectrometer.

The sample holder is rotating during preparation and growth to ensure good homogeneity or at least radially symmetric growth conditions. During rotation, the wafer can tilt in the holder slightly, which influences the obtained spectrum. This results in a spurious oscillations and variation of the calculated substrate temperature (Fig. 4.3.b). The time period of the oscillations in the recorded temperature can clearly be correlated to the rotation period of the sample holder.

Compared with reflectance corrected pyrometry, BET has the advantages of working well with very small substrates and not being affected by coating of viewports or scattered radiation from the cells. However, BET measurements can cause local heating of the substrate and are not reliable for doped substrates. Therefore, these two methods complement each other and the two measurements are often cross-calibrated. Our MBE tool is equipped with NIR spectrometer that acquires the transmission spectrum which then is analyzed by in-house made software (LabView) and converted to temperature, providing real-time temperature measurements.

4.4 *Ex-situ* growth characterization techniques

4.4.1 Atomic Force Microscopy (AFM)

AFM technique allows to visualise with a sub-nanometer resolution the true three-dimensional morphology of the surface unlike electron microscope that provides a two-dimensional projection or a two-dimensional image of a sample . The AFM principle is based on the interaction between the sample surface to analyze and a tip of nanometer scale sharpness, fixed under a cantilever. The tip sweeps the surface and follows the sample topography. This movement is measured by focusing a laser beam on the back of the cantilever with a photodiode giving a three-dimensional image of the surface.

AFM can be performed in three modes: contact, non-contact or tapping mode. We used tapping mode in this study since it gives the highest resolution. AFM offers unique advantages for surface measurement in terms of simplicity and high resolution, but it also has its unique problems of image artifacts originating from the tip, the scanner or image processing. The tip sharpness and its side angle could alter the lateral dimension of the surface features. For a feature smaller than the tip apex, the imaged object size could be larger than the real size. The non-linear relationship between the scanner extension and the voltage applied causes distortion in lateral dimension of the image, which is more pronounced in larger scale scans. Therefore, it is necessary to optimize the image quality before analyzing them using commercial software [202]. Gwyddion software was used in this study to process the images, find the Root Mean Square (RMS) roughness and do line profile measurements. The most common method for image leveling is the so called line by line flattening to eliminate the surface bowing due to the scanner non-linearity or sample tilt. Flattening command in the software uses all unmasked portions of scan lines to calculate individual least-square fit polynomials for each line.

4.4.2 Nomarski Differential Interference Contrast (DIC) microscopy

Nomarski microscopy that is also known as Nomarski interference contrast (NIC) or DIC microscopy is one of the most convenient *ex-situ* tools for the characterization of epilayers. The surface morphology of the grown structures were analyzed using a Nikon Optiphot-66 Nomarski DIC microscope that is equipped with a SPOT digital camera. Surface defects or contamination existing on top of the samples, are better resolved under Nomarski compared with conventional optical microscopy. Using the

concept of polarization, the specimen's surface is imaged with a shadowed-like deceptive three dimensional appearance. The light generated by a lamp and passed through a polarizer is separated into two slightly displaced orthogonally polarized beams using a Wollaston prism. These two coherent beams travel into the sample surface. Changes in the sample such as thickness or refractive index, will result in an optical path difference between the two beams reflected from the surface causing destructive or constructive interference, dependent on the surface step height. These beams are recombined by another Wollaston prism. In order to bring the beams into the same plane, an adjustable offset phase is designed by adding a polarizer to modulate the position at zero optical path difference, and the contrast is recorded as the shear distance, which is marked in corresponding intensity or colour. The surface information is observed with a pseudo 3-dimensional appearance. However, the images does not necessarily represent real topographic features of the surface because the shadows that result from the phase difference may not correspond to low and high relief on the surface but from difference in either the optical path or refractive index [202].

For the grown wafers presented in this work, Nomarski images were acquired using a 5× and 40× magnification with an exposure time of $\sim 50-200$ ms. Each acquired image has 2592 × 1944 pixels. For 40× magnification, this gives lateral resolution better than $\sim 0.5\mu m$, but allows registering defects which are even smaller. The vertical resolution is much higher, approaching 1 nm with careful tuning.

4.4.3 Scanning transmission electron microscopy (Scanning Transmission Electron Microscopy (STEM))

TEM is used to obtain morphological, compositional, and crystalline information. Crystallographic information includes lattice structures and defects. Examples of defects are twins, stacking faults, dislocations, and grain boundaries. In addition, material chemical composition can be obtained using Electron Energy Loss Spectroscopy (EELS) in TEM.

Annular dark-field imaging is a method of mapping samples in an STEM in which images are formed by collecting scattered electrons with an annular dark-field detector. An annular dark field detector collects electrons from an annulus around the beam, sampling far more scattered electrons than can pass through an objective aperture. This gives an advantage in terms of signal collection efficiency and allows the main beam to pass to an EELS detector, allowing both types of measurement to be performed simultaneously.

High-Angle Annular Dark- Field (HAADF) is an STEM technique which produces an annular dark field image formed by very high angle (an angle of >5°), incoherently scattered electrons (Rutherford scattered from the nucleus of the atoms) — as opposed to Bragg scattered electrons. This technique is highly sensitive to variations in the atomic number of atoms in the sample (Z-contrast images). For elements with a higher Z, more electrons are scattered at higher angles due to greater electrostatic interactions between the nucleus and electron beam. Because of this, the HAADF detector senses a greater signal from atoms with a higher Z, causing them to appear brighter in the resulting image. This high dependence on Z (with contrast approximately proportional to Z^2) makes HAADF a useful way to easily identify small areas of an element with a high Z in a matrix of material with a lower Z .

4.4.4 STEM Moiré GPA (SMG)

Atomically resolved electron microscopy has enabled obtaining the atomic arrangement within a crystalline structure as well as the local strain field by measuring the relative positions of the atoms. The development of stable aberration correctors on the probe-forming lens has enabled the use of STEM to image atoms with picometer precision and has become a widely used high resolution imaging technique. Geometrical Phase Analysis (GPA) is another method mapping the strain field [203] from high resolution micrographs and is designed to work with lower sampling conditions by virtue of Fourier-based data processing. The technique allows the user to obtain strain maps with a slightly larger Field of View (FOV) compared to the real-space methods. Nevertheless, these techniques are relatively limited to FOVs of around 100 nm (dependent on the crystal structure and the number of pixels of the electron micrograph). Interferometry is a method allowing the visualization of physical phenomena at a desired length scale by superposing multiple waves. The principle of interferometry is generating an interference pattern between two selected diffracted beams of the same lattice periodicity from two different regions of the sample. This leads to the formation of a set of Moiré fringes (hologram) on a large length scale where the fringe spacing and orientation amplify the difference between the underlying local lattice periodicity in the two regions. It is then possible to experimentally modulate the hologram FOV and map the local lattice periodicity differences onto a large area (up to a few micrometers in size).

Today's stability of scanning coils and electronics, has enabled the exploitation of such concept in STEM imaging. STEM Moiré GPA (SMG), is a recent strain characterization method capable of mapping the two-dimensional strain field on single crystal materials over a large FOV [204, 205]. In this method, the two similar periodic elements

interfering coherently with each other to generate a hologram are the crystal lattice and the scanning grid of the beam raster. The scanning grid corresponds to the localized and periodic positions of the STEM probe when acquiring the electron micrograph. When considering only a Rutherford scattering type interaction that gives rise to the Z-contrast in HAADF images, a STEM Moiré hologram is generated when the probe is smaller than the interatomic spacing and the scanning grid periodicity is set to be close to an integer multiple of the crystal lattice spacing.

The STEM probe scans the specimen at discrete locations, sampling the crystal periodicity at a fixed interval defined as the pixel size. The STEM Moiré hologram embeds the variations of the crystalline lattice periodicity and can be translated into a deformation field using the GPA algorithm. A STEM Moiré hologram is generated when the probe is smaller than the interatomic spacing and the scanning grid periodicity is set to be close to an integer multiple of the crystal lattice spacing. In order to acquire the proper sampled signal at the precise location of the probe, the probe size has to be smaller than the sampling interval (pixel size). Since the experimental conditions are known, the crystal periodicity can be found by analyzing the frequency and the orientation of the Moiré fringes. Please refer to Appendix A for further details about GPA and SMG and recovering lattice strain information from the Moiré holograms.

The Scanning Moiré Fringe (SMF) is formed due to an artifact that originates in the middle range of magnification in HAADF STEM. In HAADF STEM imaging, SMFs appear when the pixel size of scanning grating (d_s) is close to the lattice plane spacing d_l or its multiple. Figure 4.4 shows a schematic of translational SMFs (Fig. 4.4.c) formed by the harmonic interference between the lattice spacing d_l (Fig. 4.4.a) and the scanning grating spacing d_s (Fig. 4.4.b). In Fig. 4.4.c, the SMFs appear curved due to variation in the lattice spacing. The SMF spacing d_{SMF} increases as the lattice spacing increases when $d_l < d_s$, while it decreases as the lattice spacing increases when $d_l > d_s$. By using a formulation for translational moiré fringes, d_l can be calculated as expressed in Eq. 4.21 [206].

$$d_l = \frac{d_{SMF} d_s}{d_{SMF} + d_s}, d_l < d_s \quad ; \quad d_l = \frac{d_{SMF} d_s}{d_{SMF} - d_s}, d_l > d_s \tag{4.21}$$

4.4.5 X-ray Photoelectron Spectroscopy (XPS)

XPS is a technique commonly used to explore surface chemistry. The data obtained from XPS provides the quantified composition of the outer few nanometers of a material.

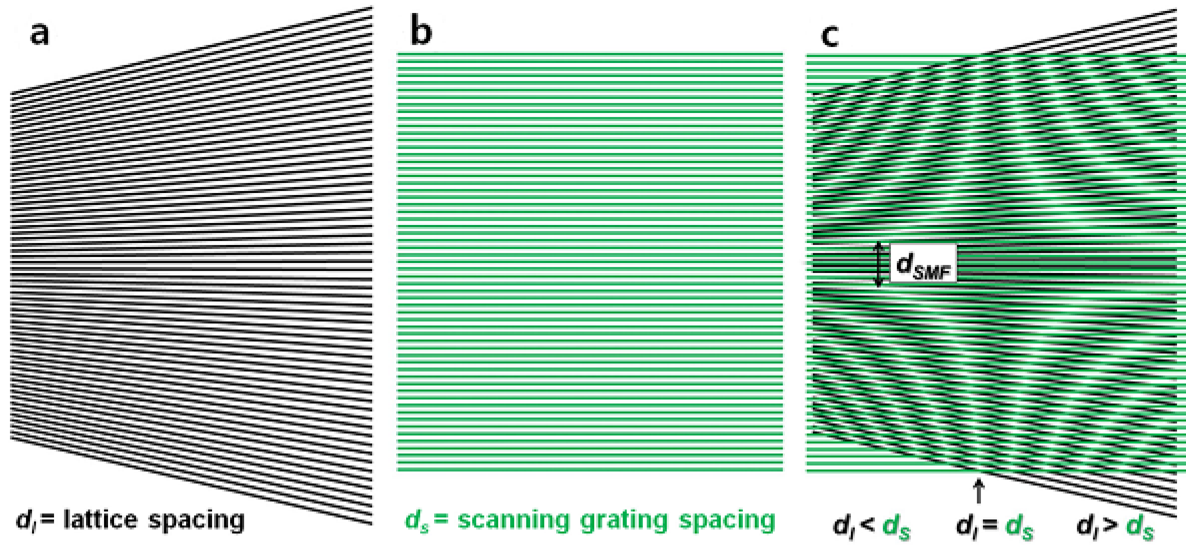

Figure 4.4: Schematic of translational SMFs formed by the harmonic interference between lattice spacing d_l and the scanning grating with a spacing of d_s. a) The lattice spacing d_l represents a strain field that linearly increases along the horizontal direction, b) scanning grating spacing as acquired via STEM imaging, and c) SMFs formed by overlapping of the lattice spacing d_l and scanning grating spacing d_s [206] ©AIP Publishing. Used with permission.

In other words, it details both the elements present and the chemical states of those elements. Typical analysis area and depth are in the range of μm^2 and 10 nm, respectively. XPS is based on the photoelectric effect in which electron population spectra are obtained by irradiating a material with a beam of X-rays. Material properties are inferred from the measurement of the kinetic energy and the number of the ejected electrons. XPS requires high vacuum (10^{-6} Torr) or ultra-high vacuum (10^{-7} Torr) condition. The binding energy, E_B^F, of the photoelectrons is found according to the modified Einstein relation as in Eq. 4.22.

$$E_B^F = h\nu - E_{kin}^{SP} - \Phi_{SP} \tag{4.22}$$

where E_{kin}^{SP} and Φ_{SP} are the kinetic energy of the photoelectrons measured at the detector and the detector work function. An important implication of Eq. 4.22 is that any change in the sample work function does not affect the position of core-level XPS peaks with respect to the Fermi level, E_B^F. They will be, however, shifted with respect to

the vacuum level. It is thus important for these limitations of the XPS technique to be understood if there are any modifications of the surface dipoles, which are masked by the nature of the method.

XPS analysis can be extended into a material through a process known as depth profiling, which slowly removes material using an ion beam, collecting data after each etching cycle. Depth profiling enables a composition profile with high depth resolution to be measured. Depth profiles can be used to see how the composition changes from surface to bulk; for example, due to oxidation of the surface or annealing, or to understand the chemistry at interfaces where different materials are joined together.

4.4.6 Low energy electron diffraction (LEED)

LEED complemented with dynamical intensity calculation and first principle Density Functional Theory (DFT) calculation has been used to study surface structures, surface relaxation, and surface reconstruction. LEED, RHEED and TEM are categorized based on the primary incident electron energy, E,: LEED with 10 $eV < E < 300eV$, RHEED with 1 $keV < E < 30keV$, and TEM with 120 $keV < E < 300keV$. LEED requires the most stringent vacuum conditions of around 10^{-10} Torr. Any intrinsic contamination of the sample or extrinsic gas adsorption on the surface under a poor vacuum condition can degrade the quality of the LEED pattern. Higher energy electrons can penetrate deeper into solids, and surface contamination has less effect on pattern observation as compared to that of LEED. LEED patterns are usually collected under the normal or near normal incident angle while RHEED patterns are collected at a glancing incident angle. For TEM, the incident electron beam relative to the sample can be adjusted from normal incidence to a tilt angle up to 45° by a sample tilt mechanism with two tilt axes (x and y) in the plane of the sample [200].

When performing an experiment using electrons as an excitation source, one needs to know the electron Inelastic Mean Free Path (IMFP) in solids. IMFP is the distance that the lectron travels into the solid before its energy drops to less than 1/e of its initial value according to $I_d = I_0 e^{(-d/\lambda)}$, where I_0 and I_d are the intensity before and after travelling a distance of d into the solid, and λ is the IMFP. Fig. 4.5 shows a summary plot of the calculated IMFPs for 41 elemental solids as a function of energy from 50 eV to 30 keV. The minimum values of a few angstrom ($\approx 0.5nm$) IMFPs occur between 10 and 100 eV. LEED uses this minimum IMFP, which is the most surface sensitive.

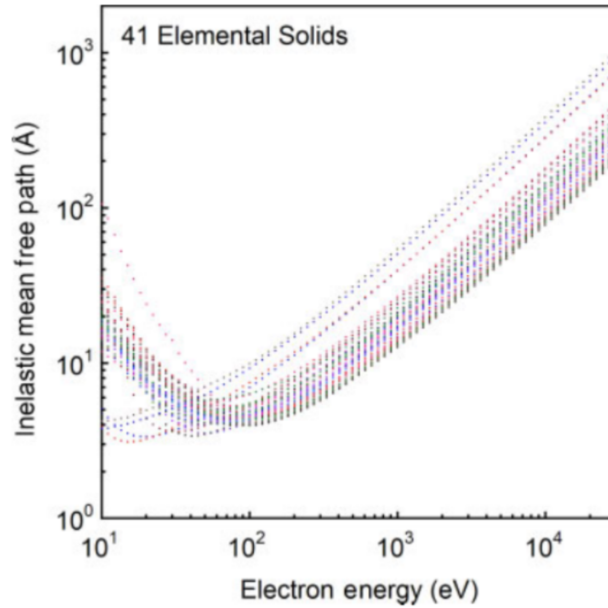

Figure 4.5: Calculated inelastic electron mean free path from experimental optical data as a function of primary electron energy from 41 elemental solids [207] ©John Wiley and Sons. Used with permission.

4.4.7 High Resolution X-Ray Diffraction HRXRD

HRXRD technique is used to determine a number of parameters such as thickness and composition. In a HRXRD scan, the position of a peak follows Bragg equation as in Eq. 4.23:

$$n\lambda = 2\frac{a_k^{\perp}}{\sqrt{h^2 + k^2 + l^2}} sin\theta \tag{4.23}$$

where λ is the x-ray wavelength, (hkl) are the Miller indices of a particular plane and n is the diffraction order. In this study, a Jordan Valley QC3 Bruker HRXRD diffractometer was used that employs a Cu $K\alpha_1$ x-ray with a wavelength of 1.54 Å. Triple-axis couple $\omega - 2\theta$ scans were done on the samples at diffraction plane of (222). The composition of the layer is found based on Eq. 4.9 and Eq. 4.12 and Eq. 4.23. The HRXRD data were fitted using the Jordan Valley-HRXRD analysis software (Rocking-Curve Analysis by Dynamical Simulation (RADS)) which is the leading simulation, analysis and fit software for HRXRD of epitaxial thin-film structures on single crystal substrates. The actual thickness of the

individual epi-layers for a strained structure is found by fitting Pendellösung fringes with a RADS model. The measured HRXRD of a SL exhibits satellite peaks (order $n = \pm 1, \pm 2, \ldots$) centered around the average composition peak (order $n = 0$). The angular separation between the satellite peaks is given by Eq. 4.24 [208]:

$$\Lambda = \frac{\pm n\lambda}{2(sin\theta_n - sin\theta_0)} \tag{4.24}$$

where Λ is the period of the SL (equals the sum of the epi-layers), θ_n is the diffraction angle for order n and θ_0 is the diffraction angle for the zero-order peak ($n = 0$).

Crystal defects lead to local variations in the lattice parameters and cause broadening of the peaks in $\omega - 2\theta$ geometry.

4.5 Collaborative works

It should be mentioned that the SMG was done in collaboration with Dr. Alexander Pofelski from Prof. Jianluigi Botton research group at the Canadian Centre for Electron Microscopy at McMaster University. Alex developed the SMG technique, and has over 10 years of experience in the field.

In addition, the surface reconstruction analysis by LEED and XPS as well as DFT calculations were done in collaboration with Dr. Hanieh Farkhondeh from Prof. Kam Tong Leung research group at WatLab at the University of Waterloo. Hanieh is an expert in the area of surface chemistry.

The great motivation and knowledge of Alex and Hanieh in the aforementioned fields, facilitated understanding the behavior of growth on InP(111) substrates, which led to unraveling the mysteries of growth on (111) substrates. The outcome of this collaborative work was the growth of morphologically smooth and microstructurally defect free InGaAs/InAlAs SL that sets the stage advancing the field of Terahertz (THz)-Time Domain Spectroscopy (TDS).

Chapter 5

Optimum off-cut angle for growth

5.1 Experiment

InP(111)A and InP(111)B semi-insulating substrates were used in this study. The substrates had bowed edges which resulted from the standard process of polishing and epi-ready surface preparation. $In_{0.53}Ga_{0.47}As$ and $In_{0.52}Al_{0.48}As$ can be grown lattice-matched to InP (Fig. 5.1). Structures were grown using a Veeco GEN10 Molecular Beam Epitaxy (MBE) system. The growths were done with As_4 using Veeco Mark V As cracker cell with a cracking zone temperature of 650°C. The growth chamber pressure was around 10^{-8} Torr during the growths, which was maintained using a cryogenic and an ion pump. Substrates were heated radiatively using a Mo block heater. Substrates were rotated using a manipulator for better compositional uniformity. All the growths were done with 20 rpm substrate rotation.

Substrates were outgassed in the load lock at 200° C for 4 hours, maintained at 10^{-8} and then outgassed inside preparation chamber at 300° C for 2 hours maintained, at an Ultra-High Vacuum (UHV) of 10^{-9} before being transferred to the growth chamber. Inside the growth chamber, substrates were oxide desorbed just prior to the onset of the growths. Oxide desorption was done at 458°C for about 7 min with arsenic (As) overpressure to substitute for any phosphorous (P) loss during annealing period. This is because P desorbs at temperatures lower than the oxide desorption temperatures. Using lower temperatures will only yield to partial desorption of oxide layer since only indium (In) oxide desorbs. It should be mentioned that oxide desorption was done in the pressure of As and not P since our system is not equipped with a P cell.

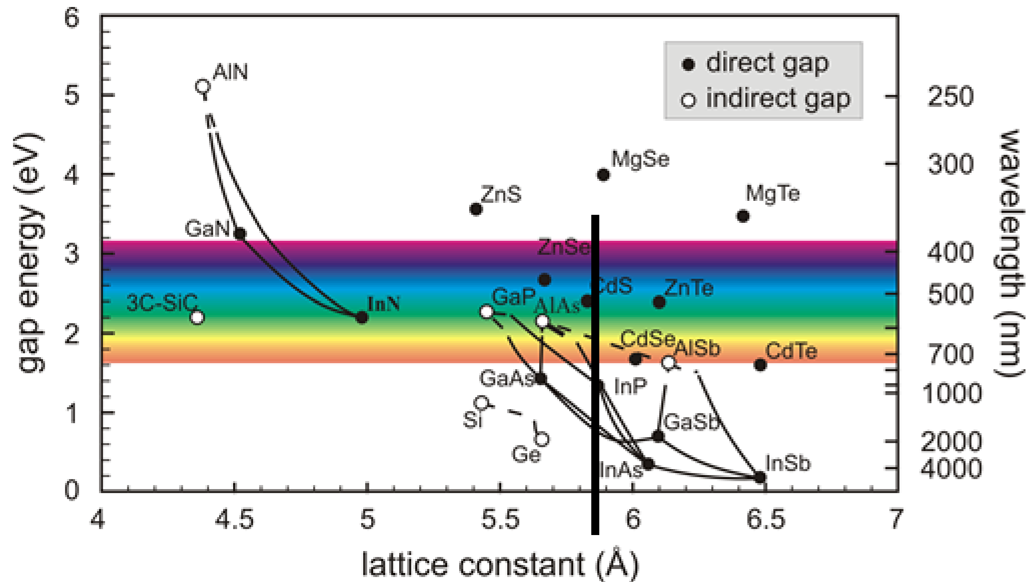

Figure 5.1: Lattice constants and bandgaps of common III-V semiconductors.

Beam Flux Monitoring (BFM) ion gauge was used to measure the group III atomic fluxes, while the group V pressure was monitored using an ion gauge located outside of the cryopanel in the main pumping port. The V/III flux ratio was calibrated in a separate experiment. The 1:1 ratio was found at the transition point from As stable to Ga stable reconstruction during GaAs homoepitaxy at 580°C. The substrate temperature during the growth was monitored using Band Edge Thermometry (BET). Staib 15 keV electron gun and kSA400 Reflection High Energy Electron Diffraction (RHEED) monitoring system triggered at selected azimuths were used to monitor surface reconstruction during deposition. The wafer was illuminated by a pair of Light Emitting Diode (LED)s at 470 and 950 nm, and the reflected light beams were collected by the SVT camera as a function of time.

Quarter 2-inch InP(111)B and InP(111)A substrates were used in this study. Two methods of substrate mounting were employed. Both of them ensured proper epitaxial growth not only on the center portion of the wafer but also on the wafer edge. The first method involved mounting the InP substrates on mechanical grade semi-insulating GaAs wafers using In-Ga eutectic. In the second method, each wafer was suspended on six small tabs of a Mo spring-plate and secured from the back with a sapphire plate (Fig. 5.2). The latter was spaced out from the wafer with three small pieces of thin Tantalum (Ta) wire. Generally, the substrate heater temperature is higher than what BET measures since the

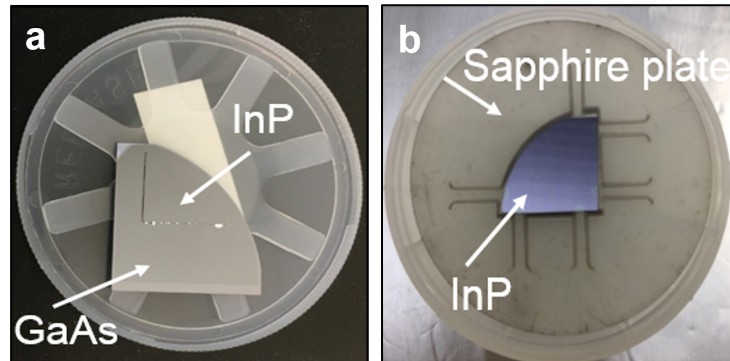

Figure 5.2: a) InP mounted on GaAs using In-Ga eutectic and b) free floating InP on sapphire plate ©American Vacuum Society. Used with permission.

Sample	Structure	Substrate	Growth rate (Å/s)
A1	200nm InGaAs/ 200nm InAlAs	rounded edge InP(111)A	0.5
A2	200nm InGaAs/ 200nm InAlAs	rounded edge InP(111)B	1
A3	200nm InGaAs	rounded edge InP(111)B	1

Table 5.1: Summary of the growths.

heater is not touching the substrate. The temperature difference between the heater thermocouple and BET depends on the mounting technique. It was higher by 50° C when InP wafers were mounted using In-Ga eutectic, but it was about 100°-150° C higher when smaller size InP wafers were mounted against a sapphire plate.

Individual 200 nm thick InGaAs and InAlAs epilayers as well as InGaAs/InAlAs heterostructures were grown to investigate the effect of growth conditions on the surface morphology at the center and on the edge of the wafer edge. Multiple growths were done at different As overpressures and growth rates. Different growth temperatures of 300°C, 460°C and 490°C were employed. The surface morphologies of the grown structures were analyzed using Nikon Nomarski Differential Interference Contrast (DIC) microscope and Bruker Icon Atomic Force Microscopy (AFM) in tapping mode.

The first principle total energy Density Functional Theory (DFT) calculations were carried out for InP(111)B surface to compare the migration length of different atomic

species. Calculations were done using the Vienna Ab-initio Simulation Package (VASP, version 5.4) with the Materials Exploration and Design Analysis platform (MedeA, version 2.19, Materials Design, Inc.). The projector augmented wave (PAW) method [209, 210] was used to describe the electron-ion interactions. The generalized gradient approximation (GGA) with the exchange-correlation functional of Perdew-Burke-Ernzerhof (PBE) was incorporated [211]. The Brillouin zone was sampled at the Γ point with a k-point spacing of 0.5 $Å^{-1}$. A cutoff energy of 400 eV was used for the convergence of the plane wave expansion. The conjugate-gradient algorithm was used to optimize the electronic structure and ionic geometry. All In and P atom positions were relaxed until the forces on all atoms were less than 0.01 eV/ Å and the convergence of the self-consistent field was set to 10^{-5} eV with the Methfessel-Paxton smearing of 0.2 eV. The unreconstructed P-terminated InP(111)B-(1 × 1) surface was modeled by a slab geometry consisting of four InP double layers, and the bottom-most layer was terminated by H atoms with a vacuum gap of 10 Å perpendicular to the slab surface. A periodic supercell composed of 2 × 2 surface unit cells were used to calculate adatom adsorption energies.

5.2 Results and Discussion

The main challenge for growth on on-axis (singular) (111)B oriented substrates by conventional MBE is surface roughness and/or formation of unwanted three-faceted pyramidal hillocks (surface steps). The use of misoriented substrates has been the main strategy to avoid the hillocks and improve the surface morphology. Hillock-free surface morphology was also demonstrated on on-axis (111)B GaAs substrates using Migration Enhanced Epitaxy (MEE) [22, 82]. However, there has not been a systematic study to find the optimum off-cut angle for growth on InP(111) substrates. Most of the works done were on GaAs(111) substrate. This could be due to the fact that it is harder to desorb the oxide layer from InP substrates. At higher oxide desoprion temperatures that is needed for removal of both P and In oxides, P desorbs from the surface leading to In droplet formations. At lower oxide desorption temperatures, only In oxide desorbs. Oxide desorption in the presence of As overpressure instead of P leads to the formation of an unavoidable highly strained thin InAs layer between the substrate and the film due to the substitution of As for any desorbed P atom.

A separate study was done to investigate the effect of the oxide desorption procedure on the surface morphology. Although an Inficon Transpector® MPH RGA facing towards the substrate did now show signs of P desorption from the surface during the oxide desorption, *ex-situ* measurements using Nomarski DIC microscopy after the growth

showed evidence of P desorption and In droplet formation when the growth was done in the absence of As overpressure.

In this study we did a systematic study to find the optimum off-cut angle for growth on InP(111) substrates. For this purpose we used substrates that were flat in the centre (on-axis (111)) but rounded at the edge (vicinal (111)) to encompass a range of off-cut angles and azimuths. Oxide desorption was done in the presence of As overpressure. Clear signature of the oxide desorption was seen from a decrease in the diffused RHEED background,which is the characteristic of the amorphous native oxide layer as well as appearance of sharper streaks. The monoatomic steps were observed *ex-situ* on the surface after oxide desorption performed with and without the As overpressure. Figure 5.3 depicts AFM images of the bare substrate showing the decrease in the terrace size by moving from the center of the substrate towards its edge as was expected. The substrate surface steps were observed before the oxide desorption as well, which shows that the substrates had excellent epi-ready quality.

The effect of growth temperature was also studied. It was shown that the growth at 460°C provided the smoothest surface morphology both at the center and at the edge. To study *in-situ* the effect of the As overpressure, the RHEED pattern and the intensity of selected features were monitored at the wafer central area during the growth. The optimum As overpressure was found to be approximately $3 \times P_{min}$. Here P_{min} stands for the minimum As overpressure ensuring As stable surface reconstruction during GaAs growth on GaAs(001) substrate at 580°C and using an equivalent group III flux. At overpressures below the optimum, elongated defects were observed on the bowed wafer edge. On the other hand, increasing the As overpressure beyond its optimum value resulted in the surface degradation on the entire wafer surface. Several deposition rates were tested and the best results were obtained at the slowest growth rate used, which was 1 Å/s for growth on InP(111)B. At this growth rate, growth temperature of 460°C and As overpressure of $3 \times P_{min}$, a smooth region at the edge of the wafer was obtained for InP(111)B substrate, however, a smooth region at the edge of InP(111)A was non-existent at the growth conditions studied as shown in Fig. 5.4. For growth on InP(111)B, the presence of such a smooth region was dependent on the growth conditions; it was almost non-existent at the growth rate of 2.5 Å/s, or at the growth temperatures of 300°C or 490°C.

Continuous evolution of hillock density and shape, and their elimination with increasing the off-cut angle by moving towards the edge of the wafer was observed at the transition to smooth region (Fig. 5.5.a). Although a smooth morphology was seen at the edge, the surface morphology was poor in the center, which is on-axis (111)B. Fig. 5.6.a shows a map of smooth, transition and rough growth regions versus position on

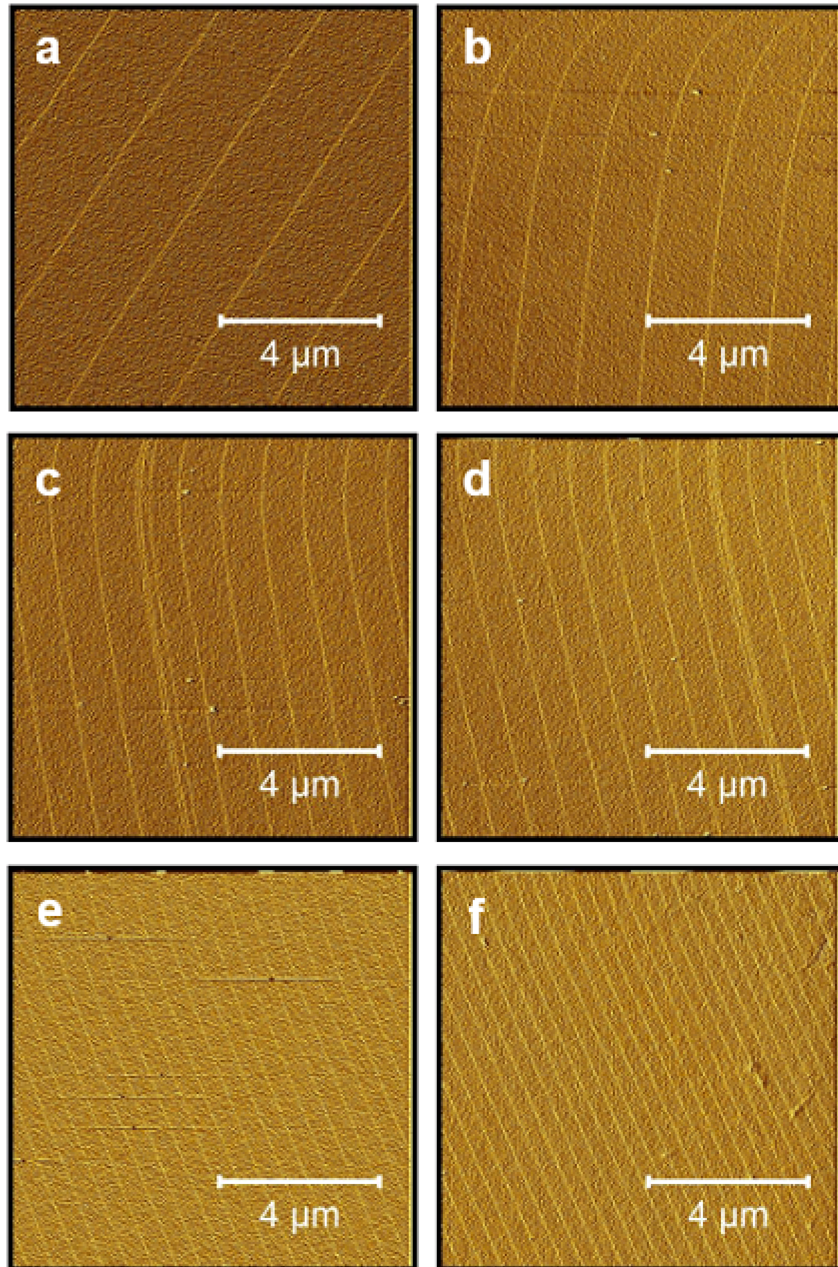

Figure 5.3: AFM height images of the bare InP(111)B singular substrate with rounded edge at a) centre and b-f) increasing distance from the flat centre towards the edge.

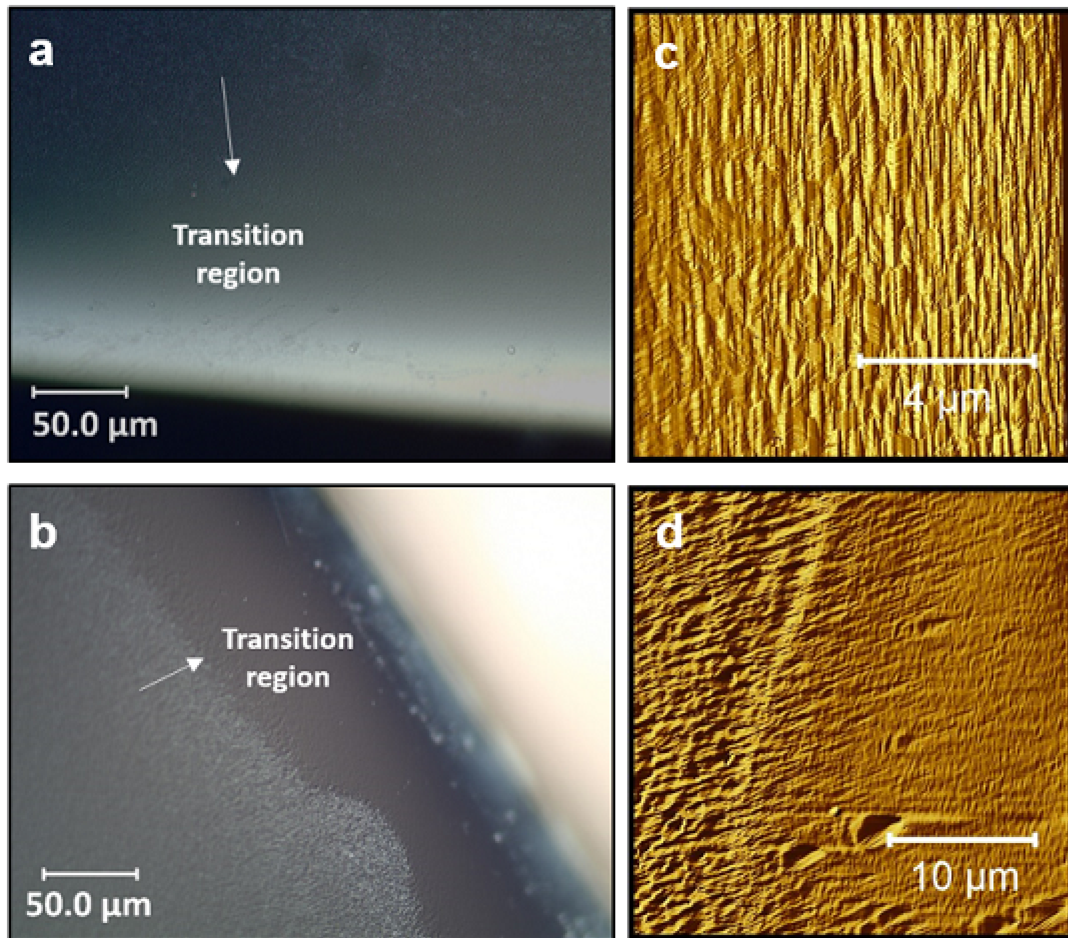

Figure 5.4: Nomarski images taken at the edge of a) sample A1 showing no apparent smooth region and b) sample A2 showing a smooth edge where there is mis-cut. Corresponding AFM height images of c) sample A1 at the edge showing an RMS roughness of 22.01±3.58 nm and d) sample A2 at the transition from smooth to rough region ©American Vacuum Society. Used with permission.

the wafer.

The optimum off-cut angle was found from the facet angle of the pyramids at the boundary of the smooth and pyramid-like regions. We conclude that (111)B substrate with off-cut angle of 0.4° or larger should be used for conventional MBE growth in order to avoid growth associated problems related to on-axis (111)B substrates. The obtained

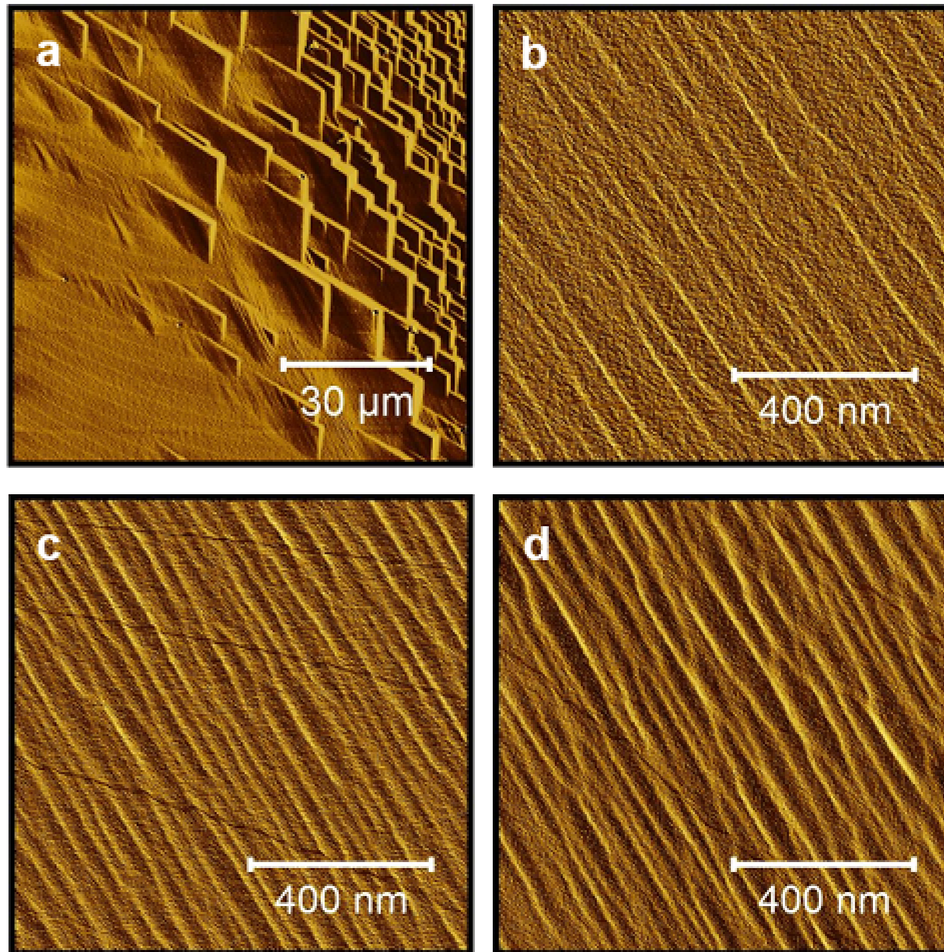

Figure 5.5: AFM height images of sample A3 showing a) evolution of the hillocks at the edge, b) monolayer step-flow growth mode adjacent to the pyramidal hillocks at an off-cut angle of 0.4° (RMS roughness = 0.52± 0.04 Å), step bunching at an off-cut angle of c) 1.7° with an average step height of 3.5 monolayers (RMS roughness = 0.74± 0.06 Å) and d) 3° with an average step height of 5.5 monolayers (RMS roughness = 4.3± 0.4 Å).

results do not allow to positively establish the upper value for such optimal off-cut angle, however, as discussed later, too large of an off-cut angle leads to step bunching. At smaller misorientation angles, complete pyramidal hillocks were seen. A step-flow growth mode was observed adjacent to the pyramids. The hillock formation is expected to be suppressed when the adatom migration length is larger than half the terrace width.

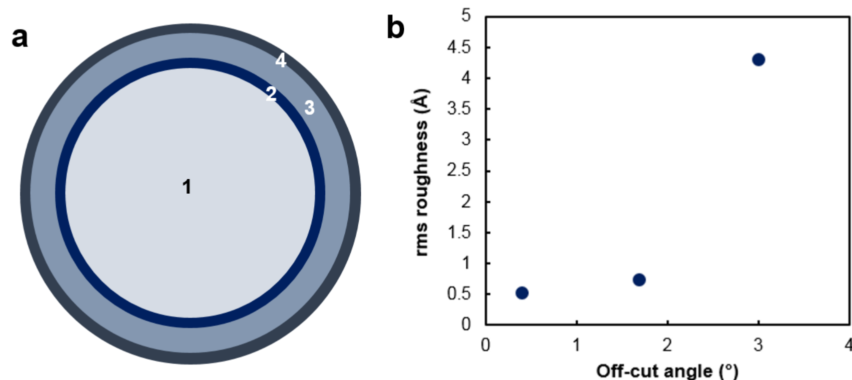

Figure 5.6: A contour map illustrating (not in scale) the rough center region (1), transition region where the hillocks are forming (2), smooth region (3) and rough region at the very edge of sample A3 (4). The rough edge region, the smooth region and the transition region are about 75, 150 and 50 μ m wide, and b) the change of RMS roughness versus off-cut angle ©American Vacuum Society. Used with permission.

Smaller off-cut angles than the optimum measured produce terraces that are wider than the migration length of the adatoms, therefore, two-dimensional nuclei form on the terrace before adatoms can migrate long enough to attach to the upper or lower step edge.

It was seen that the step ledges are not perfectly straight. Wavy steps on vicinal surfaces were also observed by Kasu and Kobayashi [85] on Metal Organic Chemical Vapor Deposition (MOCVD) grown GaAs. The authors postulated that the waviness is correlated with the attachment of the atomic species to not only the kink sites but also other sites of the monoatomic steps. From our observations, the surface was very smooth with one Mono-Layer (ML) step leading to an effective RMS roughness of 0.52± 0.04 Å (Fig. 5.5.b). To the best of our knowledge this is the best morphology for the growth of InGaAs on InP(111)B substrate reported so far. In our experiments, the smooth region at the bowed edge was also observed for the growth of 200 nm InGaAs followed by a 200 nm InAlAs epilayer. We did not observe such a smooth region at the substrate edge for the growth of InAlAs epilayer at the growth conditions studied.

Although growth on misoriented substrates may avoid the formation of hillocks, it is susceptible to step bunching which can lead to the formation of surface pits and morphology degradation. Step bunching, which is the result of the coalesce of the terrace steps at the growth front to relieve strain [121], leads to a reduction in the surface energy by the formation of low energy facets. It was predicted by a thermodynamic model that

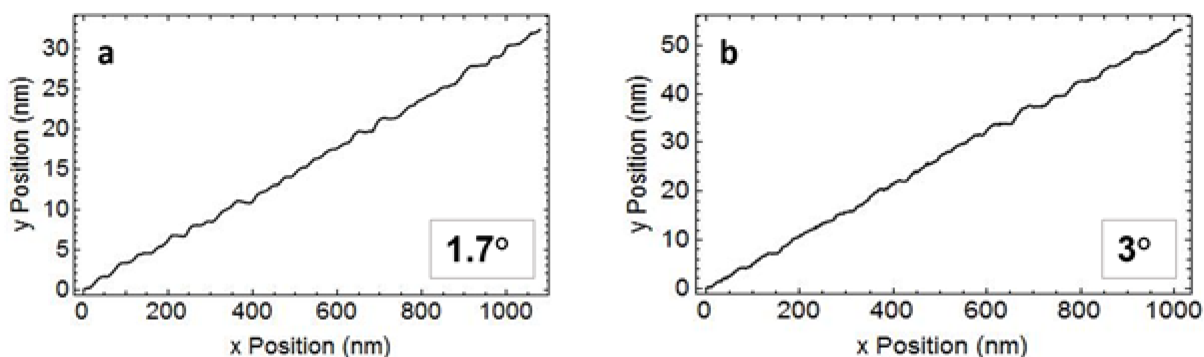

Figure 5.7: Step leveling to find the off-cut angle for a) Fig. 5.5.c and b) Fig. 5.5.d ©American Vacuum Society. Used with permission.

the steps move freely with the constraint that the formation of kinks cost energy [124]. Step bunching often occurs at higher off-cut angles since the steps are under-saturated. Bunching of the steps together increases the adatom density at the steps closer to its equilibrium value. Step bunching is more pronounced at higher growth temperatures when the diffusion lengths of the adsorbed species are large. Another condition which leads to pronounced step bunching is when the As desorption rate is high. Therefore, higher As overpressures were proposed to help alleviate step bunching [23].

In our experiments, the growths were prone to step bunching closer to the wafer edge away from where the pyramids evolved into smooth surface, i.e. for larger surface misorientations (Fig. 5.5.c-d). These steps are several nanometers tall. At misorientation angle of 1.7° from (111)B, the steps are 3.5 ML tall on average with the tallest being 7 ML high. At misorientation angle of 3°, they are on average 5.5 ML tall with the tallest step being 11 ML high.

It should be mentioned that the off-cut angles were obtained by numerical leveling of the widest terraces simultaneously at the high and low elevation ends of the scan using a linear transformation of the numerical data, one for each AFM scan (Fig. 5.7). However, for the 1 ML tall steps (Fig. 5.5.b), the signal to noise ratio was not sufficient to use such leveling. Hence, we derived the 0.4° off-cut angle from the known atomic step height (3.4 Å) and an average terrace width. Occurrence of pronounced step bunching taking place on 2° off-cut InP(111)B substrates under a wide range of growth conditions was also reported by Yerino et al. [212].

We further investigated the surface morphology at different azimuths of the effective off-cut angle. Our investigation showed that the optimum off-cut angle is not azimuth

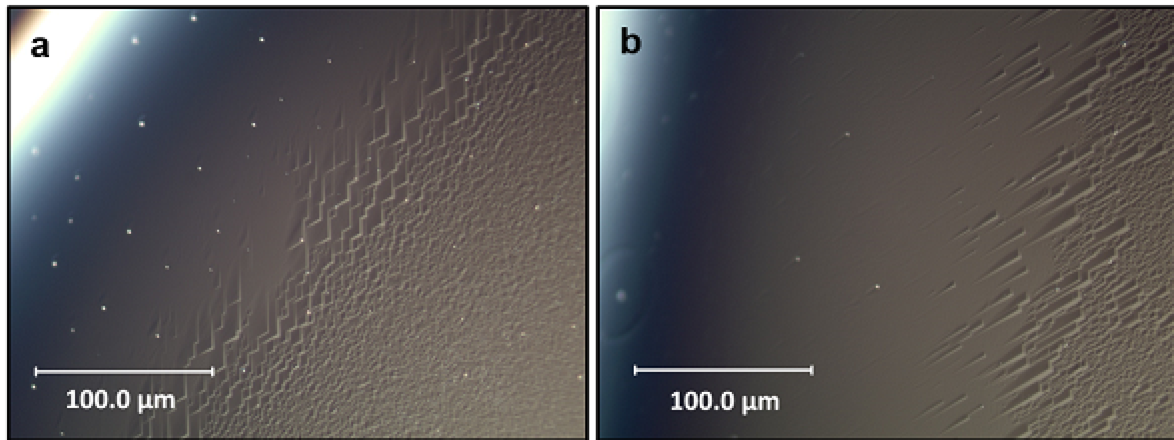

Figure 5.8: The Nomarski DIC images at the edge of sample A3 at different azimuths; a) $[1\bar{2}1]$ and b) $[0\bar{1}1]$ showing different hillocks' geometry. The width of the smooth region is 181 μm

dependent. This finding implies that it is the presence of the monolayer surface steps, not their exact orientation, which play the key role in the growth kinetic. Indeed, specular surface is achieved in a very broad range of azimuths examined. Fig. 5.8 shows the result of our examination of the smooth region and the shape of the pyramidal hillocks around the wafer edge using Nomarski DIC microscopy. The cleaved wafer we examined contained the two mostly studied $[1\bar{1}0]$ and $[1\bar{2}1]$ azimuths as well as other azimuths. We observed that different azimuths only led to a change in the hillocks' geometry at the transition region from slabs to symmetrical pyramids, while the width of the smooth region remained approximately the same. This pyramid shape evolution with varying azimuth on the wafer can be readily explained by the evolution in the relative orientation of the exposed vicinal surface and the fixed orientation of the hillock's facets.

It should be mentioned that the hillocks may form due to the growth twinning when growth is done on (111) substrates since {111} are the primary twin planes. In the case of GaAs, twinning was attributed to the Ga atoms forming single bonds on the surface, which gives freedom to the other bonds to rotate 60°. However, if the Ga atoms are attached to the surface steps with more bonds, twinning is suppressed. Hence, misoriented substrates with higher density of steps compared to the singular substrates are effective in avoiding hillock formation [5]. Based on this observation and the reported here lack of clear azimuthal dependence of the transition region, we conclude that the density of hillocks is primarily determined by the step density, i.e. off-cut angle, not by the exact

off-cut azimuth. Notwithstanding the lack of dependence of the width of the smooth region on the off-cut azimuth, it should be pointed out that the shape of the terraces could be affected by different off-cut azimuths. For instance, Schowalter et al. [6] showed that zigzag terraces are formed when the misorientation direction is towards $[\bar{2}11]$ or $[2\bar{1}\bar{1}]$, while straight-edge terraces dominate when misorientation is towards $[2\bar{1}\bar{1}]$ for growth on GaAs(111)B substrates.

To investigate the effect of different adatom species on the optimum misorientation angle needed for a smooth growth DFT calculation was carried out. The aim of this calculation was solely to compare the adsorption energies of the Al, Ga, In, and As adatoms. For that purpose, the single adatoms were placed on a few select adsorption sites including atop, bridge, Face Centred Cubic (FCC), and Hexagonal Close Packed (HCP) sites where their lateral positions and the positions of the slab atoms were fixed allowing the adsorbate height to relax. The resulting adsorption energies for Al, Ga, In, and As adatoms are shown in Fig. 5.9. Our calculations revealed a closely related diffusion pattern for all four adatoms with minor differences on the equilibrium InP(111)B surface. While the FCC site is the most favorable adsorption site for all four adatoms, adsorption on atop sites is the least favorable except for the As adatoms. To hop from one FCC site to another, the Al adatom must diffuse over the bridge and then HCP sites. This process entails the partial bond breaking between the Al adatom and three As atoms of the FCC site and the formation of new bonds between Al and As atoms at the bridge site. Since the potential energy difference between the FCC and bridge sites are larger for Al adatoms than that for Ga adatoms, the Al adatom diffusion process is kinetically less favorable to occur. This implies that the migration length for Al is smaller than that for Ga, therefore, smaller surface terrace sizes are required for the epitaxial growth of Al containing layer to occur. Also, this could affect the formation of ordered phase or phase separation during the InAlAs film growth because in the migration competition among the three adatoms, Al would be the kinetically limiting factor. This result was also confirmed by Scanning Transmission Electron Microscopy (STEM). It was seen that for the growth of InAlAs on rounded edge InP(111)B substrate (not shown here) a larger misorientation angle is needed at the optimized growth condition to avoid hillocks.

5.3 Summary

- The use of rounded edge substrates consolidated most of the so far inconclusive reports where studies were conducted on substrates with one particular off-cut angle and azimuth, with large scatter of these values from report to report.

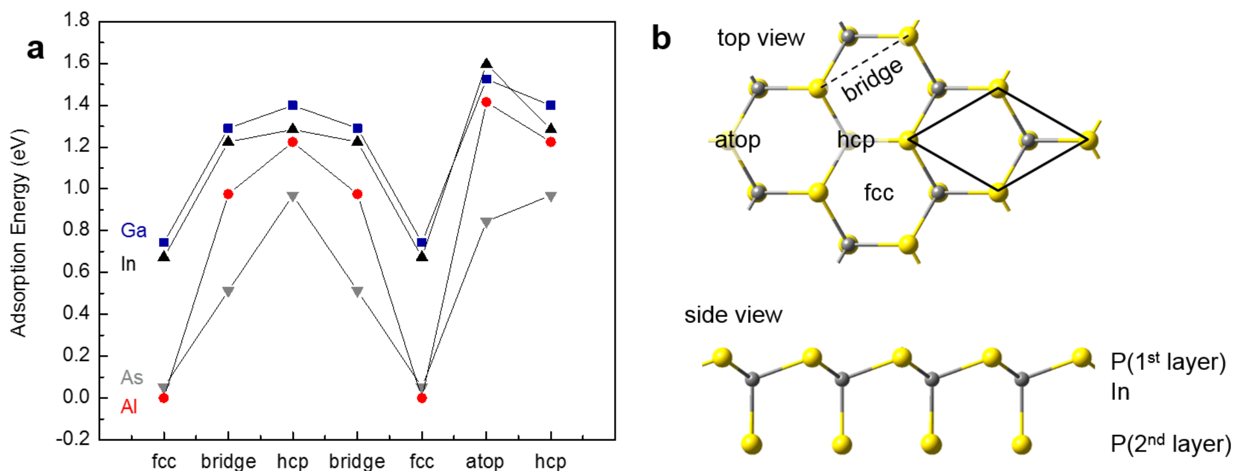

Figure 5.9: a) Calculated adsorption energies (in eV) for Al (red circles), Ga (blue squares), In (black triangles), and As (grey inverted triangles) adatoms on the P-terminated InP(111)B-1×1 surface as a function of adsorption site. b) Schematic atomic structure (top and side views) for the InP(111)B-1×1 surface. The surface unit cell and the potential adsorption sites are shown.

- Growth of InGaAs epilayer and InAlAs/InGaAs layers on rounded edge InP(111)B resulted in a atomically smooth region at the edge of the substrate where there is a range of misorientation angles. A well-defined transition from a morphology dominated by pyramids to an atomically smooth surface was observed at the edge. Such a transition was observed at a small off-cut angle of approximately 0.4° for the growth of InGaAs epilayers, where the surface was dominated by terraces and 1 ML height steps.
- Step bunching was observed at larger misorientation angles. Increasing the off-cut angle was found to lead to progressively increasing effect of step bunching and related morphology deterioration. At off-cut of ∼ 1.7°, step bunching formed surface steps as high as 7ML, while up to 11ML high steps were detected at 3.0° off-cut.
- Importantly, the off-cut angle where the transition to specular morphology was observed did not show detectable dependence on the off-cut azimuth in the entire range of azimuths investigated.
- The optimum off-cut angle found for the growth is subject to change for the growth

of other compound such as InAlAs or more complex structures; something which needs further investigation. We did not achieve a smooth region at the edge of the substrate when we grew InAlAs on InP(111)B.

- DFT calculations showed the presence of a larger energy barrier for the migration of Al atoms compared to Ga on the InP(111)B surface. This is due to the fact that Al forms stronger bond, which leads to a larger potential energy difference between the different adsorption sites. Hence, Al has slower mobility and smaller migration length on the surface and kinetically limits the growth. This implies that a larger misorientation angle is required for the growth of InAlAs on InP(111) compared to InGaAs.

- Growth on InP(111)A did not lead to any smooth region at the edge of the wafer at a variety of growth conditions studied, therefore, we decided not to pursue with conventional MBE on (111)A surface.

Chapter 6

The origin of the surface steps

6.1 Experiment

The microstructure of InAlAs(200 nm)/InGaAs (200 nm) layers grown on rounded edge InP(111)B substrate (sample A) was analyzed using Scanning Transmission Electron Microscopy (STEM) to find the underpinning of the surface steps. For the STEM analysis, the samples were cut in cross-section along the $[01\bar{1}]$ direction with the [111] direction pointing up, using a Zeiss NVision 40 dual-beam instrument and a 30 keV gallium focused ion beam (FIB). A final 5 keV clean-up process was performed to remove most of the amorphized parts on each side of the lamellae. High Resolution Scanning Transmission Electron Microscopy (HRSTEM) was done using an FEI Titan Cubed 80-300 equipped with CEOS correctors on both the probe and image forming lens systems operating at 200 keV. The STEM acquisition conditions were set to obtain Z-contrast type imaging using a High-Angle Annular Dark- Field (HAADF) detector. Electron Energy Loss Spectroscopy (EELS) was used to map the presence of compositional modulation. An EELS spectrum image was acquired along the growth to identify different layers. The spectrum was taken using phosphorus K edge at 2146 eV, gallium L2 and L3 edges at 1142 eV and 1115 eV, respectively, aluminum K edge at 1560 eV, arsenic L2 and L3 edges at 1359 and 1323 eV, respectively, and indium M4,5 edge at 443 eV. Strain characterization was performed based on Moiré interferometry in STEM and Geometrical Phase Analysis (GPA) method called STEM Moiré GPA (SMG) technique and processed using the STEM-Moire-GPA Python script.

6.2 Results and Discussion

Growth of one layer of InGaAs/InAlAs on singular InP(111)B substrate (sample A) was done to investigate the underpinning of the hillock formation on (111) surface. Fig. 6.1 shows cross-sectional HAADF STEM images from the center (singular (111)) and edge (misoriented (111)) of sample A. The specimen was oriented along the $[01\bar{1}]$ zone axis with the [111] direction pointing upwards. Figure 6.1.a-c show the STEM images from the center of the wafer corresponding to the exact (111)B surface. Hillocks were seen on the surface, which resulted in surface roughening. V-type twinning (Fig. 6.1.b) as well as a high density of stacking faults (Fig. 6.1.c) were observed below the hillocks. This showed that the twins are the underpinning of the hillocks when growth is done on exact (111)B surface. Therefore, microstructural defects lead to morphological instability. Stacking faults originate from the substrate/film interface and persist as the film grows. A stacking fault in a Zinc Blende (ZB) structure is formed by missing of for example a B bilayer in a stacking sequence of ABCABC, which results in a stacking sequence of ABCA|C|A. The CACA sequence represents a single segment of Wurtzite (W) phase [133]. Hence, a stacking fault in the ZB(111) structure is an insertion of one monolayer of W structure, between two ZB structures that have been rotated 60° along the growth direction [132]. The formation of stacking faults was attributed to the small energy difference for the formation of ZB and W crystalline phases in the [111] growth direction [213]. The lower nucleation barrier of Wcompared to ZB was explained as another mechanism for the polytypic phase existence [130]. These leads to the reversal of ZB and W phases during the growth and the formation of rotational twins [214].

Twins are formed by the insertion of a stacking fault (1 Mono-Layer (ML) of W) between two single crystalline ZB structures rotated by 60° [30]. Twins, as were seen by STEM in this study, were reported to have a V-shape characteristic due to the formation of a twin complex. The ease of the formation of twins was attributed to the {111} being the primary twin plane. Twinning was seen before in the Molecular Beam Epitaxy (MBE) growth of GaAs on GaAs(111)B substrates. The formation of growth twins was attributed to the possibility of the rotation of the three group III atoms' bonds when they are attached to the terrace by a single bond [5]. A 60° rotation of these bonds from their perfect crystal position leaves the crystal structure unchanged with only the stacking sequence altered, resulting in a twin. However, if the incoming group III atoms attach to the substrate by more than one bond, such as for example at a surface step, the possibility of rotation is vastly reduced, making the twining difficult. Increasing the migration length of the group III atoms on the surface to reach the surface steps before incorporating into the crystal lattice can vastly reduce the twin density. This can be achieved by using misoriented

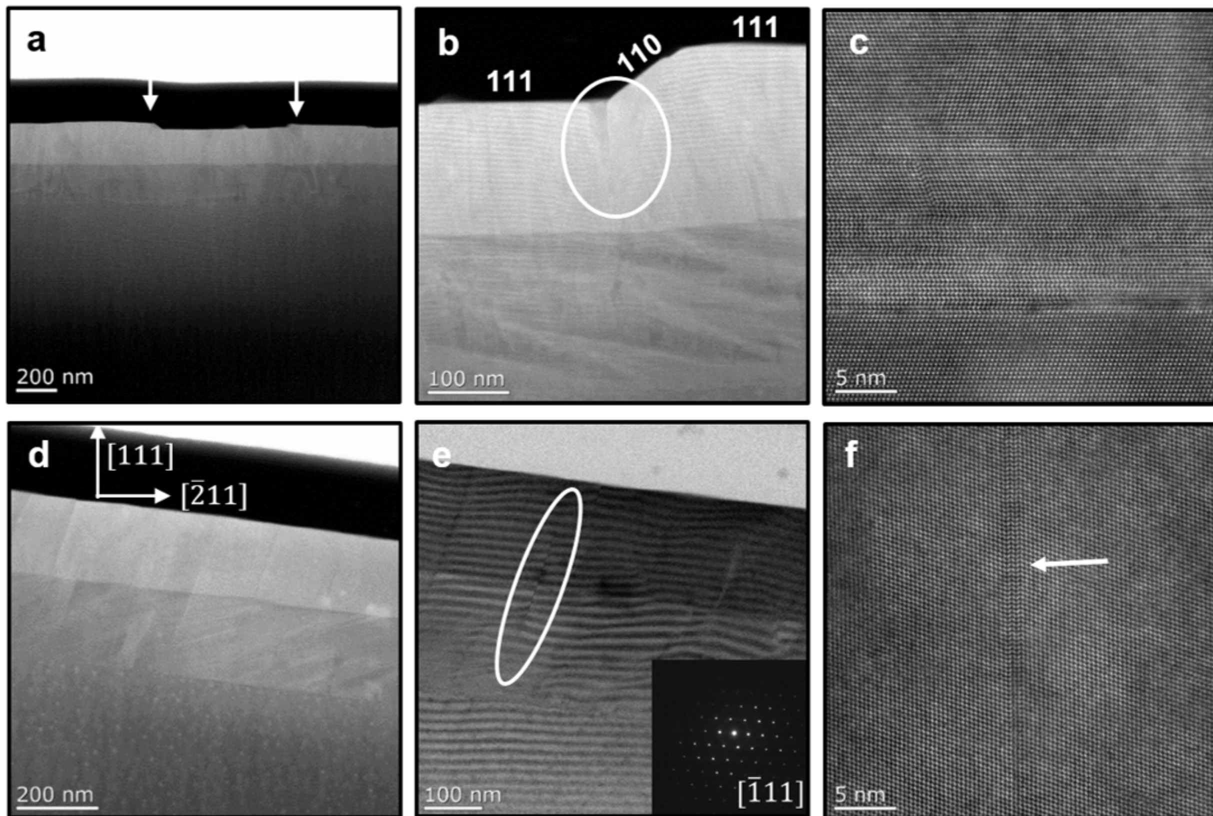

Figure 6.1: STEM images of sample A on a-c) singular (111) and d-f) vicinal (111) surface. The striations in Fig. e are the STEM Moiré fringes which are indicative of strain variations in InGaAs and InAlAs epilayers due to compositional non-uniformities and defects. A stacking fault and a twin are circled in Figs. e and b, respectively. The diffraction pattern is shown as the inset of Fig. e. HRSTEM images of a stacking fault in the smooth region (f) and a high density of stacking faults at the center of the wafer (c) are shown.

substrates with reduced terrace width as well as by reducing the growth rate to promote the step-flow growth.

Although growth on singular (111)B substrates is dominated by the formation of high density of stacking faults, polytypism and twining, deviation from the exact [111] direction and introduction of a misorientation angle could avoid the phase instability. Fig. 6.1.d-f show the cross-section STEM micrographs from the smooth edge region at the edge of the wafer. The (111) atomic planes are horizontal and a 7° surface tilt from the (111) planes was measured at this specific cut. No hillock was seen at this misorientation

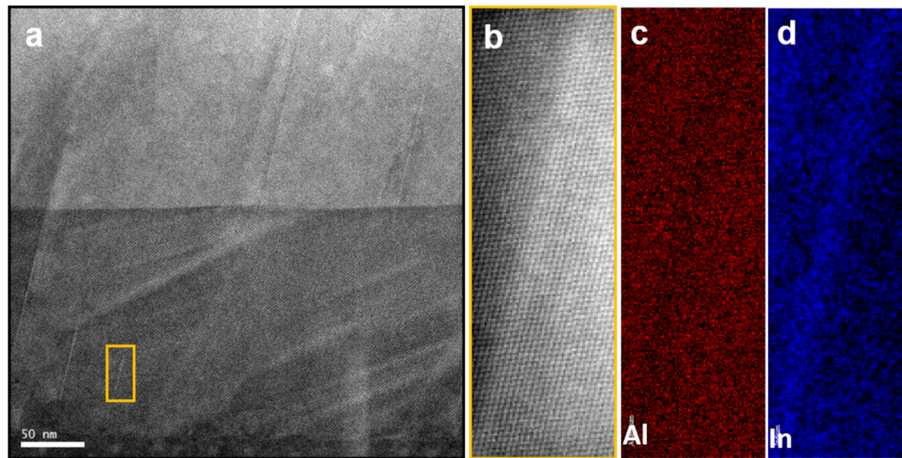

Figure 6.2: STEM image of sample A at a) higher magnification, b) lower magnification showing the white-ish defect and c,d) EELS maps showing phase separation in the InAlAs layer.

angle. STEM Moiré fringes as seen in Fig. 6.1.e were used to locate the defects such as stacking faults. A local change in the atomic arrangement modifies the Moiré fringes spacing and orientation making them sensitive to a deformation field in the sample [204]. The particularity of the STEM Moiré interferometry technique is to display the Moiré fringes arrangement over a large Field of View (FOV) and thus map the strain field within a couple of micrometers FOV. It was seen that both interfaces were coherent and disregistry of the atoms were not observed meaning that the plastic deformation did not occur in the epilayers. A few stacking faults as shown in Fig. 6.1.f were observed.

Besides stacking faults and twinning, phase separation and ordering are other growth challenges. Figure 6.2 shows the EELS maps of the InGaAs/InAlAs layers. These maps showed regions of high concentration of In and Al indicative of the presence of phase separation in the InAlAs layer, however, no phase separation was seen in the InGaAs layer. Phase separation leads to strain inhomogeneity in the system and may be the cause of the STEM Moiré fringes spacing and orientation variations. The Selected Area Diffraction (SAD) pattern of the epilayers is shown as the inset in Fig. 6.1.e. No extra spot was revealed in the SAD pattern indicating that no ordering occurred since ordered phases lead to additional spots in the diffraction pattern. This may be related to a relatively low growth temperature used to activate the ordering process. It was also previously reported that for the growth of InAlAs on (111) substrate, ordering happens at a specific growth temperature [142].

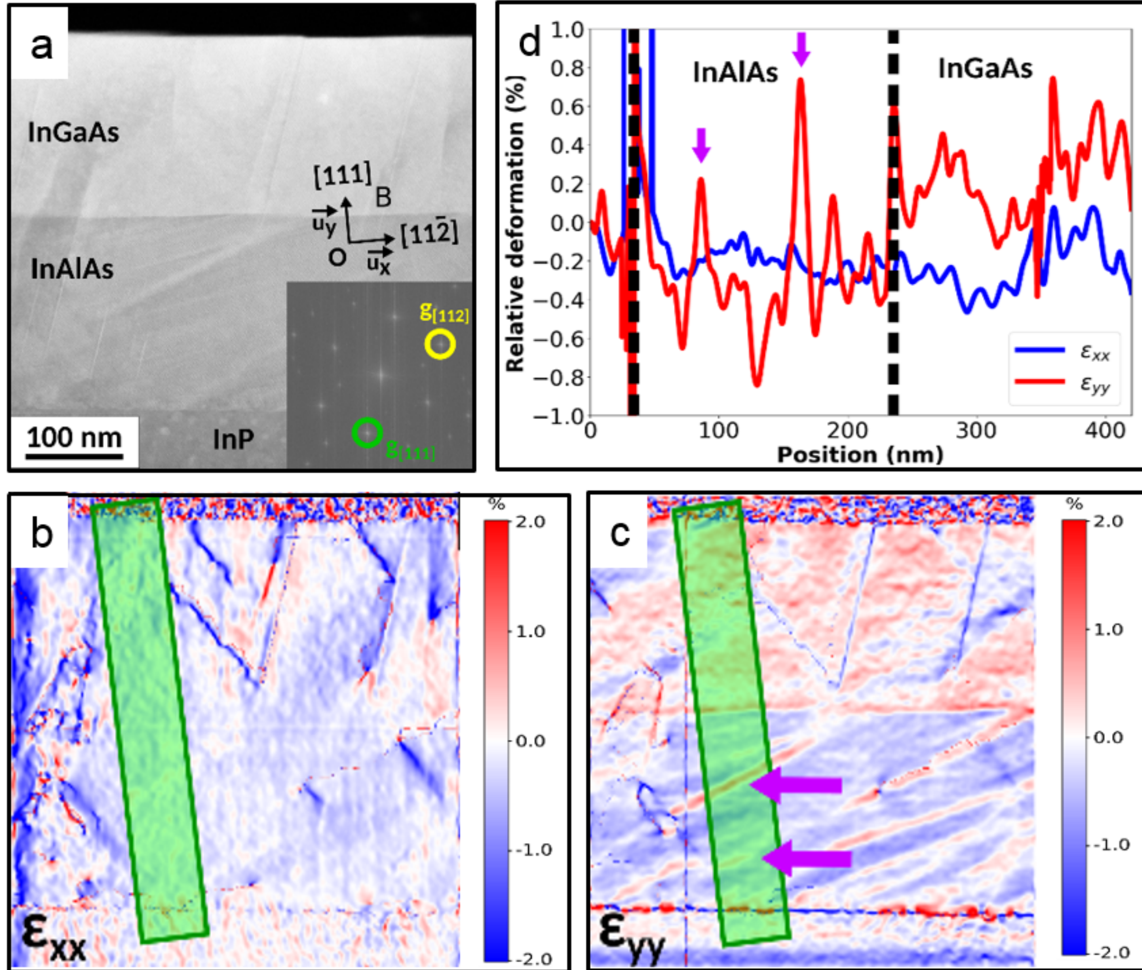

Figure 6.3: SMG relative deformation maps of sample A recorded in the smooth region using the InP as the unstrained reference state. a) STEM Moiré hologram covering the InP/InAlAs/InGaAs stack and its Fourier transform (inset) highlighting the Moiré vectors used for SMG. Deformation maps from the 2D strain and rotation tensors components b) ϵ_{xx} and c) ϵ_{yy} projected on the orthonormal base $B = (O, (u_x), (u_y))$ oriented along the $[\bar{2}11]$ and [111] directions. d) ϵ_{xx} and ϵ_{yy} deformation profiles along the green rectangles in b) and c). The purple arrows show the In rich lines going along $[11\bar{1}]$ direction indicating phase separation in InAlAs layer.

Figure 6.3 shows the result of strain analysis on the smooth region. Globally, the SMG deformation maps confirm that the InAlAs/InGaAs epitaxy is nearly lattice matched to the InP substrate since $\epsilon_{xx} \simeq 0$. The deformation profiles along the [111]/growth direction, ϵ_{yy}, (Fig. 6.3.c) shows the presence of strain in the InGaAs and InAlAs layers due to tetragonal distortion. The strain is negative in the InAlAs layer meaning that the layer is tensily strained in-plane and compressively strained in the growth direction. On the other hand, the InGaAs layer is compressively strained in-plane and tensily strained vertically. The ϵ_{yy} map also shows some strain at the interface between the InP and InAlAs, which comes from the perturbance at the interface after the oxide desorption. The blue lines in the InGaAs layer going along [110] directions correspond to an abrupt change in the microstructure due to the stacking faults. Whenever there is an abrupt change in the microstructure, there is a change of contrast in the strain map. The ϵ_{yy} map in the InAlAs layer highlights a few red lines going along $[11\overline{1}]$. These are positively and negatively deformed regions that correspond to In rich (purple arrows in Figs. 6.3.c-d) and Al rich areas, respectively, confirming the phase separation observed in EELS maps. These strain variations can be converted to In compositional change as follows. For the isotropic case assuming plane-stress condition and Vegards law we have [215]:

$$\epsilon_{xx} = \frac{a_{InAlAs} - a^0_{InAlAs(x)}}{a^0_{InAlAs}} \tag{6.1}$$

$$\epsilon_{yy} = \frac{c_{InAlAs} - a^0_{InAlAs(x)}}{a^0_{InAlAs}} \tag{6.2}$$

$$\epsilon_{yy} = \frac{-2\nu(x)}{1-\nu(x)}\epsilon_{xx} = -2\frac{C_{12}}{C_{11}}\epsilon_{xx} \tag{6.3}$$

$$\nu_{InAlAs(x)} = x\,\nu_{InAs} + (1-x)\,\nu_{AlAs} \tag{6.4}$$

$$a^0_{InAlAs(x)} = x a_{InAs} + (1-x)a_{AlAs} \tag{6.5}$$

$$a^0_{InAlAs(x)} = (1 - \frac{\nu-1}{\nu+1}\epsilon_{yy})a_{InP} \tag{6.6}$$

in which C_{11} and C_{12} are the elastic constants. a and ν are the lastice constant and poisson ratio, respectively. a^0_{InAlAs} is the relaxed lattice constant of InAlAs, and a^0_{InAlAs}

and a^0_{InAlAs} are the tetragonally distorted lattice constants of InAlAs. Considering lattice matching in the x direction i.e. $[\bar{2}11]$, a change from 46.2% to 57.5% was calculated in In composition in the layer for the isotropic case. We then took into account the anisotropy. The elastic constants for growth in [001] direction (i.e. basis of e_1=[100], e_2=[010], e_3=[111]) are tabulated in Table 6.1 from the literature. For the anisotropic case, the elasticity matrix was transformed from the basis of e_1=[100], e_2=[010], e_3=[001] to m_1=$[0\bar{1}1]$, $m_2 = [\bar{2}11]$, m_3=[111] to reflect the growth in [111] direction. Using the transformation matrix as in Eq. 6.7 and the elasticity matrix in the basis of e_1=[100], e_2=[010], e_3=[001] as expressed in Eq. 6.8 and Eq. 6.10 for InAlAs and InGaAs, respectively, we derived the elasticity matrix as in Eq. 6.9 and Eq. 6.11 for InAlAs and InGaAs, respectively, in the basis of m_1=$[0\bar{1}1]$, $m_2 = [\bar{2}11]$, m_3=[111]. A more detailed calculation to find anisotropic elasticity matrix with the change of basis can be found in Appendix B.

$$\Omega = m_i.e_j = \begin{bmatrix} m_1.e_1 & m_1.e_2 & m_1.e_3 \\ m_2.e_1 & m_2.e_2 & m_2.e_3 \\ m_3.e_1 & m_3.e_2 & m_3.e_3 \end{bmatrix} = \begin{bmatrix} 0 & -0.7 & 0.7 \\ -0.82 & 0.41 & 0.41 \\ 0.58 & 0.58 & 0.58 \end{bmatrix} \tag{6.7}$$

$$C_{ij}(InAlAs) = \begin{bmatrix} 103.1 & 49.1 & 49.1 & 0 & 0 & 0 \\ 49.1 & 103.1 & 49.1 & 0 & 0 & 0 \\ 49.1 & 49.1 & 103.1 & 0 & 0 & 0 \\ 0 & 0 & 0 & 46.6 & 0 & 0 \\ 0 & 0 & 0 & 0 & 46.6 & 0 \\ 0 & 0 & 0 & 0 & 0 & 46.6 \end{bmatrix} \tag{6.8}$$

$$C^T_{ij}(InAlAs) = \begin{bmatrix} 122.7 & 42.6 & 36 & -9.3 & 0 & 0 \\ 42.6 & 122.7 & 36 & 9.3 & 0 & 0 \\ 36 & 36 & 129.2 & 0 & 0 & 0 \\ -9.3 & 9.3 & 0 & 33.5 & 0 & 0 \\ 0 & 0 & 0 & 0 & 33.5 & -9.3 \\ 0 & 0 & 0 & 0 & -9.3 & 40.1 \end{bmatrix} \tag{6.9}$$

$$C_{ij}(InGaAs) = \begin{bmatrix} 99.9 & 49.3 & 49.3 & 0 & 0 & 0 \\ 49.3 & 99.9 & 49.3 & 0 & 0 & 0 \\ 49.3 & 49.3 & 99.9 & 0 & 0 & 0 \\ 0 & 0 & 0 & 48.9 & 0 & 0 \\ 0 & 0 & 0 & 0 & 48.9 & 0 \\ 0 & 0 & 0 & 0 & 0 & 48.9 \end{bmatrix} \tag{6.10}$$

$$C_{ij}^{T}(InGaAs) = \begin{bmatrix} 123.5 & 41.4 & 33.6 & -11.1 & 0 & 0 \\ 41.4 & 123.5 & 33.6 & 11.1 & 0 & 0 \\ 33.6 & 33.6 & 131.4 & 0 & 0 & 0 \\ -11.1 & 11.1 & 0 & 33.2 & 0 & 0 \\ 0 & 0 & 0 & 0 & 33.2 & -11.1 \\ 0 & 0 & 0 & 0 & -11.1 & 41.0 \end{bmatrix} \quad (6.11)$$

The relaxed lattice parameter of InAlAs was found as in Eq. 6.12:

$$a^{0}_{InAlAs(x)} = \frac{2C_{13} + C_{33}(1 + \epsilon_{yy})}{2C_{13} + C_{33}} a_{InP} \quad (6.12)$$

in which C_{13} and C_{33} are taken from Eq. 6.9. This resulted in a change of In composition from 45% to 60% within the InAlAs layer when we considered the anisotropic case.

	C_{11}	C_{12}	C_{44}	E_{iso}	ν_{iso}
InP	101.1	56.1	45.6	101.1	0.36
InGaAs	99.9	49.3	48.9	99.9	0.35
InAlAs	103.1	49.2	46.6	103.1	0.37

Table 6.1: Elastic properties of InP, InGaAs and InAlAs [216, 217].

In the InGaAs layer, the ϵ_{yy} map looks more uniform (except around the defects) confirming the good mixing between In and Ga adatoms. One important thing to notice is the presence of a spike in the deformation map at the InP/InAlAs interface. This shows the formation of an InAs layer at the interface, which resulted from the P desorption and As substitution during the oxide desorption process.

6.3 Summary

- Microstructural analysis showed that twinning is the underpinning of the surface steps. Increasing the surface step density by using vicinal surfaces increases the chance of adatom attachment to the step edges. This eliminates twinning since adatoms form more bonds at the step edges, due to the larger number of dangling bonds at the steps. This locks the orientation of remaining dangling bonds to ZB

configuration, preventing forming W domains. Stacking faults and twins form when a change in bond direction occurs. Hence, proper choice of misorientation angle that promotes the step-flow growth mode, i.e. adatom attachment to the steps, eliminates their formation.

- Phase separation was observed in the InAlAs layer. This could be due to the slower growth rate of InAlAs layer. Compositional Modulation (CM) diminishes when growth kinetic is limited such as by increasing the growth rate. We did not observe such phase separation in the InGaAs layer that was grown at a much faster growth rate. It should be mentioned that phase separation might be beneficial within the InAlAs layer since it could lead to the formation of deep level traps effective in capturing excess carriers from the InGaAs layer.

Chapter 7

Surface analysis of InP(111)A and InP(111)B substrates

As the demand for high-performance materials increases, so does the importance of surface engineering. The surface of a material is the point of interaction with the external environment and other materials; therefore, many of the problems associated with modern materials can be solved only by understanding the physical and chemical interactions that occur at the surface or the interfaces of a material's layers. In fact different reconstructions associated with different III-V growth surfaces can create different interfacial roughness [218].

A surface layer is defined as being up to three atomic layers thick ($\sim 1nm$), depending upon the material. Layers up to approximately 10 nm are considered ultra-thin films, and layers up to approximately 1 μm are defined as thin films. The remainder of the solid is referred to as bulk material. This terminology is not definitive, however, and the distinction between the layer types can vary depending upon the material and its application.

Surface analysis techniques are therefore very important to understand surface chemistry of a material and investigate the efficacy of surface engineering, material failures, or the development of new devices. In the case of InP(111) substrates, the surface could terminate in either In that makes it (111)A or P that makes it (111)B. These surfaces are two sides of the wafer. If you flip a (111)A surface, it will be (111)B. Different terminations lead to different surface reconstructions. Epitaxial thin film quality is dramatically affected by the substrate surface reconstruction. In addition, surface reconstruction and relaxation processes directly affect the formation of surface states. The occupation of these states,

in turn, can have a profound influence on device performance [96].

7.1 Experiment

In this chapter we did a systematic study to understand the behavior of (111)A and (111)B surfaces. The effect of substrate cleaning procedure on the surface reconstruction was studied. Surface of the InP(111)A and InP(111)B Substrate were cleaned by flash (direct current) annealing and by sputtering followed by annealing at 250° C, 300° C, 400° C, 450° C and 500° C.

All experiments were performed in a multi-chamber Ultra-High Vacuum (UHV) (Omicron Nanotechnology, Inc.) with a base pressure lower than 5×10^{-11} Torr. The analysis chamber was equipped with an X-ray photoelectron spectrometer and a variable temperature Scanning Tunneling Microscopy (STM) and a Low energy electron diffraction (LEED). The X-ray Photoelectron Spectroscopy (XPS) spectrometer consisted of a monochromatized Al $K\alpha$ (photon energy = 1486.6 eV) X-ray source (XM 1000 MkII), a SPHERA hemispherical electron analyzer, and a 7-channeltron detector assembly. The XPS measurements were performed at normal emission as well as grazing emission (Angle-Resolved X-Ray Photoelectron Spectroscopy (ARXPS)) geometries. For grazing emission the sample was tilted by 80° leading to an angle of 10° with respect to the normal emission angle (so the take off angle or θ was 80°). A schematic showing the difference between the normal emission and grazing emission is depicted in Fig. 7.1.

Single-side polished, n-type InP(111)A (0.35 mm thick) and InP(111)B (0.45 mm thick) chips (11×2 mm^2) with a carrier concentration of $(1-8) \times 10^{18}$ (AXT wafer, Inc.) were used as the substrates. The samples were first cleaned with acetone and isopropanol alcohol in an ultrasound cleaner and then introduced into the chamber. The sample preparation procedure includes an Ar ion sputtering step with 5kV ion beam energy for 10 minutes followed by annealing at 250 °C, 400 °C and 500 °C using an electron beam heater. For flash annealing, the sample was heated to its glowing temperature ($\sim$ 525°) by passing a current of 3 A through it. The samples were conductive enough to allow current to pass through. The substrate was kept at the glowing temperature until a pressure rise within the chamber was detected (about 10 sec). The XPS and LEED measurements were conducted before sample preparation and after each preparation step. The XPS spectra were recorded at a pass energy of 20 eV with an energy resolution of 0.7 eV Full Width at Half Max (FWHM) for the Ag $3d_{5/2}$ photoline at 368.3 eV. Using the Casa XPS software, Gaussian-Lorentzian line shapes were employed to fit the spectra after appropriate correction with the Shirley background.

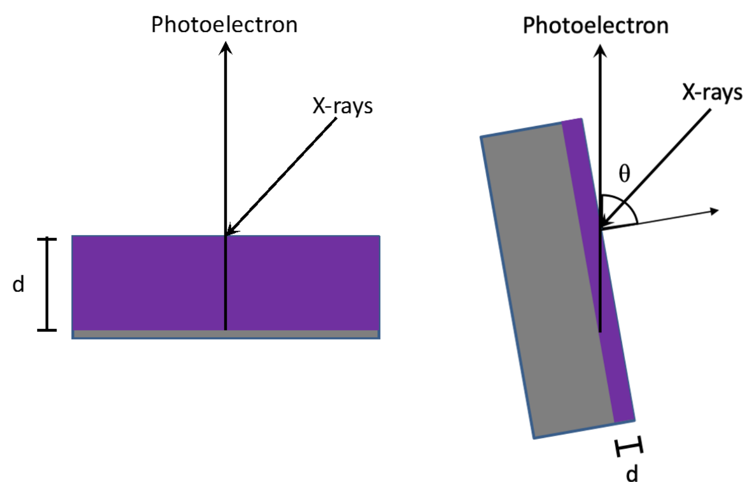

Figure 7.1: Schematic representations of take-off angle variation and sampling depth in ARXPS, normal emission (left) showing a take-off angle of 0° and angle-resolved emission (right) showing the take-off angle of θ°. Increased take-off angle results in reduced sampling depth (d).

7.2 Results and Discussion

Substrates that were prepared by flash annealing had rough surfaces since higher LEED beam energies were required to acquire the surface reconstructions. Both InP(111)A and InP(111)B showed a (1 × 1) unreconstructed surface (Fig. 7.2). According to Atomic Force Microscopy (AFM) analysis, it seems that some In droplets have formed when surface was flash annealed (Fig. 7.3). STM analysis on both flash annealed InP(111)A and InP(111)B at room temperature as well as low temperature (cooled by liquid nitrogen) did not lead to any atomically resolved images, which could be as a result of a rough surface. Figure 7.4 shows an example of STM images acquired on InP(111)B after flash annealing.

Figure 7.5 shows the surface reconstruction of InP(111)B surface after being sputtered by Ar ions and annealed at different temperatures. XPS analysis showed that the oxide layer has been removed as no oxide related peak was detected. LEED pattern shows a (1 × 1) unreconstructed surface after annealing at different temperatures of 250° C to 400° C following sputtering. Thus, the atoms on the surface have the same arrangement as the atoms in the bulk of the substrate. This shows that the InP(111)B is thermally stable. Figure 7.6 shows the surface reconstruction of InP(111)A surface after sputtering by Ar ions and annealing at different temperatures. The surface reconstruction after

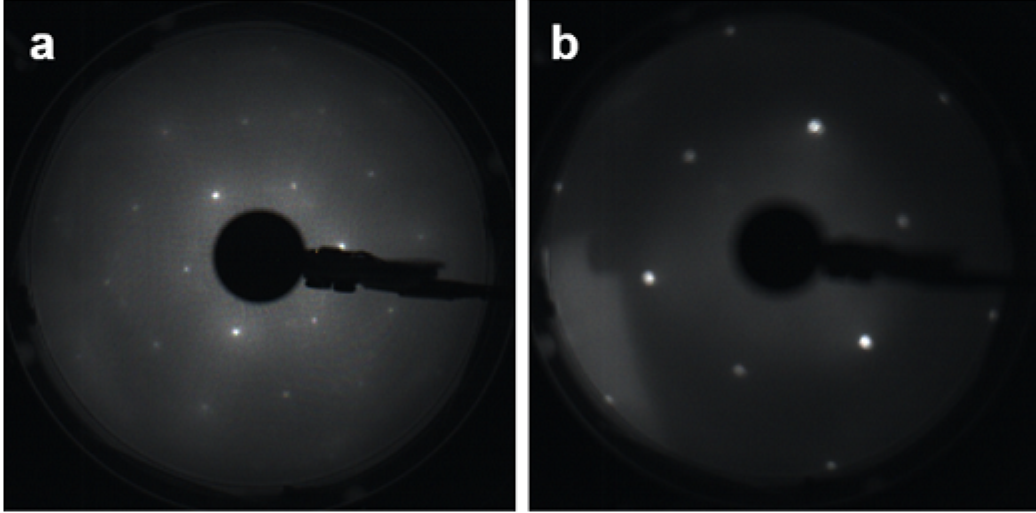

Figure 7.2: LEED images of flash annealed substrates at 460° C. a) InP(111)A at a beam energy of 135.6 eV and InP(111)B at a beam energy of 51.9 eV.

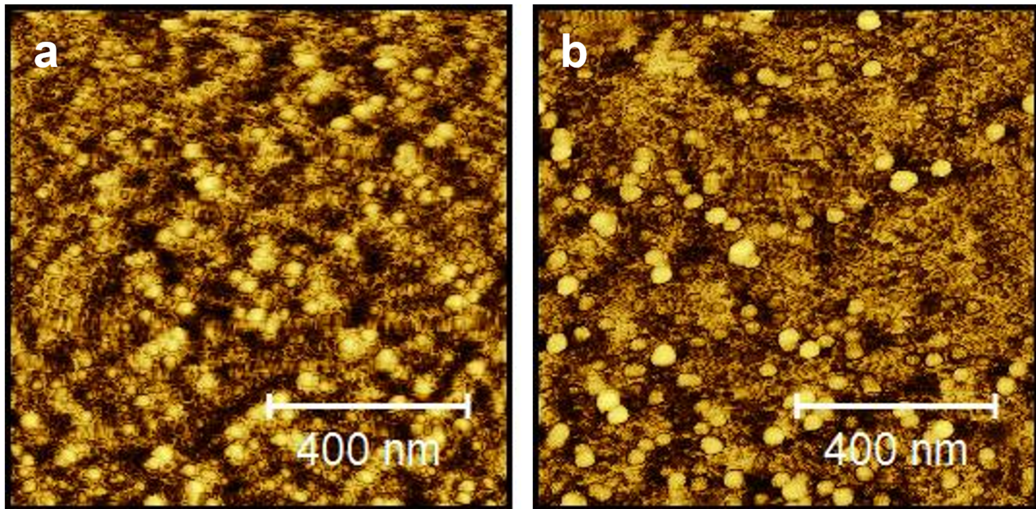

Figure 7.3: InP(111)B a) annealed inside the MBE main chamber (RMS roughness = 6.68±0.94 Å) and b) flash annealed (RMS roughness = 5.28±1.04 Å), at 458° C.

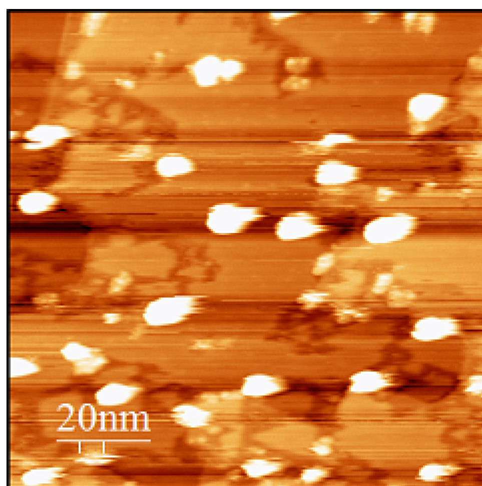

Figure 7.4: STM images of InP(111)B at low temperature after flash annealing.

sputtering followed by a very short annealing period at 250° C is a (1 × 1). It is observed that the surface reconstruction after annealing at 250° C, 300° C and 400° C is a mixture of (2 × 2) and (3 × 3). It can be seen that the most intense diffraction spots are those of the (2 × 2) reconstruction although faint spots of (3 × 3) reconstruction also coexist. This states that there are more domains of (2 × 2) compared to (3 × 3). Increasing the annealing temperature to 450° C reduces the domains of (2 × 2) reconstruction substantially according to LEED pattern which shows a more or less (3 × 3) pattern. Increasing the annealing temperature to 500° C, the LEED pattern shows a completely (3 × 3) reconstruction. Therefore, unlike B surface, InP(111)A surface is thermally unstable, and the atoms on the surface do not have the same arrangement as the atoms in the bulk of the substrate.

There has not been much work done on the surface reconstruction of InP(111) substrates. Theoretical calculations suggested a (2 × 2) and ($\sqrt{3} \times \sqrt{3}$) reconstructions for InP(111)B with ($\sqrt{3} \times \sqrt{3}$) being a meta-stable reconstruction since it does not obey the electron counting rule [107]. For the case of InP(111)A, theoretical investigation by Yi [104] showed a (2 × 2) reconstruction. Shimomura et al. [106] observed a (2 × 2) surface reconstruction after ion bombardment and annealing at 300-400° C. However, the ($\sqrt{3} \times \sqrt{3}$) as well as (2 × 2) were reported by Li et al. [103]. There is no report of a (3 × 3) on InP(111) surface to the best of our knowledge.

It should be mentioned that the stability of the unreconstructed surface requires that the surface charge transfers from the surface to the bulk in order to reduce the surface

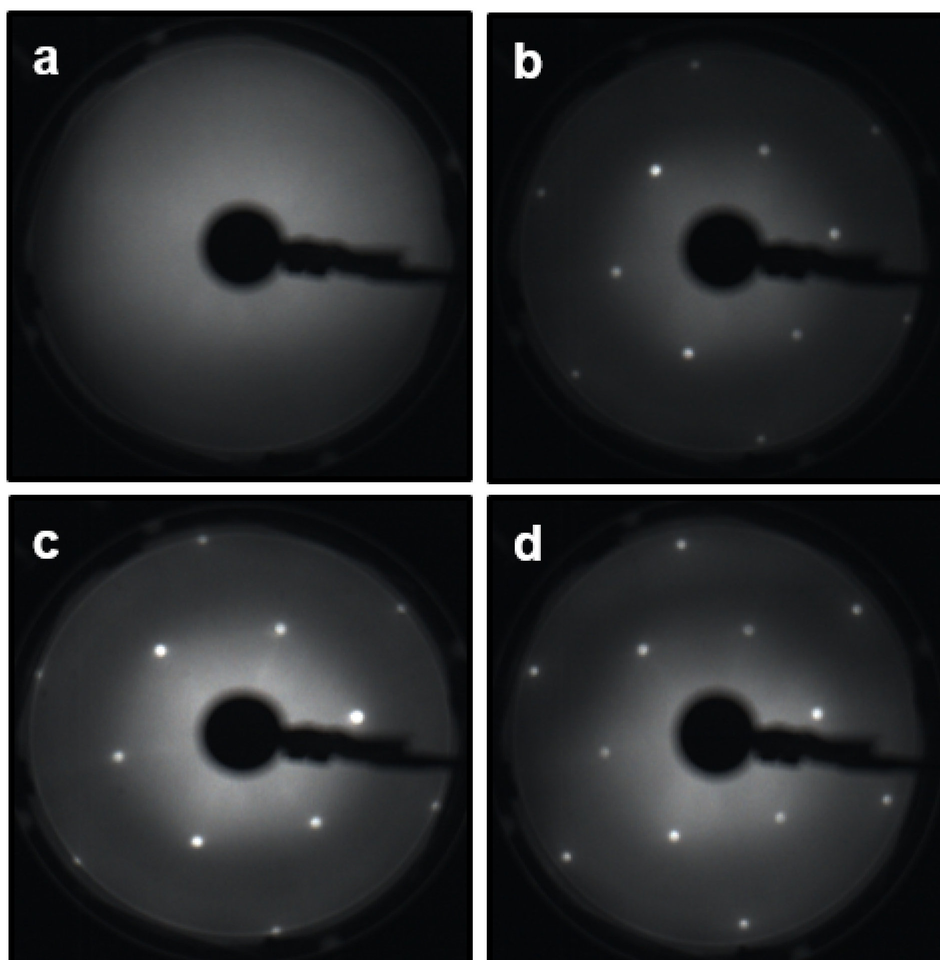

Figure 7.5: LEED pattern of InP(111)B a) before sputter annealing, Ar ion sputtered at 5kV for 20 min and annealed at b) 250° C, c) 300° C and b) 400° C. Electron beam energies were 75.2 eV, 53.7 eV, 51 eV and 59.1 eV for a, b, c and d, respectively.

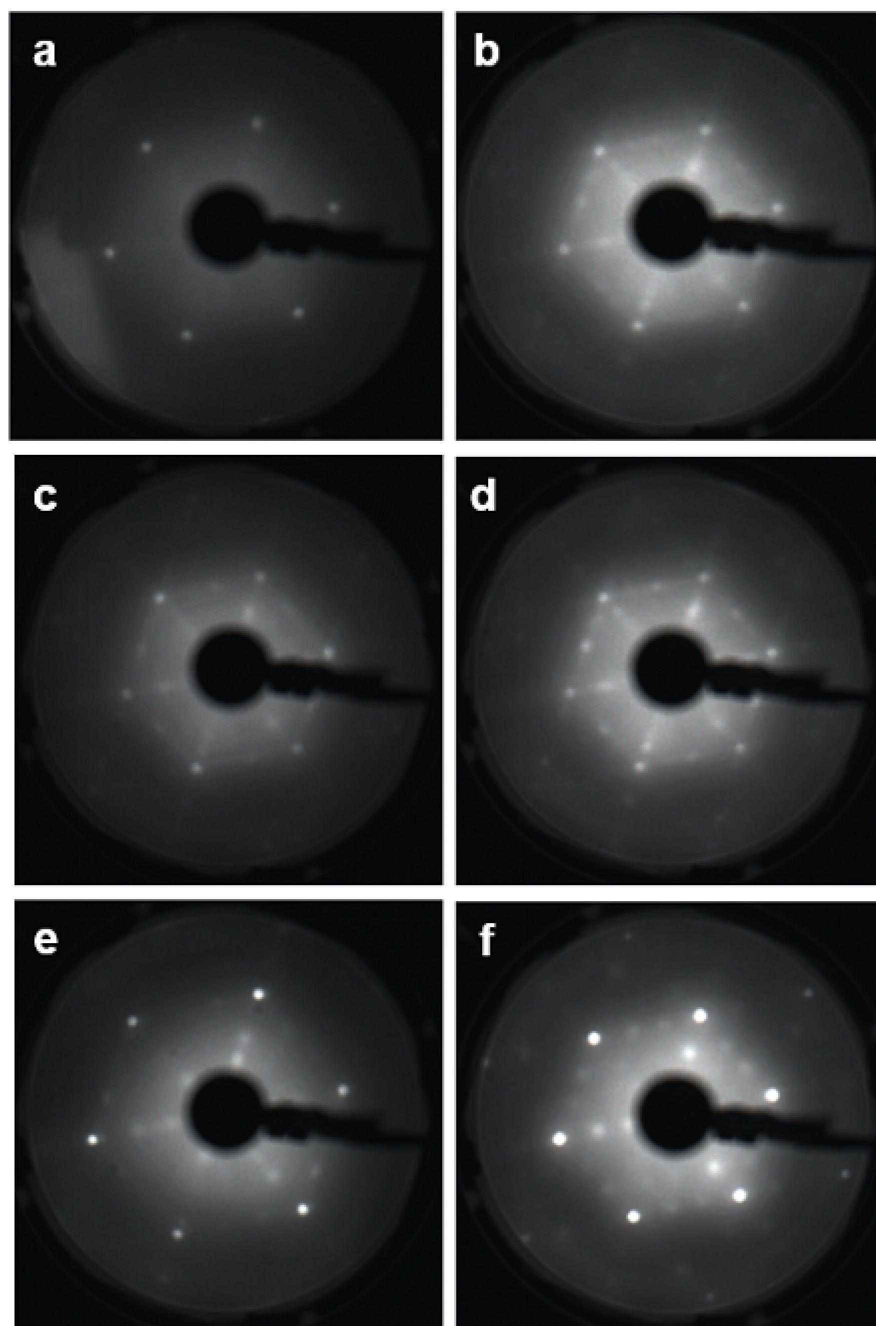

Figure 7.6: LEED pattern of InP(111)A after a) sputtering at 5kV for 20 min and annealed at b) 250° C, c) 300° C, d) 400° C, e) 450° C and f) 500° C. Electron beam energies were 59.1 eV, 60.4 eV, 59.1 eV, 40.8 and 32.7 eV for a, b, c, d and e, respectively.

dipole. If a charge transfer cannot be achieved, the surface reconstructs so that the charge transfers from the surface to the bulk through the atom re-positioning or vacancy formation. Based on the charge distribution calculations done on InP(111) surface along the surface normal, the charge is more easily displaced towards the cation planes. Hence, in the case of (111)B surface that terminates with P, the surface charge is transferred to the In cation plane underneath. On the other hand, in the case of (111)A surface that terminates in In, the charge is on the surface cation plane. Since the charge does not transfer to the bulk, the surface should reconstructs. The charge transfer is facilitated by the asymmetric bulk potential, which is due to the different atomic radii of In and P [114].

Figures 7.7 and 7.8 show the evolution of grazing emission XPS spectra of In3d and P2p core levels using Al $K\alpha$ excitation measured on InP(111)B and InP(111)A surfaces, respectively, after various surface treatments. These spectra were normalized to the same height and deconvoluted into several peaks by fitting to reflect the local environment of In and P atoms on the surface. In3d has well separated spin-orbit components of $In3d_{3/2}$ and $In3d_{5/2}$ separated by 7.54 eV. P2p also has separated $P2p_{1/2}$ and $P2p_{3/2}$ peaks by 0.5 eV. We first measured the composition of the (111)B and (111)A surfaces with native oxides. The XPS spectra of the as-received (111)A and B surfaces are shown in Figs. 7.7 and 7.8, respectively. The relative area ratio of In3d to P2p for the (111)B surface was ~ 1.11 and that of (111)A surface was ~ 1.25 in the grazing emission geometry at a take of angle of 80°, reflecting the difference in the composition of the as-received surfaces. The deconvolution of the In3d lines shows the presence of two overlapped peaks. The peaks from $In3d_{3/2}$ and $In3d_{5/2}$ at the lower binding energy (444.5 and 452.04 eV) are related to In-P bond, and the ones at higher binding energies shifted by 0.657 eV (445.157 and 452.697), correspond to In-O (In_2O_3). The P2p line also was deconvoluted to two peaks corresponding to In-P at lower binding energies (128.568 and 129.068 eV corresponding to $2p_{1/2}$ and $2p_{3/2}$, respectively) that is more intense and P-P at higher binding energies (129.408 and 129.908 eV corresponding to $2p_{1/2}$ and $2p_{3/2}$, respectively) that is less intense showing the presence of less P-P compared to In-P bonds on the surface. The less intense peak at 133.221 eV corresponds to P-O (P_2O_5). The insets of Figs. 7.7.b and 7.8.b show the P-O peak at 133.221 eV. It is seen in Figs. 7.7 and 7.8 that the amount of P-oxide on (111)B surface is larger than on (111)A, whereas (111)A surface is richer in In oxide.

After sputtering the FWHM of the In and P peaks increases in both (111)A and (111)B surfaces indicating that the surface has become rough. It also shows that the stoichiometry has changed due to the presence of defects for example vacancies. The In/P ratio increased after sputtering for both InP(111)B and InP(111)A surfaces showing a preferential sputtering of P atoms. It is also possible that there are some In islands on the surface

responsible for the increased ratio of In/P. The In peak in both 7.7.a and 7.8.a has become more symmetric and has only one component due to the oxide removal. The P peak has also become more symmetric in both 7.7.b and 7.8.b Figs. showing that the ratio of P-P bonds to In-P bond has increased on the surface. The P-P bonds could be due to the presence of P islands on the surface. It is also seen that the P-O peak has disappeared in both (111)A and (111)B cases.

After annealing, the surfaces smooth out and the FWHM of all the peaks reduces. The In/P ratio reduces to its value before sputtering. It is seen that after sputtering a loss feature has appeared at higher binding energy. The peak disappear after annealing, however, it re-appears after annealing at higher temperature of 500° C for the case of InP(111)A surface 7.7.a or after flash annealing for the case of InP(111)B 7.8.a. After annealing (111)A surface at 500° C, a shoulder appear in In peak at 443 eV that is related to In-In bond. As the metallic In $3d_{5/2}$ peak at 443 eV is exposed, a significant plasmon loss feature grows in at a higher binding energy than its parent peak [219]. The In/P ratio has increased to 2.08 at this annealing temperature. In3d/P2p ratio after different surface treatment for InP(111)B and InP(111)A are tabulated in Table 7.1. The oxide layer thickness was found taking into account the ratio of oxide-related and bulk XPS peaks and using Eq. 7.1 as follows [220, 221]:

$$d_{ox} = \lambda cos\theta ln(\frac{I_S}{I_O}) \tag{7.1}$$

where θ is the take-off angle, I_O and I_S are the peak intensities before and after oxide desorption, respectively, and λ is the Inelastic Mean Free Path (IMFP) in unit of Mono-Layer (ML) which is found according to Eq. 7.2 [222]:

$$\lambda = \frac{2170}{E^2} + 0.72(aE)^{1/2} \tag{7.2}$$

where E and a are the electron kinetic energy and monolayer thickness in nm, respectively. Using a take-off angle of 80°, the oxide layer thickness was estimated to be 0.25 nm and 0.35 nm for (111)B and (111)A surfaces, respectively.

Another aspect of spectral changes induced by sputtering clearly visible in Figs. 7.7 and 7.8 are binding energy shifts of the In metal and P element peaks. The primary reason for peak shifts in XPS is a change in the chemical bonding state. Preferential sputtering of lighter components (P) likely results in an increased metallic character of the ion-beam modified surface layer and peak shifts towards metallic positions (i.e. towards lower binding energy). The fraction of atoms that is not sputtered away is subject to a

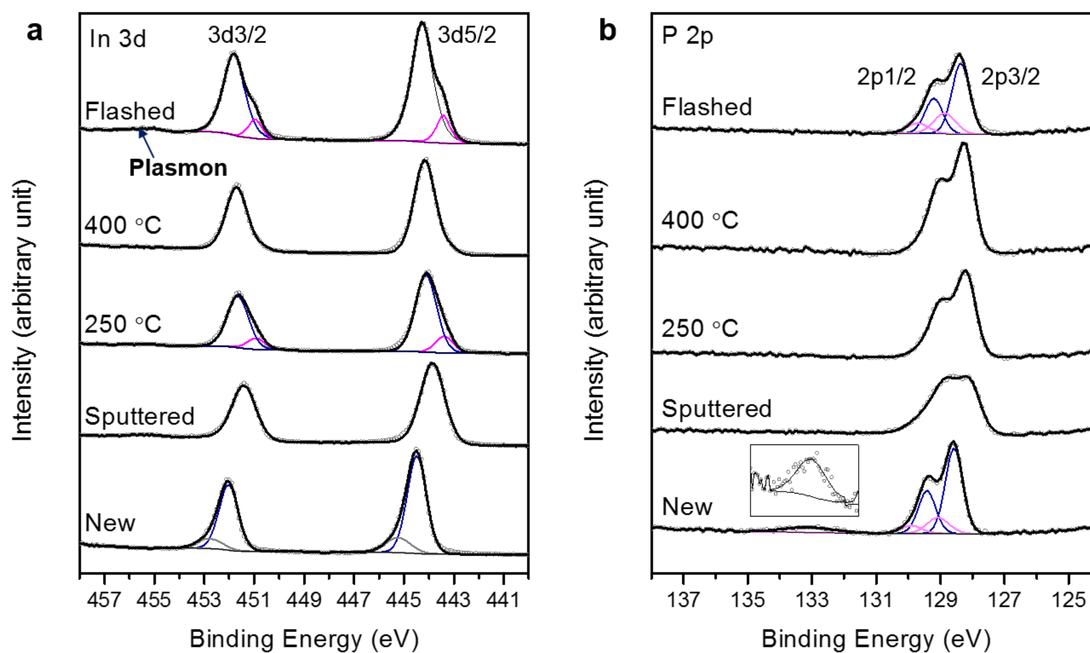

Figure 7.7: a) In3d and b) P2p grazing emission XPS spectra from InP(111)B surface after various annealing treatment.

complete rearrangement during collision cascades and likely ends up in a new bonding configuration (hence with modified distribution of valence charge) in a disordered surface layer. The existence of substoichiometric stable phases after sputtering could be the dominant mechanism. The potential influence of surface roughening, and Ar implantation cannot be neglected. All above factors can give rise to binding energy shifts. In addition, as XPS is highly sensitive to surface electrical potential, peak shifts can also result as a consequence of modified electrical properties in the Ar beam affected layer. In such case, purely spectroscopic effects like different charging state and/or modified screening properties become essential. Additional complication in spectral interpretation is that the overall spectrum apart from the Ar modified layer may also contain contributions from the deeper lying region that has not been affected by the Ar ion beam.

Growth on InP(111)A using conventional MBE did not lead to as smooth surface as on InP(111)B. Reflection High Energy Electron Diffraction (RHEED) pattern at high symmetry azimuths after the oxide desorption on InP(111)A surface showed a (2 × 2) surface reconstruction as shown in Fig. 7.9. This surface reconstruction leaves each

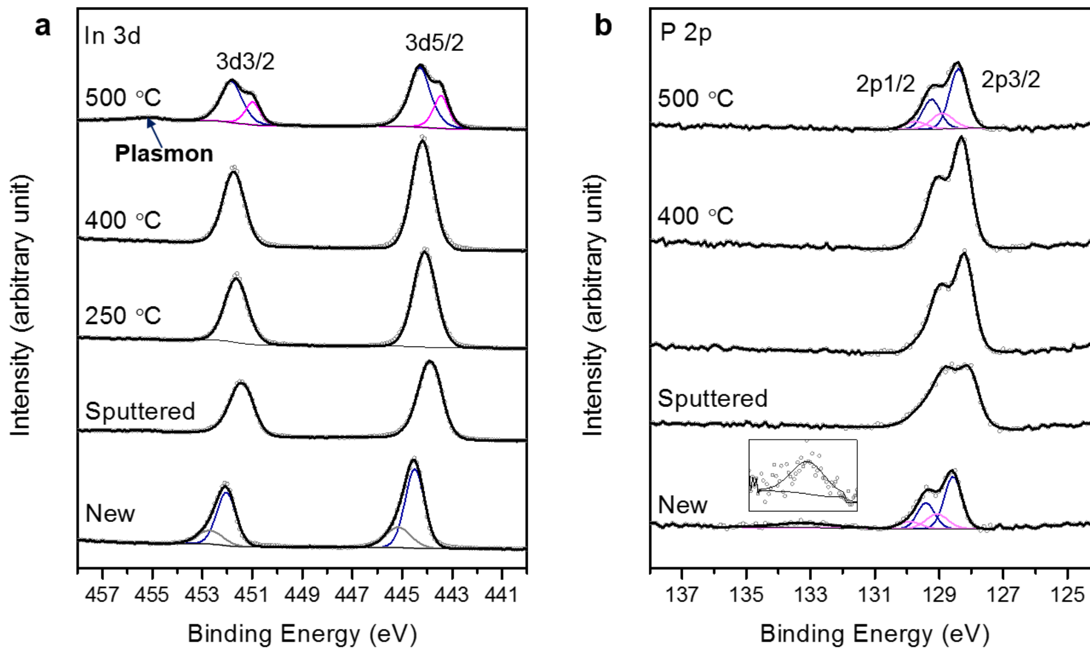

Figure 7.8: a) In3d and b) P2p grazing emission XPS spectra from InP(111)A surface after various annealing treatment.

phosphorous atom on the surface with 3 dangling bonds as well as one In atom vacancy per each surface unit cell. A schematic representation of the buckling In-vacancy and P-trimer structures of a (2×2) surface reconstruction is shown in Fig. 7.10 and Fig. 7.11, respectively. It was shown for the case of GaAs(111)A that the As-trimer configuration is stable at As-rich condition [223, 224]. In this experiment, the sputtering and annealing were done under no overpressure of P or As. Hence, we assumed that the In-vacancy structure is stable after sputtering and annealing. Further calculations or STM analysis is required to confirm our hypothesis. The buckling in In-vacancy model brings about an increase (or decrease) in the orbital electronegativity of As (or Ga), induces charge transfer from Ga to As, and finally makes Ga (or As) dangling bonds empty (or filled). As a result, there are no unsaturated bonds at the surface [100]. The In-vacancy (2×2) with one missing In vacancy per each surface unit cell leads to a smaller sticking coefficient of arsenic on (111)A surface. Therefore, most of the growth conditions do not lead to as good results that are found for growth on (111)B substrate. InP(111)B has a (1×1) unreconstructed surface after oxide desorption as evidenced by RHEED (Fig. 7.12), which leaves each surface phosphorous atom with one dangling bond. A schematic of a (1×1)

	In/P - InP(111)A	In/P - InP(111)B
As received (grazing emission)	1.25	1.11
Sputtered	1.63	1.57
Sputtered - annealed at 250° C	1.61	1.33
Sputtered - annealed at 400° C	1.30	1.11
Sputtered - annealed at 500° C	2.08	–
Flash annealed - $\sim$ 525° C	–	1.2

Table 7.1: In/P ratio measured by XPS on InP(111)A and InP(111)B after different annealing treatment.

unreconstructed surface is shown in Fig. 7.13.

7.3 Summary

The purpose of this chapter was to study the surface reconstruction of InP(111)A and InP(111)B and to compare them since growth quality is dramatically affected by the surface reconstruction. It was seen that:

- InP(111)B substrate is thermally stable. It always has an unreconstructed (1×1) surface after oxide desorption using different procedures such as outgassing inside the MBE system, or flash annealing or sputtering followed by annealing at different temperatures.
- InP(111)A substrate is thermally unstable. It is typically unstable in the unreconstructed surface. The surface reconstruction of InP(111)A changes by the oxide desorption procedure. Outgassing inside the MBE chamber at 460° C, mostly produces a (1×1) or (2×2) surface reconstruction, while cleaning by flash annealing resulted in a (1×1) reconstruction. Sputter annealing resulted in a (2×2), a mixture of (2×2) and (3×3) and a (3×3) at low (250 °C), medium (up to 450 °C) and high annealing temperatures (500 °C).

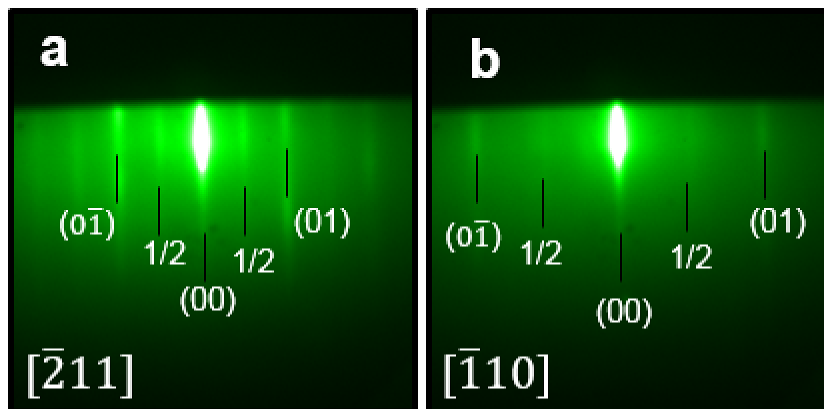

Figure 7.9: RHEED pattern of InP(111)A surface showing a (2 × 2) surface reconstruction.

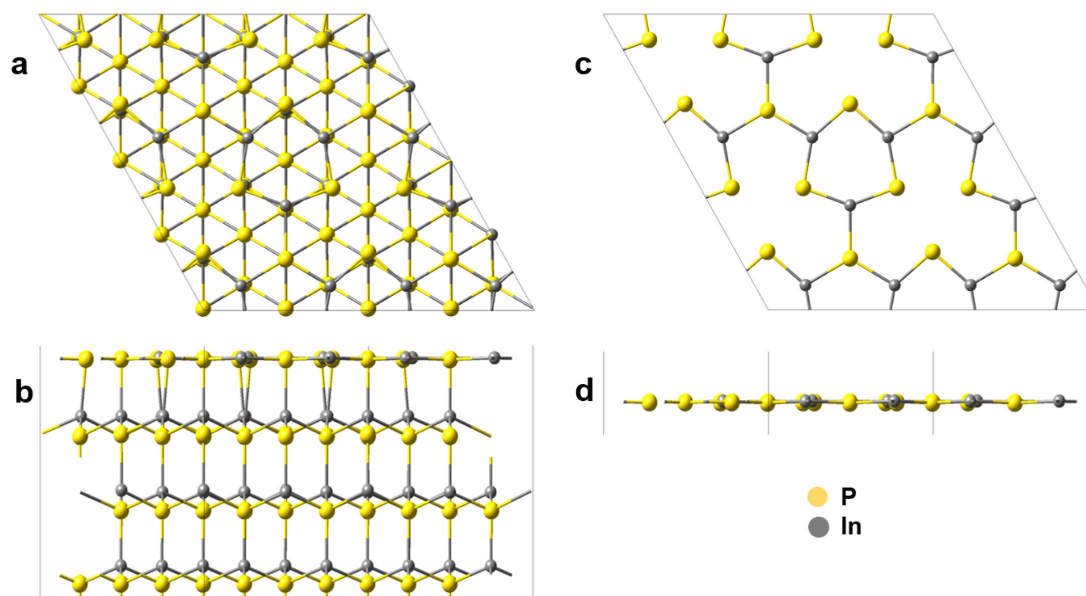

Figure 7.10: A shematic showing the buckling In-vacancy (2 × 2) surface reconstruction of InP(111)A surface. a) top view, b)topmost layer, c) side view of a and d) side view of b.

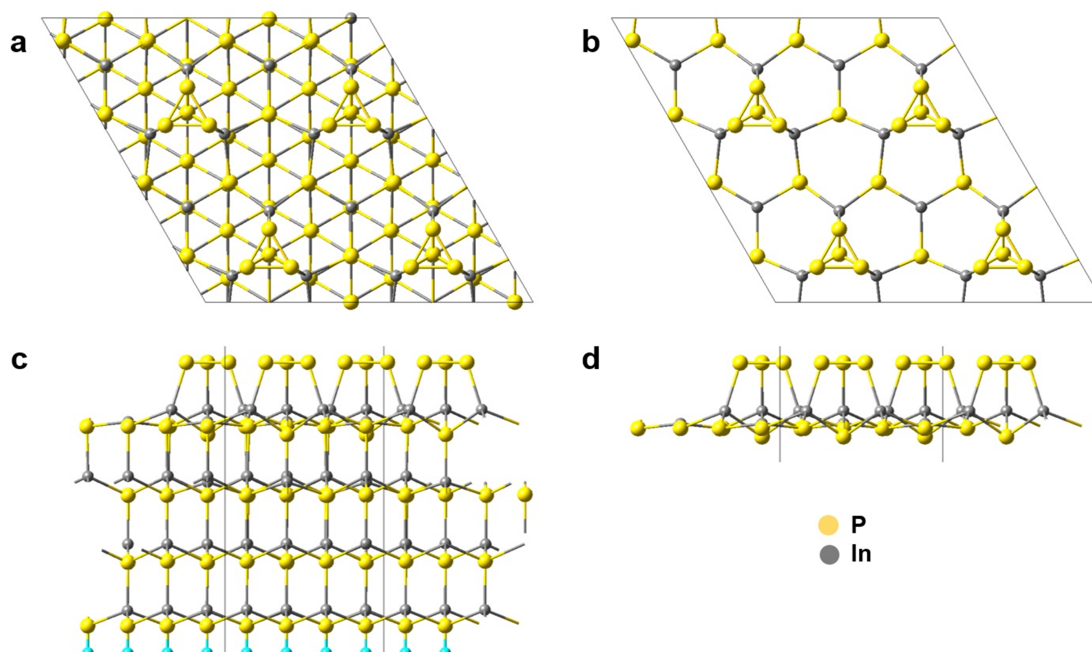

Figure 7.11: A shematic showing the P-trimer (2 × 2) surface reconstruction of InP(111)A surface. a) top view, b)topmost layer, c) side view of a and d) side view of b.

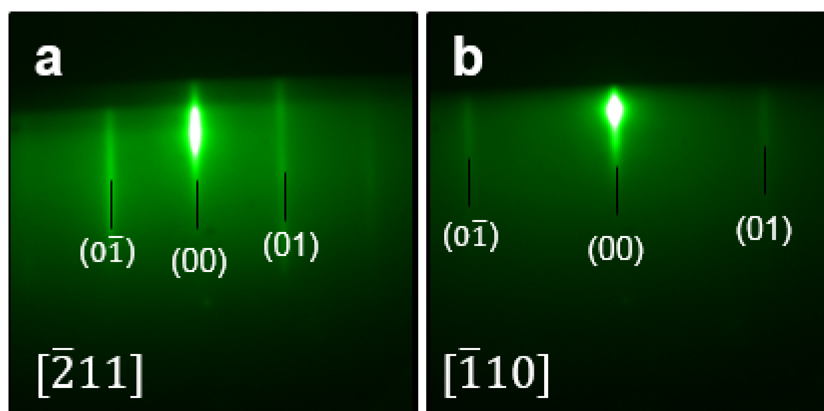

Figure 7.12: RHEED pattern of InP(111)B surface showing a (1 × 1) surface reconstruction.

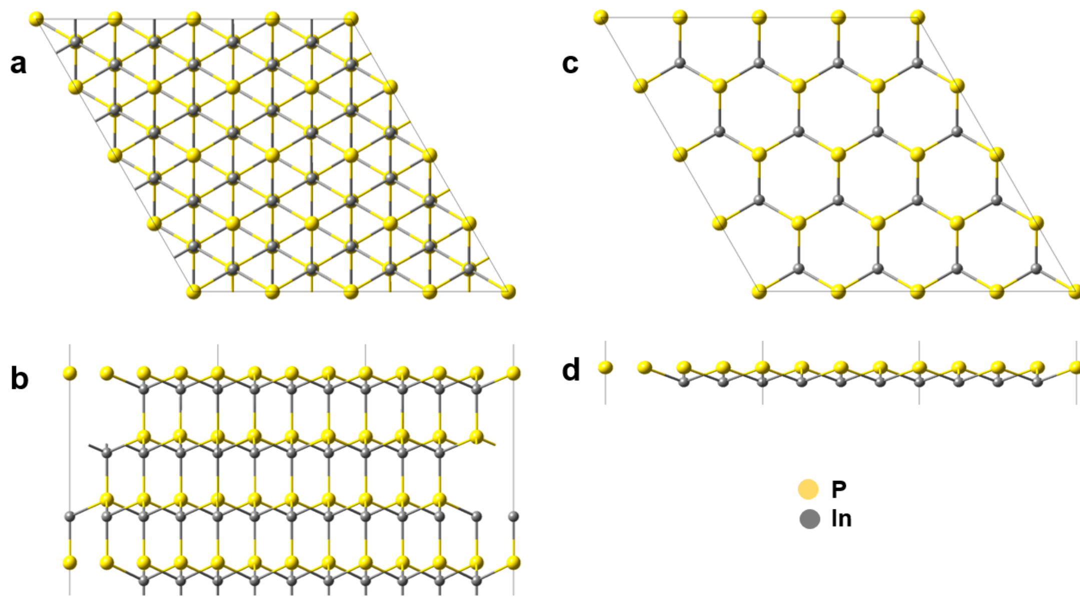

Figure 7.13: A shematic showing the (1 × 1) surface reconstruction of InP(111)B surface. a) top view, b)topmost layer, c) side view of a and d) side view of b.

- The surface reconstruction of InP(111)A makes it a more challenging substrate to grow on compared to InP(111)B.

Chapter 8

Growth of InGaAs-InAlAs superlattice

8.1 Experiment

Misoriented InP(111)B semi-insulating substrates were used in this study. The substrate were misoriented by 0.45°, 1°and 2°towards $[\bar{2}11]$. The off-cut angle for the 2° off-cut substrate was confirmed using High Resolution X-Ray Diffraction (HRXRD) rocking curves at different azimuths from -180° to 180° at increasing steps of 10°, i.e. 36 scans. The angle corresponding to the maximum intensity for each rocking curve was recorded and plotted versus the azimuth angle Fig. 8.1. The amplitude of this curve corresponds to the off-cut angle, which was shown to be exactly 2°. Nominally lattice-matched InGaAs epilayer and InGaAs/InAlAs SuperLattice (SL) (Fig. 8.2) were grown to investigate the effect of misorientation angle as well as growth conditions on the surface morphology. Depositions were not done on misoriented InP(111)A surface since we did not obtain a smooth surface at the edge of the substrate when we deposited on the rounded edge substrates at the growth conditions we used. Multiple growths were done at different growth rates and a fixed As overpressure and growth temperature. Table 8.1 lists the samples that were analyzed.

The microstructure of the growths was analyzed using Scanning Transmission Electron Microscopy (STEM). For the STEM analysis, the samples were cut in cross-section along the $[01\bar{1}]$ direction with the [111] direction pointing up, using a Zeiss NVision 40 dual-beam instrument and a 30 keV gallium focused ion beam (FIB). A final 5 keV clean-up process was performed to remove most of the amorphized parts on each side of the lamellae. High Resolution Scanning Transmission Electron Microscopy (HRSTEM) was done using an FEI Titan Cubed 80-300 equipped with CEOS correctors on both the

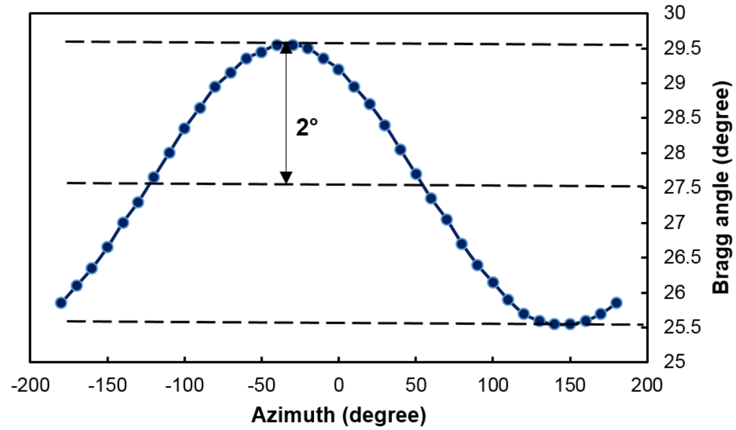

Figure 8.1: Plot of Bragg angle at different azimuths from 0 to 360° measured by HRXRD rocking curves.

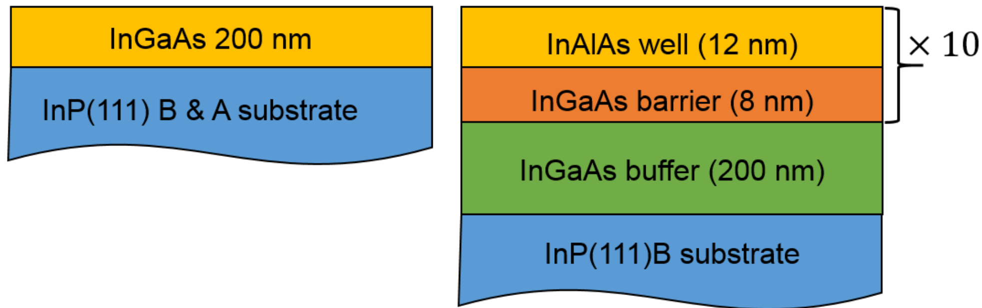

Figure 8.2: Schematic of different structures grown.

Sample	InGaAs/InAlAs Structure	Substrate mis-orientation	Growth rate (Å/s) InGaAs/InAlAs
B	InGaAs	0.45°	0.5
C	10 period SL	1°	0.5/0.5
D	10 period SL	1°	0.5/0.25
E	10 period SL	1°	0.5/0.08
F	10 period SL	2°	1/0.16
G	10 period SL	2°	0.5/0.06

Table 8.1: Summary of the growths.

probe and image forming lens systems operating at 200 keV. The STEM acquisition conditions were set to obtain Z-contrast type imaging using a High-Angle Annular Dark-Field (HAADF) detector. Electron Energy Loss Spectroscopy (EELS) was used to map the presence of compositional modulation. An EELS spectrum image was acquired along the growth to identify different layers. The spectrum was taken using phosphorus K edge at 2146 eV, gallium L2 and L3 edges at 1142 eV and 1115 eV, respectively, aluminum K edge at 1560 eV, arsenic L2 and L3 edges at 1359 and 1323 eV, respectively, and indium M4,5 edge at 443 eV. Strain characterization was performed based on Moiré interferometry in STEM and Geometrical Phase Analysis (GPA) method called STEM Moiré GPA (SMG) technique and processed using the STEM-Moire-GPA Python script.

8.2 Results and Disscusion

Growth on singular (111) substrates is challenging due to the formation of morphological and microstructural defects that lead to surface roughening. The morphological defects are mainly three faceted pyramids, while the microstructural defects are mainly stacking faults, twins and dislocations. Three faceted hillocks are formed on (111) surfaces, since the (001) facets are energetically favorable. In another words, formation of hillocks is attributed to an insufficient migration length when growth is performed on singular (111) surfaces. This is attributed to the number of dangling bonds present on the surface. (001) surface has double dangling bond per P atom while (111)B has one dangling bond per P atom. Double dangling bond is energetically favorable for growth. Single dangling bond may lead to Zinc Blende (ZB)-Wurtzite (W) phase instability. A diffusion length of the adatoms smaller than half the terrace width will increase the probability of adatom incorporation onto the terrace and nucleation of a new island. For a larger diffusion length, adatoms will tend to attach to the step edges, contributing to the desirable step flow growth mode. The realization of such step flow growth mode is an effective way to eliminate hillock formation. Using misoriented substrates was reported as an effective way to reduce the hillock density. The misorintation angle determines the terrace width, therefore, it affects the growth mode. It should also be noted that the growth conditions such as growth rate could be as important as the misorientation angle in determining the growth mode. It is also noteworthy to mention that the optimum misorientation angle for growth is different for different compounds since different group III atomic species have different migration lengths on the surface. On the other hand, the microstructural defects such as stacking faults, twins and dislocations were said to have small energy barrier to their formation and are consequently easily formed in ZB material systems.

For the growth of InGaAs on InP(111)B we showed that a minimum misorientation angle of 0.4° is needed to avoid hillocks at the optimized growth conditions [173].

To implement the result of Density Functional Theory (DFT) calculations along with STEM analysis three different substrates with misorientation angles of 0.45°, 1° and 2° towards $[\bar{2}11]$ direction were used. Since the DFT calculations and STEM observations showed that Al adatoms have smaller migration length compared to Ga adatoms, the growth rates of InGaAs and InAlAs layers within the InGaAs/InAlAs superlattice were adjusted accordingly. This was made possible since our Molecular Beam Epitaxy (MBE) system is equipped with two In cells to allow separate optimization of the epilayers. Figure 8.3 shows Atomic Force Microscopy (AFM) images of sample B-G. The growth rate of InAlAs layer was decreased from 0.5 Å/s to 0.06 Å/s, while the growth rate of the InGaAs layer was kept constant at 0.5 Å/s for all growths. The V/III ratio was kept constant at 7 for both layers. It was seen that at misorientation angle of 1° even at the growth rate of 0.06 Å/s still surface features were present, however, for the growth on 2° misorientation substrates (sample G) the surface morphology improved substantially to a hillock-free surface as the lowest growth rate used. This was the first report of atomically smooth defect free InGaAs/InAlAs on (111) substrate.

It should be mentioned that although the surface of sample G was atomically smooth with a Root Mean Square (RMS) roughness of 4.29 ± 0.37 Å, step bunching, i.e., transition from monoatomic steps to multi-layer steps was seen. The average step height was 2.5 Mono-Layer (ML). Strain-induced step bunching on vicinal surfaces was reported to happen due to elastic relaxation at steps that produces a long-range attractive interaction between the steps. The overlap of stress fields at the adjacent steps makes the surface unstable against step bunching [120]. Step bunching was attributed to the low concentration of adatoms at the steps as the misorientation angle increases. Coalescence of the steps increases the adatom concentration at the steps to the equilibrium value [122].

Fig. 8.4 shows Nomarski images of the sample B-G. It can be seen that there are still some hillocks present on the surface for growth on 1° off substrates at the slowest growth rate used (Fig. 8.4.d), however, the surface is very smooth with very minimal surface defects when the misorientation angle was increased to 2° for the same growth conditions (Fig. 8.4.f). Note that a higher misorientation angle is required for the growth of SL compared to the 0.4° suggested off-cut for the growth of InGaAs in Chapter 5. This is because of the slower migration of Al atoms requiring both a larger misorientation angle, i.e. smaller terrace size, as well as a very slower growth rate to promote the step-flow growth mode.

Fig. 8.5 shows *in-situ* reflectivity signals recorded on sample G at 470 nm and 950

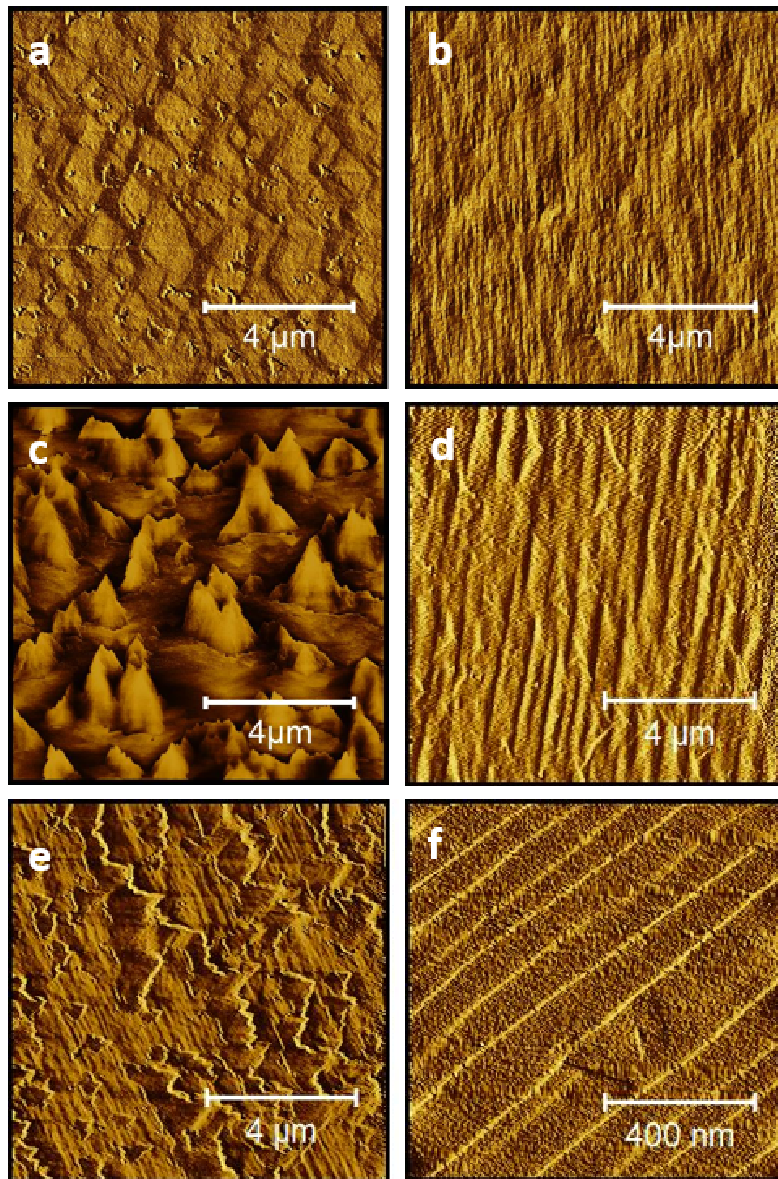

Figure 8.3: AFM height images of the a) sample B showing an RMS roughness of 23.9 ± 5.5 Å, b) sample C showing an RMS roughness of 19.2 ± 3.0 Å, c) sample D showing an RMS roughness of 47.5 ± 10.8 Å, d) sample E showing an RMS roughness of 6.3 ± 0.7 Å, e) sample F showing an RMS roughness of 50.78 ± 10.3 Å and f) sample G showing an RMS roughness of 4.29 ± 0.37 Å. The average ML height is 2.5 ML. Please see table 8.1 for sample description.

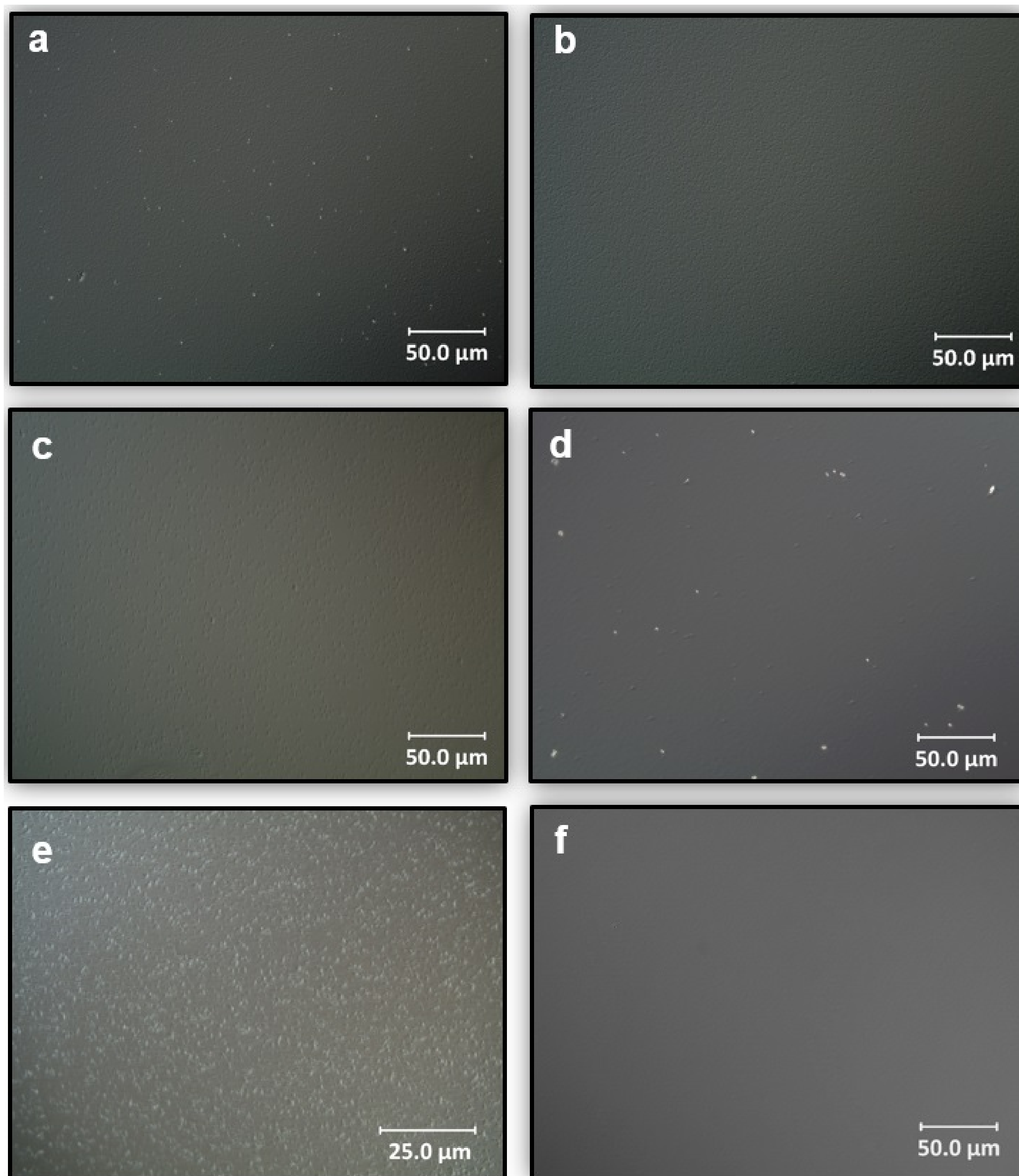

Figure 8.4: Nomarski images of samples a) B, b) C, c) D, d) E, e) F and f) G.

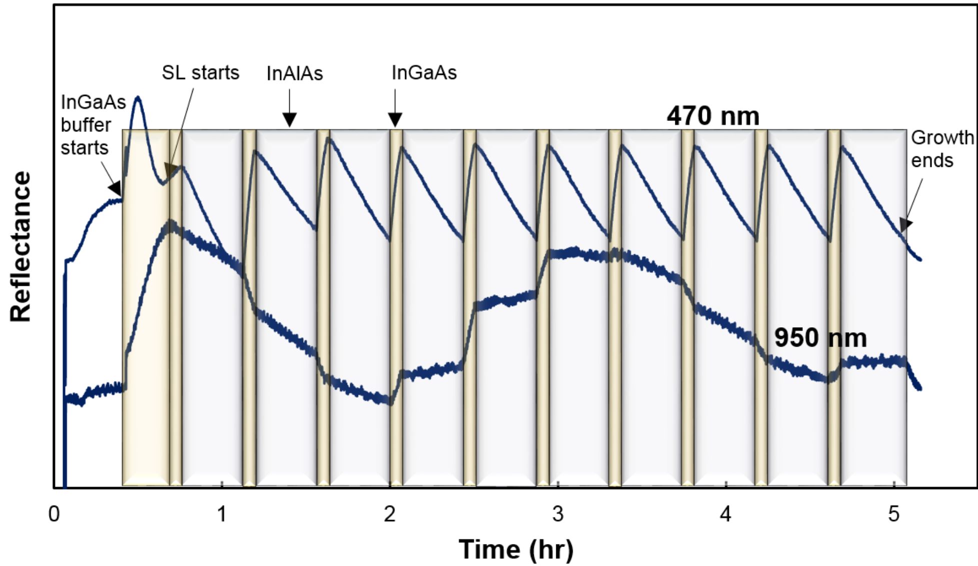

Figure 8.5: 950 nm and 470 nm reflectance monitoring of sample G.

nm wavelengths in real time during the InGaAs/InAlAs SL growth process. The 470 nm wavelength is more sensitive to early stage roughness. If the surface starts to roughen, the reflectance intensity drops due to light scattering. When the surface is illuminated with a parallel beam of light with a wavelength of λ, the reflectance may be divided into two components, one arises from specular reflection and the other from diffuse reflection or scattering. According to Davies' theory, the expression for measured reflectance R is as follows:

$$R = R_0 exp[-\frac{(4\pi\sigma)^2}{\lambda^2}] + R_0 \frac{2^5\pi^4}{m^2}(\frac{\sigma}{\lambda})^4(\Delta\theta)^2 \tag{8.1}$$

the first term in Eq. 8.1 is the specular reflactance of a rough surface and the second term is the contribution from the diffuse reflectance if the normal reflectance is measured with an instrumental acceptance angle of $\Delta\theta$. R_0 is the specular reflectance from a perfectly smooth surface, and σ and m are the root mean square roughness and the root mean square slope of the profile of the surface. At sufficiently long wavelengths the contribution from the diffuse reflectance becomes negligible [225].

The reflectance at 470 nm in Fig. 8.5 shows ups and downs related to the growth of InGaAs and InAlAs layers with different refractive indices. Regular oscillations of the reflectivity signal during a 2D growth at 950 nm wavelength corresponding to the

same ups and downs from the 470 nm wavelength are seen. Growth oscillations are time dependent, periodic modulations of the reflectivity during growth. The temporal oscillations are due to alternating constructive and destructive interference between reflections from the (growing) top surface and the buried layers with different values of dielectric constant. The oscillations are faster during the InGaAs layer growth and slower during the InAlAs layer growth primarily because the InGaAs layer growth rate is higher.

Fig. 8.6 shows the HRXRD $\omega - 2\theta$ triple axis scan of (222) x-ray reflection of sample G. The HRXRD pattern of the SL structure shows three dominating features. First, the most intense peak at 0 arcsec belongs to the (222) reflection of the InP substrate. The second feature are the zero-order reflection from the SL structure and its higher-order satellites. The presence of high-order satellite peaks indicates good layer thickness control in the grown structure. The numbers in Fig. 8.6 denote the satellite peak order, n. The SL zero, first and second order SL peaks are visible. The SL period, Λ, can be found from the position of the satellite peaks according to Eq. 4.24. For the zero-order SL peak ($n = 0$), its angular position reflects the average lattice constant of the InGaAs/InAlAs SL stack. Here, the zero-order SL peak, SL_0, is on the left-hand side of the substrate peak, and is separated from the substrate peak by -206 arcsec. This indicates that the average lattice constant of the SL layers is slightly larger than the substrate lattice constant. The exact Bragg angle for SL_0 is set by the vertical size of the tetragonally distorted average unit cell of the SL. The third feature is the appearance of additional fringes in between of the SL peaks caused by the interference of x-rays reflected from the sample surface and the deepest interference of the SL. They are commonly referred to as interference or Pendellösung fringes.

The presence of strong satellite peaks and clearly visible Pendellösung fringes is an indication of high structural quality and excellent thickness and compositional homogeneity perpendicular and parallel to the crystal surface since structural imperfections such as interface roughness or poor periodicity result in damping of the characteristic features in the SL HRXRD pattern. These features can be used to accurately determine the layers' thicknesses. The HRXRD data were used to fit a model using Rocking-Curve Analysis by Dynamical Simulation (RADS) software. The layers parameter that were obtained from the model are shown in table 8.2. The experimental data could fit the dynamical model by assuming a tetragonal distortion of the epilayers' lattices. Simulation result suggested the presence of an 8 Å (~ 2 ML) thick InAs layer at the interface between the buffer layer and the substrate. This layer has resulted from the InP substrate oxide desorption process in the presence of As overpressure. As substitutes any missing P atoms. Formation of an InAs layer was also reported by Averbeck et al. [195]. Substitution

of P by As and formation of InAs layer on the substrate during the oxide desorption was also shown in a previous work on (001) oriented InP [195]. Another notable feature present in Fig. 8.6 is the good match of the intensities of the zeroth and first order HRXRD and simulation peaks, providing evidence of abrupt interfaces in the SL, while the second order peaks are weaker. The less intense 2nd order SL peaks shows the presence of some non-abruptness in the interfaces, which is later shown in STEM results to come from the interfaces when growth is switched from InGaAs to InAlAs layer.

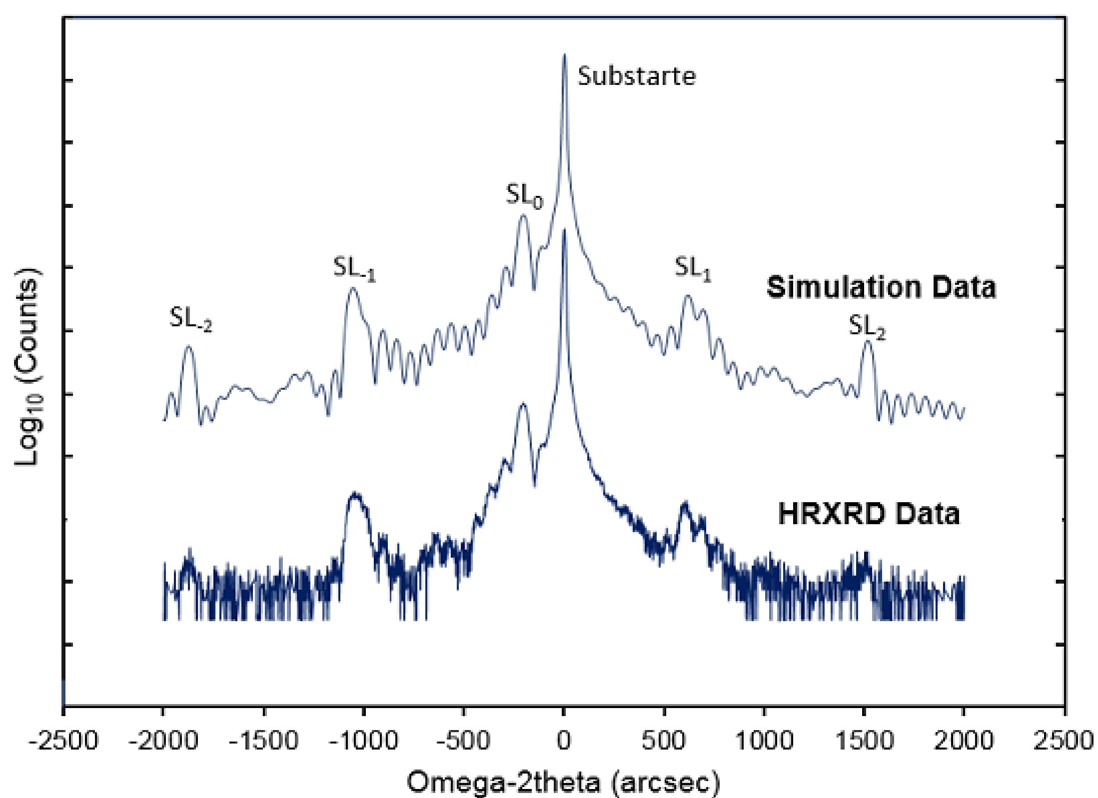

Figure 8.6: HRXRD on sample G.

Cross-sectional STEM investigations were carried out on sample G to characterize the microstructure. The micrographs in Fig. 8.7.a-c reveal that the SL has a good crystalline quality and sharp interfaces. The crystalline lattices of the Face Centred Cubic (FCC) crystal structure (oriented along the $[01\bar{1}]$ direction with the [111] growth direction aligned vertically) are recognizable in Fig. 8.7.c. It is seen from Fig. 8.7.c that the InGaAs-on-InAlAs interface looks different than that of InAlAs-on-InGaAs. InGaAs-on-

Layer	Thickness (nm)	Composition
$In_xGa_{1-x}As/In_xAl_{1-x}As$ SL	13.5/9	0.551/0.535
$In_xGa_{1-x}As$ Buffer	57	0.551
InAs	0.8	1
InP	∞	–

Table 8.2: RADS simulation results.

InAlAs interface looks sharp, while InAlAs-on-InGaAs interface looks more diffused. Segregation is a kinetically limited process. Since InAlAs grows very slowly, there is ample time for Al and Ga to exchange, leading to a segregated interface. InGaAs layer grows at a much faster growth rate, therefore, limiting the Ga segregation kinetically. This effect is more amplified by the very larger tendency of Ga atoms to segregate compared to Al Atoms [226]. The STEM image in Fig. 8.7.d focuses on the buffer layer between the InP and the SL layers. It is noticed that the roughness of the SL/InP interface is significantly higher than the interfaces within the SL. The InP surface roughness is mitigated by the buffer layer offering a smooth surface for the SL epitaxial growth. No defects such as stacking faults or twins were observed within the whole lamellae analyzed. In addition, no sign of phase separation was present. This is due to the fact that the layers were grown at a slower growth rate compared to sample A giving more time to the adatoms to diffuse to the desirable step edges to bond.

SMG strain characterization was carried out to map the strain within the layers. Fig. 8.8.a-b show the ϵ_{xx} and ϵ_{yy} relative deformation maps, and Fig. 8.8.c highlights the averaged ϵ_{xx} and ϵ_{yy} vertical deformation profiles within the layers. In general, $\epsilon_{xx} \approx 0$ throughout the structure confirming that the MBE growth is indeed lattice matched along the $[\bar{2}11]$ direction. Consistent with HRXRD results, the ϵ_{yy} deformation map shows a slightly positive strain within both the buffer layer and the SL suggesting that an elastic strain remains in the layers grown ($\epsilon_{xx} \neq \epsilon_{yy}$) leading to a tetragonal distortion responsible for the separation of the 0th order SL peak from the substrate peak as was seen in Fig. 8.6. This shows the presence of a small mismatch between the substrate and the SL that is accommodated by a tetragonal distortion of the lattice, i.e. the layers remained unrelaxed. It is seen from the ϵ_{yy} strain map that the InAlAs layer is almost lattice matched to the substrate, while InGaAs layer has a small mismatch to the substrate. This is in accordance with the HRXRD simulation data tabulated in Table 8.2. The sharp spike in the deformation map at the substrate/SL interface shows the presence of an InAs layer formed at the interface. Nevertheless, the deformation field magnitude is sufficiently low to lead to a very high quality epitaxial growth.

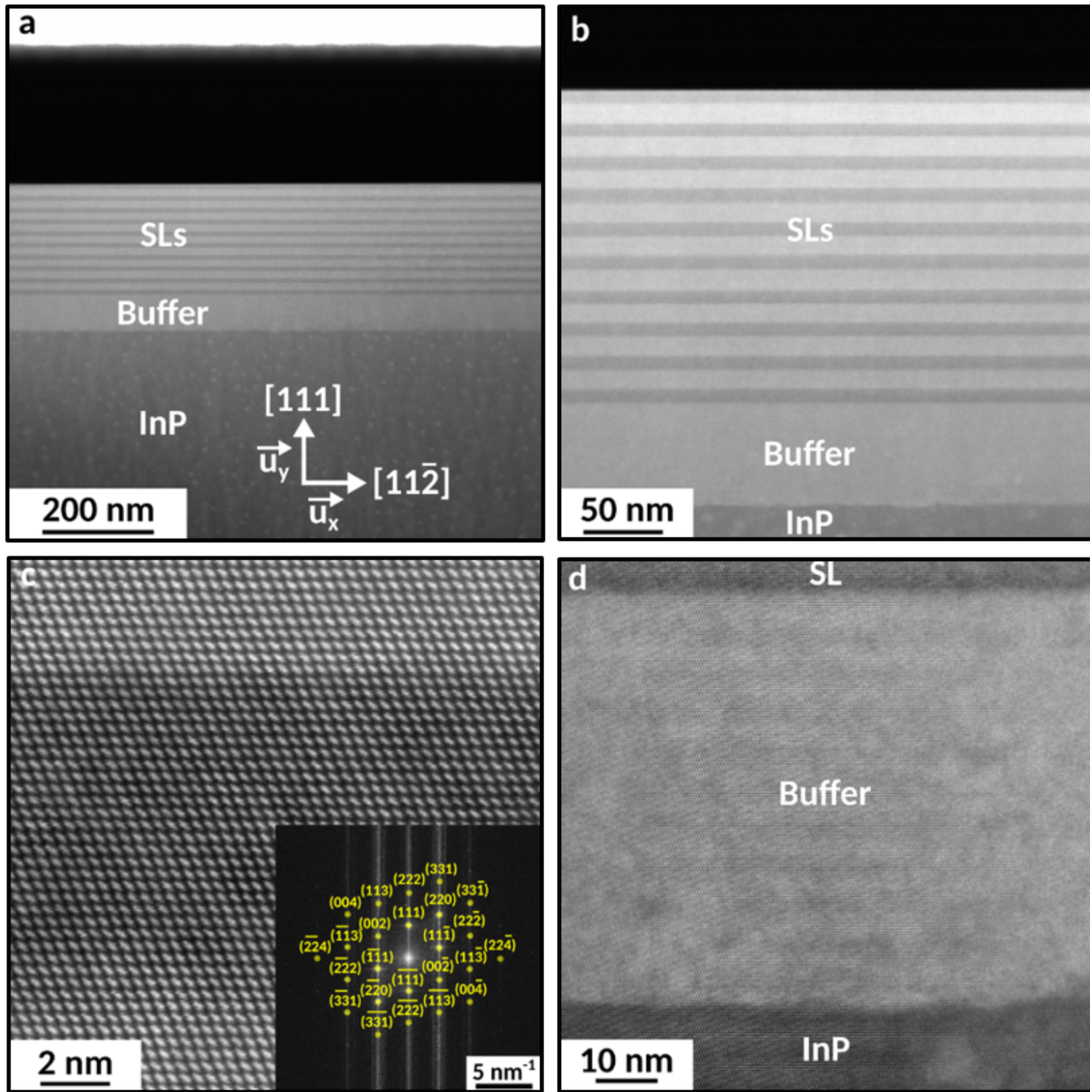

Figure 8.7: STEM images of sample G at a-c) three different magnifications. A cropped Fourier transform of a STEM micrograph in the SL (not present in the figure) is shown as an inset in c) to highlight the resolved crystalline lattices and d) the buffer layer.

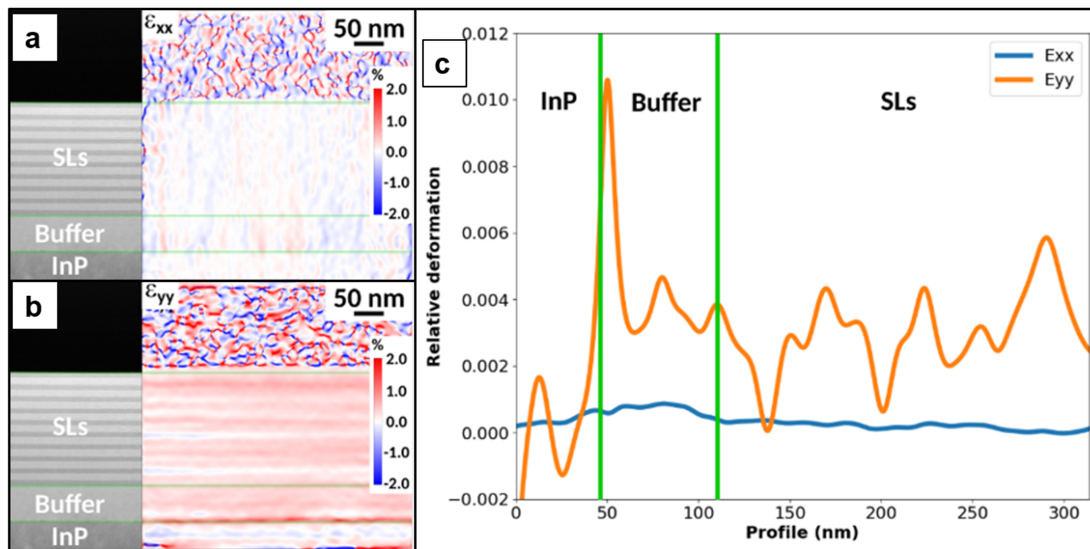

Figure 8.8: a) ϵ_{xx} and b) ϵ_{yy} SMG relative deformation maps. The STEM micrographs on the left of the maps are present to help identifying the different regions (InP, buffer, SL). c) the ϵ_{xx} and ϵ_{yy} vertical deformation profiles from the strain maps in a-b).

8.3 Summary

- Growth of morphologically smooth and microstructurally defect free InGaAs/InAlAs SL on InP(111)B substrate was achieved for the first time. Such a structure was obtained as a result of i) finding the optimum substrate misorientation angle to promote the step-flow growth mode; ii) separately optimizing the growth rate of InAlAs and InGaAs epilayers according to the different mobilities or migration lengths of Al and Ga atoms for growth on the same vicinal surface; and iii) optimization of the growth temperature and arsenic overpressure.

- Our MBE system is equipped with two In cells allowing for accommodation of two different growth rates for growth of InGaAs and InAlAs epilayers. In the event one's MBE system is equipped with one In cell, Migration Enhanced Epitaxy (MEE) growth technique might be of interest. This growth method is discussed in the next chapter.

Chapter 9

Growth of InGaAs-InAlAs superlattice using Migration Enhanced Epitaxy (MEE) and Metal Modulation Epitaxy (MME) techniques

9.1 Experiment

Growth of SuperLattice (SL) was also done using MEE and MME. As introduced in chapter 3, MEE and MME that are modified versions of conventional Molecular Beam Epitaxy (MBE) with modulated beams enhance the mobility of the adatoms. Fig. 9.1 compares MBE with MEE and MME schematically. A few SLs were grown using these techniques (as tabulated in Table 9.1) to investigate how the surface morphology and microstructure of the films are affected. MEE was used for growth on singular InP(111)B, while MME was used for growth on singular InP(111)A substrate. We did a few growths on (111)A surface using MEE, which did not produce good surface morphology. The shutter opening time for group III elements were set to grow 1 Mono-Layer (ML) at each cycle. This was followed by an annealing period Fig. 9.2. Annealing was done after group III deposition to enhance group III adatom migration in the absence (MEE) or presence of a smaller As flux (MME). Annealing after As deposition interrupts the growth.

Sample	Growth method	InGaAs/InAlAs SL period	Substrate	InGaAs/InAlAs Growth rate (Å/s)	Growth Temperature (° C)
I	MBE	20	Singular InP(111)B	1	460
J	MEE	20	Singular InP(111)B	0.5	295
K	MME	5	Singular InP(111)A	1.8	500
L	MME	8	Singular InP(111)A	1	295
M	MBE	InGaAs	Singular InP(111)A	0.5	460
N	MME	InGaAs	Singular InP(111)A	1.8	500

Table 9.1: Summary of the growths.

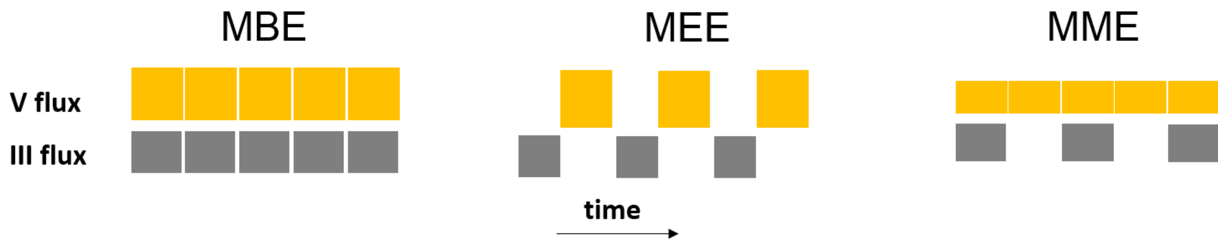

Figure 9.1: A schematic comparison between MBE, MEE and MME.

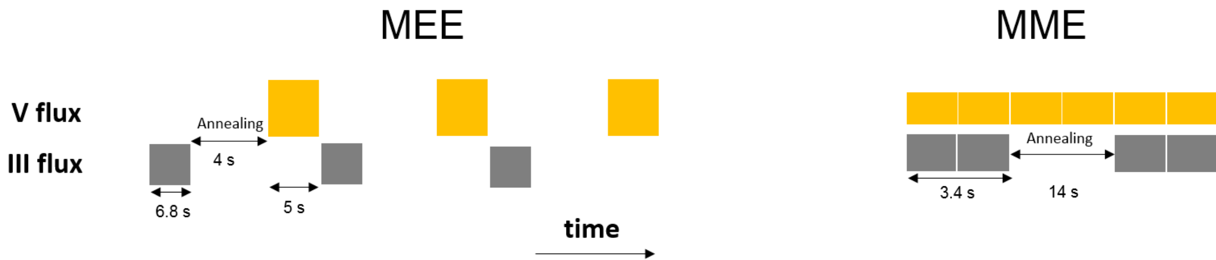

Figure 9.2: A schematic showing the experiment set-up for MEE and MME growths.

9.2 Results and Discussions

Growth on singular (111) substrate using conventional MBE showed clear surface quality degradation according to reflectance monitoring (Fig. 9.3), High Resolution X-Ray Diffraction (HRXRD) (Fig. 9.4) and Atomic Force Microscopy (AFM). HRXRD data and simulated result of sample I is shown in Fig. 9.4, which shows broadening of the peaks due to the presence of defects. The structure is lattice-matched as evidenced by the matching of the substrate and 0th order SL peak. Few growths were done using MEE and MME methods on singular InP(111)B and InP(111)A substrates, respectively, that are discussed in this chapter. Although these techniques seem promising for growth on exact (111) substrates, the growths might need further optimization of the parameters. For this study, we decided to focus more on the conventional MBE since MEE and MME techniques demand numerous shutter opening and closing. For example for a SL of 120 Å InGaAs/80 Å InAlAs each cell shutter opens and closes 60 times per one repeat of the SL, i.e., 6000 times for a SL consisting of 100 repeats. This extensive shutter opening and closing shortens the lifetimes of the cell shutters and adds to the already highly maintenance demanding MBE system.

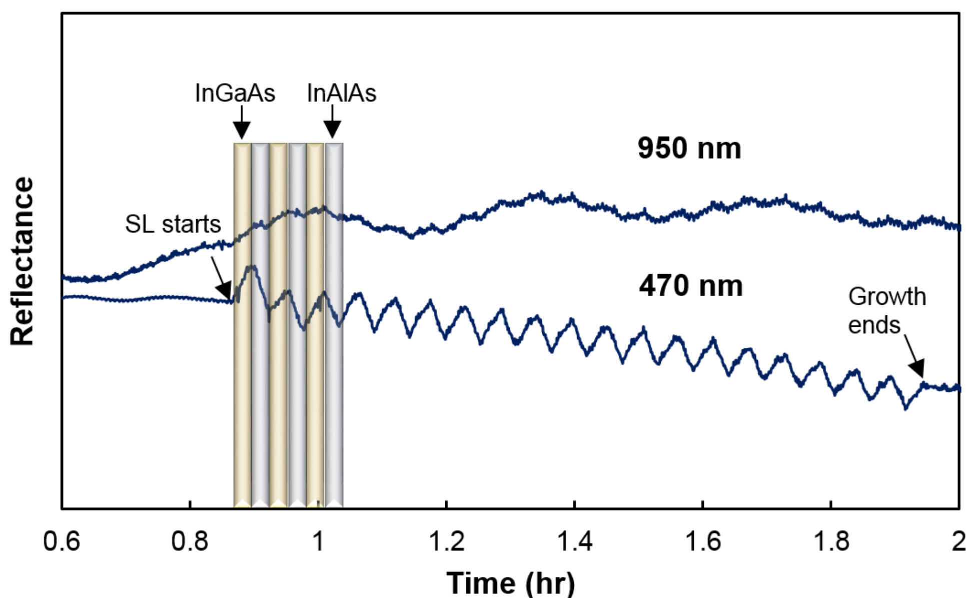

Figure 9.3: 950 nm and 470 nm reflectance monitoring of sample I.

Fig. 9.5 shows the result of reflectance monitoring during the growth of sample J.

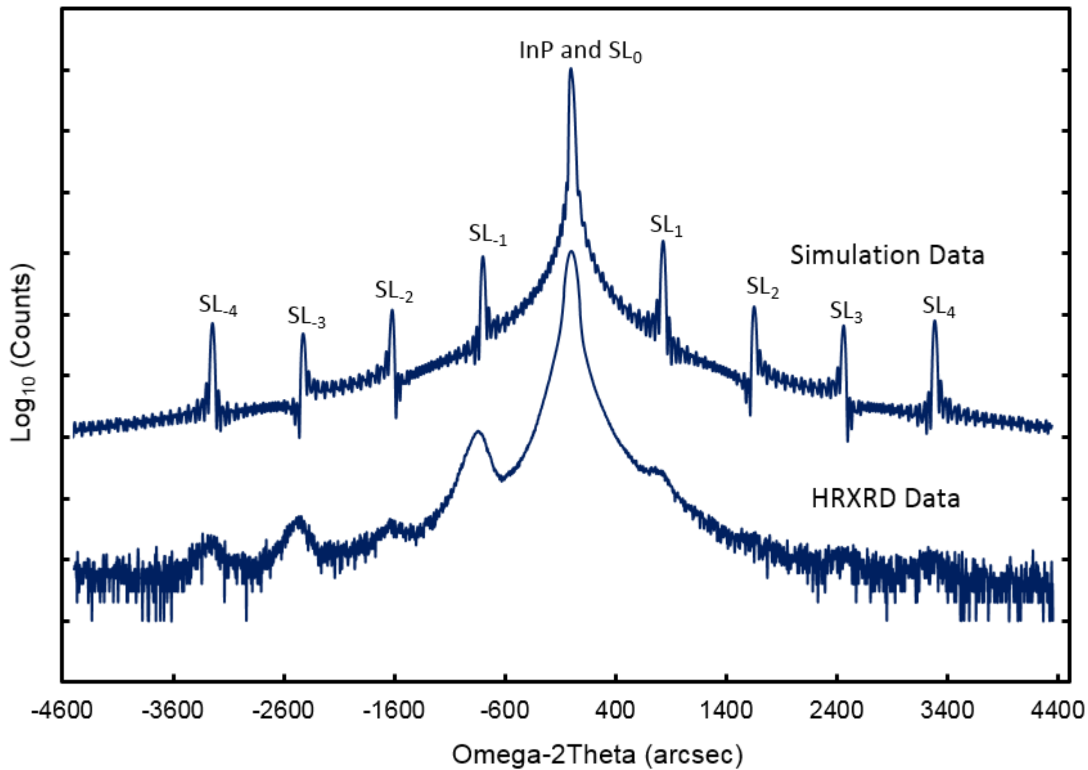

Figure 9.4: HRXRD and simulation data for growth of sample I.

Reflectance at 470 nm shows only a small drop in the signal pertaining to a relatively good epitaxial quality. Figure 9.6.b-d shows the Scanning Transmission Electron Microscopy (STEM) micrographs of sample J. Although large number of stacking faults where observed (Fig. 9.6.d), they did not evolve into V-type twins or surface steps (Fig. 9.6.c). Hence, no hillocks were observed on the surface. This is an indication of an increased migration length during the MEE growth and attachment of the adatoms to the step edges rather than on the terraces. Increased migration length to several orders of magnitude during MEE growth were reported before [82, 158]. For example, Horikoshi and Kawashima reported an increase in the diffusion coefficient for the growth of GaAs by a factor of 20 [38]. Although the surface was atomically smooth with an Root Mean Square (RMS) roughness of 0.90 ± 0.13 Å according to AFM analysis (Fig. 9.6.a), the stacking faults led to a mixed Zinc Blende (ZB) and Wurtzite (W) structure, and hence phase instability. As mentioned before, this is due to the small energy difference between the W and ZB phases in the [111] growth direction [213]. This suggest that the meta-stable

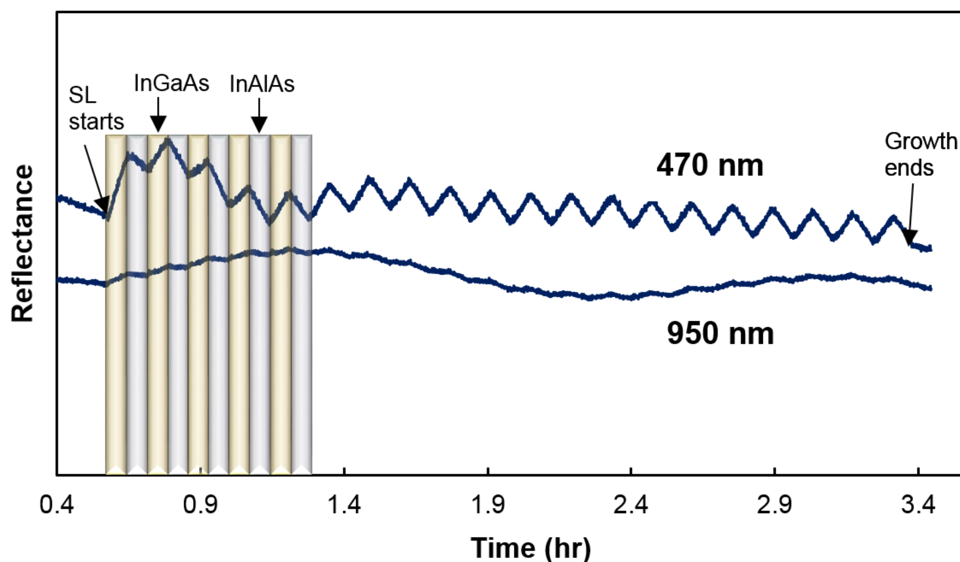

Figure 9.5: 950 nm and 470 nm reflectance monitoring of sample J.

W phase may be more stable at lower growth temperatures. We did not observe any dislocation within the structure. The overpressure was measured at 1.3 during the MEE growth. The Electron Energy Loss Spectroscopy (EELS) study of the interface between the InAlAs and the InP substrate showed the formation of a rich non-stoichiometric As layer, which could be due to the lower growth temperature used and adsorption of As to the surface even in the absence of available group III atom dangling bond (Fig. 9.6.b).

Figure 9.7 shows the reflectance monitoring result of Sample K and L. Clear drop in the 470 nm reflectance from sample L (Fig. 9.7.b) shows the degradation of the growth quality. Figure 9.8 shows the Reflection High Energy Electron Diffraction (RHEED) monitoring result of Sample K and L. It is seen that RHEED pattern of sample L is becoming spotty showing that the surface is developing three-dimensional features. The AFM analysis on sample K showed the presence of the so-called "wedding cakes" on the surface (Fig. 9.9). Figure 9.10 shows the STEM micrographs as well as AFM images of Sample L. Numerous stacking faults and twins were seen. The interfaces between the SL layers are very wavy resulting in a rough surface morphology. Comparison between sample K and L shows the effect of growth temperature for growth on (111)A surface. It seems that a higher growth temperature is preferred on this substrate. Such a temperature dependent growth quality on (111)A surface could be attributed to the surface reconstruction change by changing the temperature as was evidenced by Low energy electron diffraction (LEED) analysis

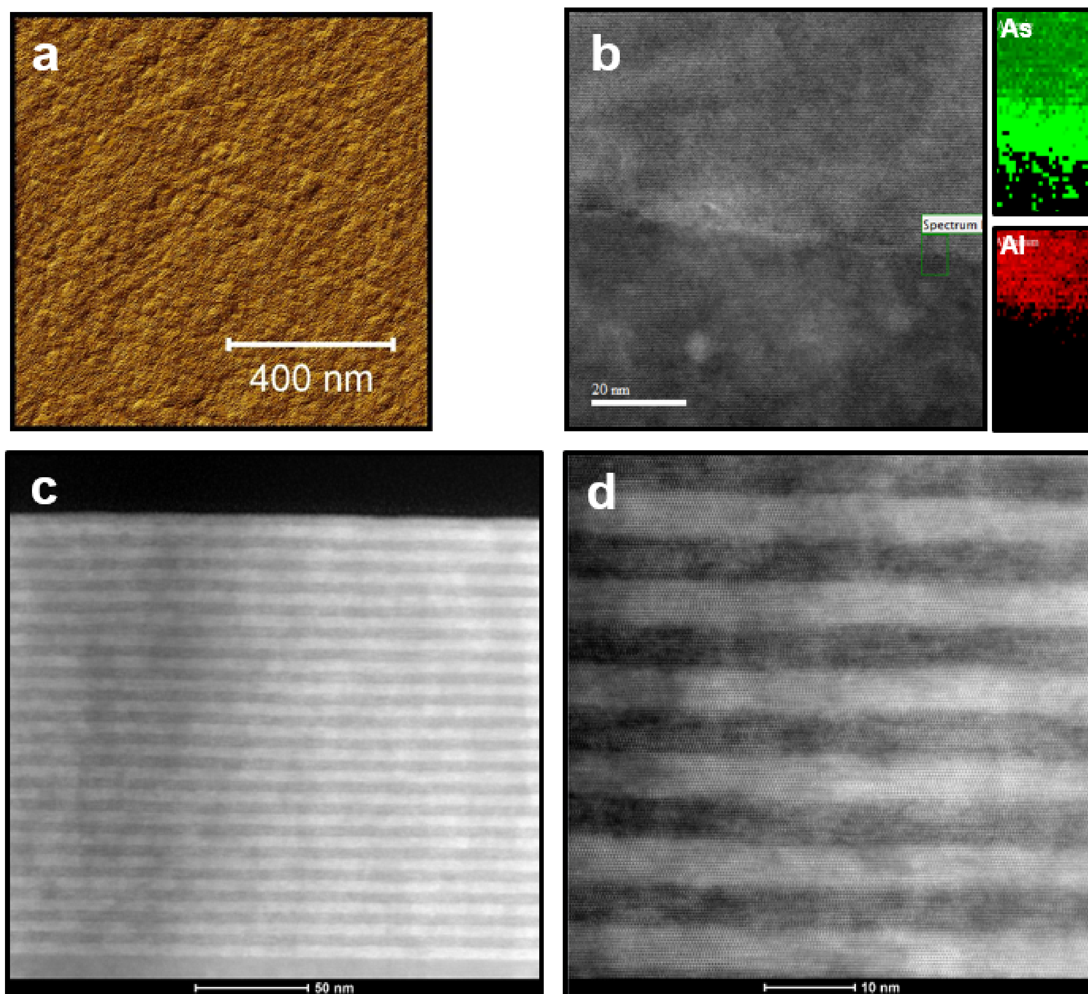

Figure 9.6: a)1 μm^2AFM scan of sample J showing an RMS roughness of 0.90 ± 0.13 Å, b) EELS maps at the interface c) low magnification STEM micrograph showing no hillock on the surface and d) higher magnification STEM micrograph showing the presence of numerous stacking faults resulted in phase instability between ZB and Wphases.

and discussed in Chapter 6 and a strong dependence of the growth quality on the surface reconstruction. Although MME on InP(111)A improved the surface as was evidenced by RHEED during the growth of InGaAs layer (Fig. 9.11), growth of SL using MME still needs further optimization. One reason for the observed growth quality improvement when using MME technique may be the supply of additional In atoms to compensate for the In-vacant (2 × 2) surface of InP(111)A.

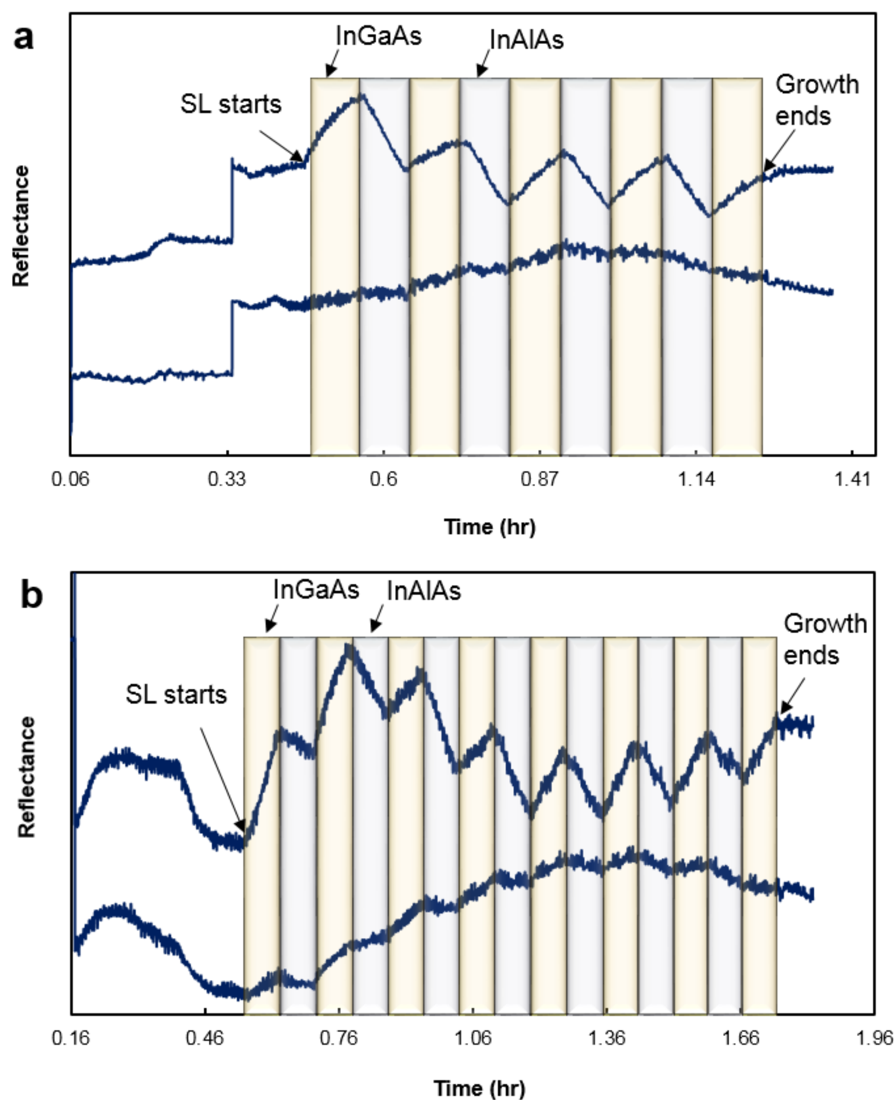

Figure 9.7: 950 nm and 470 nm reflectance monitoring of sample a) K and b) L.

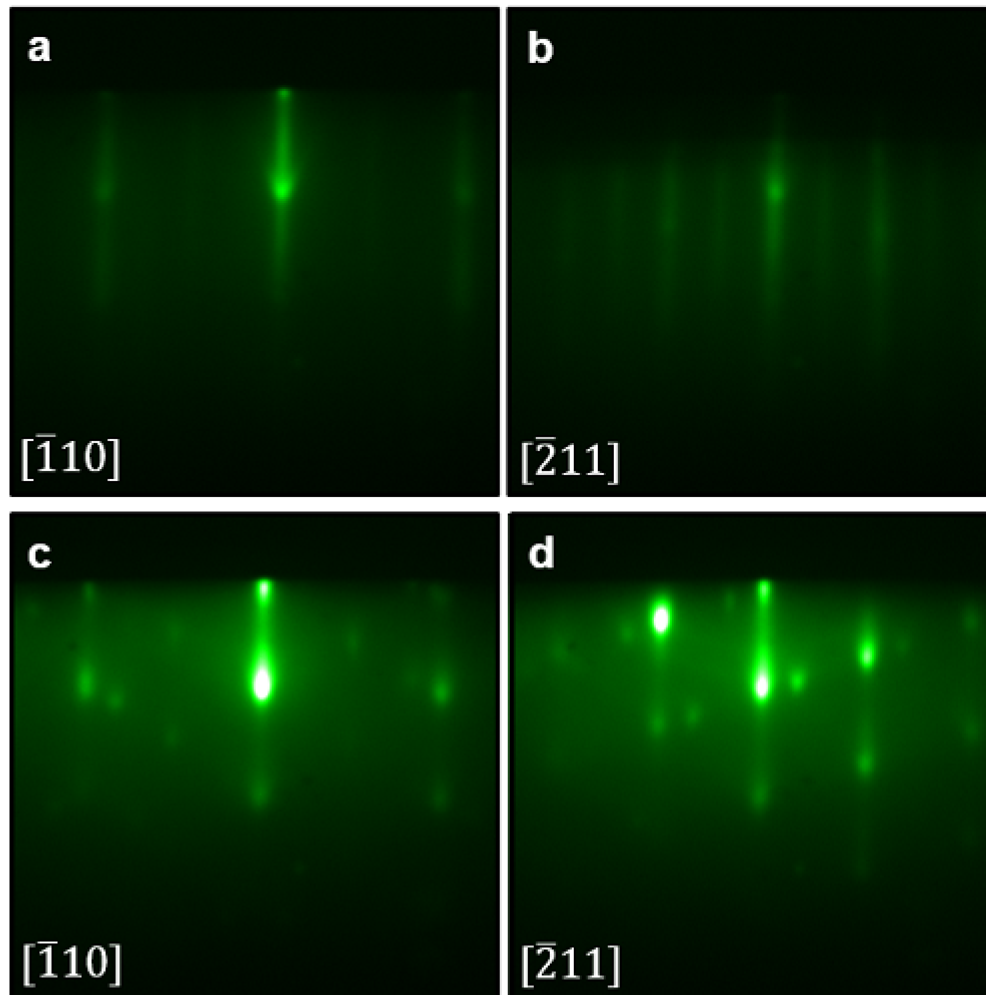

Figure 9.8: RHEED pattern of sample a-b) sample K and c-d) sample L at the high symmetry azimuths.

9.3 Summary

- Growth on exact (111) surfaces has proven to result in surface steps and morphology degradation. Use of misoriented substrates was shown to be a way to improve the surface morphology since vicinal surfaces are effective in promoting the step-flow growth mode. This was shown in Chapters 5,6 and 8. However, there are certain limitations for using this technique for growth of InAlAs since it requires

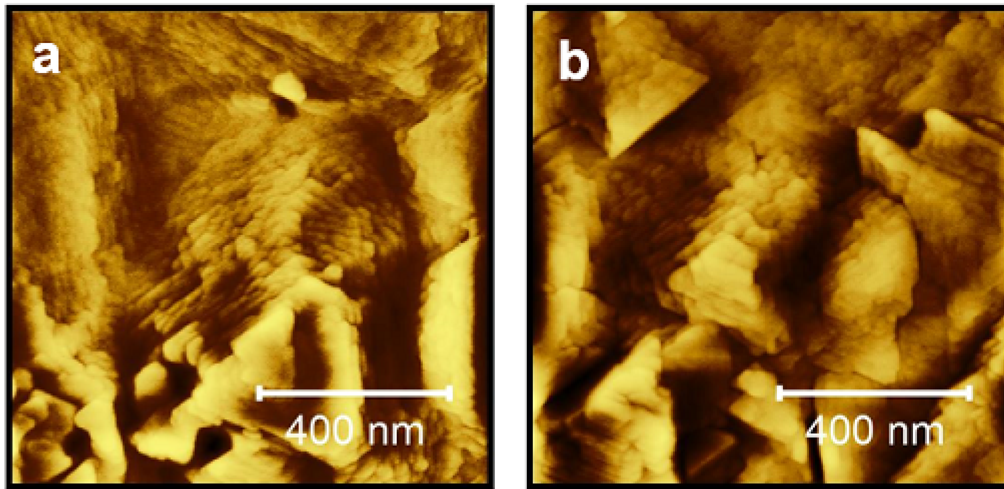

Figure 9.9: AFM images of sample K at the a) center with an RMS roughness of 2.0 ± 1.2 nm and b) edge of the wafer with an RMS roughness of 2.65 ± 1nm. The wedding cake in a) is about 6 nm tall and those in b) are in average about 7 nm tall.

extremely slow growth rate of 0.06 Å/s as was shown in Chapter 8. Such a slow growth rate and prolonged growth time could increase the chance of other MBE growth related problems such as instability in the fluxes. In addition, for growth at lower temperatures, even slower growth rates (slower than 0.06 Å/s) will be required using conventional MBE. Hence, there might be a need for another techniques in such cases.

- MEE and MME methods are promising techniques to grow epitxial InGaAs/InAlAs SL on singular InP(111)B and InP(111)A substrates, respectively. They were shown to produce abrupt interfaces [36–39]. These techniques are also effective in increasing the migration length in order for the step-flow growth to happen. They do so by minimizing the amount of As on the surface that will bind to the cations. Here we showed that these techniques are promising to improve the surface morphology when growth is done on exactly (111) surfaces. Microstructural analysis only showed the presence of stacking faults when MEE was used on InP(111)B substrate.

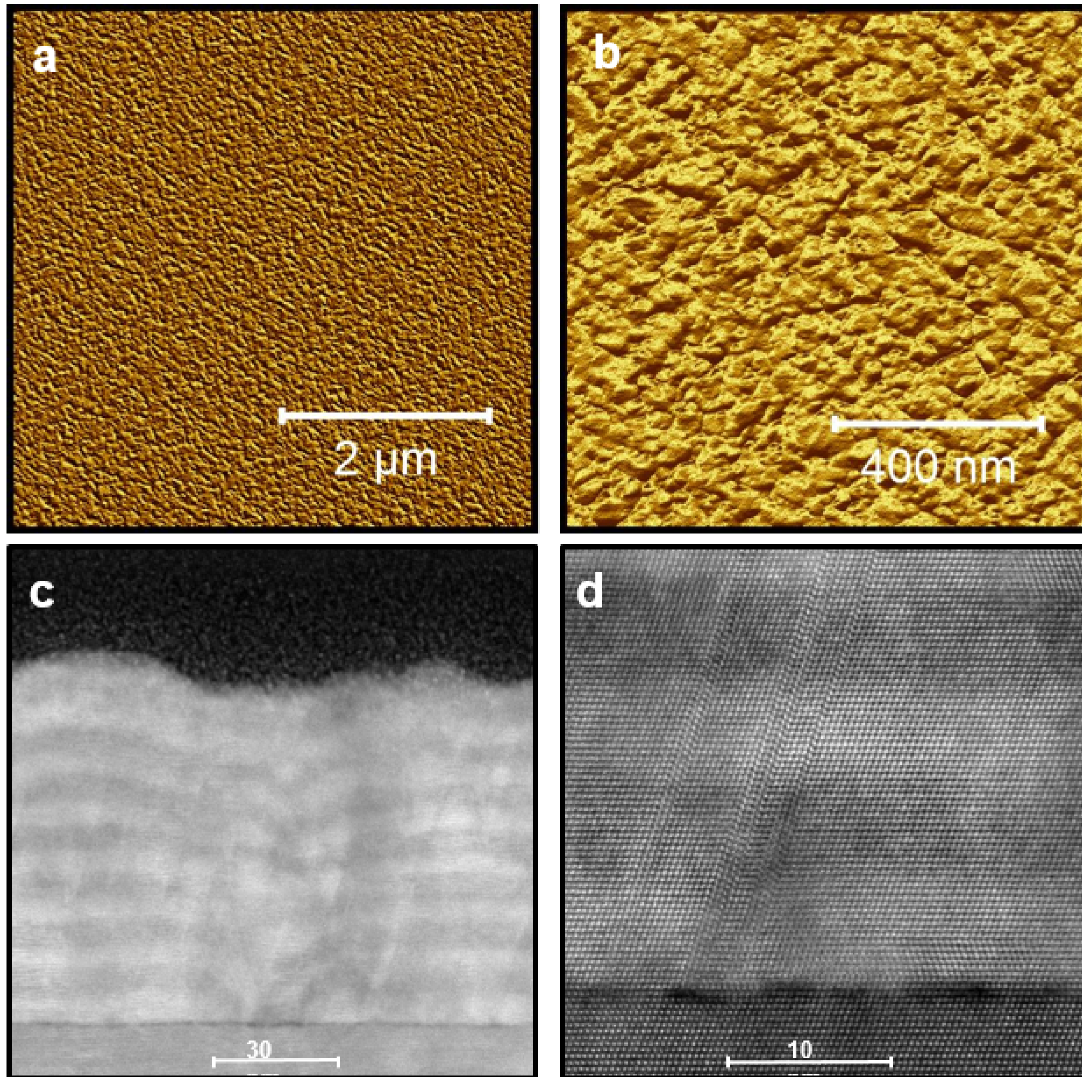

Figure 9.10: a-b) AFM and c-d) STEM images of sample L showing the presence of morphological and microstructural defects. The RMS roughness measured on a) and b) is 2.97 nm.

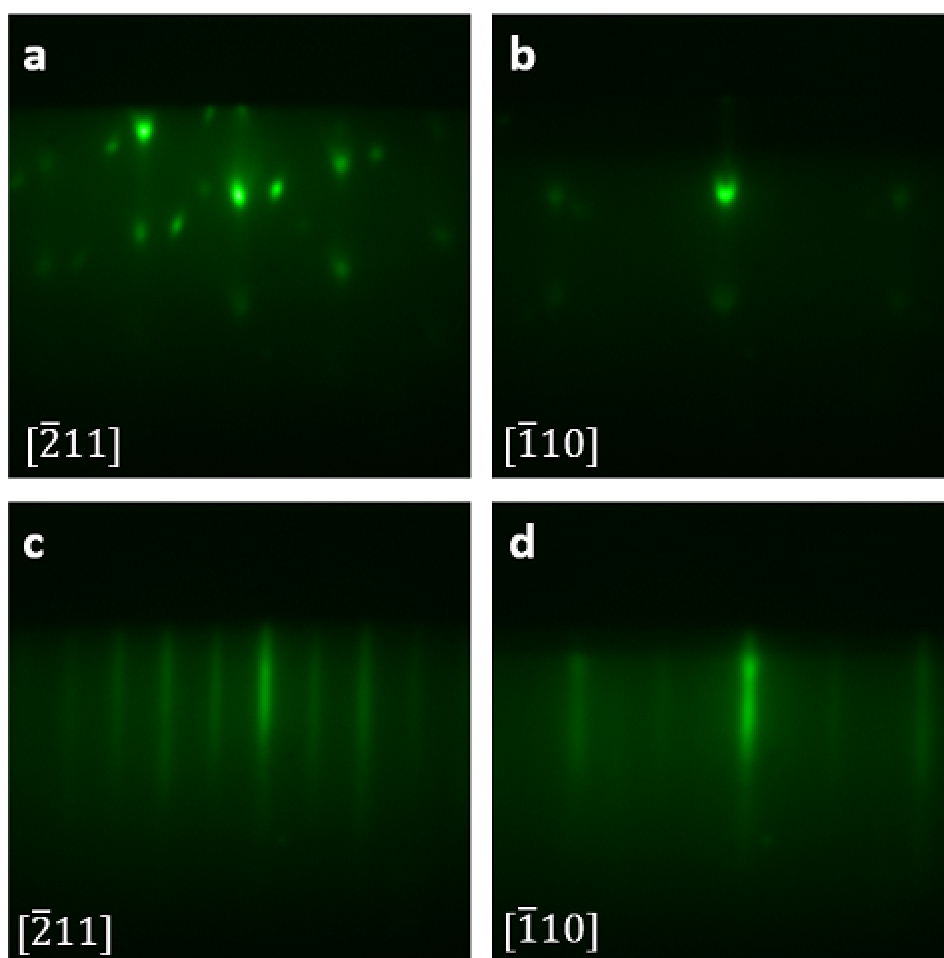

Figure 9.11: RHEED pattern at high symmetry azimuths of sample a-b) sample M and c-d) sample N.

Chapter 10

Defect analysis in InGaAs-InAlAs superlattices

10.1 Experiment

Gowth of InGaAs/InAlAs SuperLattice (SL) was done for 95 periods using conventional Molecular Beam Epitaxy (MBE) on InP(111)B substrate.

10.2 Results and Discussion

Fig. 10.1 shows the result of reflectance monitoring during the growth of sample H. As mentioned earlier, reflectance at 470nm is very sensitive to epitaxial growth quality. Here it shows a gradual drop in the signal. The drop in the reflectance intensity could be a result of progressive surface roughening or partial relaxation due to lattice mismatch between the SL and substrate. The effect of strain on the morphology and microstructure was investigated. The High Resolution X-Ray Diffraction (HRXRD) scan on sample H is shown in Fig. 10.2. The separation between the substrate and SL 0th order peaks confirms the presence of lattice mismatch and that the structure is compressively strained. This was the result of unintentional flux drift. The broadening of the SL peaks indicated degraded crystallographic quality of the structure. Correspondingly, the surface morphology degraded and showed roughening as evidenced by Nomarski images shown in Fig. 10.3. It should be mentioned that the controllability of the film composition and thickness

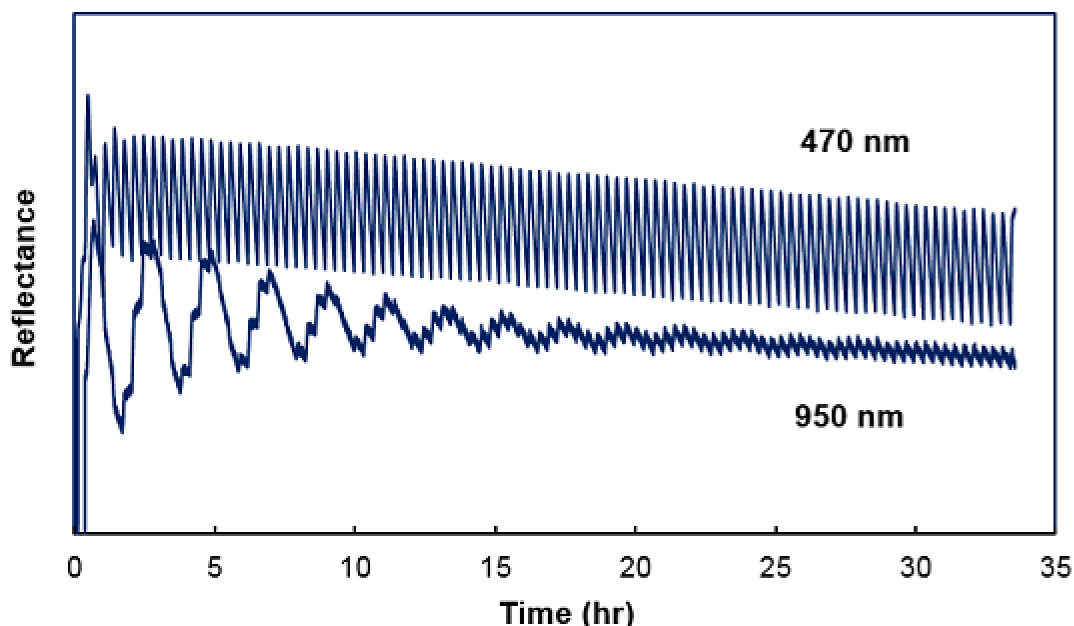

Figure 10.1: 950 nm and 470 nm reflectance monitoring of sample H.

depends critically on the reproducability of the effective surface temperature of the group III melts in the effusion cells. Even when the thermocouple temperature is precisely controlled, the effective cell temperature may vary and may cause flux variations because a number of factors that determine the thermal environment of the cells change over the time. For example, the open and close operation of a shutter changes the radiative heat loss from the cell and causes an appreciable time variation of flux [158].

Figure 10.4 shows the Atomic Force Microscopy (AFM) images of sample H. Although the surface is atomically smooth at small lateral scale with visible atomic steps and terraces with an Root Mean Square (RMS) roughness of 2.29 ± 0.5 Å (Fig. 10.4.d), larger scale scan revealed the presence of some triangular features on the surface (Fig. 10.4.c) increasing the RMS roughness to 4.53 ± 1.11 Å on a $2\mu m^2$ scan.

The large Field of View (FOV) Scanning Transmission Electron Microscopy (STEM) micrograph in Fig. 10.5.a shows that the growth is mostly perturbed by crystal defects in both the SL and the buffer layer. Similar defects based on their contrast variation are grouped into families and shown by the same color arrows in Fig. 10.5.d-f. The blue arrow highlights the disturbed interface between the InP and the buffer layer. The red arrows focus on the perturbations in the buffer layer showing a contrast change. Yellow arrows

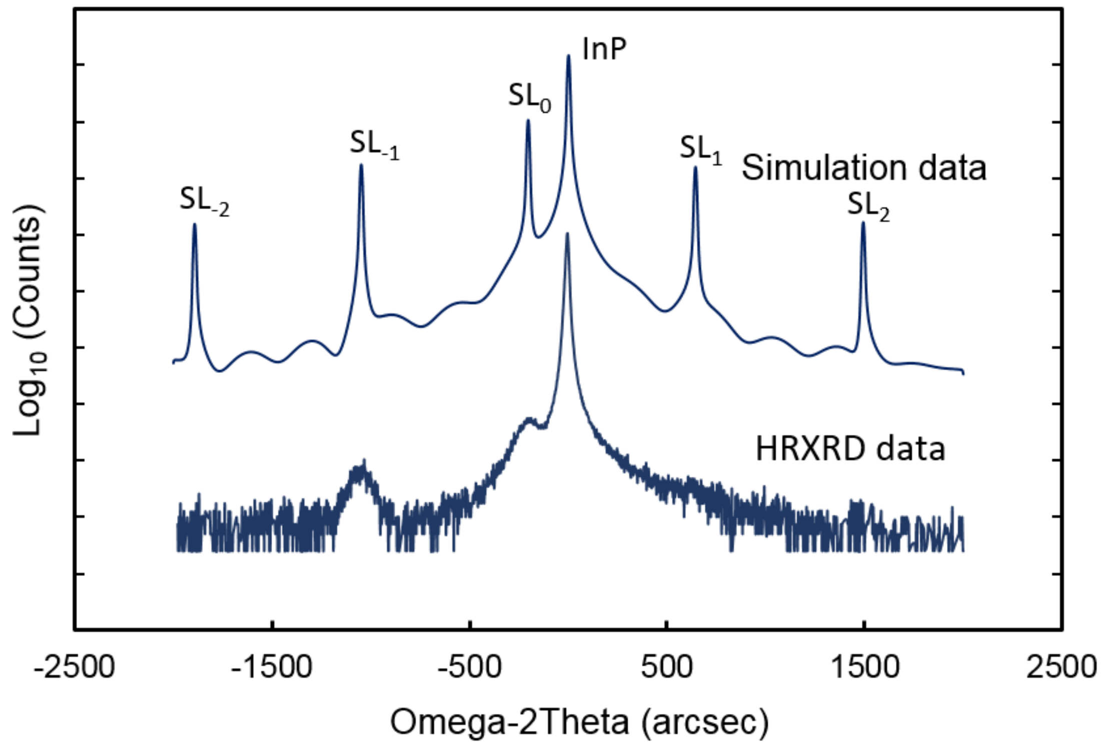

Figure 10.2: HRXRD data and simulation result of sample H.

point to the sharp white lines aligned along the [112] direction. The orange arrows mark the faint lines aligned along the [110] direction. The purple features point to the extended change of contrast indicating a change in composition (Z contrast). Nonetheless, high-quality epitaxial growth was achieved between these aforementioned perturbations as seen in Fig. 10.5.b-c.

As it was observed in Fig. 8.7 for sample G, the interface between the InP and the buffer layer is not smooth likely due to the incomplete oxide desorption forcing a lattice accommodation in the buffer layer. Misfit dislocations are expected at the interface between the buffer and the substrate if the strain is relaxed. Fig. 10.6 shows the miscrostructure of the buffer layer and the interface between the InP substrate and the buffer. Different types of defects are highlighted in Fig. 10.6.a by different color arrows as mentioned above. The misfit dislocations were not directly observed at the InP and buffer layer interface (Fig. 10.6.a,f), however, numerous stacking faults were noticed right above the InP interface. The dissociation of [110] misfit dislocations into [112] partial dislocations associated with stacking faults is known to happen in diamond crystal

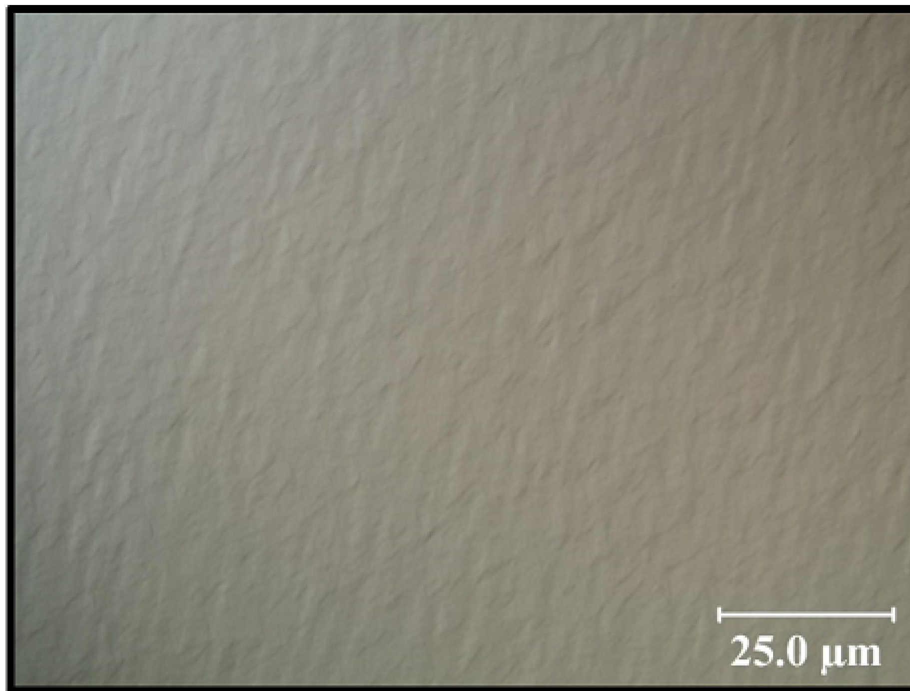

Figure 10.3: Nomarski image of the sample H.

structure [162, 227, 228]. The Burgers circuit in Fig. 10.6.c crossing the stacking fault highlights a Burger vector aligned along the $[\bar{2}11]$ direction and correspond to a 30° Shockley partial dislocation. Such defects can be related to the [110] misfit dislocation dissociation, therefore, it can be linked to the strain relaxation at the buffer layer.

Interestingly the stacking fault formation is not abrupt as seen in Fig 10.6.b. Transition from the proper crystal periodicity to the stacking fault is made through 9 atomic planes in this image. Intrinsic stacking fault (formed by removal of an atomic plane) as shown in Fig. 10.6.d is a typical defect in diamond crystal structure. Extrinsic stacking faults which are addition of extra atomic planes are not probable since their formation involves more bond breaking and rotation in the crystal. The defect above the stacking fault corresponding to the perturbation pointed by the orange arrow (digitally magnified in Fig. 10.6.e) will be addressed later in Fig. 10.7. In addition to the stacking faults, twin defects were also observed as shown in Fig. 10.6.f. The twin defect and associated stacking fault are digitally magnified in Fig. 10.6.g. The formation of a twin defect can also be expected from the [110] misfit dislocation in diamond crystal structure [162]. Fig. 10.6.h shows a large density of stacking faults in the surrounding of the twin boundary and just above

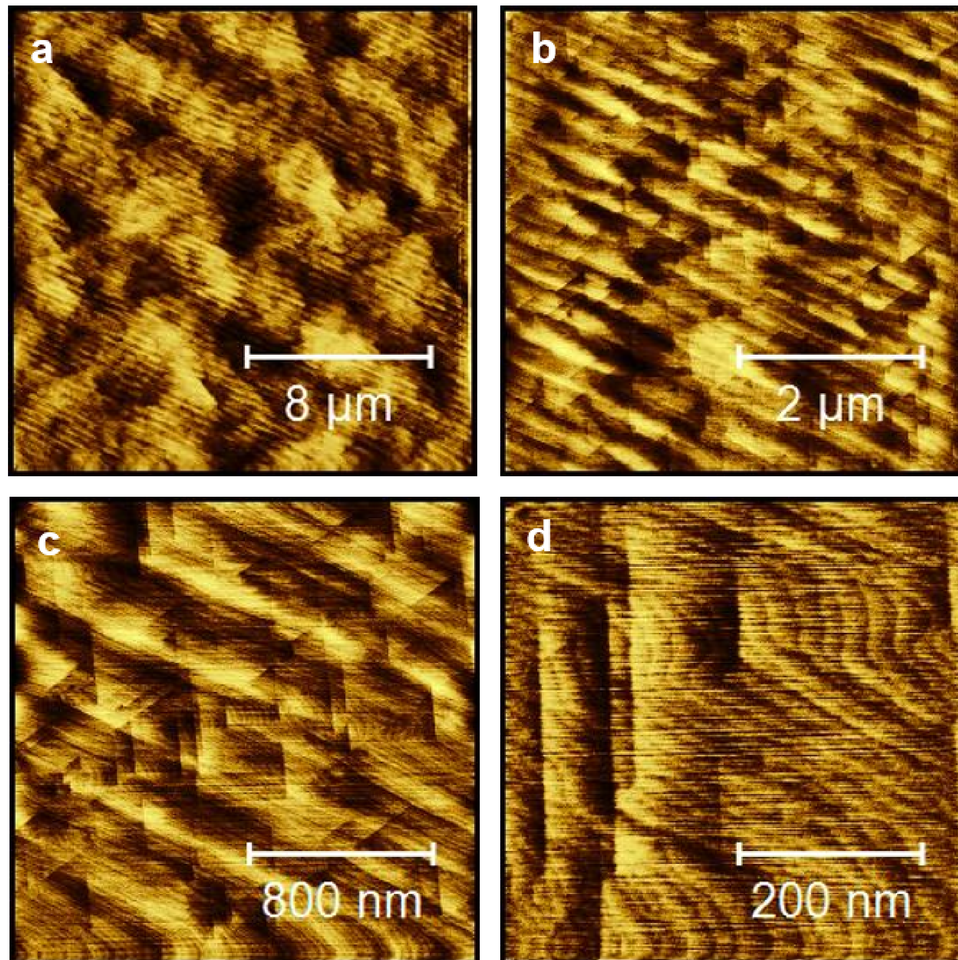

Figure 10.4: AFM height images of sample H showing a) an over view of the surface (RMS roughness=1.63 ± 0.32 nm), b) 5 μm^2 (RMS roughness=7.18 ± 1.53 Å) and c) 2 μm^2 (RMS roughness=4.53 ± 1.11 Å) scans showing surface triangle features and d) smooth surface morphology in between of the triangle features (RMS=2.29 ± 0.5 Å).

the substrate buffer layer interface. These defects may be a result of an incomplete oxide desorption and resulting localized problems with proper epitaxial growth. These large number of stacking faults correspond to the contrast change pointed by red arrow in Fig. 10.6.d. Above the red arrows the density of stacking faults is reduced.

The presence of defects is not limited to the buffer layer. The defects pointed in yellow, orange and purple are also present in the SL. Fig. 10.7 shows some examples.

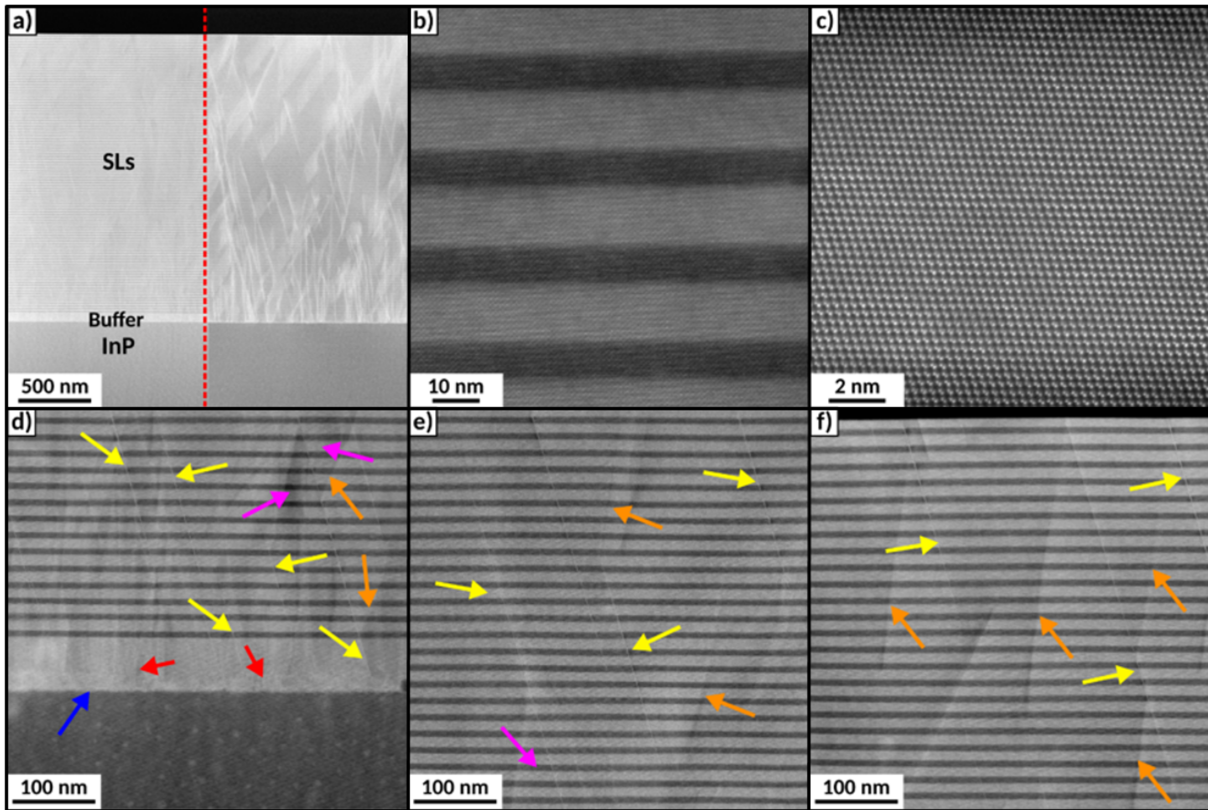

Figure 10.5: STEM micrographs of sample H at different magnifications: a) low magnification HAADF (left) and diffraction contrast (right) images providing a general overview of the entire growth, b,c) high magnification resolving the crystalline lattices in the SL and d-f) intermediate magnification from the bottom to the top of the stack focusing on the defects' distribution. The left and right images in a) are recorded on the same area with a low Z contrast and a high diffraction contrast camera length, respectively.

The Burgers circuit in Fig. 10.7.a crossing a stacking fault reveals a Burgers vector of a/6 [112] and corresponds to the same family of possible [110] dislocation dissociation. As observed in Fig. 10.6.b, the formation of stacking faults is not abrupt.

An interesting atomic arrangement is observed near the stacking faults in Fig. 10.7.a pointed by orange arrow and is digitally magnified in Fig. 10.7.d. The contrast variation suggests a rotation of the crystal about the [110] axis and the crystal seems to propagate along the same [110] direction. The crystal within this region is rotating along the [110] axis from bottom to top in a revolving way resulting in the presence of rotation variant

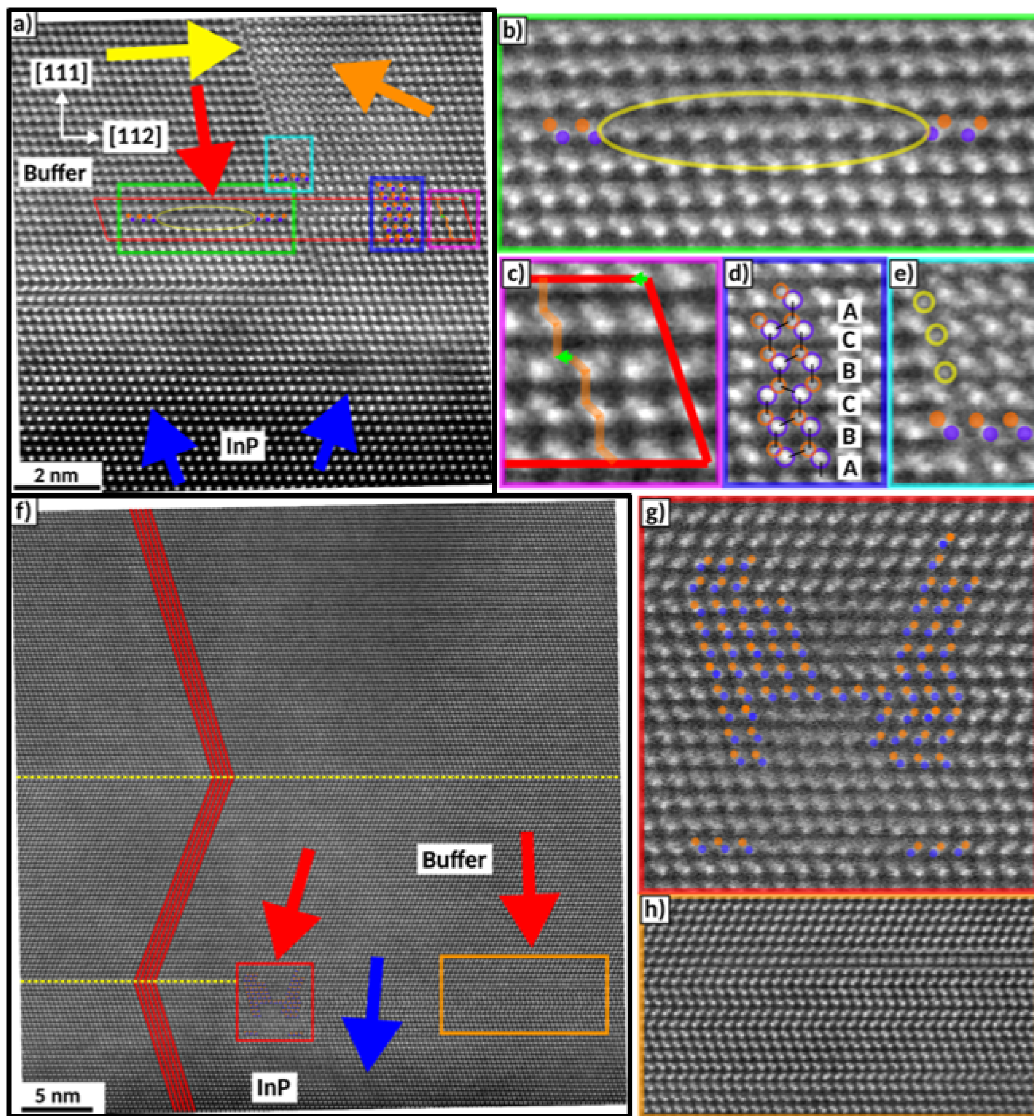

Figure 10.6: Visualization of the defects observed in the buffer layer of sample H. The arrows refer to the families of perturbations mentioned in Fig. 10.5. a) HRSTEM electron micrograph centered on multiple defects in the buffer layer and near the interface with the InP substrate. b-d) digitally magnified version of a) showing a stacking fault defect with the associated Burgers vector along the [112] direction. e) Inset of a) highlighting crystal rotation showed by orange arrow. f) HRSTEM micrograph on the buffer layer highlighting a twin defect. g-h) digitally magnified version of f) focused on the twin and the stacking faults defects.

crystalline regions. Figure 10.8 represents a projection of such crystal rotation. Presence of nuclei of rotation variant growth could be attributed to the strain due to the lattice mismatch between the epilayers and the substrate that is exacerbated by the strain at the InP interface due to an incomplete oxide desorption. The rotation likely reduces the lattice the strain for growth. This is similar to the defect pointed by orange arrow in Fig. 10.6.a in which the same rotation about the [110] axis is observed in that area.

The contrast variation pointed out by purple arrows as in Fig. 10.7.e, shows a change in composition as demonstrated by EELS chemical maps (Fig. 10.7.f-i). The white sharp line along the [112] direction is related to an In rich and Al poor region in the InAlAs layer and a Ga poor region in the InGaAs layer. The dark shadow to the right of the white line in Fig. 10.7.e is related to an In poor region rich in Ga or Al in the InGaAs or InAlAs layers, respectively. This shows that phase separation or chemical ordering is another mechanism to relieve the strain within the growing layers. Misfit strain was shown to produce morphological instabilities and surface corrugations. The morphological instability is induced by the presence of coherency strain in the lattice in the presence of stress. The coherency strain is the result of a growing lattice-mismatched epilayer following the adatom registry of the substrate. As a result of this strain, the surface becomes sinusoidally perturbed allowing the strain to be relaxed at for example the crests and increased for the same magnitude at the troughs. Hence, there will be a strain gradient on the surface driving the diffusion from a highly strained troughs to the crests increasing the amplitude of the perturbance. This destablizing diffusion is balanced by a diffusion in the opposite direction from the crests to the troughs due to the interfacial energy, which reduces the perturbance amplitude [150, 151]. Such corrugations impose a change of lattice spacing at the troughs and crests promoting a preferential attachment of larger atoms at the areas with larger lattice spacing and vice versa, which leads to a compositional modulation [135]. For example, in the case of a compressively strained layers the strain relaxation leads to an increased lattice spacing at the crests and a decreased lattice spacing at the troughs. Hence, larger atoms are attracted to the crests and smaller atoms are attracted to the troughs. Alternative compressively and tensily strained regions were seen in the strain map (vertical red and blue lines in the ϵ_{xx} map) (Fig. 10.9.b). This could be potentially related to such undulation in a smaller scale originated from the local difference in the chemical composition. Rounded features at the interface between the buffer layer and the SL seen in the STEM Moiré GPA (SMG) map in Fig. 10.9 could be related to the perturbed interface due to the oxide desorption in the presence of As overpressure. We postulated that the early issues with proper layer nucleation on the substrate created strains in the layer and generated defects related to substantial lattice mismatch.

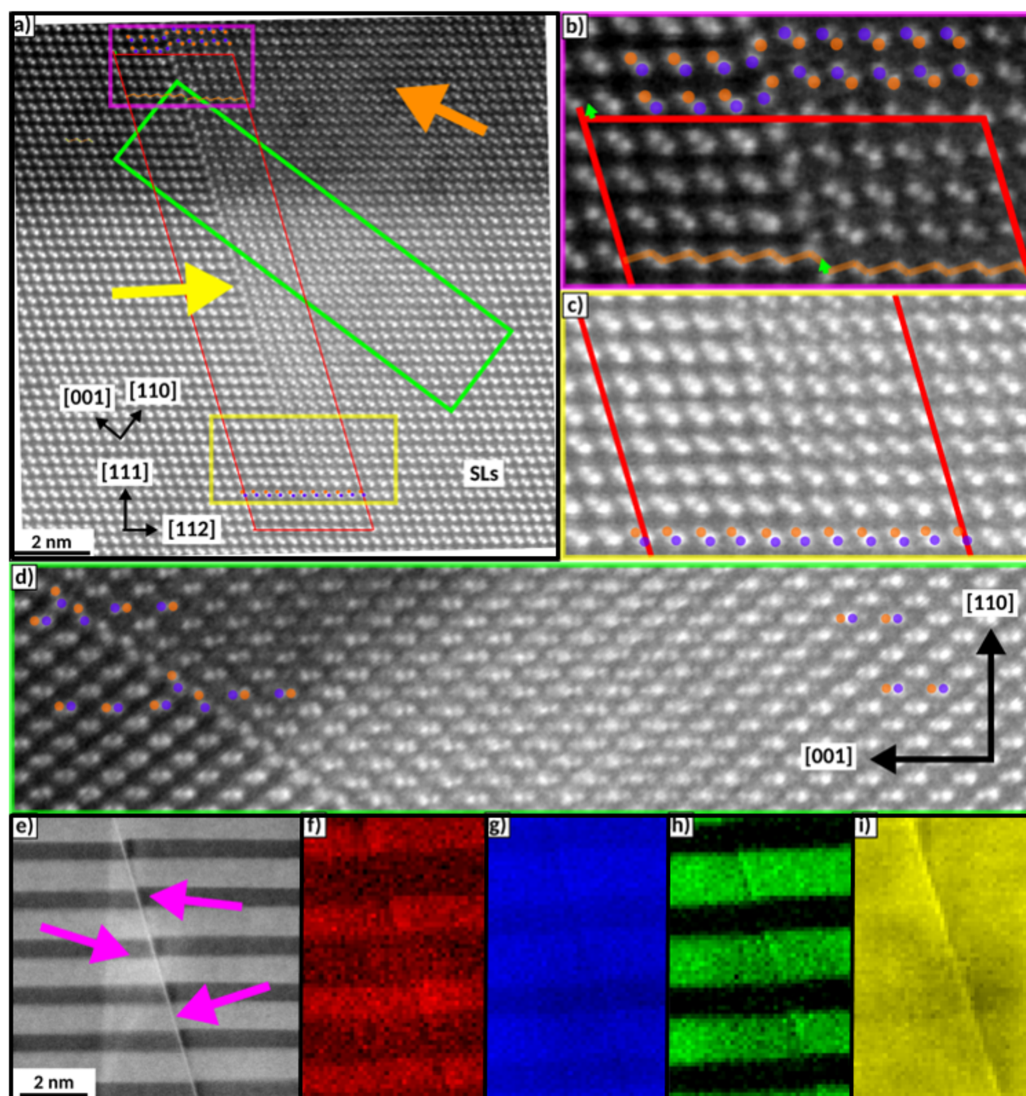

Figure 10.7: High magnification STEM images of sample H focusing on different defects pointed out by different color arrows within the SL. a) HRSTEM micrograph in the SL capturing the defects pointed by yellow and orange arrows. b,c) insets from a) showing a stacking fault along the [112] direction. d) inset of a) focused on the crystal rotation near the stacking fault that is propagating along the [110] direction. e) STEM micrograph centered on the defect highlighted by the magenta arrows showing a region of phase separation. f-i) EELS chemical maps from the Al K edge, the As L2,3 edge, the Ga L2,3 and the In M4,5 edge respectively on the defect pointed in e).

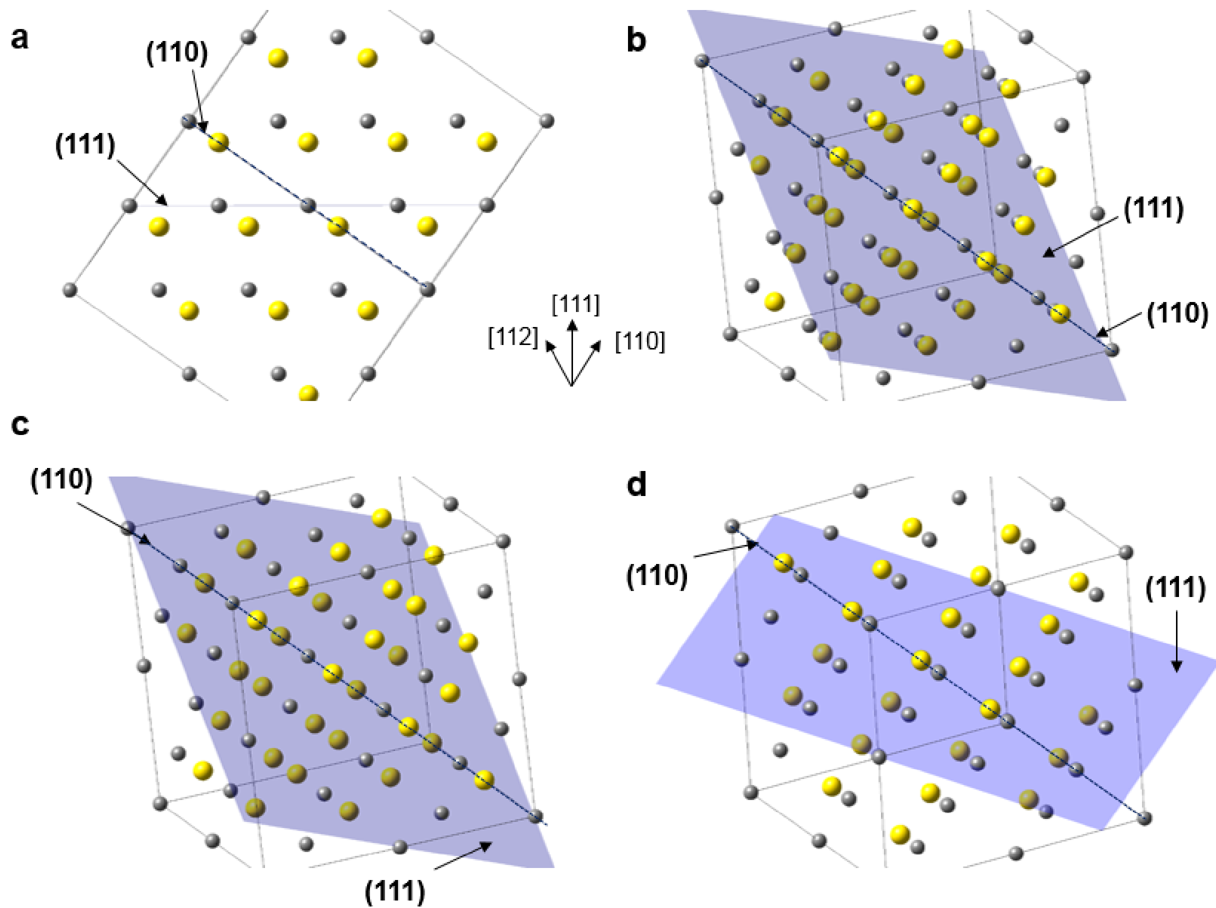

Figure 10.8: Representation of rotational variant nuclei seen in Fig. 10.7.d. The side view of the rotating crystal structures viewed in orthographic projection. The (111) plane showed and marked in purple. The (110) plane is showed by royal blue dashed line. a) unrotated crystal showing the alignment and stack of dumbbells within the crystal along the [111] growth direction, b-d) crystal being rotated along the [110] axis.

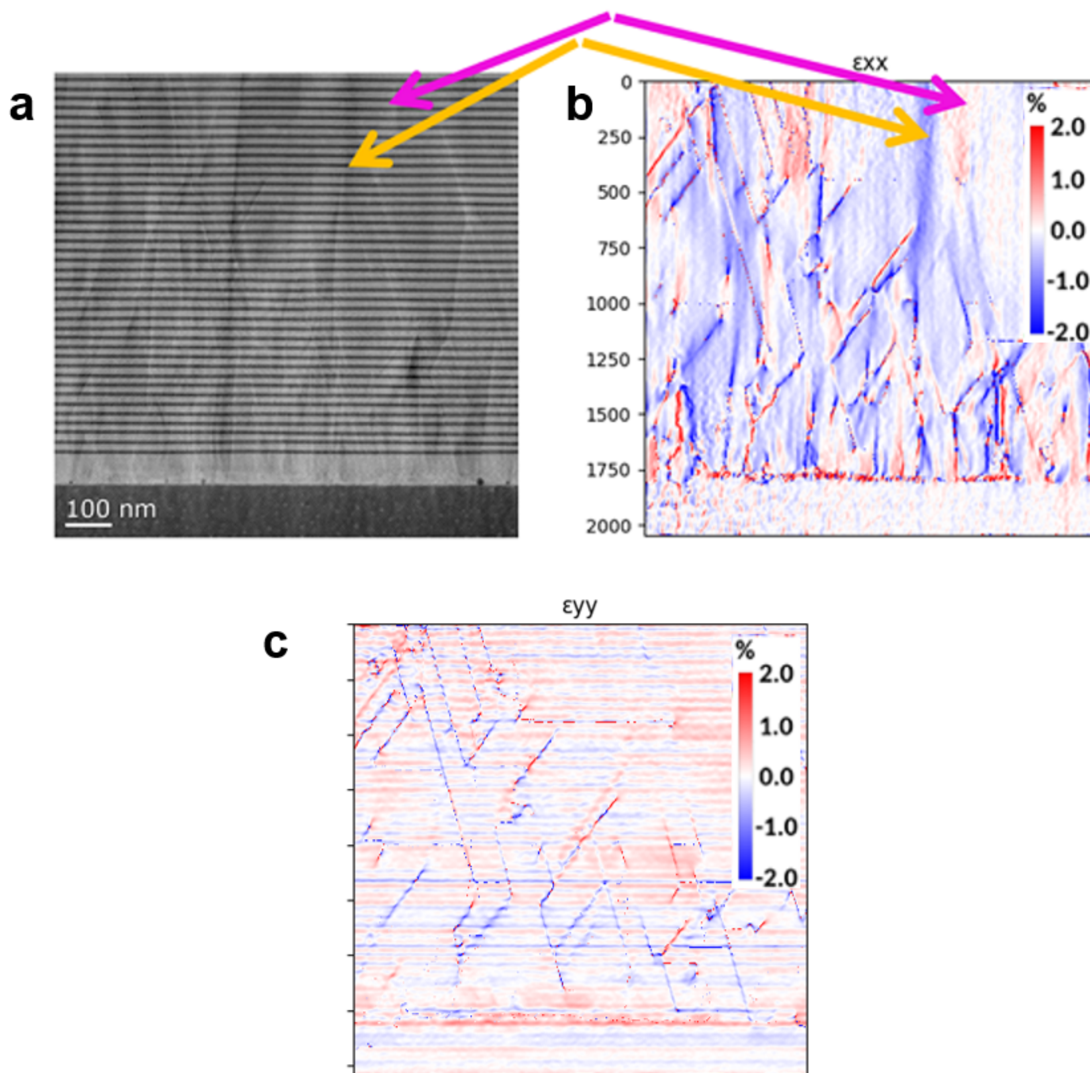

Figure 10.9: a) STEM HAADF image of the sample H. b) ϵ_{xx} strain map showing alternative regions of compressively and tensily strained (yellow and purple arrows). c) ϵ_{yy} showing the presence of alternate compressively and tensily strained epilayers. Any change of contrast shows the presence of defect in the microsctructure.

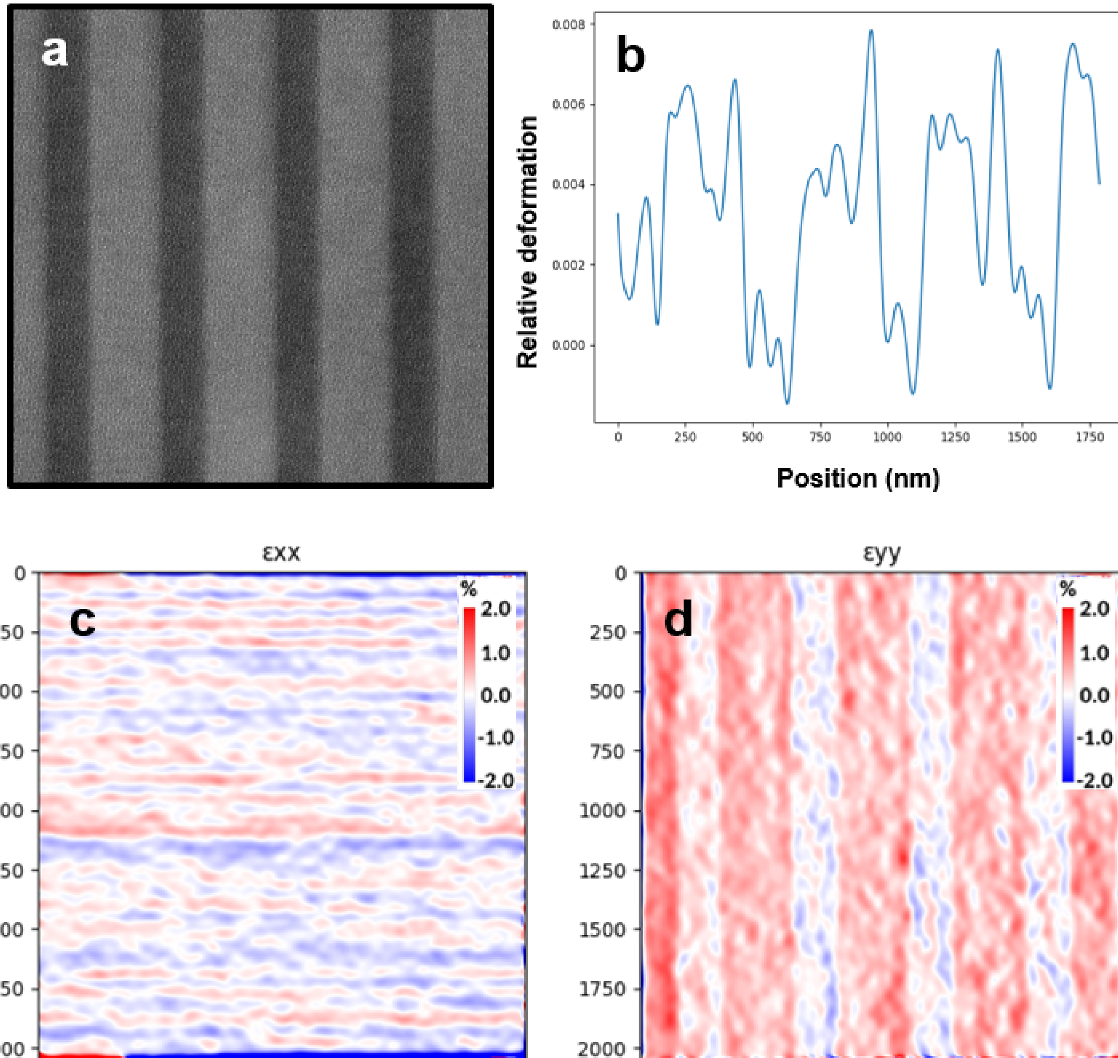

Figure 10.10: STEM HAADF image of of sample H from a clean area. b) ϵ_{yy} deformation profile showing the presence of strain along the growth direction in the InGaAs layer, while InAlAs layers are almost unstrained. c) ϵ_{xx} and d) ϵ_{yy} SMG relative deformation maps. InAlAs layer was taken as the reference, therefore, the relative deformation is around 0 within this layer.

Fig. 10.10 shows the strain maps of sample H. The ϵ_{yy} relative deformation line profile in Fig. 10.10.b shows in general a positive strain within the InGaAs (the layer is compressively strained in-plane and tensily strained along the growth direction) leading to a tetragonal distortion and consequently separation of 0th order SL peak from substrate peak as was seen in Fig. 10.2. This shows that the InGaAs layers have a larger lattice constant than the InP substrate, therefore, are richer in In. The layers seem to be partially relaxed with some strain left within the structure since the ϵ_{xx} and ϵ_{yy} maps are not showing the same contrast that is a sign of presence of strain ($\epsilon_{xx} \neq \epsilon_{yy}$) and there are dislocation presents in the microstructure that is a sign of relaxation. The lattice mismatched is accommodated by the ϵ_{xx} in plane of the growth, while Compositional Modulation (CM) is seen along the growth direction that could have been induced by strain.

10.3 Summary

In summary, we showed that:

- Growth of thick lattice mismatched layers result in the introduction of defects in the epilayers to relive the strain. The stress-relief mechanism was shown to be :
  - Misfit dislocation formation that are dissociated into stacking faults (planar defects) bounded by partial dislocations (line defects),
  - Phase separated regions consisting of regions of rich in In and poor in Ga or Al in InGaAs or InAlAs layers, respectively, adjacent to regions of poor in In and rich in Ga or Al,
  - Rotation of the crystal to lower the mismatch between the epilayer and the substrate.
- The formation of a large number of such defects is additionally exacerbated by the structural imperfection at the starting InP surface after the oxide desorption process. This emphasizes the importance of the oxide desorption process on the quality of the layers grown.

Chapter 11

Summary and Conclusions

In summary, we achieved growth of atomically smooth InGaAs/InAlAs on InP(111)B substrate by molecular beam epitaxy. This was the first step to further engineer the structure through addition of dopants, strain and composition to make the structure suitable for Terahertz (THz) Time Domain Spectroscopy (TDS) system.

We did a systematic optimization process for growth on InP(111) substrate. We first grew on rounded edge InP(111)A and InP(111)B substrates, which had bowed edges that encompassed a range of off-cut angles and azimuths. At the growth condition studied, it was seen that there is a smooth region at the edge of the wafer for InP(111)B surface. The minimum growth rate was used for these growths was 0.5 Å/s, which did not result in any clear smooth region for growth on InP(111)A surface. We found the optimum off-cut angle for growth on InP(111)B from the facet angle of the hillocks where the smooth region starts. The optimum off-cut angle depends greatly on the growth conditions utilized. It was non-existent at not well-optimized growth conditions. It was seen that although growth temperature, As overpressure and growth rate all affects the surface quality, the effect of growth rate is more profound. It was also seen that the optimum off-cut angle is dependent on the materials studied. A larger off-cut angle is required for growth of InAlAs compared to InGaAs. This is because Al has a larger adsorption energy which results in a strong bond to the surface. Therefore, Al limits the growth kinetically.

Optimum off-cut angle for the growth of InGaAs on InP(111)B was shown to be 0.4°, which resulted in an atomically smooth surface with an Root Mean Square (RMS) roughness of 0.5 Å. We did a systematic growth optimization process for growth of InGaAs/InAlAs SuperLattice (SL) using 0.45 °, 1 ° and 2 ° misoriented InP(111)B substrates. Growth at lower misorientation angles of 0.45 ° and 1 ° did not result in a smooth SL even at the

lowest growth rate studied for InAlAs which was 0.06 Å/s. However, at a misorientation angle of 2 ° using growth rate of 0.5 Å/s and 0.06 Å/s for InGaAs and InAlAs, respectively, we were able to obtain morphologically smooth with an RMS roughness of 4.3 Å and microstructurally defect free InGaAs/InAlAs SL on InP(111)B substrate.

Growth of unintentionally strained layers of InGaAs/InAlAs on InP(111)B showed the presence of stacking faults, twins, misfit dislocation, phase separation and crystal rotation. The layers were partially relaxed. The strain was relieved through three mechanisms; 1) formation of misfit dislocations that are dissociated into stacking faults bounded by partial dislocations, 2) phase separation that is a result of morphological instabilities and 3) rotation of crystal along [110] axis to reduce the mismatch. The phase separation and In compositional variation was more pronounced in the InAlAs layer. This could be attributed to the lower mobility of Al compared to Ga. Furthermore, it was seen that the SL interface is very sharp when growth switches from InAlAs to InGaAs, while the interface is diffused when growth switches from InGaAs to InAlAs. This could be attributed to the combination of slower growth rate of InAlAs layer leaving ample time for Ga diffusion in the layer, and higher segregation tendency of Ga compared to Al in III-V semiconductors.

Atomically smooth (with an RMS roughness of 0.9 Å) growth of InGaAs/InAlAs was also achieved on exact InP(111)B surface using Migration Enhanced Epitaxy (MEE) at a low growth temperature of 295° C using a growth rate of 0.5Å/s for InGaAs/InAlAs. MEE increases the migration length of the adatoms through the use of modulated group III and V fluxes. MEE did not result in a smooth surface morphology when growth was done on InP(111)A substrate. On the other hand, Metal Modulation Epitaxy (MME) was shown to greatly improve the growth morphology when growth is done on (111)A surface. This surface morphology improvement was seen when growth was done at a higher temperature of 500° C. This is because the InP(111)A surface has a (2×2) surface reconstruction with In vacancy; additional In supplied during MME growth possibly compensates for the In-vacancies .

We did a comprehensive study to understand the behaviour of InP(111)A and InP(111)B substrates for epitaxial growth since the epitaxial growth quality is dramatically affected by the surface reconstruction. InP(111)A and InP(111)B were sputtered and annealed at different temperatures. It was seen that for annealing temperatures up to 500° C, (111)B substrate always has an unreconstructed (1×1) surface, while (111)A substrate changes its reconstruction from (1×1) after sputtering and short annealing to a mixture of (2×2) and (3×3) at medium annealing temperatures and finally to a (3×3) reconstruction at higher annealing temperature of 500° C. This could explain the greatly temperature dependant growth on (111)A surface, while growth on (111)B is less affected by the temperature.

Chapter 12

Future work

In this work we optimized growth of nominally lattice matched InGaAs/InAlAs SuperLattice (SL) on InP(111)B substrate to eliminate morphological and microstructural defects that are detrimental for electronic properties. Our work sets the stage for developing InGaAs/InAlAs SL on (111) substrate with potential use as Photo-Conductive Antenna (PCA) in Terahertz (THz)-Time Domain Spectroscopy (TDS) system and other photonic and electronic devices which can benefit from engineered embedded piezoelectric fields. Future work should focus on tuning the properties of this structure by doping, strain and composition to make them suitable for such application. For this structure we expect the InGaAs layer with smaller bandgap to act as the current carrying layer, while the InAlAs layer with larger bandgap to increase the dark resistivity.

The first step is to perform the growth at lower substrate temperatures to embed excess As within the layers. However, since excess As is only desirable within the InAlAs layer that is responsible to increase the dark resistivity, growth for InAlAs layer should be performed using conventional Molecular Beam Epitaxy (MBE), while growth of InGaAs should be performed using Migration Enhanced Epitaxy (MEE). Since MEE technique works by separately supplying group III and V atoms to the surface, it allows for excess As desorption, therefore, a highly stoichiometric layer will result.

Second, growth conditions should be optimized for lattice mismatched strained layers to induce the piezoelectric field. In the presence of piezoelectric field, an As interstitial that is thermally emitted from a precipitate is swept away by the peizoelectric field towards the InAlAs layer through the proper engineering of the strain within the layers. Also, the electric filed will quickly split electron-hole pairs towards barriers, where they will recombine.

Third, to further enhance the above mentioned process the InGaAs and InAlAs layers could be doped so that after annealing the structure, the excess As precipitates form and coarsen on the InAlAs layer rather than the InGaAs layer. This will be achieved by doping the InGaAs layer with acceptors such as Be, while the InAlAs layer with donors such as Si.

Letters of copyright permission

RE: copyright permission

pubscopyright <copyright@osa.org>
Mon 7/12/2021 12:27 PM
To: Ida Sadeghi <ida.sadeghi@uwaterloo.ca>; pubscopyright <copyright@osa.org>

Dear Ida,

Thank you for contacting The Optical Society. I'm sorry that we could not respond to your message earlier.

For the use of figures 2 and 3 from B. Sartorius, H. Roehle, H. Künzel, J. Böttcher, M. Schlak, D. Stanze, H. Venghaus, and M. Schell, "All-fiber terahertz time-domain spectrometer operating at 1.5 µm telecom wavelengths," Opt. Express 16, 9565-9570 (2008) and figure 1 from Roman J. B. Dietz, Marina Gerhard, Dennis Stanze, Martin Koch, Bernd Sartorius, and Martin Schell, "THz generation at 1.55 µm excitation: six-fold increase in THz conversion efficiency by separated photoconductive and trapping regions," Opt. Express 19, 25911-25917 (2011):

> OSA considers your requested use of its copyrighted material to be Fair Use under United States Copyright Law. It is requested that a complete citation of the original material be included in any publication.

While your publisher should be able to provide additional guidance, OSA prefers the below citation formats:

> For citations in figure captions:
>
> [Reprinted/Adapted] with permission from [ref #] © The Optical Society. (Please include the full citation in your reference list)
>
> For images without captions:
>
> Journal Vol. #, first page (year published) An example: Biomed. Opt. Express 6, 793 (2015)

Please let me know if you have any questions.

Kind Regards,
Hannah Greenwood

Hannah Greenwood
July 12, 2021
Authorized Agent, The Optical Society

The Optical Society (OSA)
2010 Massachusetts Ave., NW
Washington, DC 20036 USA
www.osa.org

Reflecting a Century of Innovation

From: Ida Sadeghi <ida.sadeghi@uwaterloo.ca>
Sent: Friday, July 9, 2021 9:30 AM
To: pubscopyright <copyright@osa.org>
Subject: Fw: copyright permission

CCC RightsLink®

Home | Help | Live Chat | Ida Sadeghi

CCC RightsLink®

Home | Help | Live Chat | Ida Sadeghi

Crystal Structure Of Lt Gaas Layers Before And After Annealing

Author: Zuzanna Liliental-Weber
Publication: MRS Online Proceedings Library
Publisher: Springer Nature
Date: Aug 1, 1991

Copyright © 1991, The Materials Research Society

Order Completed

Thank you for your order.

This Agreement between University of Waterloo -- Ida Sadeghi ("You") and Springer Nature ("Springer Nature") consists of your license details and the terms and conditions provided by Springer Nature and Copyright Clearance Center.

Your confirmation email will contain your order number for future reference.

License Number	5104221397097
License date	Jul 08, 2021

Printable Details

Licensed Content

Licensed Content Publisher	Springer Nature
Licensed Content Publication	MRS Online Proceedings Library
Licensed Content Title	Crystal Structure Of Lt Gaas Layers Before And After Annealing
Licensed Content Author	Zuzanna Liliental-Weber
Licensed Content Date	Aug 1, 1991

Order Details

Type of Use	Thesis/Dissertation
Requestor type	academic/university or research institute
Format	electronic
Portion	figures/tables/illustrations
Number of figures/tables/illustrations	2
Will you be translating?	no
Circulation/distribution	1 - 29
Author of this Springer Nature content	no

About Your Work

Title	Student
Institution name	University of Waterloo
Expected presentation date	Jul 2021

Additional Data

Portions	Fig. 1 and 3

Home Help Live Chat Ida Sadeghi

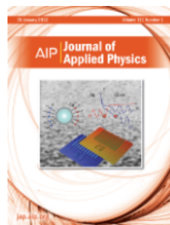

The effect of arsenic overpressure on the structural properties GaAs grown at low temperature

Author: M. Lagadas, Z. Hatzopoulos, K. Tsagaraki, et al
Publication: Journal of Applied Physics
Publisher: AIP Publishing
Date: Oct 15, 1996

Rights managed by AIP Publishing.

Order Completed

Thank you for your order.

This Agreement between University of Waterloo -- Ida Sadeghi ("You") and AIP Publishing ("AIP Publishing") consists of your license details and the terms and conditions provided by AIP Publishing and Copyright Clearance Center.

Your confirmation email will contain your order number for future reference.

License Number	5104221505211
License date	Jul 08, 2021

Printable Details

Licensed Content

Licensed Content Publisher	AIP Publishing
Licensed Content Publication	Journal of Applied Physics
Licensed Content Title	The effect of arsenic overpressure on the structural properties GaAs grown at low temperature
Licensed Content Author	M. Lagadas, Z. Hatzopoulos, K. Tsagaraki, et al
Licensed Content Date	Oct 15, 1996
Licensed Content Volume	80
Licensed Content Issue	8

Order Details

Type of Use	Thesis/Dissertation
Requestor type	Student
Format	Electronic
Portion	Figure/Table
Number of figures/tables	1
Will you be translating?	No

About Your Work

Title	Student
Institution name	University of Waterloo
Expected presentation date	Jul 2021

Additional Data

Portions	Fig. 5

CCC | Marketplace™

Order Number: 1131620
Order Date: 08 Jul 2021

Payment Information

Ida Sadeghi
i2sadegh@uwaterloo.ca
Payment method: Invoice

Billing Address:
Ida Sadeghi
University of Waterloo
200 University Ave W.
Waterloo, ON N2L 3G1
Canada

+1 (519) 722-2217
i2sadegh@uwaterloo.ca

Customer Location:
Ida Sadeghi
University of Waterloo
200 University Ave W.
Waterloo, ON N2L 3G1
Canada

Order Details

1. Annual review of materials research

Billing Status: Open

Order License ID	1131620-1
Order detail status	Completed
ISSN	1545-4118
Type of use	Republish in a thesis/dissertation
Publisher	ANNUAL REVIEWS
Portion	Image/photo/illustration

0.00 CAD
Republication Permission

LICENSED CONTENT

Publication Title	Annual review of materials research	**Rightsholder**	Annual Reviews, Inc.
Date	01/01/2001	**Publication Type**	e-Journal
Language	English	**URL**	http://arjournals.annualreviews.org/loi/matsci
Country	United States of America		

REQUEST DETAILS

Portion Type	Image/photo/illustration	**Distribution**	Worldwide
Number of images / photos / illustrations	2	**Translation**	Original language of publication
Format (select all that apply)	Electronic	**Copies for the disabled?**	No
		Minor editing privileges?	No

Home Help Live Chat Ida Sadeghi

SPRINGER NATURE

Microstructure of annealed low-temperature-grown GaAs layers

Author: Z. Liliental-Weber et al
Publication: Applied Physics A: Materials Science & Processing
Publisher: Springer Nature
Date: Jan 1, 1991

Copyright © 1991, Springer-Verlag

Order Completed

Thank you for your order.

This Agreement between University of Waterloo -- Ida Sadeghi ("You") and Springer Nature ("Springer Nature") consists of your license details and the terms and conditions provided by Springer Nature and Copyright Clearance Center.

Your confirmation email will contain your order number for future reference.

License Number	5104230090773
License date	Jul 08, 2021

Printable Details

Licensed Content

Licensed Content Publisher	Springer Nature
Licensed Content Publication	Applied Physics A: Materials Science & Processing
Licensed Content Title	Microstructure of annealed low-temperature-grown GaAs layers
Licensed Content Author	Z. Liliental-Weber et al
Licensed Content Date	Jan 1, 1991

Order Details

Type of Use	Thesis/Dissertation
Requestor type	academic/university or research institute
Format	electronic
Portion	figures/tables/illustrations
Number of figures/tables/illustrations	1
Will you be translating?	no
Circulation/distribution	1 - 29
Author of this Springer Nature content	no

About Your Work

Title	Student
Institution name	University of Waterloo
Expected presentation date	Jul 2021

Additional Data

Portions	Fig. 6

Home | Help | Live Chat | Ida Sadeghi

Extended defects and precipitates in LT□GaAs, LT□InAlAs and LT□InP

Author: Alain Claverie,Zuzanna Liliental-Weber
Publication: Materials Science and Engineering: B
Publisher: Elsevier
Date: 20 December 1993

Copyright © 1993 Published by Elsevier B.V.

Order Completed

Thank you for your order.

This Agreement between University of Waterloo -- Ida Sadeghi ("You") and Elsevier ("Elsevier") consists of your license details and the terms and conditions provided by Elsevier and Copyright Clearance Center.

Your confirmation email will contain your order number for future reference.

License Number	5104230185609
License date	Jul 08, 2021

Printable Details

Licensed Content

Licensed Content Publisher	Elsevier
Licensed Content Publication	Materials Science and Engineering: B
Licensed Content Title	Extended defects and precipitates in LT□GaAs, LT□InAlAs and LT□InP
Licensed Content Author	Alain Claverie,Zuzanna Liliental-Weber
Licensed Content Date	Dec 20, 1993
Licensed Content Volume	22
Licensed Content Issue	1
Licensed Content Pages	10

Order Details

Type of Use	reuse in a thesis/dissertation
Portion	figures/tables/illustrations
Number of figures/tables/illustrations	1
Format	electronic
Are you the author of this Elsevier article?	No
Will you be translating?	No

About Your Work

Title	Student
Institution name	University of Waterloo
Expected presentation date	Jul 2021

Additional Data

Portions	Fig. 10

Home | Help | Live Chat | Ida Sadeghi

GaAs, AlGaAs, and InGaAs epilayers containing As clusters: Semimetal/semiconductor composites

Author: M.R. Melloch,J.M. Woodall,N. Otsuka,K. Mahalingam,C.L. Chang,D.D. Nolte
Publication: Materials Science and Engineering: B
Publisher: Elsevier
Date: 20 December 1993

Copyright © 1993 Published by Elsevier B.V.

Order Completed

Thank you for your order.

This Agreement between University of Waterloo -- Ida Sadeghi ("You") and Elsevier ("Elsevier") consists of your license details and the terms and conditions provided by Elsevier and Copyright Clearance Center.

Your confirmation email will contain your order number for future reference.

Printable Details

License Number	5104230942268
License date	Jul 08, 2021

Licensed Content

Licensed Content Publisher	Elsevier
Licensed Content Publication	Materials Science and Engineering: B
Licensed Content Title	GaAs, AlGaAs, and InGaAs epilayers containing As clusters: Semimetal/semiconductor composites
Licensed Content Author	M.R. Melloch,J.M. Woodall,N. Otsuka,K. Mahalingam,C.L. Chang,D.D. Nolte
Licensed Content Date	Dec 20, 1993
Licensed Content Volume	22
Licensed Content Issue	1
Licensed Content Pages	6

Order Details

Type of Use	reuse in a thesis/dissertation
Portion	figures/tables/illustrations
Number of figures/tables/illustrations	2
Format	electronic
Are you the author of this Elsevier article?	No
Will you be translating?	No

About Your Work

Title	Student
Institution name	University of Waterloo
Expected presentation date	Jul 2021

Additional Data

Portions	Fig. 3 and 5

Home | Help | Live Chat | Ida Sadeghi

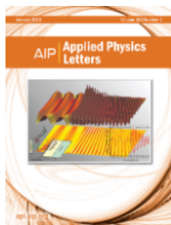

Reflection high-energy electron diffraction oscillations from vicinal surfaces—a new approach to surface diffusion measurements

Author: J. H. Neave, P. J. Dobson, B. A. Joyce, et al
Publication: Applied Physics Letters
Publisher: AIP Publishing
Date: Jul 15, 1985

Rights managed by AIP Publishing.

Order Completed

Thank you for your order.

This Agreement between University of Waterloo -- Ida Sadeghi ("You") and AIP Publishing ("AIP Publishing") consists of your license details and the terms and conditions provided by AIP Publishing and Copyright Clearance Center.

Your confirmation email will contain your order number for future reference.

License Number	5104230286862
License date	Jul 08, 2021

Printable Details

Licensed Content

Licensed Content Publisher	AIP Publishing
Licensed Content Publication	Applied Physics Letters
Licensed Content Title	Reflection high-energy electron diffraction oscillations from vicinal surfaces—a new approach to surface diffusion measurements
Licensed Content Author	J. H. Neave, P. J. Dobson, B. A. Joyce, et al
Licensed Content Date	Jul 15, 1985
Licensed Content Volume	47
Licensed Content Issue	2

Order Details

Type of Use	Thesis/Dissertation
Requestor type	Student
Format	Electronic
Portion	Figure/Table
Number of figures/tables	1
Will you be translating?	No

About Your Work

Title	Student
Institution name	University of Waterloo
Expected presentation date	Jul 2021

Additional Data

Portions	Fig. 1

SciPris

(/sciprisaps/Home/Index)

Scientific Publishing and Remittance Integration services

APS physics

Mrs. Ida Sadeghi

Rights and Permissions Request Details

Article Information

Title:

Electron counting model and its application to island structures on molecular-beam epitaxy grown GaAs(001) and ZnSe(001)

Author:

M. D. Pashley

Publication:

Physical Review B

DOI:

10.1103/PhysRevB.40.10481

Publisher:

American Physical Society

Date:

08-Jul-2021

Reuse Information

Reuse Category:

Reuse in a thesis/dissertation

Reuse By:

Student

Items for Reuse:

Figures/Tables

Number of figures/tables:

1

Figures and tables description:

Fig. 2

Format for Reuse:

Electronic

Information about New Publication

Does your reuse require significant modifications of the original content?: No

University/Publisher

University of Waterloo

Title of dissertation/thesis

Realization of atomically smooth defect free InGaAs/InAlAs superlattice on InP(111) substrates by molecular beam epitaxy

Expected completion date

Jul. 2021

Author(s)

Ida of Sadeghi

Specify intended distribution locations:

Canada

License Requester Information

Name:

Ida Sadeghi

Email ID:

aida_sadeghi@yahoo.com

Country:

Canada

Request Id:

RNP/21/JUL/042023

Rights and Permissions request status

Status:

Complete

☐ **Please acknowledge the Terms and Conditions to download your license.**

Back View License

Note: *The rights and permissions license will be issued in this name.*

CCC RightsLink®

Home | Help | Live Chat | Ida Sadeghi

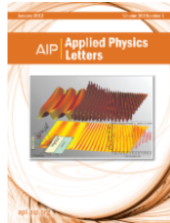

Surface reconstruction phase diagram and growth on GaAs(111)B substrates by molecular beam epitaxy

Author: K. Yang, L. J. Schowalter
Publication: Applied Physics Letters
Publisher: AIP Publishing
Date: Apr 13, 1992

Rights managed by AIP Publishing.

Order Completed

Thank you for your order.

This Agreement between University of Waterloo -- Ida Sadeghi ("You") and AIP Publishing ("AIP Publishing") consists of your license details and the terms and conditions provided by AIP Publishing and Copyright Clearance Center.

Your confirmation email will contain your order number for future reference.

License Number	5104230380347
License date	Jul 08, 2021

Printable Details

Licensed Content

Licensed Content Publisher	AIP Publishing
Licensed Content Publication	Applied Physics Letters
Licensed Content Title	Surface reconstruction phase diagram and growth on GaAs(111)B substrates by molecular beam epitaxy
Licensed Content Author	K. Yang, L. J. Schowalter
Licensed Content Date	Apr 13, 1992
Licensed Content Volume	60
Licensed Content Issue	15

Order Details

Type of Use	Thesis/Dissertation
Requestor type	Student
Format	Electronic
Portion	Figure/Table
Number of figures/tables	1
Will you be translating?	No

About Your Work

Title	Student
Institution name	University of Waterloo
Expected presentation date	Jul 2021

Additional Data

Portions	Fig. 2

SciPris

(/sciprisaps/Home/Index)

Scientific Publishing and Remittance Integration services

APS physics

Mrs. Ida Sadeghi

Rights and Permissions Request Details

Article Information

Title:

GaAs(111)A-(2x2) reconstruction studied by scanning tunneling microscopy

Author:

K. W. Haberern and M. D. Pashley

Publication:

Physical Review B

DOI:

10.1103/PhysRevB.41.3226

Publisher:

American Physical Society

Date:

08-Jul-2021

Reuse Information

Reuse Category:

Reuse in a thesis/dissertation

Reuse By:

Student

Items for Reuse:

Figures/Tables

Number of figures/tables:

1

Figures and tables description:

Fig. 1

Format for Reuse:

Electronic

Information about New Publication

Does your reuse require significant modifications of the original content?: No

University/Publisher

University of Waterloo

Title of dissertation/thesis

Realization of atomically smooth defect free InGaAs/InAlAs superlattice on InP(111) substrates by molecular beam epitaxy

Expected completion date

Jul. 2021

Author(s)

Ida of Sadeghi

Specify intended distribution locations:

Canada

License Requester Information

Name:

Ida Sadeghi

Email ID:

aida_sadeghi@yahoo.com

Country:

Canada

Request Id:

RNP/21/JUL/042025

Rights and Permissions request status

Status:

Complete

☐ Please acknowledge the Terms and Conditions to download your license.

Back View License

***Note**: The rights and permissions license will be issued in this name.*

SciPris

APS physics

(/sciprisaps/Home/Index)

Scientific Publishing and Remittance Integration services

Mrs. Ida Sadeghi

Rights and Permissions Request Details

Article Information

Title:

Reconstructions of GaAs(1- 1- 1-) surfaces observed by scanning tunneling microscopy

Author:

D. K. Biegelsen et al.

Publication:

Physical Review Letters

DOI:

10.1103/PhysRevLett.65.452

Publisher:

American Physical Society

Date:

08-Jul-2021

Reuse Information

Reuse Category:

Reuse in a thesis/dissertation

Reuse By:

Student

Items for Reuse:

Figures/Tables

Number of figures/tables:

1

Figures and tables description:

Fig. 2.d

Format for Reuse:

Electronic

Information about New Publication

Does your reuse require significant modifications of the original content?: No

University/Publisher

University of Waterloo

Title of dissertation/thesis

Realization of atomically smooth defect free InGaAs/InAlAs superlattice on InP(111) substrates by molecular beam epitaxy

Expected completion date

Jul. 2021

Author(s)

Ida of Sadeghi

Specify intended distribution locations:

Canada

License Requester Information

Name:

Ida Sadeghi

Email ID:

aida_sadeghi@yahoo.com

Country:

Canada

Request Id:

RNP/21/JUL/042024

Rights and Permissions request status

Status:

Complete

☐ **Please acknowledge the Terms and Conditions to download your license.**

Back View License

***Note**: The rights and permissions license will be issued in this name.*

Home | Help | Live Chat | Ida Sadeghi

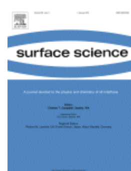

Semiconductor polar surfaces: mechanisms of the stability of non-reconstructed III–V (1̄1̄1̄) surfaces

Author: S. Mankefors,P.O. Nilsson,J. Kanski
Publication: Surface Science
Publisher: Elsevier
Date: 20 December 1999

Copyright © 1999 Elsevier Science B.V. All rights reserved.

Order Completed

Thank you for your order.

This Agreement between University of Waterloo -- Ida Sadeghi ("You") and Elsevier ("Elsevier") consists of your license details and the terms and conditions provided by Elsevier and Copyright Clearance Center.

Your confirmation email will contain your order number for future reference.

License Number	5104230523338
License date	Jul 08, 2021

Printable Details

Licensed Content

Licensed Content Publisher	Elsevier
Licensed Content Publication	Surface Science
Licensed Content Title	Semiconductor polar surfaces: mechanisms of the stability of non-reconstructed III–V (1̄1̄1̄) surfaces
Licensed Content Author	S. Mankefors,P.O. Nilsson,J. Kanski
Licensed Content Date	Dec 20, 1999
Licensed Content Volume	443
Licensed Content Issue	3
Licensed Content Pages	6

Order Details

Type of Use	reuse in a thesis/dissertation
Portion	figures/tables/illustrations
Number of figures/tables/illustrations	2
Format	electronic
Are you the author of this Elsevier article?	No
Will you be translating?	No

About Your Work

Title	Student
Institution name	University of Waterloo
Expected presentation date	Jul 2021

Additional Data

Portions	Figs. 2 and 4

Home | Help | Live Chat | Ida Sadeghi

Facet growth of InP/InGaAs layers on SiO2-masked InP by chemical beam epitaxy

Author: Hideo Sugiura,Toshio Nishida,Ryuzo Iga,Takeshi Yamada,Toshiaki Tamamura

Publication: Journal of Crystal Growth

Publisher: Elsevier

Date: 1 August 1992

Copyright © 1992 Published by Elsevier B.V.

Order Completed

Thank you for your order.

This Agreement between University of Waterloo -- Ida Sadeghi ("You") and Elsevier ("Elsevier") consists of your license details and the terms and conditions provided by Elsevier and Copyright Clearance Center.

Your confirmation email will contain your order number for future reference.

License Number	5104230700369
License date	Jul 08, 2021

Printable Details

Licensed Content

Licensed Content Publisher	Elsevier
Licensed Content Publication	Journal of Crystal Growth
Licensed Content Title	Facet growth of InP/InGaAs layers on SiO2-masked InP by chemical beam epitaxy
Licensed Content Author	Hideo Sugiura,Toshio Nishida,Ryuzo Iga,Takeshi Yamada,Toshiaki Tamamura
Licensed Content Date	Aug 1, 1992
Licensed Content Volume	121
Licensed Content Issue	4
Licensed Content Pages	8

Order Details

Type of Use	reuse in a thesis/dissertation
Portion	figures/tables/illustrations
Number of figures/tables/illustrations	1
Format	electronic
Are you the author of this Elsevier article?	No
Will you be translating?	No

About Your Work

Title	Student
Institution name	University of Waterloo
Expected presentation date	Jul 2021

Additional Data

Portions	Fig. 10

Home Help Email Support Ida Sadeghi

Chapter:
8 Reflection High Energy Electron Diffraction Studies of the Dynamics of Molecular Beam Epitaxy

Book: Molecular Beam Epitaxy

Author: Philip I. Cohen,Gale S. Petrich,Gregory J. Whaley

Publisher: Elsevier

Date: 1995

Copyright © 1995 Noyes Publications. Published by Elsevier Inc. All rights reserved.

Order Completed

Thank you for your order.

This Agreement between University of Waterloo -- Ida Sadeghi ("You") and Elsevier ("Elsevier") consists of your license details and the terms and conditions provided by Elsevier and Copyright Clearance Center.

Your confirmation email will contain your order number for future reference.

License Number	5104400885151
License date	Jul 08, 2021

Printable Details

Licensed Content

Licensed Content Publisher	Elsevier
Licensed Content Publication	Elsevier Books
Licensed Content Title	Molecular Beam Epitaxy
Licensed Content Author	Philip I. Cohen,Gale S. Petrich,Gregory J. Whaley
Licensed Content Date	Jan 1, 1995
Licensed Content Pages	76

Order Details

Type of Use	reuse in a thesis/dissertation
Portion	figures/tables/illustrations
Number of figures/tables/illustrations	1
Format	electronic
Are you the author of this Elsevier chapter?	No
Will you be translating?	No

About Your Work

Title	Student
Institution name	University of Waterloo
Expected presentation date	Jul 2021

Additional Data

Portions	Fig. 8.27

Home Help Live Chat Ida Sadeghi

Atomic step organization in homoepitaxial growth on GaAs(111)B substrates

Author: Leo J. Schowalter, Kai Yang, Thomas Thundat
Publication: Journal of Vacuum Science & Technology B
Publisher: American Vacuum Society
Date: Jul 1, 1994

Rights managed by AIP Publishing.

Order Completed

Thank you for your order.

This Agreement between University of Waterloo -- Ida Sadeghi ("You") and AIP Publishing ("AIP Publishing") consists of your license details and the terms and conditions provided by AIP Publishing and Copyright Clearance Center.

Your confirmation email will contain your order number for future reference.

License Number	5104220954306
License date	Jul 08, 2021

Printable Details

Licensed Content

Licensed Content Publisher	American Vacuum Society
Licensed Content Publication	Journal of Vacuum Science & Technology B
Licensed Content Title	Atomic step organization in homoepitaxial growth on GaAs(111)B substrates
Licensed Content Author	Leo J. Schowalter, Kai Yang, Thomas Thundat
Licensed Content Date	Jul 1, 1994
Licensed Content Volume	12
Licensed Content Issue	4

Order Details

Type of Use	Thesis/Dissertation
Requestor type	Student
Format	Electronic
Portion	Figure/Table
Number of figures/tables	2
Will you be translating?	No

About Your Work

Title	Student
Institution name	University of Waterloo
Expected presentation date	Jul 2021

Additional Data

Portions	Fig. 1 and 2

Home | Help | Live Chat | Ida Sadeghi

Molecular-beam epitaxy on exact and vicinal GaAs(1̄1̄1̄) substrates

Author: K. Yang, L. J. Schowalter, B. K. Laurich, et al
Publication: Journal of Vacuum Science & Technology B
Publisher: American Vacuum Society
Date: May 1, 1993

Rights managed by AIP Publishing.

Order Completed

Thank you for your order.

This Agreement between University of Waterloo -- Ida Sadeghi ("You") and AIP Publishing ("AIP Publishing") consists of your license details and the terms and conditions provided by AIP Publishing and Copyright Clearance Center.

Your confirmation email will contain your order number for future reference.

License Number	5104230846294
License date	Jul 08, 2021

Printable Details

Licensed Content

Licensed Content Publisher	American Vacuum Society
Licensed Content Publication	Journal of Vacuum Science & Technology B
Licensed Content Title	Molecular-beam epitaxy on exact and vicinal GaAs(1̄1̄1̄) substrates
Licensed Content Author	K. Yang, L. J. Schowalter, B. K. Laurich, et al
Licensed Content Date	May 1, 1993
Licensed Content Volume	11
Licensed Content Issue	3

Order Details

Type of Use	Thesis/Dissertation
Requestor type	Student
Format	Electronic
Portion	Figure/Table
Number of figures/tables	1
Will you be translating?	No

About Your Work

Title	Student
Institution name	University of Waterloo
Expected presentation date	Jul 2021

Additional Data

Portions	Fig. 4

Home Help Email Support Ida Sadeghi

Formation and reduction of pyramidal hillocks on InGaAs/InP(111)A

Author: Hisashi Yamada, Osamu Ichikawa, Noboru Fukuhara, et al

Publication: physica status solidi (b) basic solid state physics

Publisher: John Wiley and Sons

Date: Dec 2, 2015

© 2015 WILEY-VCH Verlag GmbH & Co. KGaA, Weinheim

Order Completed

Thank you for your order.

This Agreement between University of Waterloo -- Ida Sadeghi ("You") and John Wiley and Sons ("John Wiley and Sons") consists of your license details and the terms and conditions provided by John Wiley and Sons and Copyright Clearance Center.

Your confirmation email will contain your order number for future reference.

Printable Details

License Number	5104440448564
License date	Jul 08, 2021

Licensed Content

Licensed Content Publisher	John Wiley and Sons
Licensed Content Publication	physica status solidi (b) basic solid state physics
Licensed Content Title	Formation and reduction of pyramidal hillocks on InGaAs/InP(111)A
Licensed Content Author	Hisashi Yamada, Osamu Ichikawa, Noboru Fukuhara, et al
Licensed Content Date	Dec 2, 2015
Licensed Content Volume	253
Licensed Content Issue	4
Licensed Content Pages	4

Order Details

Type of use	Dissertation/Thesis
Requestor type	University/Academic
Format	Electronic
Portion	Figure/table
Number of figures/tables	2
Will you be translating?	No

About Your Work

Title	Student
Institution name	University of Waterloo
Expected presentation date	Jul 2021

Additional Data

Portions	Figs. 2 and 3

CCC RightsLink®

Home | Help | Email Support | Ida Sadeghi

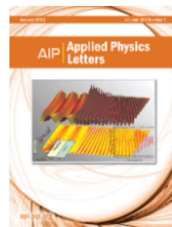

Growth control of GaAs epilayers with specular surface free of pyramids and twins on nonmisoriented (111)B substrates

Author: P. Chen, K. C. Rajkumar, A. Madhukar
Publication: Applied Physics Letters
Publisher: AIP Publishing
Date: Apr 22, 1991

Rights managed by AIP Publishing.

Order Completed

Thank you for your order.

This Agreement between University of Waterloo -- Ida Sadeghi ("You") and AIP Publishing ("AIP Publishing") consists of your license details and the terms and conditions provided by AIP Publishing and Copyright Clearance Center.

Your confirmation email will contain your order number for future reference.

License Number	5104410063905
License date	Jul 08, 2021

Printable Details

Licensed Content

Licensed Content Publisher	AIP Publishing
Licensed Content Publication	Applied Physics Letters
Licensed Content Title	Growth control of GaAs epilayers with specular surface free of pyramids and twins on nonmisoriented (111)B substrates
Licensed Content Author	P. Chen, K. C. Rajkumar, A. Madhukar
Licensed Content Date	Apr 22, 1991
Licensed Content Volume	58
Licensed Content Issue	16

Order Details

Type of Use	Thesis/Dissertation
Requestor type	Student
Format	Electronic
Portion	Figure/Table
Number of figures/tables	1
Will you be translating?	No

About Your Work

Title	Student
Institution name	University of Waterloo
Expected presentation date	Jul 2021

Additional Data

Portions	Fig. 1

Home Help Email Support Ida Sadeghi

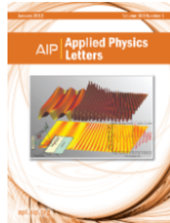

Behavior and mechanism of step bunching during metalorganic vapor phase epitaxy of GaAs

Author: Masanori Shinohara, Naohisa Inoue
Publication: Applied Physics Letters
Publisher: AIP Publishing
Date: Apr 10, 1995

Rights managed by AIP Publishing.

Order Completed

Thank you for your order.

This Agreement between University of Waterloo -- Ida Sadeghi ("You") and AIP Publishing ("AIP Publishing") consists of your license details and the terms and conditions provided by AIP Publishing and Copyright Clearance Center.

Your confirmation email will contain your order number for future reference.

License Number	5104410189637
License date	Jul 08, 2021

Printable Details

Licensed Content

Licensed Content Publisher	AIP Publishing
Licensed Content Publication	Applied Physics Letters
Licensed Content Title	Behavior and mechanism of step bunching during metalorganic vapor phase epitaxy of GaAs
Licensed Content Author	Masanori Shinohara, Naohisa Inoue
Licensed Content Date	Apr 10, 1995
Licensed Content Volume	66
Licensed Content Issue	15

Order Details

Type of Use	Thesis/Dissertation
Requestor type	Student
Format	Electronic
Portion	Figure/Table
Number of figures/tables	1
Will you be translating?	No

About Your Work

Title	Student
Institution name	University of Waterloo
Expected presentation date	Jul 2021

Additional Data

Portions	Fig. 3

Home Help Email Support Ida Sadeghi

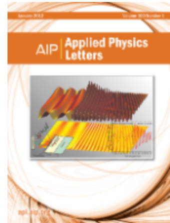

Surface step bunching and crystal defects in InAlAs films grown by molecular beam epitaxy on (111)B InP substrates

Author: N. Bécourt, F. Peiró, A. Cornet, et al

Publication: Applied Physics Letters

Publisher: AIP Publishing

Date: Nov 17, 1997

Rights managed by AIP Publishing.

Order Completed

Thank you for your order.

This Agreement between University of Waterloo -- Ida Sadeghi ("You") and AIP Publishing ("AIP Publishing") consists of your license details and the terms and conditions provided by AIP Publishing and Copyright Clearance Center.

Your confirmation email will contain your order number for future reference.

License Number	5104410374879	Printable Details
License date	Jul 08, 2021	

Licensed Content

Licensed Content Publisher	AIP Publishing
Licensed Content Publication	Applied Physics Letters
Licensed Content Title	Surface step bunching and crystal defects in InAlAs films grown by molecular beam epitaxy on (111)B InP substrates
Licensed Content Author	N. Bécourt, F. Peiró, A. Cornet, et al
Licensed Content Date	Nov 17, 1997
Licensed Content Volume	71
Licensed Content Issue	20

Order Details

Type of Use	Thesis/Dissertation
Requestor type	Student
Format	Electronic
Portion	Figure/Table
Number of figures/tables	2
Will you be translating?	No

About Your Work

Title	Student
Institution name	University of Waterloo
Expected presentation date	Jul 2021

Additional Data

Portions	Figs. 2.a and 3.a

Home | Help | Email Support | Ida Sadeghi

Analysis of twin defects in GaAs(111)B molecular beam epitaxy growth

Author: Yeonjoon Park, Michael J. Cich, Rian Zhao, et al
Publication: Journal of Vacuum Science & Technology B
Publisher: American Vacuum Society
Date: May 1, 2000

Rights managed by AIP Publishing.

Order Completed

Thank you for your order.

This Agreement between University of Waterloo -- Ida Sadeghi ("You") and AIP Publishing ("AIP Publishing") consists of your license details and the terms and conditions provided by AIP Publishing and Copyright Clearance Center.

Your confirmation email will contain your order number for future reference.

License Number 5104410723145 | Printable Details

License date Jul 08, 2021

Licensed Content

Licensed Content Publisher	American Vacuum Society
Licensed Content Publication	Journal of Vacuum Science & Technology B
Licensed Content Title	Analysis of twin defects in GaAs(111)B molecular beam epitaxy growth
Licensed Content Author	Yeonjoon Park, Michael J. Cich, Rian Zhao, et al
Licensed Content Date	May 1, 2000
Licensed Content Volume	18
Licensed Content Issue	3

Order Details

Type of Use	Thesis/Dissertation
Requestor type	Student
Format	Electronic
Portion	Figure/Table
Number of figures/tables	1
Will you be translating?	No

About Your Work

Title	Student
Institution name	University of Waterloo
Expected presentation date	Jul 2021

Additional Data

Portions	Fig. 1

Home Help Email Support Ida Sadeghi

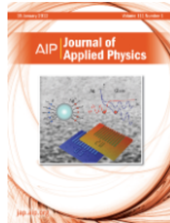

"A transmission electron microscope study of twin structure in GaAs/GaAs (111)B grown via molecular-beam epitaxy"

Author: K. C. Rajkumar, P. Chen, A. Madhukar
Publication: Journal of Applied Physics
Publisher: AIP Publishing
Date: Feb 15, 1991

Rights managed by AIP Publishing.

Order Completed

Thank you for your order.

This Agreement between University of Waterloo -- Ida Sadeghi ("You") and AIP Publishing ("AIP Publishing") consists of your license details and the terms and conditions provided by AIP Publishing and Copyright Clearance Center.

Your confirmation email will contain your order number for future reference.

License Number	5104410541704
License date	Jul 08, 2021

Printable Details

Licensed Content

Licensed Content Publisher	AIP Publishing
Licensed Content Publication	Journal of Applied Physics
Licensed Content Title	"A transmission electron microscope study of twin structure in GaAs/GaAs (111)B grown via molecular-beam epitaxy"
Licensed Content Author	K. C. Rajkumar, P. Chen, A. Madhukar
Licensed Content Date	Feb 15, 1991
Licensed Content Volume	69
Licensed Content Issue	4

Order Details

Type of Use	Thesis/Dissertation
Requestor type	Student
Format	Electronic
Portion	Figure/Table
Number of figures/tables	1
Will you be translating?	No

About Your Work

Title	Student
Institution name	University of Waterloo
Expected presentation date	Jul 2021

Additional Data

Portions	Fig. 5

Re: copyright permission

Permissions <permissions@ioppublishing.org>
Fri 7/9/2021 10:08 AM
To: Ida Sadeghi <ida.sadeghi@uwaterloo.ca>

Dear Ida Sadeghi,

Thank you for your request to reuse JSAP material *in your dissertation,* ***"Realization of atomically smooth defect free InGaAs/InAlAs superlattice on InP(111) substrates by molecular beam epitaxy"***

Regarding:

- ***Figures 1** & **3** from **"Nonexistence of Long-Range Order in Ga0.5In0.5P Epitaxial Layers Grown on (111)B and (110)GaAs Substrates"***
- ***Figure 4** from **"Optimum Growth Conditions of GaAs(111)B Layers for Good Electrical Properties by Molecular Beam Epitaxy"***

We are happy to grant permission for the use you request, provided:

- The Copyright Policy of JSAP is followed https://www.jsap.or.jp/english/copyright-policy
- The article is cited as a reference
- The copyright line including year of publication is added to the reproduced content (at the end of the figure captions):
  - Copyright ([year of publication]) The Physical Society of Japan and The Japan Society of Applied Physics

This does not apply to any material/figure which is credited to another source in the publication or has been obtained from a third party. Express permission for such materials/figures must be obtained from the copyright owner.

Kind regards,

Sophie
Copyright & Permissions Team
Sophie Brittain - Rights & Permissions Assistant
Cameron Wood - Legal & Rights Adviser
Contact Details
E-mail: permissions@ioppublishing.org

For further information about copyright and how to request permission:
https://publishingsupport.iopscience.iop.org/copyright-journals/
See also: https://publishingsupport.iopscience.iop.org/
Please see our Author Rights Policy https://publishingsupport.iopscience.iop.org/author-rights-policies/
Please note: We do not provide signed permission forms as a separate attachment. Please print this email and provide it to your publisher as proof of permission. **Please note**: Any statements made by IOP Publishing to the effect that authors do not need to get permission to use any content where IOP Publishing is not the publisher is not intended to constitute any sort of legal advice. Authors must make their own decisions as to the suitability of the content they are using and whether they require permission for it to be published within their article.

Home Help Email Support Ida Sadeghi

Strong ordering in GaInP alloy semiconductors; Formation mechanism for the ordered phase

Author: Tohru Suzuki,Akiko Gomyo,Sumio Iijima

Publication: Journal of Crystal Growth

Publisher: Elsevier

Date: 1988

Copyright © 1988 Published by Elsevier B.V.

Order Completed

Thank you for your order.

This Agreement between University of Waterloo -- Ida Sadeghi ("You") and Elsevier ("Elsevier") consists of your license details and the terms and conditions provided by Elsevier and Copyright Clearance Center.

Your confirmation email will contain your order number for future reference.

License Number	5104410892613
License date	Jul 08, 2021

Printable Details

Licensed Content

Licensed Content Publisher	Elsevier
Licensed Content Publication	Journal of Crystal Growth
Licensed Content Title	Strong ordering in GaInP alloy semiconductors; Formation mechanism for the ordered phase
Licensed Content Author	Tohru Suzuki,Akiko Gomyo,Sumio Iijima
Licensed Content Date	Jan 1, 1988
Licensed Content Volume	93
Licensed Content Issue	1-4
Licensed Content Pages	10

Order Details

Type of Use	reuse in a thesis/dissertation
Portion	figures/tables/illustrations
Number of figures/tables/illustrations	2
Format	electronic
Are you the author of this Elsevier article?	No
Will you be translating?	No

About Your Work

Title	Student
Institution name	University of Waterloo
Expected presentation date	Jul 2021

Additional Data

Portions	Figs. 1 and 2

Home

Help

Email Support

Ida Sadeghi

SPRINGER NATURE

Spontaneous Lateral Composition Modulation in III-V Semiconductor Alloys

Author: J. Mirecki Millunchick et al
Publication: MRS Bulletin
Publisher: Springer Nature
Date: Jul 1, 1997

Copyright © 1997, The Materials Research Society

Order Completed

Thank you for your order.

This Agreement between University of Waterloo -- Ida Sadeghi ("You") and Springer Nature ("Springer Nature") consists of your license details and the terms and conditions provided by Springer Nature and Copyright Clearance Center.

Your confirmation email will contain your order number for future reference.

License Number	5104431218523	Printable Details
License date	Jul 08, 2021	

Licensed Content

Licensed Content Publisher	Springer Nature
Licensed Content Publication	MRS Bulletin
Licensed Content Title	Spontaneous Lateral Composition Modulation in III-V Semiconductor Alloys
Licensed Content Author	J. Mirecki Millunchick et al
Licensed Content Date	Jul 1, 1997

Order Details

Type of Use	Thesis/Dissertation
Requestor type	academic/university or research institute
Format	electronic
Portion	figures/tables/illustrations
Number of figures/tables/illustrations	2
Will you be translating?	no
Circulation/distribution	1 - 29
Author of this Springer Nature content	no

About Your Work

Title	Student
Institution name	University of Waterloo
Expected presentation date	Jul 2021

Additional Data

Portions	Figs. 4 and 6

Home Help Email Support Ida Sadeghi

Surface spinodal decomposition in low temperature Al0.48In0.52As grown on InP(001) by molecular beam epitaxy

Author:
G. Grenet,M. Gendry,M. Oustric,Y. Robach,L. Porte,G. Hollinger,O. Marty,M. Pitaval,C. Priester

Publication: Applied Surface Science

Publisher: Elsevier

Date: 1 January 1998

Copyright © 1998 Published by Elsevier B.V.

Order Completed

Thank you for your order.

This Agreement between University of Waterloo -- Ida Sadeghi ("You") and Elsevier ("Elsevier") consists of your license details and the terms and conditions provided by Elsevier and Copyright Clearance Center.

Your confirmation email will contain your order number for future reference.

License Number	5104431496582
License date	Jul 08, 2021

Printable Details

Licensed Content

Licensed Content Publisher	Elsevier
Licensed Content Publication	Applied Surface Science
Licensed Content Title	Surface spinodal decomposition in low temperature Al0.48In0.52As grown on InP(001) by molecular beam epitaxy
Licensed Content Author	G. Grenet,M. Gendry,M. Oustric,Y. Robach,L. Porte,G. Hollinger,O. Marty,M. Pitaval,C. Priester
Licensed Content Date	Jan 1, 1998
Licensed Content Volume	123
Licensed Content Issue	n/a
Licensed Content Pages	5

Order Details

Type of Use	reuse in a thesis/dissertation
Portion	figures/tables/illustrations
Number of figures/tables/illustrations	1
Format	electronic
Are you the author of this Elsevier article?	No
Will you be translating?	No

About Your Work

Title	Student
Institution name	University of Waterloo
Expected presentation date	Jul 2021

Additional Data

Portions	Fig. 2.a

Home

Help

Email Support

Ida Sadeghi

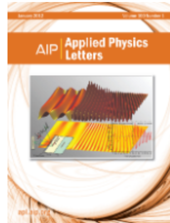

Growth rate and critical temperatures to avoid the modulation of composition of InGaAs epitaxial layers

Author: D. González, G. Aragón, D. Araújo, et al

Publication: Applied Physics Letters

Publisher: AIP Publishing

Date: May 3, 1999

Rights managed by AIP Publishing.

Order Completed

Thank you for your order.

This Agreement between University of Waterloo -- Ida Sadeghi ("You") and AIP Publishing ("AIP Publishing") consists of your license details and the terms and conditions provided by AIP Publishing and Copyright Clearance Center.

Your confirmation email will contain your order number for future reference.

License Number	5104440118331
License date	Jul 08, 2021

Printable Details

Licensed Content

Licensed Content Publisher	AIP Publishing
Licensed Content Publication	Applied Physics Letters
Licensed Content Title	Growth rate and critical temperatures to avoid the modulation of composition of InGaAs epitaxial layers
Licensed Content Author	D. González, G. Aragón, D. Araújo, et al
Licensed Content Date	May 3, 1999
Licensed Content Volume	74
Licensed Content Issue	18

Order Details

Type of Use	Thesis/Dissertation
Requestor type	Student
Format	Electronic
Portion	Figure/Table
Number of figures/tables	1
Will you be translating?	No

About Your Work

Title	Student
Institution name	University of Waterloo
Expected presentation date	Jul 2021

Additional Data

Portions	Fig. 2

Home | Help | Email Support | Ida Sadeghi

Vertical composition fluctuations in (Ga,In)(N,As) quantum wells grown on vicinal (111)B GaAs

Author: E. Luna,A. Trampert,J. Miguel-Sánchez,A. Guzmán,K.H. Ploog

Publication: Journal of Physics and Chemistry of Solids

Publisher: Elsevier

Date: February–March 2008

Copyright © 2007 Elsevier Ltd. All rights reserved.

Order Completed

Thank you for your order.

This Agreement between University of Waterloo -- Ida Sadeghi ("You") and Elsevier ("Elsevier") consists of your license details and the terms and conditions provided by Elsevier and Copyright Clearance Center.

Your confirmation email will contain your order number for future reference.

License Number 5104430981097 — Printable Details

License date Jul 08, 2021

Licensed Content

Licensed Content Publisher	Elsevier
Licensed Content Publication	Journal of Physics and Chemistry of Solids
Licensed Content Title	Vertical composition fluctuations in (Ga,In)(N,As) quantum wells grown on vicinal (111)B GaAs
Licensed Content Author	E. Luna,A. Trampert,J. Miguel-Sánchez,A. Guzmán,K.H. Ploog
Licensed Content Date	February–March 2008
Licensed Content Volume	69
Licensed Content Issue	2-3
Licensed Content Pages	4

Order Details

Type of Use	reuse in a thesis/dissertation
Portion	figures/tables/illustrations
Number of figures/tables/illustrations	1
Format	electronic
Are you the author of this Elsevier article?	No
Will you be translating?	No

About Your Work

Title	Student
Institution name	University of Waterloo
Expected presentation date	Jul 2021

Additional Data

Portions	Fig. 3

Home Help Email Support Ida Sadeghi

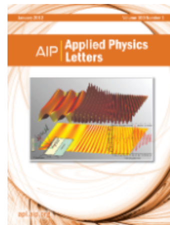

Critical layer thickness on (111)B-oriented InGaAs/GaAs heteroepitaxy

Author: Takayoshi Anan, Kenichi Nishi, Sigeo Sugou

Publication: Applied Physics Letters

Publisher: AIP Publishing

Date: Jun 22, 1992

Rights managed by AIP Publishing.

Order Completed

Thank you for your order.

This Agreement between University of Waterloo -- Ida Sadeghi ("You") and AIP Publishing ("AIP Publishing") consists of your license details and the terms and conditions provided by AIP Publishing and Copyright Clearance Center.

Your confirmation email will contain your order number for future reference.

License Number	5104430830953
License date	Jul 08, 2021

Printable Details

Licensed Content

Licensed Content Publisher	AIP Publishing
Licensed Content Publication	Applied Physics Letters
Licensed Content Title	Critical layer thickness on (111)B-oriented InGaAs/GaAs heteroepitaxy
Licensed Content Author	Takayoshi Anan, Kenichi Nishi, Sigeo Sugou
Licensed Content Date	Jun 22, 1992
Licensed Content Volume	60
Licensed Content Issue	25

Order Details

Type of Use	Thesis/Dissertation
Requestor type	Student
Format	Electronic
Portion	Figure/Table
Number of figures/tables	2
Will you be translating?	No

About Your Work

Title	Student
Institution name	University of Waterloo
Expected presentation date	Jul 2021

Additional Data

Portions	Figs. 1 and 2

CCC | Marketplace™

Order Number: 1131777
Order Date: 08 Jul 2021

Payment Information

Ida Sadeghi
i2sadegh@uwaterloo.ca
Payment method: Invoice

Billing Address:
Ida Sadeghi
University of Waterloo
200 University Ave W.
Waterloo, ON N2L 3G1
Canada

+1 (519) 722-2217
i2sadegh@uwaterloo.ca

Customer Location:
Ida Sadeghi
University of Waterloo
200 University Ave W.
Waterloo, ON N2L 3G1
Canada

Order Details

1. Chemical Society reviews

Billing Status: Open

Article: Nanoscale surface chemistry over faceted substrates: structure, reactivity and nanotemplates.

Order License ID	1131777-1
Order detail status	Completed
ISSN	0306-0012
Type of use	Republish in a thesis/dissertation
Publisher	ROYAL SOCIETY OF CHEMISTRY, ETC.]
Portion	Image/photo/illustration

0.00 CAD
Republication Permission

LICENSED CONTENT

Publication Title	Chemical Society reviews	**Rightsholder**	Royal Society of Chemistry
Article Title	Nanoscale surface chemistry over faceted substrates: structure, reactivity and nanotemplates.	**Publication Type**	Journal
		Start Page	2310
		Issue	10
		Volume	37
Author/Editor	CHEMICAL SOCIETY (GREAT BRITAIN)		
Date	01/01/1972		
Language	English		
Country	United Kingdom of Great Britain and Northern Ireland		

SciPris

APS physics

(/sciprisaps/Home/Index)

Scientific Publishing and Remittance Integration services

Mrs. Ida Sadeghi

Rights and Permissions Request Details

Article Information

Title:

Finite-temperature phase diagram of vicinal Si(100) surfaces

Author:

O. L. Alerhand et al.

Publication:

Physical Review Letters

DOI:

10.1103/PhysRevLett.64.2406

Publisher:

American Physical Society

Date:

08-Jul-2021

Reuse Information

Reuse Category:

Reuse in a thesis/dissertation

Reuse By:

Student

Items for Reuse:

Figures/Tables

Number of figures/tables:

1

Figures and tables description:

Fig. 1

Format for Reuse:

Electronic

Information about New Publication

Does your reuse require significant modifications of the original content?: No

University/Publisher

University of Waterloo

Title of dissertation/thesis

Ida of SadeghiRealization of atomically smooth defect free InGaAs/InAlAs superlattice on InP(111) substrates by molecular beam epitaxy

Expected completion date

Jul. 2021

Author(s)

Ida of Sadeghi

Specify intended distribution locations:

Canada

License Requester Information

Name:

Ida Sadeghi

Email ID:

aida_sadeghi@yahoo.com

Country:

Canada

Request Id:

RNP/21/JUL/042027

Rights and Permissions request status

Status:

Complete

☐ Please acknowledge the Terms and Conditions to download your license.

Back View License

***Note**: The rights and permissions license will be issued in this name.*

CCC RightsLink®

Home | Help | Email Support | Ida Sadeghi

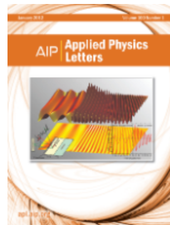

Material properties of bulk InGaAs and InAlAs/InGaAs heterostructures grown on (111)B and (111)B misoriented by 1° towards 〈211〉 InP substrates

Author: W. Yeo, R. Dimitrov, W. J. Schaff, et al

Publication: Applied Physics Letters

Publisher: AIP Publishing

Date: Dec 25, 2000

Rights managed by AIP Publishing.

Order Completed

Thank you for your order.

This Agreement between University of Waterloo -- Ida Sadeghi ("You") and AIP Publishing ("AIP Publishing") consists of your license details and the terms and conditions provided by AIP Publishing and Copyright Clearance Center.

Your confirmation email will contain your order number for future reference.

License Number	5104421505318
License date	Jul 08, 2021

Printable Details

Licensed Content

Licensed Content Publisher	AIP Publishing
Licensed Content Publication	Applied Physics Letters
Licensed Content Title	Material properties of bulk InGaAs and InAlAs/InGaAs heterostructures grown on (111)B and (111)B misoriented by 1° towards 〈211〉 InP substrates
Licensed Content Author	W. Yeo, R. Dimitrov, W. J. Schaff, et al
Licensed Content Date	Dec 25, 2000
Licensed Content Volume	77
Licensed Content Issue	26

Order Details

Type of Use	Thesis/Dissertation
Requestor type	Student
Format	Electronic
Portion	Figure/Table
Number of figures/tables	2
Will you be translating?	No

About Your Work

Title	Student
Institution name	University of Waterloo
Expected presentation date	Jul 2021

Additional Data

Portions	Figs. 2 and 3

Home | Help | Email Support | Ida Sadeghi

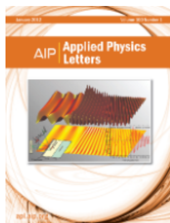

Surfactant-mediated growth of InGaAs multiple-quantum-well lasers emitting at 2.1μm by metalorganic vapor phase epitaxy

Author: Tomonari Sato, Manabu Mitsuhara, Takao Watanabe, et al

Publication: Applied Physics Letters

Publisher: AIP Publishing

Date: Nov 21, 2005

Rights managed by AIP Publishing.

Order Completed

Thank you for your order.

This Agreement between University of Waterloo -- Ida Sadeghi ("You") and AIP Publishing ("AIP Publishing") consists of your license details and the terms and conditions provided by AIP Publishing and Copyright Clearance Center.

Your confirmation email will contain your order number for future reference.

License Number	5104421069200	Printable Details
License date	Jul 08, 2021	

Licensed Content

Licensed Content Publisher	AIP Publishing
Licensed Content Publication	Applied Physics Letters
Licensed Content Title	Surfactant-mediated growth of InGaAs multiple-quantum-well lasers emitting at 2.1μm by metalorganic vapor phase epitaxy
Licensed Content Author	Tomonari Sato, Manabu Mitsuhara, Takao Watanabe, et al
Licensed Content Date	Nov 21, 2005
Licensed Content Volume	87
Licensed Content Issue	21

Order Details

Type of Use	Thesis/Dissertation
Requestor type	Student
Format	Electronic
Portion	Figure/Table
Number of figures/tables	1
Will you be translating?	No

About Your Work

Title	Student
Institution name	University of Waterloo
Expected presentation date	Jul 2021

Additional Data

Portions	Fig. 3

Home | Help | Email Support | Ida Sadeghi

Surfactant enhanced growth of GaNAs and InGaNAs using bismuth

Author: S. Tixier,M. Adamcyk,E.C. Young,J.H. Schmid,T. Tiedje
Publication: Journal of Crystal Growth
Publisher: Elsevier
Date: April 2003

Copyright © 2002 Elsevier Science B.V. All rights reserved.

Order Completed

Thank you for your order.

This Agreement between University of Waterloo -- Ida Sadeghi ("You") and Elsevier ("Elsevier") consists of your license details and the terms and conditions provided by Elsevier and Copyright Clearance Center.

Your confirmation email will contain your order number for future reference.

License Number	5104420202381
License date	Jul 08, 2021

Printable Details

Licensed Content

Licensed Content Publisher	Elsevier
Licensed Content Publication	Journal of Crystal Growth
Licensed Content Title	Surfactant enhanced growth of GaNAs and InGaNAs using bismuth
Licensed Content Author	S. Tixier,M. Adamcyk,E.C. Young,J.H. Schmid,T. Tiedje
Licensed Content Date	Apr 1, 2003
Licensed Content Volume	251
Licensed Content Issue	1-4
Licensed Content Pages	6

Order Details

Type of Use	reuse in a thesis/dissertation
Portion	figures/tables/illustrations
Number of figures/tables/illustrations	1
Format	electronic
Are you the author of this Elsevier article?	No
Will you be translating?	No

About Your Work

Title	Student
Institution name	University of Waterloo
Expected presentation date	Jul 2021

Additional Data

Portions	Fig. 1

Home | Help | Email Support | Ida Sadeghi

Chapter:
Chapter 1 Molecular beam epitaxy fundamentals, historical background and future prospects

Book: Molecular Beam Epitaxy

Author: Secondo Franchi

Publisher: Elsevier

Date: 2013

Copyright © 2013 Elsevier Inc. All rights reserved.

Order Completed

Thank you for your order.

This Agreement between University of Waterloo -- Ida Sadeghi ("You") and Elsevier ("Elsevier") consists of your license details and the terms and conditions provided by Elsevier and Copyright Clearance Center.

Your confirmation email will contain your order number for future reference.

License Number	5104441444312
License date	Jul 08, 2021

Printable Details

Licensed Content

Licensed Content Publisher	Elsevier
Licensed Content Publication	Elsevier Books
Licensed Content Title	Molecular Beam Epitaxy
Licensed Content Author	Secondo Franchi
Licensed Content Date	Jan 1, 2013
Licensed Content Pages	46

Order Details

Type of Use	reuse in a thesis/dissertation
Portion	figures/tables/illustrations
Number of figures/tables/illustrations	1
Format	electronic
Are you the author of this Elsevier chapter?	No
Will you be translating?	No

About Your Work

Title	Student
Institution name	University of Waterloo
Expected presentation date	Jul 2021

Additional Data

Portions	Fig. 1.4

CCC RightsLink®

Home | Help | Email Support | Ida Sadeghi

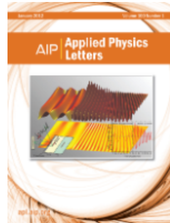

Scanning moiré fringe imaging for quantitative strain mapping in semiconductor devices

Author: Suhyun Kim, Sungho Lee, Yoshifumi Oshima, et al

Publication: Applied Physics Letters

Publisher: AIP Publishing

Date: Apr 22, 2013

Rights managed by AIP Publishing.

Order Completed

Thank you for your order.

This Agreement between University of Waterloo -- Ida Sadeghi ("You") and AIP Publishing ("AIP Publishing") consists of your license details and the terms and conditions provided by AIP Publishing and Copyright Clearance Center.

Your confirmation email will contain your order number for future reference.

License Number	5105121415767
License date	Jul 09, 2021

Printable Details

Licensed Content

Licensed Content Publisher	AIP Publishing
Licensed Content Publication	Applied Physics Letters
Licensed Content Title	Scanning moiré fringe imaging for quantitative strain mapping in semiconductor devices
Licensed Content Author	Suhyun Kim, Sungho Lee, Yoshifumi Oshima, et al
Licensed Content Date	Apr 22, 2013
Licensed Content Volume	102
Licensed Content Issue	16

Order Details

Type of Use	Thesis/Dissertation
Requestor type	Student
Format	Electronic
Portion	Figure/Table
Number of figures/tables	1
Will you be translating?	No

About Your Work

Title	Student
Institution name	University of Waterloo
Expected presentation date	Jul 2021

Additional Data

Portions	Fig. 1

Home Help Email Support Ida Sadeghi

Calculations of electron inelastic mean free paths. IX. Data for 41 elemental solids over the 50 eV to 30 keV range

Author: S. Tanuma,, C. J. Powell, D. R. Penn
Publication: Surface & Interface Analysis
Publisher: John Wiley and Sons
Date: Feb 8, 2011

Copyright © 2010 John Wiley & Sons, Ltd.

Order Completed

Thank you for your order.

This Agreement between University of Waterloo -- Ida Sadeghi ("You") and John Wiley and Sons ("John Wiley and Sons") consists of your license details and the terms and conditions provided by John Wiley and Sons and Copyright Clearance Center.

Your confirmation email will contain your order number for future reference.

License Number	5104450476297
License date	Jul 08, 2021

Printable Details

Licensed Content

Licensed Content Publisher	John Wiley and Sons
Licensed Content Publication	Surface & Interface Analysis
Licensed Content Title	Calculations of electron inelastic mean free paths. IX. Data for 41 elemental solids over the 50 eV to 30 keV range
Licensed Content Author	S. Tanuma,, C. J. Powell, D. R. Penn
Licensed Content Date	Feb 8, 2011
Licensed Content Volume	43
Licensed Content Issue	3
Licensed Content Pages	25

Order Details

Type of use	Dissertation/Thesis
Requestor type	University/Academic
Format	Electronic
Portion	Figure/table
Number of figures/tables	1
Will you be translating?	No

About Your Work

Title	Student
Institution name	University of Waterloo
Expected presentation date	Jul 2021

Additional Data

Portions	Fig. 25

Home Help Email Support Ida Sadeghi

On the optimum off-cut angle for the growth on InP(111)B substrates by molecular beam epitaxy

Author: Ida Sadeghi, Man Chun Tam, Zbigniew Roman Wasilewski
Publication: Journal of Vacuum Science & Technology B
Publisher: American Vacuum Society
Date: May 1, 2019

Rights managed by AIP Publishing.

Order Completed

Thank you for your order.

This Agreement between University of Waterloo -- Ida Sadeghi ("You") and AIP Publishing ("AIP Publishing") consists of your license details and the terms and conditions provided by AIP Publishing and Copyright Clearance Center.

Your confirmation email will contain your order number for future reference.

Printable Details

License Number	5104450837380
License date	Jul 08, 2021

Licensed Content

Licensed Content Publisher	American Vacuum Society
Licensed Content Publication	Journal of Vacuum Science & Technology B
Licensed Content Title	On the optimum off-cut angle for the growth on InP(111)B substrates by molecular beam epitaxy
Licensed Content Author	Ida Sadeghi, Man Chun Tam, Zbigniew Roman Wasilewski
Licensed Content Date	May 1, 2019
Licensed Content Volume	37
Licensed Content Issue	3

Order Details

Type of Use	Thesis/Dissertation
Requestor type	Author (original article)
Format	Electronic
Portion	Figure/Table
Number of figures/tables	4
Will you be translating?	No

About Your Work

Title	Student
Institution name	University of Waterloo
Expected presentation date	Jul 2021

Additional Data

Portions	Figs. 1, 3, 4, 5

References

[1]K. Sato, M. R. Fahy, and B. A. Joyce, “The growth of high quality GaAs on GaAs(111)A”, Japanese journal of applied physics **33**, L905 (1994).

[2]N. Bécourt, F. Peiró, A. Cornet, J. Morante, P. Gorostiza, G. Halkias, K. Michelakis, and A. Georgakilas, “Surface step bunching and crystal defects in InAlAs films grown by molecular beam epitaxy on (111)B InP substrates”, Applied physics letters **71**, 2961–2963 (1997).

[3]M. Fahy, K. Sato, and B. Joyce, “Reflection high-energy electron diffraction intensity oscillations during the growth by molecular beam epitaxy of GaAs(111)A”, Applied physics letters **64**, 190–192 (1994).

[4]H. Hou and C. Tu, “Homoepitaxial growth of InP on (111)B substrates by gas-source molecular beam epitaxy”, Applied physics letters **62**, 281–283 (1993).

[5]K. Rajkumar, P. Chen, and A. Madhukar, “A transmission electron microscope study of twin structure in GaAs/GaAs(111)B grown via molecular-beam epitaxy”, Journal of applied physics **69**, 2219–2223 (1991).

[6]L. J. Schowalter, K. Yang, and T. Thundat, “Atomic step organization in homoepitaxial growth on GaAs(111)B substrates”, Journal of Vacuum Science & Technology B: Microelectronics and Nanometer Structures Processing, Measurement, and Phenomena **12**, 2579–2583 (1994).

[7]D. Woolf, D. Westwood, and R. Williams, “The homoepitaxial growth of GaAs (111)A and (111)B by molecular beam epitaxy: an investigation of the temperature-dependent surface reconstructions and bulk electrical conductivity transitions”, Semiconductor science and technology **8**, 1075 (1993).

[8]T. Yamamoto, M. Inai, A. Shinoda, T. Takebe, and T. Watanabe, “Misorientation dependence of crystal structures and electrical properties of Si-doped AlAs grown on (111)A GaAs by molecular beam epitaxy”, Japanese journal of applied physics **32**, 3346 (1993).

[9]K. Yang, L. Schowalter, B. Laurich, I. Campell, and D. Smith, "Molecular beam epitaxy on exact and vicinal GaAs(111) substrates", Journal of Vacuum Science & Technology B: Microelectronics and Nanometer Structures Processing, Measurement, and Phenomena **11**, 779–782 (1993).

[10]J. McFee, B. Miller, and K. Bachmann, "Molecular beam epitaxial growth of InP", Journal of the Electrochemical Society **124**, 259 (1977).

[11]G. Wang, B. Liu, A. Balocchi, P. Renucci, C. Zhu, T. Amand, C. Fontaine, and X. Marie, "Gate control of the electron spin-diffusion length in semiconductor quantum wells", Nature communications **4**, 1–5 (2013).

[12]M. Yamada, F. Kuroda, M. Tsukahara, S. Yamada, T. Fukushima, K. Sawano, T. Oguchi, and K. Hamaya, "Spin injection through energy-band symmetry matching with high spin polarization in atomically controlled ferromagnet/ferromagnet/semiconductor structures", NPG Asia Materials **12**, 1–9 (2020).

[13]C. D. Yerino, P. J. Simmonds, B. Liang, D. Jung, C. Schneider, S. Unsleber, M. Vo, D. L. Huffaker, S. Höfling, M. Kamp, et al., "Strain-driven growth of gaas (111) quantum dots with low fine structure splitting", Applied Physics Letters **105**, 251901 (2014).

[14]C. F. Schuck, R. A. McCown, A. Hush, A. Mello, S. Roy, J. W. Spinuzzi, B. Liang, D. L. Huffaker, and P. J. Simmonds, "Self-assembly of (111)-oriented tensile-strained quantum dots by molecular beam epitaxy", Journal of Vacuum Science & Technology B, Nanotechnology and Microelectronics: Materials, Processing, Measurement, and Phenomena **36**, 031803 (2018).

[15]C. F. Schuck, S. K. Roy, T. Garrett, Q. Yuan, Y. Wang, C. I. Cabrera, K. A. Grossklaus, T. E. Vandervelde, B. Liang, and P. J. Simmonds, "Anomalous stranski-krastanov growth of (111)-oriented quantum dots with tunable wetting layer thickness", Scientific reports **9**, 1–10 (2019).

[16]K. Ueno, T. Shimada, K. Saiki, and A. Koma, "Heteroepitaxial growth of layered transition metal dichalcogenides on sulfur-terminated GaAs (111) surfaces", Applied physics letters **56**, 327–329 (1990).

[17]Y. Takagaki and B. Jenichen, "Epitaxial growth of Bi_2Se_3 layers on inp substrates by hot wall epitaxy", Semiconductor Science and Technology **27**, 035015 (2012).

[18]Y. Onose, R. Yoshimi, A. Tsukazaki, H. Yuan, T. Hidaka, Y. Iwasa, M. Kawasaki, and Y. Tokura, "Pulsed laser deposition and ionic liquid gate control of epitaxial Bi_2Se_3 thin films", Applied physics express **4**, 083001 (2011).

[19]R. J. Dietz, M. Gerhard, D. Stanze, M. Koch, B. Sartorius, and M. Schell, "THz generation at 1.55 μm excitation: six-fold increase in THz conversion efficiency by separated photoconductive and trapping regions", Optics express **19**, 25911–25917 (2011).

[20]A. Chin, P. Martin, P. Ho, J. Ballingall, T.-h. Yu, and J. Mazurowski, "High quality (111)B GaAs, AlGaAs, AlGaAs/GaAs modulation doped heterostructures and a GaAs/InGaAs/-GaAs quantum well", Applied physics letters **59**, 1899–1901 (1991).

[21]L. Vina and W. Wang, "AlGaAs/GaAs (111) heterostructures grown by molecular beam epitaxy", Applied physics letters **48**, 36–37 (1986).

[22]P. Chen, K. Rajkumar, and A. Madhukar, "Growth control of GaAs epilayers with specular surface free of pyramids and twins on nonmisoriented (111)B substrates", Applied physics letters **58**, 1771–1773 (1991).

[23]K. Tsutsui, H. Mizukami, O. Ishiyama, S. Nakamura, and S. Furukawa, "Optimum growth conditions of GaAs(111)B layers for good electrical properties by molecular beam epitaxy", Japanese journal of applied physics **29**, 468 (1990).

[24]C. Guerret-Piecourt and C. Fontaine, "Temperature effect on surface flatness of molecular beam epitaxy homoepitaxial layers grown on nominal and vicinal (111)B GaAs substrates", Journal of Vacuum Science & Technology B: Microelectronics and Nanometer Structures Processing, Measurement, and Phenomena **16**, 204–209 (1998).

[25]A. Gomyo, T. Suzuki, S. Iijima, H. Hotta, H. Fujii, S. Kawata, K. Kobayashi, Y. Ueno, and I. Hino, "Nonexistence of long-range order in $Ga_{0.5}In_{0.5}P$ epitaxial layers grown on (111)B and (110) GaAs substrates", Japanese journal of applied physics **27**, L2370 (1988).

[26]T. Hayakawa, M. Kondo, T. Suyama, K. Takahashi, S. Yamamoto, and T. Hijikata, "Reduction in threshold current density of quantum well lasers grown by molecular beam epitaxy on 0.5°misoriented (111)B substrates", Japanese journal of applied physics **26**, L302 (1987).

[27]A. Cho, "Morphology of epitaxial growth of GaAs by a molecular beam method: the observation of surface structures", Journal of Applied Physics **41**, 2780–2786 (1970).

[28]T. Anan, K. Nishi, and S. Sugou, "Critical layer thickness on (111)B-oriented InGaAs/-GaAs heteroepitaxy", Applied physics letters **60**, 3159–3161 (1992).

[29]L.-C. Chou, Y.-R. Lin, C.-T. Wan, and H.-H. Lin, "[111]B-oriented GaAsSb grown by gas source molecular beam epitaxy", Microelectronics journal **37**, 1511–1514 (2006).

[30]E. Caridi, T. Chang, K. Goossen, and L. Eastman, “Direct demonstration of a misfit strain-generated electric field in a [111] growth axis zinc-blende heterostructure”, Applied physics letters **56**, 659–661 (1990).

[31]K. Nishi and T. Anan, “Optical characterizations of (111) oriented InGaAs/InAlAs strained quantum wells grown on inp substrates”, Journal of applied physics **70**, 5004–5009 (1991).

[32]M. Hopkinson, J. David, E. Khoo, A. Pabla, J. Woodhead, and G. Rees, “$In_xGa_{1-x}As$/InP quantum well structures grown on [111] B InP”, Microelectronics journal **26**, 805–810 (1995).

[33]W. Yeo, R. Dimitrov, W. Schaff, and L. Eastman, “Material properties of bulk InGaAs and InAlAs/InGaAs heterostructures grown on (111)B and (111)B misoriented by 1°towards <211> InP substrates”, Applied Physics Letters **77**, 4292–4294 (2000).

[34]T. Higashino, Y. Kawamura, M. Fujimoto, A. Kondo, H. Takasaki, and N. Inoue, “Molecular beam epitaxial growth and characterization of $GaAs_{1-y}Sb_y$ layers on (111)B InP substrates”, Japanese journal of applied physics **41**, 1012 (2002).

[35]G. Olsen, T. Zamerowski, and F. Hawrylo, “Vapor growth of InGaAs and InP on (100), (110), (111), (311) and (511) InP substrates”, Journal of Crystal Growth **59**, 654–658 (1982).

[36]H. Yamaguchi, M. Kawashima, and Y. Horikoshi, “Migration-enhanced epitaxy”, Applied Surface Science **33-34**, 406–412 (1988).

[37]Y. Horikoshi, M. Kawashima, and H. Yamaguchi, “Migration-enhanced epitaxy of GaAs and AlGaAs”, Japanese journal of applied physics **27**, 169 (1988).

[38]Y. Horikoshi and M. Kawashima, “Migration-enhanced epitaxy of GaAs and AlGaAs”, Journal of Crystal Growth **95**, 17–22 (1989).

[39]Y. Horikoshi, H. Yamaguchi, F. Briones, and M. Kawashima, “Growth process of III-V compound semiconductors by migration-enhanced epitaxy”, Journal of crystal growth **105**, 326–338 (1990).

[40]H. Imamoto, F. Sato, K. Imanaka, and M. Shimura, “Migration-enhanced epitaxy on a (111)B oriented GaAs substrate”, Applied physics letters **55**, 115–116 (1989).

[41]M. A. Wistey, A. K. Baraskar, U. Singisetti, G. J. Burek, B. Shin, E. Kim, P. C. McIntyre, A. C. Gossard, and M. J. Rodwell, “Control of InGaAs facets using metal modulation epitaxy (MME)”, arXiv preprint arXiv:1408.3714 (2014).

[42]M. Ilg, D. Eissler, C. Lange, and K. Ploog, “Surfactant-mediated molecular beam epitaxy of high-quality (111)B-GaAs”, Applied Physics A **56**, 397–399 (1993).

[43]M. Pillai, S.-S. Kim, S. Ho, and S. Barnett, "Growth of $In_xGa_{1-x}As/GaAs$ heterostructures using Bi as a surfactant", Journal of Vacuum Science & Technology B: Microelectronics and Nanometer Structures Processing, Measurement, and Phenomena **18**, 1232–1236 (2000).

[44]N. M. Burford and M. O. El-Shenawee, "Review of terahertz photoconductive antenna technology", Optical Engineering **56**, 010901 (2017).

[45]M. Tonouchi, "Cutting-edge terahertz technology", Nature photonics **1**, 97–105 (2007).

[46]B. Sartorius, H. Roehle, H. Künzel, J. Böttcher, M. Schlak, D. Stanze, H. Venghaus, and M. Schell, "All-fiber terahertz time-domain spectrometer operating at 1.5 μm telecom wavelengths", Optics express **16**, 9565–9570 (2008).

[47]A. Takazato, M. Kamakura, T. Matsui, J. Kitagawa, and Y. Kadoya, "Terahertz wave emission and detection using photoconductive antennas made on low-temperature-grown InGaAs with 1.56 μ m pulse excitation", Applied physics letters **91**, 011102 (2007).

[48]G. Metze and A. Calawa, "Effects of very low growth rates on GaAs grown by molecular beam epitaxy at low substrate temperatures", Applied Physics Letters **42**, 818–820 (1983).

[49]J. Neave and B. Joyce, "Temperature range for growth of autoepitaxial GaAs films by MBE", Journal of Crystal Growth **43**, 204–208 (1978).

[50]M. Melloch, N. Otsuka, J. Woodall, A. Warren, and J. Freeouf, "Formation of arsenic precipitates in GaAs buffer layers grown by molecular beam epitaxy at low substrate temperatures", Applied physics letters **57**, 1531–1533 (1990).

[51]Z. Liliental-Weber, G. Cooper, R. Mariella Jr, and C. Kocot, "The role of As in molecular-beam epitaxy GaAs layers grown at low temperature", Journal of Vacuum Science & Technology B: Microelectronics and Nanometer Structures Processing, Measurement, and Phenomena **9**, 2323–2327 (1991).

[52]Z. Liliental-Weber, W. Swider, K. M. Yu, J. Kortright, F. Smith, and A. Calawa, "Breakdown of crystallinity in low-temperature-grown GaAs layers", Applied physics letters **58**, 2153–2155 (1991).

[53]Z. Liliental-Weber, "Crystal structure of LT GaAs layers before and after annealing", MRS Online Proceedings Library **241**, 101–112 (1991).

[54]K. M. Yu, M. Kaminska, and Z. Liliental-Weber, "Characterization of GaAs layers grown by low temperature molecular beam epitaxy using ion beam techniques", Journal of applied physics **72**, 2850–2856 (1992).

[55]M. Lagadas, Z. Hatzopoulos, K. Tsagaraki, M. Calamiotou, C. Lioutas, and A. Christou, "The effect of arsenic overpressure on the structural properties GaAs grown at low temperature", Journal of applied physics **80**, 4377–4383 (1996).

[56]D. C. Look, "Molecular beam epitaxial GaAs grown at low temperatures", Thin solid films **231**, 61–73 (1993).

[57]D. Eaglesham, L. Pfeiffer, K. West, and D. Dykaar, "Limited thickness epitaxy in GaAs molecular beam epitaxy near 200°C", Applied physics letters **58**, 65–67 (1991).

[58]A. Claverie and Z. Liliental-Weber, "Extended defects and precipitates in LT-GaAs, LT-InAlAs and LT-InP", in European materials research society symposia proceedings, Vol. 40 (Elsevier, 1993), pp. 45–54.

[59]R. Stall, C. Wood, P. Kirchner, and L. Eastman, "Growth-parameter dependence of deep levels in molecular-beam-epitaxial GaAs", Electronics Letters **16**, 171–172 (1980).

[60]F. Smith, A. Calawa, C.-L. Chen, M. Manfra, and L. Mahoney, "New MBE buffer used to eliminate backgating in GaAs MESFETs", IEEE Electron Device Letters **9**, 77–80 (1988).

[61]K. McIntosh, K. Nichols, S. Verghese, and E. Brown, "Investigation of ultrashort photocarrier relaxation times in low-temperature-grown GaAs", Applied physics letters **70**, 354–356 (1997).

[62]J. Y. Tsao, *Materials fundamentals of molecular beam epitaxy* (Academic Press, 2012).

[63]J. Miller and T. Low, "Low-temperature growth of GaAs and AlGaAs by MBE and effects of post-growth thermal annealing", Journal of crystal growth **111**, 30–38 (1991).

[64]Z. Liliental-Weber, K. M. Yu, J. Washburn, and D. C. Look, "Anomalies in annealed LT-GaAs samples", Journal of electronic materials **22**, 1395–1399 (1993).

[65]M. Melloch, J. Woodall, E. Harmon, N. Otsuka, F. H. Pollak, D. Nolte, R. Feenstra, and M. Lutz, "Low-temperature grown III-V materials", Annual Review of Materials Science **25**, 547–600 (1995).

[66]M. Mittendorff, M. Xu, R. J. Dietz, H. Künzel, B. Sartorius, H. Schneider, M. Helm, and S. Winnerl, "Large area photoconductive terahertz emitter for 1.55 μm excitation based on an InGaAs heterostructure", Nanotechnology **24**, 214007 (2013).

[67]Z. Liliental-Weber, A. Claverie, J. Washburn, F. Smith, and R. Calawa, "Microstructure of annealed low-temperature-grown GaAs layers", Applied physics A **53**, 141–146 (1991).

[68]G. Galiev, E. Klimova, S. Pushkarev, A. Klochkov, I. Trunkin, A. Vasiliev, and P. Maltsev, "Low-temperature epitaxial growth of InGaAs films on InP (100) and InP (411) A substrates", Crystallography Reports **62**, 589–596 (2017).

[69]J. Ibbetson, J. Speck, A. Gossard, and U. Mishra, “Observation of arsenic precipitates in GaInAs grown at low temperature on InP”, Applied physics letters **62**, 2209–2211 (1993).

[70]B. Grandidier, H. Chen, R. Feenstra, D. McInturff, P. Juodawlkis, and S. Ralph, “Scanning tunneling microscopy and spectroscopy of arsenic antisites in low temperature grown InGaAs”, Applied physics letters **74**, 1439–1441 (1999).

[71]P. Werner, Z. Liliental-Weber, K. M. Yu, and E. Weber, “Structure investigations of low-temperature MBE grown InAlAs layers on InP [001] substrate”, in Proceedings of the 7th conference on semi-insulating iii-v materials, (IEEE, 1992), pp. 167–170.

[72]K. Mahalingam, N. Otsuka, M. Melloch, and J. Woodall, “Arsenic precipitates in $Al_{0.3}Ga_{0.7}As/GaAs$ multiple superlattice and quantum well structures”, Applied Physics Letters **60**, 3253–3255 (1992).

[73]K. Mahalingam, N. Otsuka, M. Melloch, J. Woodall, and A. Warren, “Arsenic precipitate accumulation and depletion zones at AlGaAs/GaAs heterojunctions grown at low substrate temperature by molecular beam epitaxy”, Journal of Vacuum Science & Technology B: Microelectronics and Nanometer Structures Processing, Measurement, and Phenomena **10**, 812–814 (1992).

[74]M. Melloch, J. Woodall, N. Otsuka, K. Mahalingam, C. Chang, and D. Nolte, “GaAs, AlGaAs, and InGaAs epilayers containing As clusters: semimetal/semiconductor composites”, Materials Science and Engineering: B **22**, 31–36 (1993).

[75]M. Melloch, C. Chang, N. Otsuka, K. Mahalingam, J. Woodall, and P. Kirchner, “Two-dimensional arsenic-precipitate structures in GaAs”, Journal of crystal growth **127**, 499–502 (1993).

[76]M. Melloch, N. Otsuka, K. Mahalingam, C. Chang, J. Woodall, G. Pettit, P. Kirchner, F. Cardone, A. Warren, and D. Nolte, “Arsenic cluster dynamics in doped GaAs”, Journal of applied physics **72**, 3509–3513 (1992).

[77]B. Joyce, J. Neave, J. Zhang, D. Vvedensky, S. Clarke, K. Hugill, T. Shitara, and A. Myers-Beaghton, “Growth of III-V compounds on vicinal planes by molecular beam epitaxy”, Semiconductor Science and Technology **5**, 1147 (1990).

[78]M. Holland, “A simple model for MBE growth controlled by group III atom migration”, Journal of crystal growth **251**, 29–34 (2003).

[79]J. Neave, P. Dobson, B. Joyce, and J. Zhang, “Reflection high-energy electron diffraction oscillations from vicinal surfaces—a new approach to surface diffusion measurements”, Applied physics letters **47**, 100–102 (1985).

[80]B. Joyce, P. Dobson, J. Neave, K. Woodbridge, J. Zhang, P. Larsen, and B. Bolger, "RHEED studies of heterojunction and quantum well formation during MBE growth—from multiple scattering to band offsets", Surface Science **168**, 423–438 (1986).

[81]B. Joyce, P. Dobson, J. Neave, and J. Zhang, "The determination of MBE growth mechanisms using dynamic RHEED techniques", Surface Science **174**, 1–9 (1986).

[82]Y. Takano, Y. Kanaya, T. Torihata, K. Pak, and H. Yonezu, "Growth modes and reduction of hillock density in migration enhanced epitaxy of GaAs(111)B", Journal of crystal growth **102**, 341–343 (1990).

[83]T. Shitara, E. Kondo, and T. Nishinaga, "RHEED oscillation and surface diffusion length on GaAs(111)B surface", Journal of crystal growth **99**, 530–534 (1990).

[84]Y. Ababou, R. Masut, and A. Yelon, "Low-pressure metalorganic vapor phase epitaxy of InP on (111) substrates", Journal of Vacuum Science & Technology A: Vacuum, Surfaces, and Films **16**, 790–793 (1998).

[85]M. Kasu and T. Fukui, "Multi-atomic steps on metalorganic chemical vapor deposition-grown GaAs vicinal surfaces studied by atomic force microscopy", Japanese Journal of Applied Physics **31**, L864 (1992).

[86]R. Grey, J. David, G. Hill, A. Pabla, M. Pate, G. Rees, P. Robson, P. Rodriguez-Girones, T. Sale, J. Woodhead, et al., "Growth of pseudomorphic InGaAs/GaAs quantum wells on [111]B GaAs for strained layer, piezoelectric, optoelectronic devices", Microelectronics journal **26**, 811–820 (1995).

[87]M. Tanaka, T. Suzuki, and T. Nishinaga, "Surface diffusion of Al and Ga atoms on GaAs (001) and (111)B vicinal surfaces in molecular beam epitaxy", Journal of crystal growth **111**, 168–172 (1991).

[88]M. Tanaka and H. Sakaki, "Atomistic models of interface structures of $GaAs-Al_xGa_{1-x}As$ ($x = 0.2-1$) quantum wells grown by interrupted and uninterrupted MBE", Journal of crystal Growth **81**, 153–158 (1987).

[89]M. Kasu and N. Kobayashi, "Surface diffusion kinetics of GaAs and AlAs metalorganic vapor-phase epitaxy", Journal of crystal growth **170**, 246–250 (1997).

[90]T. Nishinaga, X. Shen, and D. Kishimoto, "Surface diffusion length of cation incorporation studied by microprobe-RHEED/SEM MBE", Journal of crystal growth **163**, 60–66 (1996).

[91]M. Tanaka and H. Sakaki, "Surface migration study of atoms and formation of truly-smooth top and bottom heterointerfaces in GaAs/AlAs quantum wells by temperature-switched technique in molecular beam epitaxy", Superlattices and Microstructures **4**, 237–241 (1988).

[92]N. Sibirev, V. Dubrovskii, E. Arshanskii, G. Cirlin, Y. B. Samsonenko, and V. Ustinov, "On diffusion lengths of Ga adatoms on AlAs(111) and GaAs(111) surfaces", Technical Physics **54**, 586–589 (2009).

[93]P. Chen, K. Rajkumar, and A. Madhukar, "Relation between reflection high-energy electron diffraction specular beam intensity and the surface atomic structure/surface morphology of GaAs(111)B", Journal of Vacuum Science & Technology B: Microelectronics and Nanometer Structures Processing, Measurement, and Phenomena **9**, 2312–2316 (1991).

[94]C. B. Duke, "Semiconductor surface reconstruction: the structural chemistry of two-dimensional surface compounds", Chemical reviews **96**, 1237–1260 (1996).

[95]D. L. Rode, "Surface dislocation theory of reconstructed crystals: VPE GaAs", physica status solidi (a) **32**, 425–434 (1975).

[96]H. Ruda and G. Jiang, "Role of surface interactions in determining surface structure and state formation in iii-v semiconductors", Scanning Microscopy **8**, 8 (1994).

[97]M. Pashley, "Electron counting model and its application to island structures on molecular-beam epitaxy grown GaAs(001) and ZnSe(001)", Physical Review B **40**, 10481 (1989).

[98]K. Haberern and M. Pashley, "GaAs(111)A - (2×2) reconstruction studied by scanning tunneling microscopy", Physical Review B **41**, 3226 (1990).

[99]D. Woolf, D. Westwood, and R. Williams, "Surface reconstructions of GaAs(111)A and (111)B: a static surface phase study by reflection high-energy electron diffraction", Applied physics letters **62**, 1370–1372 (1993).

[100]A. Ohtake, J. Nakamura, T. Komura, T. Hanada, T. Yao, H. Kuramochi, and M. Ozeki, "Surface structures of GaAs (111) A, B - (2×2)", Physical Review B **64**, 045318 (2001).

[101]A. Ohtake, S. Goto, and J. Nakamura, "Atomic structure and passivated nature of the Se-treated GaAs(111)B surface", Scientific reports **8**, 1–8 (2018).

[102]T. Akiyama, T. Kondo, H. Tatematsu, K. Nakamura, and T. Ito, "Ab initio approach to reconstructions of the InP(111)A surface: role of hydrogen atoms passivating surface dangling bonds", Physical Review B **78**, 205318 (2008).

[103]C. Li, Y. Sun, D. Law, S. Visbeck, and R. Hicks, "Reconstructions of the InP(111)A surface", Physical Review B **68**, 085320 (2003).

[104]H. Yi, "Theoretical study of bias-dependent scanning tunneling microscopy images of a p trimer reconstruction of a InP(111)A-(2 × 2) surface", Journal of the Korean Physical Society **52**, 1246–1249 (2008).

[105]H. Yi, "Theoretical investigations on the InP(111)A-(2 × 2) surface", Journal of the Korean Physical Society **53**, 1061–1064 (2008).

[106]M. Shimomura, Y. Sano, N. Sanada, L. Cao, and Y. Fukuda, "Surface structure and electronic states of sulfur-treated inp (111)A studied by LEED, AES, STM, and IPES", Applied surface science **244**, 153–156 (2005).

[107]H. Shu, X. Chen, R. Dong, X. Wang, and W. Lu, "Thermodynamic phase diagram for hydrogen on polar InP(111)B surfaces", Journal of Applied Physics **107**, 063516 (2010).

[108]H. Yao and K. Itaya, "Atomically resolved scanning tunneling microscopy images of InP (001),(111)A, and (111)B surfaces in sulfuric acid solution", Journal of the Electrochemical Society **145**, 3090 (1998).

[109]K. E. Sautter, C. F. Schuck, J. C. Smith, K. D. Vallejo, T. A. Garrett, J. Soares, H. J. Coleman, M. M. Henry, E. Jankowski, C. Ratsch, et al., "Self-assembly of ge and gaas quantum dots under tensile strain on inalas (111) a", Crystal Growth & Design **21**, 1674–1682 (2021).

[110]J. Thornton, D. Woolf, and P. Weightman, "Reconstructions of the GaAs(111)B surface", Applied surface science **123**, 115–119 (1998).

[111]K. Yang and L. Schowalter, "Surface reconstruction phase diagram and growth on GaAs(111)B substrates by molecular beam epitaxy", Applied physics letters **60**, 1851–1853 (1992).

[112]D. Woolf, Z. Sobiesierski, D. I. Westwood, and R. Williams, "The molecular beam epitaxial growth of GaAs/GaAs(111)B: doping and growth temperature studies", Journal of applied physics **71**, 4908–4915 (1992).

[113]D. Biegelsen, R. Bringans, J. Northrup, and L.-E. Swartz, "Reconstructions of GaAs(111) surfaces observed by scanning tunneling microscopy", Physical Review Letters **65**, 452 (1990).

[114]S. Mankefors, P. Nilsson, and J. Kanski, "Semiconductor polar surfaces: mechanisms of the stability of non-reconstructed ($\overline{111}$) surfaces", Surface science **443**, L1049–L1054 (1999).

[115]H. Sugiura, T. Nishida, R. Iga, T. Yamada, and T. Tamamura, "Facet growth of InP/InGaAs layers on SiO_2-masked InP by chemical beam epitaxy", Journal of crystal growth **121**, 579–586 (1992).

[116]R. F. Farrow, *Molecular beam epitaxy: applications to key materials* (Elsevier, 1995).

[117]J. Villain, "Continuum models of crystal growth from atomic beams with and without desorption", Journal de physique I **1**, 19–42 (1991).

[118]M. Johnson, C. Orme, A. Hunt, D. Graff, J. Sudijono, L. Sander, and B. Orr, "Stable and unstable growth in molecular beam epitaxy", Physical review letters **72**, 116 (1994).

[119]H. Yamada, O. Ichikawa, N. Fukuhara, and M. Hata, "Formation and reduction of pyramidal hillocks on InGaAs/InP(111)A", physica status solidi (b) **253**, 644–647 (2016).

[120]J. Tersoff, Y. Phang, Z. Zhang, and M. Lagally, "Step-bunching instability of vicinal surfaces under stress", Physical review letters **75**, 2730 (1995).

[121]M. Yoon, H. N. Lee, W. Hong, H. M. Christen, Z. Zhang, and Z. Suo, "Dynamics of step bunching in heteroepitaxial growth on vicinal substrates", Physical review letters **99**, 055503 (2007).

[122]M. Shinohara and N. Inoue, "Behavior and mechanism of step bunching during metalorganic vapor phase epitaxy of GaAs", Applied physics letters **66**, 1936–1938 (1995).

[123]M. Xie, S. Leung, and S. Tong, "What causes step bunching—negative ehrlich–schwoebel barrier versus positive incorporation barrier", Surface science **515**, L459–L463 (2002).

[124]K. Pond, A. Gossard, A. Lorke, and P. Petroff, "Role of steps in epitaxial growth", Materials Science and Engineering: B **30**, 121–125 (1995).

[125]K. W. Ng, W. S. Ko, F. Lu, and C. J. Chang-Hasnain, "Metastable growth of pure wurtzite InGaAs microstructures", Nano letters **14**, 4757–4762 (2014).

[126]R. Van Santen, "The ostwald step rule", The Journal of Physical Chemistry **88**, 5768–5769 (1984).

[127]N. Niekawa and M. Kitamura, "Role of epitaxy-mediated transformation in ostwald's step rule: a theoretical study", CrystEngComm **15**, 6932–6941 (2013).

[128]E. A. Anyebe, I. Sandall, Z. Jin, A. M. Sanchez, M. K. Rajpalke, T. D. Veal, Y. Cao, H. Li, R. Harvey, and Q. Zhuang, "Optimization of self-catalyzed InAs nanowires on flexible graphite for photovoltaic infrared photodetectors", Scientific reports **7**, 1–9 (2017).

[129]J. Johansson, K. A. Dick, P. Caroff, M. E. Messing, J. Bolinsson, K. Deppert, and L. Samuelson, "Diameter dependence of the wurtzite- zinc blende transition in InAs nanowires", The Journal of Physical Chemistry C **114**, 3837–3842 (2010).

[130]F. Glas, J.-C. Harmand, and G. Patriarche, "Why does wurtzite form in nanowires of III-V zinc blende semiconductors?", Physical review letters **99**, 146101 (2007).

[131]C.-Y. Yeh, Z. Lu, S. Froyen, and A. Zunger, "Zinc-blende–wurtzite polytypism in semiconductors", Physical Review B **46**, 10086 (1992).

[132]Y. Park, M. J. Cich, R. Zhao, P. Specht, E. R. Weber, E. Stach, and S. Nozaki, "Analysis of twin defects in GaAs (111)B molecular beam epitaxy growth", Journal of Vacuum Science & Technology B: Microelectronics and Nanometer Structures Processing, Measurement, and Phenomena **18**, 1566–1571 (2000).

[133]P. Caroff, K. A. Dick, J. Johansson, M. E. Messing, K. Deppert, and L. Samuelson, "Controlled polytypic and twin-plane superlattices in III–V nanowires", Nature nanotechnology **4**, 50–55 (2009).

[134]Z. Bandić, T. McGill, and Z. Ikonić, "Electronic structure of GaN stacking faults", Physical Review B **56**, 3564 (1997).

[135]J. M. Millunchick, R. Twesten, S. Lee, D. Follstaedt, E. Jones, S. Ahrenkiel, Y. Zhang, H. Cheong, and A. Mascarenhas, "Spontaneous lateral composition modulation in III-V semiconductor alloys", MRS Bulletin **22**, 38–43 (1997).

[136]A. Gomyo, K. Kobayashi, S. Kawata, I. Hino, T. Suzuki, and T. Yuasa, "Studies of $Ga_xIn_{1-x}P$ layers grown by metalorganic vapor phase epitaxy; effects of V/III ratio and growth temperature", Journal of Crystal Growth **77**, 367–373 (1986).

[137]A. Gomyo, T. Suzuki, and S. Iijima, "Observation of strong ordering in $Ga_xIn_{1-x}P$ alloy semiconductors", Physical review letters **60**, 2645 (1988).

[138]T. Kuan, W. Wang, and E. Wilkie, "Long-range order in $In_xGa_{1-x}As$", Applied physics letters **51**, 51–53 (1987).

[139]T. Kuan, T. Kuech, W. Wang, and E. Wilkie, "Long-range order in $Al_xGa_{1-x}As$", Physical Review Letter **54**, 201–204 (1985).

[140]G. Srivastava, J. L. Martins, and A. Zunger, "Atomic structure and ordering in semiconductor alloys", Physical Review B **31**, 2561 (1985).

[141]Y. Kawamura, A. Gomyo, T. Suzuki, T. Higashino, and N. Inoue, "Band-gap change in ordered/disordered $GaAs_ySb_{1-y}$ layers grown on (001) and (111)B InP substrates", Japanese journal of applied physics **41**, L447 (2002).

[142]H. Cho, J. Lee, M. Kwon, B. Lee, J.-H. Baek, and W. Han, "Observation of phase separation and ordering in the InAlAs epilayer grown on InP at the low temperature", Materials Science and Engineering: B **64**, 174–179 (1999).

[143]M. Shahid, S. Mahajan, D. Laughlin, and H. Cox, "Atomic ordering in $Ga_{0.47}In_{0.53}As$ and $Ga_xIn_{1-x}As_yP_{1-y}$ alloy semiconductors", Physical review letters **58**, 2567 (1987).

[144]T. Suzuki, A. Gomyo, and S. Iijima, "Strong ordering in GaInP alloy semiconductors; formation mechanism for the ordered phase", Journal of Crystal Growth **93**, 396–405 (1988).

[145]F. Peiró, A. Cornet, J. Morante, M. Beck, and M. Py, "Surface roughness in InGaAs channels of high electron mobility transistors depending on the growth temperature: strain induced or due to alloy decomposition", Journal of applied physics **83**, 7537–7541 (1998).

[146]G. Grenet, M. Gendry, M. Oustric, Y. Robach, L. Porte, G. Hollinger, O. Marty, M. Pitaval, and C. Priester, "Surface spinodal decomposition in low temperature $Al_{0.48}In_{0.52}As$ grown on InP(001) by molecular beam epitaxy", Applied surface science **123**, 324–328 (1998).

[147]D. Gonzalez, G. Aragon, D. Araujo, M. De Castro, and R. Garcia, "Growth rate and critical temperatures to avoid the modulation of composition of InGaAs epitaxial layers", Applied physics letters **74**, 2649–2651 (1999).

[148]F. Glas, "Elastic state and thermodynamical properties of inhomogeneous epitaxial layers: application to immiscible III-V alloys", Journal of applied physics **62**, 3201–3208 (1987).

[149]F. Glas, "Thermodynamic and kinetic instabilities of lattice-matched alloy layers: compositional and morphological perturbations", Physical Review B **62**, 7393 (2000).

[150]J. Guyer and P. W. Voorhees, "Morphological stability of alloy thin films", Physical review letters **74**, 4031 (1995).

[151]J. Guyer and P. Voorhees, "Morphological stability of alloy thin films", Physical Review B **54**, 11710 (1996).

[152]H. Woo, H. Jo, J. Kim, S. Cho, Y. Jo, C. H. Roh, J. H. Lee, Y. Seo, J. Park, H. Kim, et al., "Phase separation suppression in $In_xGa_{1-x}N$ on a si substrate using an indium modulation technique", Current Applied Physics **17**, 1142–1147 (2017).

[153]D. Follstaedt, R. Twesten, J. M. Millunchick, S. Lee, E. Jones, S. Ahrenkiel, Y. Zhang, and A. Mascarenhas, "Spontaneous lateral composition modulation in InAlAs and InGaAs short-period superlattices", Physica E: Low-dimensional Systems and Nanostructures **2**, 325–329 (1998).

[154] S. Chou, K. Hsieh, K. Cheng, and L. Chou, "Growth of $Ga_xIn_{1-x}As$ quantum wire heterostructures by the strain-induced lateral-layer ordering process", Journal of Vacuum Science & Technology B: Microelectronics and Nanometer Structures Processing, Measurement, and Phenomena **13**, 650–652 (1995).

[155] M. Herrera, D. González, M. Ujúe, Y. González, L. González, and R. Garcıía, "Composition modulation in low temperature growth of InGaAs/GaAs system: influence on plastic relaxation", Microchimica Acta **145**, 63–66 (2004).

[156] J. Yoshida, K. Kishino, D. Jang, S. Nahm, I. Nomura, and A. Kikuchi, "Self-organization mechanism of GalnP quantum wires in $(GaP)_m/(lnP)_m$ short-period binary superlattices for GalnP/AllnP multi-quantum-wire (MQWR) lasers", Optical and quantum electronics **28**, 547–556 (1996).

[157] E. Luna, A. Trampert, J. Miguel-Sánchez, A. Guzmán, and K. Ploog, "Vertical composition fluctuations in (Ga,In)(N,As) quantum wells grown on vicinal (111)B GaAs", Journal of Physics and Chemistry of Solids **69**, 343–346 (2008).

[158] R. J. Malik, *III-V semiconductor materials and devices* (Elsevier, 2012).

[159] J. Matthews and A. Blakeslee, "Defects in epitaxial multilayers: i. misfit dislocations", Journal of Crystal growth **27**, 118–125 (1974).

[160] B. R. Bennett and J. A. del Alamo, "Mismatched InGaAs/InP and InAlAs/InP heterostructures with high crystalline quality", Journal of applied physics **73**, 3195–3202 (1993).

[161] Y. Chen, P. K. Bhattacharya, and J. Singh, "Strained layer epitaxy of InGaAs by MBE and migration enhanced epitaxy—comparison of growth modes and surface quality", Journal of crystal growth **111**, 228–232 (1991).

[162] J. Hornstra, "Dislocations in the diamond lattice", Journal of Physics and Chemistry of Solids **5**, 129–141 (1958).

[163] W.-K. Burton, N. Cabrera, and F. Frank, "The growth of crystals and the equilibrium structure of their surfaces", Philosophical Transactions of the Royal Society of London. Series A, Mathematical and Physical Sciences **243**, 299–358 (1951).

[164] Y. Okano, M. Shigeta, H. Seto, H. Katahama, S. Nishine, and I. Fujimoto, "Incorporation behavior of Si atoms in the molecular beam epitaxial growth of GaAs on misoriented (111)A substrates", Japanese journal of applied physics **29**, L1357 (1990).

[165] M. A. Herman and H. Sitter, *Molecular beam epitaxy: fundamentals and current status*, Vol. 7 (Springer Science & Business Media, 2012).

[166]O. Alerhand, A. N. Berker, J. Joannopoulos, D. Vanderbilt, R. Hamers, and J. Demuth, "Finite-temperature phase diagram of vicinal Si (100) surfaces", Physical review letters **64**, 2406 (1990).

[167]D. Chadi, "Stabilities of single-layer and bilayer steps on Si (001) surfaces", Physical review letters **59**, 1691 (1987).

[168]G. Crook, L. Däweritz, and K. Ploog, "In situ monitoring of step arrays on vicinal silicon (100) surfaces for heteroepitaxy", Physical Review B **42**, 5126 (1990).

[169]T. E. Madey, W. Chen, H. Wang, P. Kaghazchi, and T. Jacob, "Nanoscale surface chemistry over faceted substrates: structure, reactivity and nanotemplates", Chemical Society Reviews **37**, 2310–2327 (2008).

[170]E. Johnson, G. Legg, and J. Curless, "Growth of AlGaAs and GaAs by atmospheric-pressure MOCVD on lenticular substrates", Journal of Crystal Growth **85**, 182–187 (1987).

[171]G. Kramer, R. Tsui, J. Curless, and M. Peffley, "Properties of AlGaAs grown by molecular beam epitaxy on lenticular substrates", GaAs and related compounds, 117 (1974).

[172]R. K. Tsui, G. D. Kramer, J. Curless, and M. S. Peffley, "Substrate misorientation effects on (A1,Ga)As And (Al,Ga)As/GaAs structures grown by molecular beam epitaxy", in Growth of compound semiconductors, Vol. 796 (International Society for Optics and Photonics, 1987), pp. 10–17.

[173]I. Sadeghi, M. C. Tam, and Z. R. Wasilewski, "On the optimum off-cut angle for the growth on inp (111)B substrates by molecular beam epitaxy", Journal of Vacuum Science & Technology B, Nanotechnology and Microelectronics: Materials, Processing, Measurement, and Phenomena **37**, 031210 (2019).

[174]E. A. Paisley, M. D. Losego, B. E. Gaddy, J. S. Tweedie, R. Collazo, Z. Sitar, D. L. Irving, and J.-P. Maria, "Surfactant-enabled epitaxy through control of growth mode with chemical boundary conditions", Nature communications **2**, 1–7 (2011).

[175]M. Copel, M. Reuter, E. Kaxiras, and R. Tromp, "Surfactants in epitaxial growth", Physical review letters **63**, 632 (1989).

[176]E. Tournie, N. Grandjean, A. Trampert, J. Massies, and K. Ploog, "Surfactant-mediated molecular-beam epitaxy of III-V strained-layer heterostructures", Journal of crystal growth **150**, 460–466 (1995).

[177]J. Massies and N. Grandjean, "Surfactant effect on the surface diffusion length in epitaxial growth", Physical Review B **48**, 8502 (1993).

[178]T. Sato, M. Mitsuhara, T. Watanabe, and Y. Kondo, "Surfactant-mediated growth of InGaAs multiple-quantum-well lasers emitting at 2.1 μm by metalorganic vapor phase epitaxy", Applied Physics Letters **87**, 211903 (2005).

[179]S. Johnson, Y. G. Sadofyev, D. Ding, Y. Cao, S. Chaparro, K. Franzreb, and Y.-H. Zhang, "Sb-mediated growth of n-and p-type AlGaAs by molecular beam epitaxy", Journal of Vacuum Science & Technology B: Microelectronics and Nanometer Structures Processing, Measurement, and Phenomena **22**, 1436–1440 (2004).

[180]Y. G. Sadofyev, S. Johnson, S. Chaparro, Y. Cao, D. Ding, J.-B. Wang, K. Franzreb, and Y.-H. Zhang, "Sb-mediated growth of Si-doped AlGaAs by molecular-beam epitaxy", Applied physics letters **84**, 3546–3548 (2004).

[181]S. Tixier, M. Adamcyk, E. Young, J. Schmid, and T. Tiedje, "Surfactant enhanced growth of GaNAs and InGaNAs using bismuth", Journal of crystal growth **251**, 449–454 (2003).

[182]E. Young, S. Tixier, and T. Tiedje, "Bismuth surfactant growth of the dilute nitride GaN_xAs_{1-x}", Journal of crystal growth **279**, 316–320 (2005).

[183]P. T. Webster, N. A. Riordan, C. Gogineni, S. Liu, J. Lu, X.-H. Zhao, D. J. Smith, Y.-H. Zhang, and S. R. Johnson, "Molecular beam epitaxy using bismuth as a constituent in InAs and a surfactant in InAs/InAsSb superlattices", Journal of Vacuum Science & Technology B, Nanotechnology and Microelectronics: Materials, Processing, Measurement, and Phenomena **32**, 02C120 (2014).

[184]D. Kandel and E. Kaxiras, "Surfactant mediated crystal growth of semiconductors", Physical review letters **75**, 2742 (1995).

[185]Y. Horikoshi, "Advanced epitaxial growth techniques: atomic layer epitaxy and migration-enhanced epitaxy", Journal of crystal growth **201**, 150–158 (1999).

[186]J. Arthur Jr, "Interaction of Ga and As_2 molecular beams with GaAs surfaces", Journal of Applied Physics **39**, 4032–4034 (1968).

[187]A. Kawaharazuka and Y. Horikoshi, "Behavior of Ga atoms deposited on GaAs(111)B and (111)A surfaces", Journal of Crystal Growth **477**, 25–29 (2017).

[188]K. Suzuki, M. Ito, and Y. Horikoshi, "Selective growth of GaAs on GaAs(111)B substrates by migration-enhanced epitaxy", Japanese journal of applied physics **38**, 6197 (1999).

[189]T. Uehara, T. Iwai, I. Yoshiba, and Y. Horikoshi, "Area-selective epitaxial growth of GaAs on GaAs(111)A substrates by migration-enhanced epitaxy", Japanese Journal of Applied Physics **46**, 496 (2007).

[190]S. D. Burnham, G. Namkoong, K.-K. Lee, and W. A. Doolittle, “Reproducible reflection high energy electron diffraction signatures for improvement of AlN using in situ growth regime characterization”, Journal of Vacuum Science & Technology B: Microelectronics and Nanometer Structures Processing, Measurement, and Phenomena **25**, 1009–1013 (2007).

[191]H. Woo, J. Kim, S. Cho, Y. Jo, C. H. Roh, J. H. Lee, Y. G. Seo, H. Kim, H. Im, and C.-K. Hahn, “Epitaxial growth of low temperature GaN using metal migration enhanced epitaxy for high-quality InGaN/GaN heterojunctions”, Superlattices and Microstructures **120**, 781–787 (2018).

[192]G. Namkoong, E. Trybus, K. K. Lee, M. Moseley, W. A. Doolittle, and D. C. Look, “Metal modulation epitaxy growth for extremely high hole concentrations above 10^{19} cm^{-3} GaN”, Applied Physics Letters **93**, 172112 (2008).

[193]W. Lau, R. Sodhi, and S. Ingrey, “Thermal desorption of oxides on InP”, Applied physics letters **52**, 386–388 (1988).

[194]D. Comedi, G. Balcaitis, B. Robinson, and D. Thompson, “Study of thermal desorption of UV/ozone oxide on InP”, Canadian journal of physics **70**, 1043–1049 (1992).

[195]R. Averbeck, H. Riechert, H. Schlötterer, and G. Weimann, “Oxide desorption from InP under stabilizing pressures of P_2 or As_4”, Applied physics letters **59**, 1732–1734 (1991).

[196]Y. Horio, J. Yuhara, and Y. Takakuwa, “Structural analysis of an InP(111)A surface using reflection high-energy electron diffraction rocking curves”, Japanese Journal of Applied Physics **58**, SIIA14 (2019).

[197]S. Ingrey, W. Lau, N. McIntyre, and R. Sodhi, “An x-ray photoelectron spectroscopy study on ozone treated InP surfaces”, Journal of Vacuum Science & Technology A: Vacuum, Surfaces, and Films **5**, 1621–1624 (1987).

[198]M. Henini, *Molecular beam epitaxy: from research to mass production* (Newnes, 2012).

[199]C. Bocchi, S. Franchi, F. Germini, A. Baraldi, R. Magnanini, D. De Salvador, M. Berti, and A. Drigo, “Measurement of aluminum concentration in the ga 1- x al x sb/gasb epitaxial system”, Journal of applied physics **86**, 1298–1305 (1999).

[200]G.-C. Wang and T.-M. Lu, *Rheed transmission mode and pole figures: thin film and nanostructure texture analysis* (Springer Science & Business Media, 2013).

[201]S. Johnson, M. Beaudoin, M. Boonzaayer, E. Grassi, and Y.-H. Zhang, "Real-time control of substrate temperature using band edge thermometry", in 2000 digest of the leos summer topical meetings. electronic-enhanced optics. optical sensing in semiconductor manufacturing. electro-optics in space. broadband optical networks (cat. no. 00th8497) (IEEE, 2000), pp. II47–II48.

[202]Y. Leng, *Materials characterization: introduction to microscopic and spectroscopic methods* (John Wiley & Sons, 2009).

[203]M. Hÿtch, E. Snoeck, and R. Kilaas, "Quantitative measurement of displacement and strain fields from hrem micrographs", Ultramicroscopy **74**, 131–146 (1998).

[204]A. Pofelski, S. Woo, B. Le, X. Liu, S. Zhao, Z. Mi, S. Löffler, and G. Botton, "2D strain mapping using scanning transmission electron microscopy moiré interferometry and geometrical phase analysis", Ultramicroscopy **187**, 1–12 (2018).

[205]A. Pofelski, V. Whabi, S. Ghanad-Tavakoli, and G. Botton, "Assessment of the strain depth sensitivity of moiré sampling scanning transmission electron microscopy geometrical phase analysis through a comparison with dark-field electron holography", Ultramicroscopy **223**, 113225 (2021).

[206]S. Kim, S. Lee, Y. Oshima, Y. Kondo, E. Okunishi, N. Endo, J. Jung, G. Byun, S. Lee, and K. Lee, "Scanning moiré fringe imaging for quantitative strain mapping in semiconductor devices", Applied Physics Letters **102**, 161604 (2013).

[207]S. Tanuma, C. Powell, and D. Penn, "Calculations of electron inelastic mean free paths. ix. data for 41 elemental solids over the 50 ev to 30 kev range", Surface and interface analysis **43**, 689–713 (2011).

[208]D. Cornet, R. LaPierre, D. Comedi, and Y. Pusep, "High resolution x-ray diffraction analysis of in ga as/ in p superlattices", Journal of applied physics **100**, 043518 (2006).

[209]P. E. Blöchl, O. Jepsen, and O. K. Andersen, "Improved tetrahedron method for brillouin-zone integrations", Physical Review B **49**, 16223 (1994).

[210]G. Kresse and D. Joubert, "From ultrasoft pseudopotentials to the projector augmented-wave method", Physical review b **59**, 1758 (1999).

[211]J. P. Perdew, K. Burke, and M. Ernzerhof, "Generalized gradient approximation made simple", Physical review letters **77**, 3865 (1996).

[212]C. D. Yerino, B. Liang, D. L. Huffaker, P. J. Simmonds, and M. L. Lee, "Molecular beam epitaxy of lattice-matched InAlAs and InGaAs layers on InP (111)A,(111)B, and (110)", Journal of Vacuum Science & Technology B, Nanotechnology and Microelectronics: Materials, Processing, Measurement, and Phenomena **35**, 010801 (2017).

[213]K. A. Dick, K. Deppert, M. W. Larsson, T. Mårtensson, W. Seifert, L. R. Wallenberg, and L. Samuelson, "Synthesis of branched'nanotrees' by controlled seeding of multiple branching events", Nature materials **3**, 380–384 (2004).

[214]K. Hiruma, T. Katsuyama, K. Ogawa, M. Koguchi, H. Kakibayashi, and G. Morgan, "Quantum size microcrystals grown using organometallic vapor phase epitaxy", Applied physics letters **59**, 431–433 (1991).

[215]J. E. Ayers, T. Kujofsa, P. Rago, and J. Raphael, *Heteroepitaxy of semiconductors: theory, growth, and characterization* (CRC press, 2016).

[216]S. Adachi, "Gaas, alas, and al x ga1- x as: material parameters for use in research and device applications", Journal of Applied Physics **58**, R1–R29 (1985).

[217]S. Adachi, "Iii-v ternary and quaternary compounds", in *Springer handbook of electronic and photonic materials* (Springer, 2017), pp. 1–1.

[218]B. Nosho, W. Weinberg, W. Barvosa-Carter, B. Bennett, B. Shanabrook, and L. Whitman, "Effects of surface reconstruction on iii–v semiconductor interface formation: the role of iii/v composition", Applied physics letters **74**, 1704–1706 (1999).

[219]Z. M. Detweiler, S. M. Wulfsberg, M. G. Frith, A. B. Bocarsly, and S. L. Bernasek, "The oxidation and surface speciation of indium and indium oxides exposed to atmospheric oxidants", Surface Science **648**, 188–195 (2016).

[220]O. Tereshchenko, V. Alperovich, and A. Terekhov, "Composition and structure of chemically prepared gaas (1 1 1) a and (1 1 1) b surfaces", Surface science **600**, 577–582 (2006).

[221]G. Greczynski and L. Hultman, "X-ray photoelectron spectroscopy: towards reliable binding energy referencing", Progress in Materials Science **107**, 100591 (2020).

[222]J. C. Vickerman and I. S. Gilmore, *Surface analysis: the principal techniques* (John Wiley & Sons, 2011).

[223]J. Thornton, P. Unsworth, M. Jackson, P. Weightman, and D. Woolf, "Existence of ga-vacancy and as-trimer induced (2× 2) phases on the gaas (111) a surface", Surface science **316**, 231–237 (1994).

[224]J. Thornton, P. Weightman, D. Woolf, and C. Dunscombe, "Comparison of the (2× 2) reconstructions of gaas {111} surfaces", Physical Review B **51**, 14459 (1995).

[225]H. Bennett and J. Porteus, "Relation between surface roughness and specular reflectance at normal incidence", JOSA **51**, 123–129 (1961).

[226]J. Moison, C. Guille, F. Houzay, F. Barthe, and M. Van Rompay, "Surface segregation of third-column atoms in group iii-v arsenide compounds: ternary alloys and heterostructures", Physical Review B **40**, 6149 (1989).

[227]C. Li, J. Poplawsky, Y. Wu, A. R. Lupini, A. Mouti, D. N. Leonard, N. Paudel, K. Jones, W. Yin, M. Al-Jassim, et al., "From atomic structure to photovoltaic properties in CdTe solar cells", Ultramicroscopy **134**, 113–125 (2013).

[228]C. Li, J. Poplawsky, Y. Yan, and S. J. Pennycook, "Understanding individual defects in CdTe thin-film solar cells via STEM: from atomic structure to electrical activity", Materials Science in Semiconductor Processing **65**, 64–76 (2017).

[229]P. Vannucci, "General anisotropic elasticity", in *Anisotropic elasticity* (Springer, 2018), pp. 19–73.

APPENDICES

Appendix A

Geometrical Phase Analysis (GPA) and STEM Moiré GPA (SMG)

A.1 GPA

To get the strain or displacement field from an High Resolution Electron Micrograph (HREM) the signal is first described in Fourier series since the atomic arrangement highlights a 2D periodic pattern. If the crystal is perfectly periodic the complex Fourier coefficient is constant on the entire HREM, however, the coefficient locally changes when there is a deformation and displacement from the perfect position. Equation A.1 describes the distribution of the intensity collected on an HREM, I(r), as a function of the position r, the crystalline wave vector g and the complex Fourier coefficient $H_g(r)$. The complex Fourier coefficient, $H_g(r)$ can be written as in Eq. A.2:

$$I(r) = \sum_g H_g exp(2\pi g.r) \tag{A.1}$$

$$H_g = A_g exp(iP_g) \tag{A.2}$$

where the modulus A_g gives the amplitude of the set of sinusoidal lattice fringes g, and the phase P_g gives the lateral position of the fringes within the original image. The phase $2\pi g.r + P_g(r)$ embeds the structural properties of the crystal. To describe variations in the image of contrast and fringe position, the Fourier components, H_g, to become a function of position:

$$I(r) = \sum_{g} H_g(r) exp(2\pi g.r) \tag{A.3}$$

The coefficients $H_g(r)$ can be interpreted as the local value of the Fourier components H_g in the image. To show how these functions can be expressed in Fourier space, we begin with the Fourier transform of the image intensity, $\widetilde{I}(k)$, as defined by the following equation:

$$I(r) = \int\int \widetilde{I}(k) exp(2\pi ikr) d\mathrm{k} \tag{A.4}$$

The Fourier transform of Eq. A.3 is then given by:

$$\widetilde{I}(k) = \sum_{g} \widetilde{H}_g(k) \otimes \delta(k-g) \tag{A.5}$$

which is the convolution of the functions $\widetilde{H}_g(k)$ with the reciprocal lattice vectors u. For the case of a perfect crystal the Fourier transform of the image will be non-zero only at the Bragg positions and the functions $\widetilde{H}_g(k)$ will be delta functions of height H_g. If there are variations in the image, however, the Fourier transform will be non-zero between the Bragg positions. For values of k within one Brillouin zone of the position u we can write:

$$\widetilde{I}_g(k) = \widetilde{H}_g(k-g) \tag{A.6}$$

This can be made explicit by introducing a masking function $\widetilde{M}(k)$ such that

$$\widetilde{M}(k) = 1 \quad \textit{inside the first Brillouin zone} \tag{A.7}$$

$$\widetilde{M}(k) = 0 \quad \textit{outside the first Brillouin zone} \tag{A.8}$$

We can therefore define $H_g(r)$ uniquely by the following equation:

$$\widetilde{H}_g(k) = \widetilde{I}(k+g)\widetilde{M}(k) \tag{A.9}$$

In this way, the Fourier transform of the image intensity, given by Eq. (5), is mapped out in terms of the functions $\widetilde{H}_g(k)$.

A.2 SMG

As a first approximation, the scanning grid is treated as a perfect undistorted grid and the crystal periodicity as a 2D Fourier series according to GPA. Therefore, the acquired image represents the discrete sampling of a 2D periodic function which is equivalent to an infinite sum of sine and cosine functions multiplied by a 2D Dirac comb function with a spatial period corresponding to the pixel size (p) in each direction (x and y in Eq. A.10 and Eq. A.11). These equations thus represent the Moiré hologram i_M as a function of the atomic column position in the crystal i_C (called "crystal signal") with its corresponding set of crystalline lattice fringe wave vectors $\vec{g}_C^k$ ($g_{C_x}^k$ and $g_{C_y}^k$) representing their respective projections in x and y directions with (x,y) representing the position in the 2D real space, and R the set of real numbers) and the sampling parameter p.

$\forall (x,y) \in R^2$

$$i_M(x,y) = \sum_k^{\infty} A_k e^{2\pi i (g_{C_x}^k x + g_{C_y}^k y)} \sum_{n=-\infty}^{\infty} \sum_{n=-\infty}^{\infty} \delta(x - np, y - mp) \tag{A.10}$$

$$i_M(x,y) = i_C(x,y) \sum_{n=-\infty}^{\infty} \sum_{n=-\infty}^{\infty} \delta(x - np, y - mp) \tag{A.11}$$

If a small deformation field is present in the structure, the phase (by allowing A_k to be a function of the position $A_k(x,y)$) or the frequency (by allowing $\vec{g}_C^k$ to be a function of the position $\vec{g}_C^k(x,y) = \vec{g}_{C_{Ref}}^k + \vec{\Delta g}_C^k(x,y)$ of the Fourier series function, will be modified and captured by the Dirac comb sampling as shown in Fig. A.1. The fig. represents the resulting Moiré holograms with their multiple sets of periodic Moiré fringes (Moiré patterns) after considering the superposition of a scanning grid with a periodicity p and a primitive cubic crystal structure with periodicity d_C undergoing different elementary deformations. Using Eq. A.11 and geometrical considerations, it is possible to recover the relative deformation field in real space, by analyzing the Moiré patterns' spacing in the Moiré hologram and the initial difference between the pixel size and the crystal periodicity in a reference area. In the simple cases, as depicted in Fig. A.1, uniaxial and biaxial deformations result in the same structure and orientation of the patterns. Only the frequencies of the Moiré patterns d M are mod-ified when compared to the strained crystal periodicity. Therefore, only the relationship between d_M and d_C is needed to determine the one-to-one correspondence between the Moiré hologram and the crystal structure (except if $p = d_C$ where the periodicity of the Moiré pattern would be infinite).

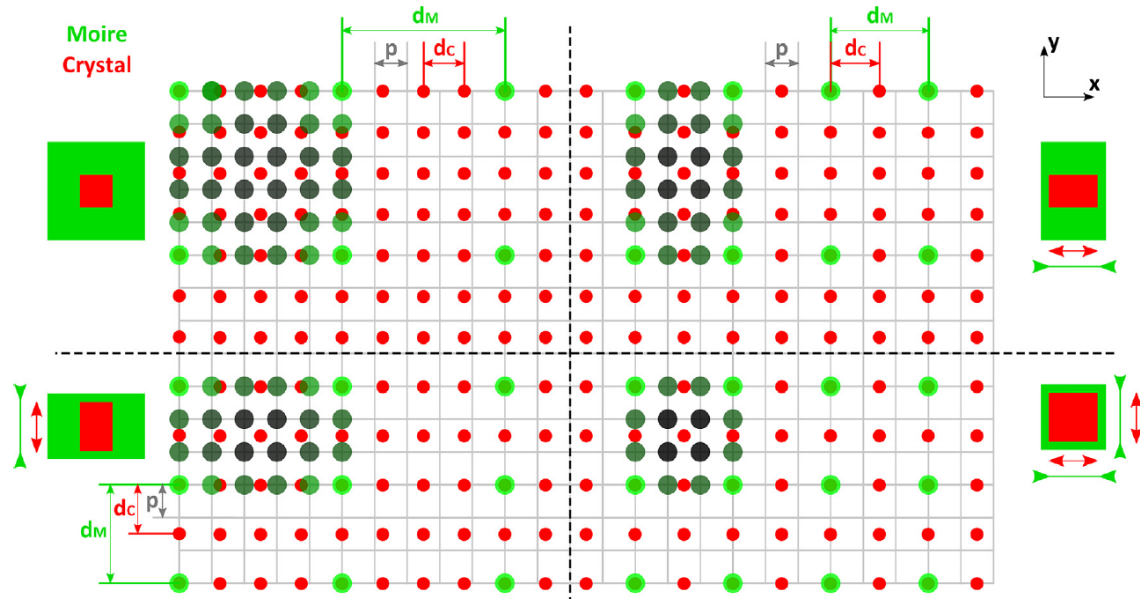

Figure A.1: Schematic illustration of the interference between the scanning grid (located at the intersection of the grey lines) and the atomic columns (red dots) resulting in the Moiré hologram (“greyscale”green dots) for the case $p < d_C$. The brightness of the green dots is related to the interaction between the atomic columns and the nodes of the scanning grid. Considering a Z-contrast mechanism only, the brightness of the green dots thus represents the intensity collected by the HAADF detector at this specific location. Each quadrant represents a relative strain state compared to the unstrained case displayed in the upper left section; upper right and bottom left show a stretch in the x and the y directions, respectively, and bottom right shows a stretch in both directions. With the same deformation field presented above, the Moiré patterns will evolve in an opposite manner (fringe space) for the case p > dc with the same magnitude [204].

Appendix B

Base change for elasticity matrix

For the change of base from B = (O,($\vec{e_1}$), ($\vec{e_2}$), ($\vec{e_3}$)) = (O,[100],[010],[001]) to B^*=(O, $(\vec{m}_1)^*$, $(\vec{m}_2)^*$, $(\vec{m}_3)^*$ = (O,$\frac{1}{\sqrt{2}}[0\bar{1}1]$, $\frac{1}{\sqrt{6}}[\bar{2}11]$, $\frac{1}{\sqrt{3}}[111]$) the transformation matrix Eq. and the rotation matrix are as follows as in Eq. B.1 and Eq. B.2, respectively:

$$\Omega = m_i.e_j = \begin{bmatrix} m_1.e_1 & m_1.e_2 & m_1.e_3 \\ m_2.e_1 & m_2.e_2 & m_2.e_3 \\ m_3.e_1 & m_3.e_2 & m_3.e_3 \end{bmatrix} = \begin{bmatrix} 0 & -0.7 & 0.7 \\ -0.82 & 0.41 & 0.41 \\ 0.58 & 0.58 & 0.58 \end{bmatrix} \tag{B.1}$$

$$R = \begin{bmatrix} R_{11} & R_{12} & R_{13} \\ R_{21} & R_{22} & R_{23} \\ R_{31} & R_{32} & R_{33} \end{bmatrix} = \begin{bmatrix} 0 & -0.82 & 0.58 \\ -0.7 & 0.41 & 0.58 \\ 0.7 & 0.41 & 0.58 \end{bmatrix} \tag{B.2}$$

$$R_{11} = 0$$

$$R_{12} = -0.82$$

$$R_{13} = R_{23} = R_{33} = 0.58$$

$$R_{21} = -0.7$$

$$R_{31} = 0.7$$

$$R_{22} = R_{32} = 0.41$$

The basis change formula for the elasticity tensor is more conveniently expressed in matrix form as in Eq. B.3 [229].

$$C^*_{ijkl} = R_{pi} R_{qj} R_{rk} R_{sl} C_{pqrs} \tag{B.3}$$

$$C^*_{1111} = R_{p1} R_{q1} R_{r1} R_{s1} C_{pqrs} \tag{B.4}$$

$$C^*_{1111} = \sum_{p=1}^{3} \sum_{q=1}^{3} \sum_{r=1}^{3} \sum_{s=1}^{3} R_{p1} R_{q1} R_{r1} R_{s1} C_{pqrs} \tag{B.5}$$

$$\begin{aligned}
C^*_{1111} = {} & R_{11}R_{11}R_{11}R_{11}C_{1111} + R_{11}R_{11}R_{21}R_{21}C_{1122} + R_{11}R_{11}R_{31}R_{31}C_{1133} + R_{11}R_{21}R_{11}R_{21}C_{1212} \\
& + R_{11}R_{21}R_{21}R_{11}C_{1221} + R_{11}R_{31}R_{11}R_{31}C_{1313} + R_{11}R_{31}R_{31}R_{11}C_{1331} + R_{21}R_{11}R_{11}R_{21}C_{2112} \\
& + R_{21}R_{11}R_{21}R_{11}C_{2121} + R_{21}R_{21}R_{11}R_{11}C_{2211} + R_{21}R_{21}R_{21}R_{21}C_{2222} + R_{21}R_{21}R_{31}R_{31}C_{2233} \\
& + R_{21}R_{31}R_{21}R_{31}C_{2323} + R_{21}R_{31}R_{31}R_{21}C_{2332} + R_{31}R_{11}R_{11}R_{31}C_{3113} + R_{31}R_{11}R_{31}R_{11}C_{3131} \\
& + R_{31}R_{21}R_{21}R_{31}C_{3223} + R_{31}R_{21}R_{31}R_{21}C_{3232} + R_{31}R_{31}R_{11}R_{11}C_{3311} + R_{31}R_{31}R_{21}R_{21}C_{3322} \\
& + R_{31}R_{31}R_{31}R_{31}C_{3333}
\end{aligned}$$

$$\begin{aligned}
C^*_{1112} = {} & R_{11}R_{11}R_{11}R_{12}C_{1111} + R_{11}R_{11}R_{21}R_{22}C_{1122} + R_{11}R_{11}R_{31}R_{32}C_{1133} + R_{11}R_{21}R_{11}R_{22}C_{1212} \\
& + R_{11}R_{21}R_{21}R_{12}C_{1221} + R_{11}R_{31}R_{11}R_{32}C_{1313} + R_{11}R_{31}R_{31}R_{12}C_{1331} + R_{21}R_{11}R_{11}R_{22}C_{2112} \\
& + R_{21}R_{11}R_{21}R_{12}C_{2121} + R_{21}R_{21}R_{11}R_{12}C_{2211} + R_{21}R_{21}R_{21}R_{22}C_{2222} + R_{21}R_{21}R_{31}R_{32}C_{2233} \\
& + R_{21}R_{31}R_{21}R_{32}C_{2323} + R_{21}R_{31}R_{31}R_{22}C_{2332} + R_{31}R_{11}R_{11}R_{32}C_{3113} + R_{31}R_{11}R_{31}R_{12}C_{3131} \\
& + R_{31}R_{21}R_{21}R_{32}C_{3223} + R_{31}R_{21}R_{32}R_{21}C_{3232} + R_{31}R_{31}R_{11}R_{12}C_{3311} + R_{31}R_{31}R_{21}R_{22}C_{3322} \\
& + R_{31}R_{31}R_{31}R_{32}C_{3333}
\end{aligned}$$

$$
\begin{aligned}
C^{*}_{1113} = {} & R_{11}R_{11}R_{11}R_{13}C_{1111} + R_{11}R_{11}R_{21}R_{23}C_{1122} + R_{11}R_{11}R_{31}R_{33}C_{1133} + R_{11}R_{21}R_{11}R_{23}C_{1212} \\
& + R_{11}R_{21}R_{21}R_{13}C_{1221} + R_{11}R_{31}R_{11}R_{33}C_{1313} + R_{11}R_{31}R_{31}R_{13}C_{1331} + R_{21}R_{11}R_{11}R_{23}C_{2112} \\
& + R_{21}R_{11}R_{21}R_{13}C_{2121} + R_{21}R_{21}R_{11}R_{13}C_{2211} + R_{21}R_{21}R_{21}R_{23}C_{2222} + R_{21}R_{21}R_{31}R_{33}C_{2233} \\
& + R_{21}R_{31}R_{21}R_{33}C_{2323} + R_{21}R_{31}R_{31}R_{23}C_{2332} + R_{31}R_{11}R_{11}R_{33}C_{3113} + R_{31}R_{11}R_{31}R_{13}C_{3131} \\
& + R_{31}R_{21}R_{21}R_{33}C_{3223} + R_{31}R_{21}R_{31}R_{23}C_{3232} + R_{31}R_{31}R_{11}R_{13}C_{3311} + R_{31}R_{31}R_{21}R_{23}C_{3322} \\
& + R_{31}R_{31}R_{31}R_{33}C_{3333}
\end{aligned}
$$

$$
\begin{aligned}
C^{*}_{1122} = {} & R_{11}R_{11}R_{12}R_{12}C_{1111} + R_{11}R_{11}R_{22}R_{22}C_{1122} + R_{11}R_{11}R_{32}R_{32}C_{1133} + R_{11}R_{21}R_{12}R_{22}C_{1212} \\
& + R_{11}R_{21}R_{22}R_{12}C_{1221} + R_{11}R_{31}R_{12}R_{32}C_{1313} + R_{11}R_{31}R_{32}R_{12}C_{1331} + R_{21}R_{11}R_{12}R_{22}C_{2112} \\
& + R_{21}R_{11}R_{22}R_{12}C_{2121} + R_{21}R_{21}R_{12}R_{12}C_{2211} + R_{21}R_{21}R_{22}R_{22}C_{2222} + R_{21}R_{21}R_{32}R_{32}C_{2233} \\
& + R_{21}R_{31}R_{22}R_{32}C_{2323} + R_{21}R_{31}R_{32}R_{22}C_{2332} + R_{31}R_{11}R_{12}R_{32}C_{3113} + R_{31}R_{11}R_{32}R_{12}C_{3131} \\
& + R_{31}R_{21}R_{22}R_{32}C_{3223} + R_{31}R_{21}R_{32}R_{22}C_{3232} + R_{31}R_{31}R_{12}R_{12}C_{3311} + R_{31}R_{31}R_{22}R_{22}C_{3322} \\
& + R_{31}R_{31}R_{32}R_{32}C_{3333}
\end{aligned}
$$

$$
\begin{aligned}
C^{*}_{1133} = {} & R_{11}R_{11}R_{13}R_{13}C_{1111} + R_{11}R_{11}R_{23}R_{23}C_{1122} + R_{11}R_{11}R_{33}R_{33}C_{1133} + R_{11}R_{21}R_{13}R_{23}C_{1212} \\
& + R_{11}R_{21}R_{23}R_{13}C_{1221} + R_{11}R_{31}R_{13}R_{33}C_{1313} + R_{11}R_{31}R_{33}R_{13}C_{1331} + R_{21}R_{11}R_{13}R_{23}C_{2112} \\
& + R_{21}R_{11}R_{23}R_{13}C_{2121} + R_{21}R_{21}R_{13}R_{13}C_{2211} + R_{21}R_{21}R_{23}R_{23}C_{2222} + R_{21}R_{21}R_{33}R_{33}C_{2233} \\
& + R_{21}R_{31}R_{23}R_{33}C_{2323} + R_{21}R_{31}R_{33}R_{23}C_{2332} + R_{31}R_{11}R_{13}R_{33}C_{3113} + R_{31}R_{11}R_{33}R_{13}C_{3131} \\
& + R_{31}R_{21}R_{23}R_{33}C_{3223} + R_{31}R_{21}R_{33}R_{23}C_{3232} + R_{31}R_{31}R_{13}R_{13}C_{3311} + R_{31}R_{31}R_{23}R_{23}C_{3322} \\
& + R_{31}R_{31}R_{33}R_{33}C_{3333}
\end{aligned}
$$

$$
\begin{aligned}
C^{*}_{2222} = {} & R_{12}R_{12}R_{12}R_{12}C_{1111} + R_{12}R_{12}R_{22}R_{22}C_{1122} + R_{12}R_{12}R_{32}R_{32}C_{1133} + R_{12}R_{22}R_{12}R_{22}C_{1212} \\
& + R_{12}R_{22}R_{22}R_{12}C_{1221} + R_{12}R_{32}R_{12}R_{32}C_{1313} + R_{12}R_{32}R_{32}R_{12}C_{1331} + R_{22}R_{12}R_{12}R_{22}C_{2112} \\
& + R_{22}R_{12}R_{22}R_{12}C_{2121} + R_{22}R_{22}R_{12}R_{12}C_{2211} + R_{22}R_{22}R_{22}R_{22}C_{2222} + R_{22}R_{22}R_{32}R_{32}C_{2233} \\
& + R_{22}R_{32}R_{22}R_{32}C_{2323} + R_{22}R_{32}R_{32}R_{22}C_{2332} + R_{32}R_{12}R_{12}R_{32}C_{3113} + R_{32}R_{12}R_{32}R_{12}C_{3131} \\
& + R_{32}R_{22}R_{22}R_{32}C_{3223} + R_{32}R_{22}R_{32}R_{22}C_{3232} + R_{32}R_{32}R_{12}R_{12}C_{3311} + R_{32}R_{32}R_{22}R_{22}C_{3322} \\
& + R_{32}R_{32}R_{32}R_{32}C_{3333}
\end{aligned}
$$

$$
\begin{aligned}
C^{*}_{1212} = {} & R_{11}R_{12}R_{11}R_{12}C_{1111} + R_{11}R_{12}R_{21}R_{22}C_{1122} + R_{11}R_{12}R_{31}R_{32}C_{1133} + R_{11}R_{22}R_{11}R_{22}C_{1212} \\
& + R_{11}R_{22}R_{21}R_{12}C_{1221} + R_{11}R_{32}R_{11}R_{32}C_{1313} + R_{11}R_{32}R_{31}R_{12}C_{1331} + R_{21}R_{12}R_{11}R_{22}C_{2112} \\
& + R_{21}R_{12}R_{21}R_{12}C_{2121} + R_{21}R_{22}R_{11}R_{12}C_{2211} + R_{21}R_{22}R_{21}R_{22}C_{2222} + R_{21}R_{22}R_{31}R_{32}C_{2233} \\
& + R_{21}R_{32}R_{21}R_{32}C_{2323} + R_{21}R_{32}R_{31}R_{22}C_{2332} + R_{31}R_{12}R_{11}R_{32}C_{3113} + R_{31}R_{12}R_{31}R_{12}C_{3131} \\
& + R_{31}R_{22}R_{21}R_{32}C_{3223} + R_{31}R_{22}R_{31}R_{22}C_{3232} + R_{31}R_{32}R_{11}R_{12}C_{3311} + R_{31}R_{32}R_{21}R_{22}C_{3322} \\
& + R_{31}R_{32}R_{31}R_{32}C_{3333}
\end{aligned}
$$

$$
\begin{aligned}
C^{*}_{1313} = {} & R_{13}R_{13}R_{11}R_{13}C_{1111} + R_{11}R_{13}R_{21}R_{23}C_{1122} + R_{11}R_{13}R_{31}R_{33}C_{1133} + R_{11}R_{23}R_{11}R_{23}C_{1212} \\
& + R_{11}R_{23}R_{21}R_{13}C_{1221} + R_{11}R_{33}R_{11}R_{33}C_{1313} + R_{11}R_{33}R_{31}R_{13}C_{1331} + R_{21}R_{13}R_{11}R_{23}C_{2112} \\
& + R_{21}R_{13}R_{21}R_{13}C_{2121} + R_{21}R_{23}R_{11}R_{13}C_{2211} + R_{21}R_{23}R_{21}R_{23}C_{2222} + R_{21}R_{23}R_{31}R_{33}C_{2233} \\
& + R_{21}R_{33}R_{21}R_{33}C_{2323} + R_{21}R_{33}R_{31}R_{23}C_{2332} + R_{31}R_{13}R_{11}R_{33}C_{3113} + R_{31}R_{13}R_{31}R_{13}C_{3131} \\
& + R_{31}R_{23}R_{21}R_{33}C_{3223} + R_{31}R_{23}R_{31}R_{23}C_{3232} + R_{31}R_{33}R_{11}R_{13}C_{3311} + R_{31}R_{33}R_{21}R_{23}C_{3322} \\
& + R_{31}R_{33}R_{31}R_{33}C_{3333}
\end{aligned}
$$

$$
\begin{aligned}
C^*_{3333} = {} & R_{13}R_{13}R_{13}R_{13}C_{1111} + R_{13}R_{13}R_{23}R_{23}C_{1122} + R_{13}R_{13}R_{33}R_{33}C_{1133} + R_{13}R_{23}R_{13}R_{23}C_{1212} \\
& + R_{13}R_{23}R_{23}R_{13}C_{1221} + R_{13}R_{33}R_{13}R_{33}C_{1313} + R_{13}R_{33}R_{33}R_{13}C_{1331} + R_{23}R_{13}R_{13}R_{23}C_{2112} \\
& + R_{23}R_{13}R_{23}R_{13}C_{2121} + R_{23}R_{23}R_{13}R_{13}C_{2211} + R_{23}R_{23}R_{23}R_{23}C_{2222} + R_{23}R_{23}R_{33}R_{33}C_{2233} \\
& + R_{23}R_{33}R_{23}R_{33}C_{2323} + R_{23}R_{33}R_{33}R_{23}C_{2332} + R_{33}R_{13}R_{13}R_{33}C_{3113} + R_{33}R_{13}R_{33}R_{13}C_{3131} \\
& + R_{33}R_{23}R_{23}R_{33}C_{3223} + R_{33}R_{23}R_{33}R_{23}C_{3232} + R_{33}R_{33}R_{13}R_{13}C_{3311} + R_{33}R_{33}R_{23}R_{23}C_{3322} \\
& + R_{33}R_{33}R_{33}R_{33}C_{3333}
\end{aligned}
$$

According to Voigt's notation:

$11 \rightarrow 1; \quad 22 \rightarrow 2; \quad 33 \rightarrow 3; \quad 12 \rightarrow 4; \quad 13 \rightarrow 5; \quad 23 \rightarrow 6$

Therefore,

$$
C^*_{ijkl} = \begin{bmatrix}
C^*_{1111} & C^*_{1122} & C^*_{1133} & C^*_{1112} & C^*_{1113} & C^*_{1123} \\
C^*_{2211} & C^*_{2222} & C^*_{2233} & C^*_{2212} & C^*_{2213} & C^*_{2223} \\
C^*_{3311} & C^*_{3322} & C^*_{3333} & C^*_{3312} & C^*_{3313} & C^*_{3323} \\
C^*_{1211} & C^*_{1222} & C^*_{1233} & C^*_{1212} & C^*_{1213} & C^*_{1223} \\
C^*_{1311} & C^*_{1322} & C^*_{1333} & C^*_{1312} & C^*_{1313} & C^*_{1323} \\
C^*_{2311} & C^*_{2322} & C^*_{2333} & C^*_{2312} & C^*_{2313} & C^*_{2323}
\end{bmatrix} \tag{B.6}
$$

Considering the cubic symmetry, the stiffness matrix will simplify as in Eq. B.7:

$$
C^*_{ijkl} = \begin{bmatrix}
C^*_{1111} & C^*_{1122} & C^*_{1133} & 0 & 0 & 0 \\
C^*_{1122} & C^*_{2222} & C^*_{2233} & 0 & 0 & 0 \\
C^*_{1133} & C^*_{2233} & C^*_{3333} & 0 & 0 & 0 \\
0 & 0 & 0 & C^*_{1212} & 0 & 0 \\
0 & 0 & 0 & 0 & C^*_{1313} & 0 \\
0 & 0 & 0 & 0 & 0 & C^*_{2323}
\end{bmatrix} \tag{B.7}
$$